AN INVESTIGATION OF THE QUALITY OF UMBILICAL ARTERY DOPPLER WAVEFORMS

Peter R Hoskins BA, MSc

PhD thesis, University of Edinburgh, 1990

Acknowledgements

I would like to thank Professor McDicken for his support and guidance throughout the duration of this thesis. I acknowledge the work performed by my colleagues which I have been able to use in this thesis, namely the design and construction of the flow phantom electronics by Mr T Anderson, the construction of specialist transducer holders by Mr R Borthwick, the mathematical modelling of Doppler speckle by Dr T Loupas, and the machine code for transfer of data from the spectrum analyser to the Archimedes microcomputer by Dr H M Brash. I thank my colleagues in the Royal Infirmary and from Edinburgh University for helpful discussions; namely Dr T Loupas, Mr T Anderson, Dr S Pye, Dr S E Chambers, Dr F D Johnstone, Mr A Millar, Mr I Marshall, Dr R Baldock, Dr R Elton and Mrs C A McIntyre. Thanks to Sisters Mary Compton and Fiona Dagbell, and Glenda White for acquiring the data from which the clinical trial was derived. Thanks to Mrs A MacMillan and Mrs D Nicholson for typing the papers from which much of this thesis was taken. Finally thanks to my parents for their continuing support and help.

I declare that the work contained in this thesis is my own and that the thesis has been composed by myself.

Peter R Hoskins

August 1990

Contents.

page

Abstract

Chapter 1. Introduction. 1

1.1 Medical ultrasonics. 1

1.2 Current ultrasonic instumentation. 1

1.2.1 B- scan devices. 1
1.2.2 Doppler effect. 2
1.2.3 Stand-alone continuous wave Doppler units. . . 2
1.2.4 Duplex systems. 4
1.2.5 Colour flow. 4

1.3 Doppler ultrasound in obstetrics. 5

1.4 Factors affecting umbilical artery Doppler waveforms. . . 12

1.4.1 Physiological variables. 12
1.4.2 Physical and technical factors. 15
1.4.3 Overall variability of waveform indices obtained in clinical practice. 19

1.5 Aims of thesis. 20

Chapter 2. Design and evaluation of a physiological flow phantom. . 22

2.1 Introduction. 22

2.2 Flow phantom. 22

2.3 Evaluation. 29

2.3.1 Flow calibration. 29
2.3.2 Distortion of the waveform shape. 30
2.3.3 Comparison of control waveforms and Doppler waveforms. 32

2.4 Conclusion. 34

Chapter 3. A comparison of the Doppler spectra from human blood and artificial blood used in the flow phantom. . . . 35

3.1 Introduction. 35

3.2 Method. 35

3.2.1 Experimental set up. 35
3.2.2 Measurement of statistical parameters. . . . 38
3.2.3 Measurement of relative Doppler power. . . . 39

3.3 Results. 41

3.4 Discussion. 47

3.5 Conclusion. 47

3.6 Appendix: first order statistics of a Rayleigh variable after baseline shift. 48

Chapter 4. Accuracy of estimation of the maximum frequency envelope and pulsatility index as a function of 3 physical variables. 50

4.1 Introduction. 50

4.2 Literature concerning the detection of the maximum frequency envelope of the Doppler waveform. . . . 50

4.3 Method. 52

4.3.1 Acquisition of Doppler waveforms. 53

4.3.1.1 Beam-vessel angle. 53
4.3.1.2 Misalignment between beam and vessel axes. . 54
4.3.1.3 Thickness of attenuating material. . . . 55

4.3.2 Processing of Doppler waveforms. 55

4.3.2.1 Ensemble averaging of Doppler waveforms. . 55
4.3.2.2 Maximum frequency follower. . . . 55
4.3.2.3 Bias and variability of the maximum frequency envelope. 57
4.3.2.4 Bias and variability of pulsatility index. . . 58

4.4 Results. 63

4.4.1 Effect of beam-vessel angle. 63
4.4.2 Effect of beam-vessel misalignment. . . . 66
4.4.3 Effect of attenuation. 70

4.5 Discussion. 73

4.6 Conclusion. 74

Chapter 5. A comparison of three different filters for speckle reduction of Doppler spectra. 75

5.1 Introduction. 75

5.2 Filtering techniques. 77

5.2.1 Double Window Modified Trimmed Mean (DWMTM) filter. 77
5.2.2 Lee's filter. 79
5.2.3 Directional filtering. 79

5.3 Local image measures. 80

5.3.1 Local statistics. 80
5.3.2 Slope. 81
5.3.3 Edge parameter. 81

5.4 Methods. 82

5.4.1 Data acquisition. 82
5.4.2 Filtering. 84
5.4.3 Ensemble averaged waveforms. 84
5.4.4 Assessment of filter performance. 85

5.5 Results. 87

5.5.1 Parametric images. 87
5.5.2 Comparison of filters. 90

5.6 Discussion. 97

5.7 Conclusion. 97

Chapter 6. The effect of noise reduction algorithms on the maximum frequency envelope and on the pulsatility index. . . 98

6.1 Introduction. 98

6.2 Methods. 98

6.2.1 Filtering of the maximum frequency envelope from unprocessed waveforms. 98
6.2.2 Filtering of the Doppler spectra from unprocessed waveforms. 99

6.3 Results. 100

6.4 Discussion. 103

6.5 Conclusion. 105

Chapter 7. A comparison of three Doppler waveform quality indices. . 106

7.1 Introduction. 106

7.2 Method. 107

7.2.1 Waveform quality indices. 108

7.2.1.1 Correlation of the maximum frequency envelope of successive waveforms. . . . 108
7.2.1.2 Measure of local linearity. 109
7.2.1.3 Frequency content of the Fourier transform of the maximum frequency envelope. . . 109

7.2.2 Dependence of the quality indices on physiological variables. 111

7.2.2.1 Pulsatility. 111
7.2.2.2 Waveform length. 111
7.2.2.3 Fetal breathing. 111

7.2.3 Comparison of quality indices with estimates of the accuracy of the maximum frequency envelope and pulsatility index. 112

7.2.3.1 Correlation of each quality index with MFE_{er} and PI_{er}. 112
7.2.3.2 Performance of each quality index when maximum acceptable values of MFE_{er} and PI_{er} are specified. 113

7.2.4 Assessment of computational efficiency of each quality index.. 113

7.3 Results. 113

7.3.1 Dependence of quality indices on physiological variables. 113
7.3.2 Dependence of quality indices on physical parameters. . 115
7.3.3 Relationship between quality indices and MFE_{er}. . . 117
7.3.4 Relationship between quality indices and PI_{er}. . . 119
7.3.5 Computational efficiency of each quality index. . . 121

7.4 Discussion. 121

7.5 Conclusion. 123

Chapter 8. The use of quality indices on waveforms on which noise reduction algorithms have been applied. 123

8.1 Introduction. 123

8.2 Method. 123

8.3 Results. 123

8.3.1 Dependence of quality indices on physiological variables. 123
8.3.2 Dependence of quality indices on physical variables. . 124
8.3.3 Relationship between quality indices and MFE_{er}. . . 126
8.3.4 Relationship between quality indices and PI_{er}. . . 128

8.4 Discussion. 129

8.5 Conclusion. 131

Chapter 9. A clinical trial of umbilical artery Doppler waveform quality indices. 133

9.1 Introduction. 133

9.2 Methods. 133

9.2.1 Acquisition of data. 134
9.2.2 Calculation of waveform parameters. . . . 134
9.2.3 Subjective assessment of waveforms. . . . 136

9.3 Results. 141

9.3.1 Reproducibility study. 141
9.3.2 Quality index values and envelope scores from the calibrated waveforms. 142
9.3.3 Results for waveforms from patients. . . . 143

9.3.3.1 Assessment of envelope clarity for the data as a whole. 143
9.3.3.2 Dependence of quality indices on various factors. 145
9.3.3.3 Results for the DWMTM filtered envelopes. 149

9.4 Discussion. 151

9.5 Conclusion. 156

Chapter 10. Future work. 157

References. 159

Appendix 1 Program listings. 180

Appendix 2 Publications. 195

ABSTRACT

In Doppler systems which automatically calculate the maximum frequency envelope and pulsatility index (PI) of umbilical artery Doppler waveforms there is the possibility of error in these parameters when the technical quality of the acquired waveform is low. Low quality waveforms may arise when there is an inappropriate set of physical parameters or when there are other sources of noise such as overlying vessels signals. In this thesis the effect of physical parameters on the envelope and on PI are investigated, and also methods for the detection of low quality waveforms are described and tested.

A flow phantom which is able to produce realistic looking umbilical artery Doppler waveforms is described. This is based upon microcomputer control of a stepping motor / gear pump combination. The statistics of the Doppler spectra produced using artificial blood and human blood in the phantom are found to be identical.

The effect of a number of physical parameters on the simulated umbilical artery waveforms produced using the phantom is investigated. The accuracy of estimation of the envelope and the PI is similar over a wide range of physical conditions.

A suitable image processing algorithm for speckle reduction of Doppler waveforms is developed and tested using simulated waveforms from the phantom. Using the flow device it was found that both filtering of the envelope and also speckle suppression of the spectrum improved the accuracy of estimation of the envelope and of the PI.

A number of quality indices based upon the degree of noise of the envelope are described. Using the flow device there is found to be a high correlation between the quality index values, and the errors in PI and errors in envelope estimation respectively. In a clinical trial the quality index values from umbilical arteries were compared with the waveform quality as assessed by a skilled observer. The clinical results show that quality indices are able to separate high and low quality waveforms when the indices are calculated from the unprocessed envelope, but not when calculated from the filtered envelope

Chapter 1.

1.1 Medical ultrasonics.

The non-invasive diagnosis and assessment of disease by ultrasonic techniques is now an established discipline which is practiced worldwide. This widespread use is reflected in the number of ultrasound units which are used; approximately 4000 in the UK and 100 times that number throughout the world. There are 2 basic techniques in diagnostic medical ultrasonics. The first is the depiction of cross sectional anatomy in real time and the second is the provision of information related to the flow of blood. These techniques are considered in the next section.

1.2 Current ultrasonic instrumentation

For detailed information on the physics of ultrasound and the different types of instrumentation in use the reader is referred to the standard textbooks on the subject; examples of which include Wells (1977), Hill (1988), McDicken (1981) and Evans et al (1989).

1.2.1 B-scan devices.

Most ultrasonic imaging is now performed using real time devices. A hand held probe is placed on the skin and ultrasound transmitted into the patient at a frequency of typically 3 to 10 MHz along a focused beam. Scattering of the ultrasound occurs in the tissue and a portion of this is detected by the transducer. The time delay of the received echoes is used to derive the depth from which the echo arose, and the power of the echo is used to modulate the brightness of the display. This is called brightness mode or B-mode scanning. The image is built up line by line at a rate sufficient to enable images to be acquired with rapid repositioning of the transducer. This allows a large volume of tissue to be interrogated quickly. Real time scanning also allows the visualisation of moving structures. A number of transducer types are used to sweep the beam through the tissue, such as linear or curvilinear arrays, mechanical sector transducers, phased array and annular arrays. Improvements in the ultrasonic image quality have

occured from the sixties to the present. Many modern scanners have multi-element transducers in which the formation and reception of the beam are controlled by a computer allowing the production of high resolution images. Improvements in digital electronic processing speed have made possible advanced techniques of real time processing of the ultrasonic images. Examples of this include automatic time gain compensation and speckle suppression.

1.2.2 Doppler Effect

The change in frequency produced by the scattering of waves by a moving object is a general effect called the Doppler effect. Using ultrasonic equipment the Doppler shift δF is given by equation 1.1 below.

$$\delta F = 2F \frac{v}{c} \cos(\theta) \qquad \text{eqn. 1.1}$$

where F is the transmitted frequency

v is the velocity of blood

θ is the beam-vessel angle

c is the speed of sound in tissue

Typically the transmitted frequency is 2-8 MHz. In arteries velocities up to 5 or 6 ms^{-1} are present producing Doppler shift frequencies up to about 20 kHz which is just within the audible range. Doppler ultrasound is mostly used to obtain velocity information from moving blood however any moving object will produce a Doppler shift. High amplitude low frequency signals produced by vessel walls moving during the cardiac cycle are filtered out by a high pass filter. Occasionally other moving structures such as the fetus produce high amplitude signals which may obliterate the Doppler signal from blood.

1.2.3 Stand alone continuous wave Doppler units

In these devices a simple pencil probe is used. Continuous wave ultrasound is emitted in a fixed direction by a transmitting element and detected by an adjacent

receiving element. The Doppler shift signal is extracted and presented in real time as a spectrum (figure 1.1). This is a display of the Doppler frequency shift against time. The Doppler frequency shift is calculated every 5-10ms. The intensity at a particular point is related to the amount of blood moving at the corresponding velocity v.

Using a stand alone continuous wave device there is no information supplied by the machine regarding the depth or location of the vessel. This limits the use of these devices to those vessels with well defined locations separate from other vessels, and to those vessels which show well defined waveform shapes.

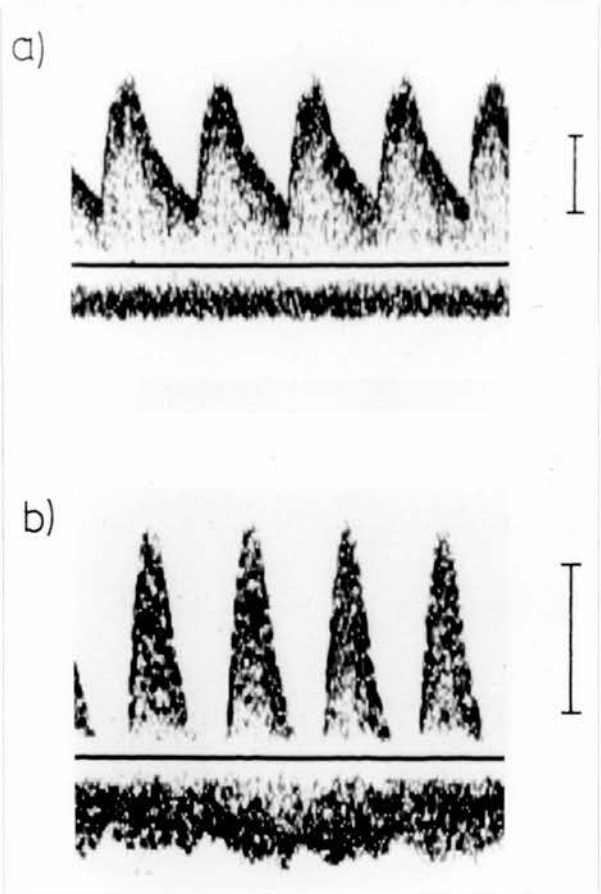

Figure 1.1. Umbilical artery Doppler waveforms acquired using a 4MHz continuous wave Doppler unit. The vertical bar indicates a 1 kHz Doppler shift. a) normal waveforms, b) abnormal waveforms.

1.2.4 Duplex systems.

A duplex system is a combination of a B-scan device and a Doppler device. A dotted line along the B-scan image can be used to give the direction of the Doppler beam. The use of pulsed Doppler enables blood flow information to be acquired from a known location along the beam. The location is identified by a cursor which can be manually moved along the line. Visualisation of the vessel in relation to the direction of the Doppler beam enables the beam vessel angle to be measured and the spectrum to be calibrated in units of velocity. A number of configurations of duplex system are available commercially. Use of a linear array or phased array allows simultaneous real time B-scanning and display of Doppler waveforms. Simultaneous real time display using a mechanical sector scanner is more difficult as the B-scan transducer must move in order to update the B-scan, and the vibrations produced are detected by the Doppler device. This usually necessitates switching the Doppler detector off during B-scan update.

1.2.5 Colour flow

Using a duplex system blood flow information is obtained from one particular location within a vessel. A colour flow system combines B-scan imaging with a superimposed real time colour image representing the flow of blood. The basic Doppler information presented at a particular point is the mean velocity. Shades of red and blue are usually used to represent velocities away from and towards the transducer. The Doppler signal processor also produces an index called variance based upon the variability over short time periods of the Doppler signal. This quantity is related to the degree of turbulence present in the flow. The variance can be displayed separately, typically as a shade of green, or mixed in with the red and blue. As with duplex systems there are a number of configurations of colour flow systems. Using linear and phased array systems simultaneous real time B-scanning and colour flow Doppler is possible. Using mechanical sector scanning this is more difficult for the reasons mentioned above. The image quality of colour

flow systems has improved considerably since their introduction in 1982. Signal processing can be performed to suppress the display of colour on moving tissue, and also to increase the sensitivity to low velocities. Use of a duplex or colour flow system is essential for obtaining Doppler signals when there are a number of closely lying vessels such as in the abdomen or fetus.

1.3 Doppler ultrasound in obstetrics

Over the last decade there has been an enormous increase in the use of non-invasive tests for the assessment of fetal growth and fetal well being. Typically a high risk pregnancy can expect to be monitored using ultrasonic imaging for assessment of fetal size, cardiotocography and biophysical profiles. In recent years there has been increasing interest in the use of Doppler ultrasound to investigate blood flow in pregnancy. Two approaches have been taken; volume flow measurement and Doppler waveform analysis. For accurate measurements of flow considerable attention must be paid to the technique used as there are a number of sources of potential error, (for example see Eik-Nes et al (1984) and Evans (1986)). Also a duplex system is essential for volume flow estimation, whereas umbilical and utero-placental waveforms have been acquired using stand alone continuous wave units. Flow has been measured in the fetal aorta (Chen et al 1988, Eik-Nes et al 1984), and in the umbilical vein (Gill et al 1984, Warren et al 1988). Using specially designed equipment the group from Sydney (Gill and co-workers) have made high quality measurements of flow in the umbilical vein and compared these with umbilical artery waveform analysis. They claim that the assessment of flow is a more accurate predictor of risk than waveform analysis. This technique could be of general interest in the future if accurate flow measurements are more readily available, however at present most centres perform only waveform analysis. The remainder of this section is devoted to waveform analysis.

In the normal placenta there is a reduction of the resistance to flow throughout pregnancy which is attributed to the continued growth and proliferation of the

tertiary stem villi (Cohen-Overbeek et al 1985). Doppler waveforms from the umbilical, utero-placental and fetal arteries have been used to assess the resistance to flow of the placenta; a high resistance indicative of disease being associated with a high pulsatility (figure 1.1). The degree of diastolic flow is characterised by simple indices of the maximum frequency envelope such as resistance index (RI) (Pourcelot 1974), pulsatility index (PI) (Gosling and King 1974), (figure 1.2), or A/B ratio (Stuart et al 1980). The basis of this approach came from observational studies made on other arteries where it was noticed that distal vasodilation resulted in increased diastolic flow and loss of pulsatility of the Doppler waveform. In the obstetric field a number of studies have been performed to investigate the validity of this approach. An increase in the pulsatility of umbilical artery Doppler

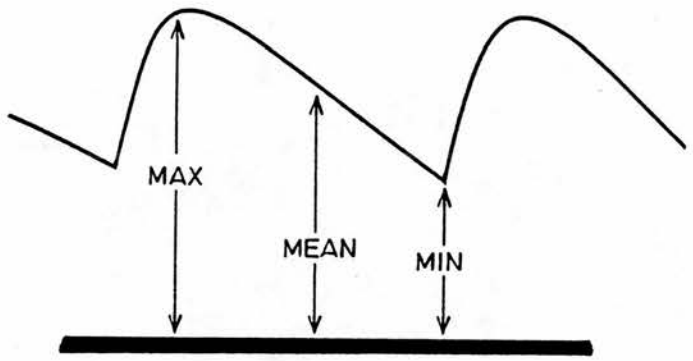

$$RI = \frac{MAX - MIN}{MAX} \qquad PI = \frac{MAX - MIN}{MEAN}$$

Figure 1.2. Two commonly used indices for characterisation of the waveform pulsatility; RI (resistance index) and PI (pulsatility index).

waveforms was associated with a decrease in the number of small arteries from the terminal villi of the placenta (Giles et al 1985, McCowan et al 1987a). Using fetal lambs it has been shown that blockade of the placental vasculature by acute embolisation with microspheres is associated with elevated pulsatilty of the umbilical artery waveform (Trudinger et al 1987b, Nimrod et al 1989, Maulik et al 1989b, Morrow et al 1989), and of fetal aorta waveforms (Noordam et al 1987). Of most interest in terms of a scientific framework to the subject is the relationship between the distal resistance assessed using arterial pressure and flow measurments, and the Doppler waveform pulsatility. This has been investigated for the umbilical artery by Nimrod et al (1989), Morrow et al (1989) and Adamson et al (1990). The first two of these studies show good correlation between the A/B ratio and the placental resistance when acute blockade of the placental circulation was performed, however both of these studies have methodological problems. Nimrod et al (1989) make no mention of pressure measurements which are essential to calculate resistance, and Morrow et al (1989) estimate flow from the time averaged Doppler maximum frequency envelope which makes the unproven assumption that the umbilical artery diameter remains unchanged throughout the study. The excellent study by Adamson (1990) showed that there is a high correlation between placental resistance and umbilical artery RI and PI for placental blockade by microspheres. They also infused a vasoconstrictor, angiotensin II, into the circulation. This produced increased resistance of the umbilical artery, but caused no change in the resistance of the placenta or the umbilical vein, and most significantly produced no significant change in the RI and PI of the umbilical artery waveforms. A complementary approach to experimental work is that of mathematical modelling. Thomson et al (1989) modelled the placental circulation and predicted that umbilical artery PI is related to the ratio of the placental resistance to the umbilical artery resistance. It should be noted that this does not fit in with the experimental measurements of Adamson et al (1990). Thomson et al

(1989) also predicted that umbilical artery pulsatility increases when placental vessels are obliterated and when their diameter is reduced. For the utero-placental circulation Clewell et al (1988) could find no correlation between distal resistance and uterine artery PI values in 3 sheep. Computer modelling of the utero-placental circulation has been performed by the group from Toronto (Mo et al 1988a, Adamson et al 1989). They predicted that increased utero-placental vascular resistance causes the appearance of a dicrotic notch in the velocity waveform, and also of elevated pulsatility. For the fetal cerebral circulation there have been no specific measurements on the relationship between cerebral resistance and the cerebral artery waveforms. In conclusion for this discussion, though there is still much work to be done it seems clear, at least for the umbilical artery waveforms, that increases in waveform pulsatility are associated with increases in resistance to flow at the placental level.

The A/B ratio is mathematically related to the RI (RI=1-1/(A/B)), so will not be referred to further, except where necessary for specific studies. The relationship between waveform indices for the umbilical artery has been considered by a number of authors. Thomson et al (1986) showed that RI and PI were highly correlated except when there was absent end diastolic flow. Hoskins et al (1989b) showed that RI and PI performed identically in discriminating those fetuses who went on to develop fetal compromise. There appears to be no strong tendency to use one or the other of RI and PI in the literature, so both will be referred to in this thesis.

The acquisition of Doppler waveforms from the umbilical cord can be performed using a non-imaging continuous wave system (Fitzgerald and Drumm 1977, Brar et al 1988), whereas for fetal vessels it is necessary to use a duplex or colour flow system. Waveforms from the more complex utero-placental circulation have been obtained using continuous wave and duplex systems. Using a duplex system it has been claimed that waveforms can be obtained from the arcuate

arteries (Campbell et al 1983), however these vessels are difficult to identify. Using a continuous wave system it is impossible to tell which level of branching is being considered, and it is known that this will affect the pulsatility of the waveforms (Bewley et al 1989, Mehalek et al 1989). A further error arises because of the similarity between waveforms from the internal iliac artery and abnormal utero-placental waveforms (Pearce and MacParland 1988). Studies have also been performed demonstrating that utero-placental waveforms have lower pulsatility when taken from the placental side of the uterus (Chambers et al 1988, Kofinas et al 1988, Bewley et al 1989). The use of colour flow for visualisation of utero-placental arteries may help in the establishment of a more reproducible and accurate technique.

Many clinical studies have considered the application of Doppler ultrasound to intra-uterine growth retardation (IUGR). Early reports using umbilical artery waveforms described the positive association between increased pulsatility and

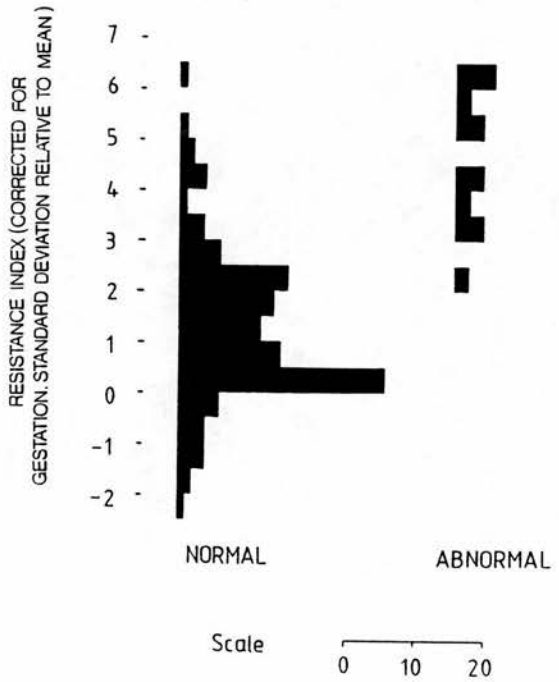

Figure 1.3. Histogram of RI values for patients with and without fetal compromise (redrawn from Chambers et al 1989 with permission).

IUGR (Reuwer et al 1984, Erskine and Ritchie 1985, Trudinger et al 1985a, Fleischer et al 1985). Later reports have focused on the prediction of fetal compromise (Trudinger et al 1985b, Reuwer et al 1987, Rochelson et al 1987, Laurin et al 1987, Haddad et al 1988, Johnstone et al 1988). Comparative studies between utero-placental and umbilical (Gudmundsson and Marsal 1988, Mulders et al 1989) and also abdominal circumference measurements (Chambers et al 1989) have been performed. All 3 studies demonstrated that prediction of fetal compromise was best performed using the umbilical artery (Specificities of 80% and 77% respectively for Mulders et al (1989) and Chambers et al (1989) for a sensitivity of 100%) (figure 1.3). The results for utero-placental waveforms were more variable with only Mulders et al (1989) reporting a high specificity (Specificities of 64% and 2% respectively for Mulders et al (1989) and Chambers et al (1989) at a sensitivity of 100%). This variability may be associated with the previously discussed difficulty in obtaining utero-placental waveforms from known and reproducible sites. Chambers et al (1989) demonstrated that identification of the small-for-dates baby using Doppler was poor compared to the standard technique of fetal abdominal circumference measurement using B-scan imaging. In other high risk groups such as diabetics Doppler waveform analysis from the umbilical artery has not been correlated with fetal compromise (Johnstone et al, in press). This has been attributed to the multifactoral nature of diabetes.

The use of umbilical artery Doppler waveform analysis in a screening population has been considered by Beattie and Dornan (1989) and Hanretty et al (1989). Beattie and Dornan (1989) considered a number of clinical endpoints including centile birthweight for gestation, ponderal index, cord blood pH and packed cell volume, but umbilical waveforms did not adequately predict any of these. Johnstone et al (1989) in a discussion of the paper by Beattie and Dornan (1989) comment that umbilical waveform analysis is perhaps more suited to the prediction of fetal compromise in a high risk population, rather than for use as a

screening tool. The use of utero-placental waveform analysis during the second trimester in a screening population has been considered by Campbell et al (1986), Arduini et al (1987) Steel et al (1988b) and Hanretty et al (1989). The first 3 of these studies have suggested that patients with abnormal waveforms are more likely to develop hypertensive disorders of pregnancy and IUGR, however this has not been supported by Hanretty et al (1989).

A number of groups have studied the fetal circulation. Fetal aorta waveform pulsatility was elevated in many cases of IUGR (Joupilla et al 1984, Griffin et al 1984, Tonge et al 1986). A study of fetal renal artery waveforms demonstrated elevated pulsatility in small for gestational age fetuses (Vyas et al 1989). Waveforms from the fetal internal carotid, middle cerebral, posterior cerebral and anterior cerebral arteries have been acquired (Wladimiroff et al 1986, 1988, Woo et al 1987, Lang et al 1988, Veille and Cohen 1990), and in IUGR the pulsatility of these waveforms decreases. It has been suggested that this is indicative of redistribution of blood flow within the fetus to favour brain blood flow.

The relationship between Doppler waveforms and fetal hypoxia, as assessed using umbilical vein blood gases, has been examined by Tyrrell et al (1989) and Bilardo et al (1990). Bilardo et al (1990) acquired waveforms from a number of vessels and found that the best correlation with a measure of asphyxia came from a combination of the fetal common carotid PI and the fetal aorta mean velocity. This combination of indices seems to be related to the changes in flow pattern occuring during brain-sparing, which suggests that this approach, though more complex, may be more sensitive than the use of individual waveforms such as the umbilical artery. Clearly more work needs to be done in this area.

There has been one small randomised trial of the use of Doppler in obstetrics. Trudinger et al (1987a) using umbilical artery waveforms reported that the availability of Doppler measurements reduced the incidence of fetal distress and caesarian section in labour. It is generally perceived that there is insufficient

knowledge to justify the widespread use of Doppler in obstetrics (Redman 1989, Neilson 1987), and that further work is needed.

1.4 Factors affecting umbilical artery Doppler waveforms

Though not yet proven, the use of umbilical artery Doppler ultrasound as a long term predictor of fetal compromise shows considerable promise. The technique relies upon identification of the maximum frequency envelope, and calculation of RI and PI to characterise waveform pulsatility. A number of factors apart from disease will affect the calculated RI and PI values. These factors will be considered in terms of physiological factors, and physical and technical factors.

1.4.1 Physiological factors.

In the normal pregnancy diastolic flow is initially absent, but appears abruptly at between 11 and 14 weeks, which it has been suggested is consistent with tertiary villous vascular formation (Fisk et al 1988, Loquet et al 1988). Pulsatility drops steadily from about 16 weeks to term (Fitzgerald et al 1984, McCowan et al 1987b, Pearce et al 1988, Hendricks et al 1989). These studies show that from 18 to 40 weeks mean RI falls from 0.8 to 0.55 (30% drop), and mean PI falls from 1.3 to 0.8 (40% drop). The normal spread at a particular gestational age can be described by the coefficient of variation; for RI this is 10 to 17%, and for PI is 15 to 17%. Most clinical studies do not correct waveform indices for gestational age, however this has been performed by Chambers et al (1989).

Fetal breathing describes the movements made by the chest and diaphragm of the fetus. If there is strong fetal breathing then considerable modulation of the waveform results (Fouron et al 1975, Hoskins et al 1988b). Many studies in the literature report acquisition of umbilical artery waveforms during fetal apneoa, and this is certainly desirable when it can be achieved, however in practice the fetus can breathe for prolonged periods. Patrick et al (1978, 1980) studied fetal breathing movements over a 24 hour period and found them to be present, on average for 31% of the time. During any one period breathing movements occured from 0% up

to 86% of the time. Hoskins et al (1988a) studied the RI and PI of good quality waveforms from 20 patients during periods of fetal breathing and fetal apneoa. The average values considered for the 20 patients as a whole were lower during breathing by 0.03 for RI and 0.10 for PI. This was considered to be a small effect. The within patient variability of RI and PI was higher during breathing, however the standard error of the mean could be reduced by averaging over more waveforms. For a standard error in RI of 0.015 or less, and in PI of 0.038 or less it was recommended that during fetal apneoa the average of 5 waveforms should be taken, whereas during breathing the average of 15 waveforms should be used, and that waveforms obtained during strong fetal breathing should be rejected. This is the current practice in our hospital. This approach is perhaps not ideal, however in a unit in which 1500 separate studies were performed in 1989, it is an attempt to overcome the very real logistical problems which would be encountered if waveforms were always obtained during fetal apneoa.

Variation in fetal heart rate is a factor which might be expected to influence RI and PI values. Intuitively it might be expected that when the heartrate decreases, the blood velocities in the umbilical artery have more time to reach a lower value,

Author	Correlation Coefficient
Mires et al 1987	0.49 to 0.65
Fairlie et al 1988	0.61
Kofinas et al 1989	0.36
Yarlgooda et al 1989	0.48 to 0.61

Table 1.1. Correlation coefficients for fetal heartrate versus A/B ratio of umbilical artery Doppler waveforms. (The A/B ratio has been reported in this table rather than RI or PI as it is common to the above 4 papers.)

hence RI, PI and also the A/B ratio will increase. A number of studies have been performed in which the correlation between heartrate and waveform indices has been investigated, (table 1.1). All of these studies demonstrate some degree of correlation between the heartrate and the A/B ratio, which is consistent with the above hypothesis. Some of these studies conclude that it is worth correcting for heartrate (Mires et al 1987), while others conclude that correction is unnecessary (Kofinas et al 1989). From these studies, where waveforms from different patients have been correlated, it is unclear what the relationship is between waveform indices and heartrate for individual patients. This is of interest since it raises the possibility of using a normalised index to reduce the within patient coefficient of variation. Hoskins et al (1989a) investigated the dependence of RI and PI on beat to beat pulse length over short time intervals for 20 individual patients. A least squares regression line was fitted to the data for each patient and normalised indices calculated based upon the slope of the line. This led to a reduction in the average coefficient of variation from 4.3% to 3.6% for RI and from 6.8% to 5.1% for PI. Acquisition of a large number of waveforms in order to derive a regression line for normalisation is impractical in the clinical situation. A common normalisation formula was derived which could be applied to individual waveforms. This led to a coefficient of variation of 3.9% for RI, which was not significantly different from the coefficient of 4.3% for the non-normalised RI values, and of 6.1% for PI, which was significantly lower than the coefficient of 6.8% for the non-normalised PI values. The very small changes in the coefficient of variation after normalisation led to the conclusion that it is not worth correcting short term changes in RI and PI values for heartrate.

The dependence of cord sampling site on waveform indices has been reported by Abramawicz et al (1989) and Mehalek et al (1989) who noted lower A/B values at the placental end of the cord compared to the fetal end of 28% and 15% respectively. This is consistent with the higher downstream resistance to flow at the

fetal end of the cord. These studies indicate that the cord sampling site could be important, however most studies, which are performed using non-imaging continuous wave Doppler units, do not take this into account.

Other factors such as behavioural state (van Eyck et al 1987, 1988) and blood viscosity (Steel et al 1988a, 1989) have been reported to affect umbilical artery waveforms. In general, apart from fetal breathing, no attempt is made to standardise for or to correct for physiological variables which could affect the umbilical artery Doppler waveforms.

1.4.2 Physical and technical variables.

Relatively little attention has been given to the physical and technical factors which influence the calculated PI and RI values. Two sources of variability are relevant. Firstly the factors influencing the Doppler spectrum, and secondly the inaccuracy and variability arising as a result of the estimation of RI and PI from the Doppler spectrum.

The Doppler ultrasound signal from blood contains a spectrum of frequencies whose amplitude is related to the velocity distribution of blood in the vessel. The relationship between the velocity distribution of blood $\Phi(v)$ in the vessel at a particular time and the Doppler frequency amplitude profile $\Psi(\delta F)$ is influenced by a number of physical factors. These factors can be illustrated with reference to steady flow, which has a parabolic velocity profile with maximum velocity v_{max}, and a velocity distribution as shown in figure 1.4a. A Doppler spectral profile will typically have the appearance shown in figure 1.4b. This was obtained from a continuous wave Doppler unit where the beam-vessel angle was 55^{o}, and the transducer-vessel depth was 5 cm. This spectral profile is very noisy. This noise is called Doppler speckle which is a characteristic of Doppler spectra derived from Fourier transform based spectrum analysers, and is considered in more detail in chapter 2. The spectral amplitude can be considered to be made up of an underlying component $\Psi_u(\delta F)$ and a Doppler speckle (noise) component $\Psi_n(\delta F)$,

such that;

$$\Psi(\delta F) = \Psi_u(\delta F) + \Psi_n(\delta F) \qquad \text{eqn. 1.2}$$

In chapter 2 it will be shown that the spectra are not correlated along the time axis. In this case, for steady flow, averaging over N adjacent spectral profiles will reduce the noise level by a factor of $(N)^{1/2}$. For large values of N the noise is reduced sufficiently to reveal the underlying spectral profile $\Psi_u(\delta F)$, which is shown in figure 1.4c. In the absence of other effects, which are considered later in this section, the shape of $\Psi_u(\delta F)$ is largely determined by the interaction between

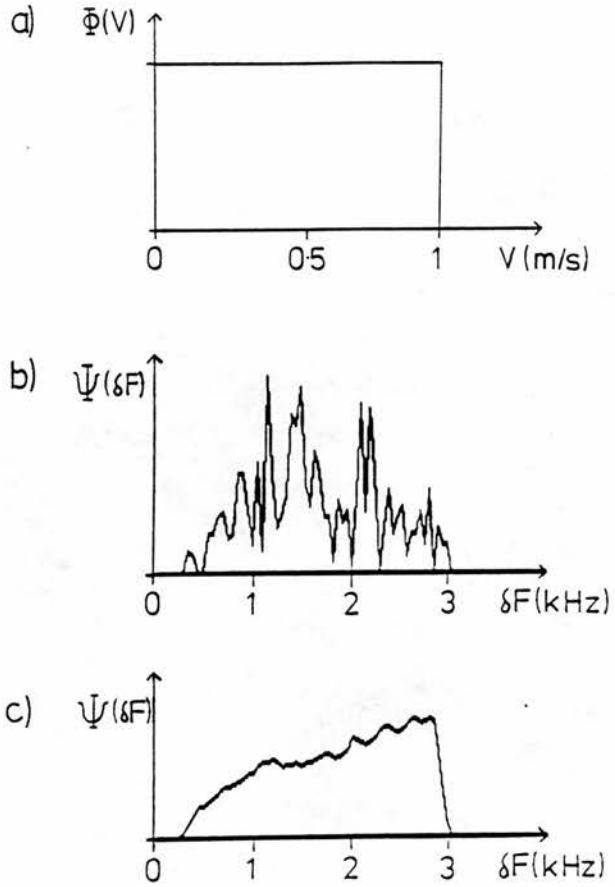

Figure 1.4. a) Velocity distribution $\Phi(v)$ for steady flow of maximum velocity v_{max} of approximately 1m/s. b) Typical single amplitude spectral profile $\Psi(\delta F)$ from a continuous wave Doppler unit. c) Underlying amplitude spectral profile $\Psi_u(\delta F)$ obtained by averaging 240 consecutive profiles.

the ultrasound beam and the pattern of flow of blood in the vessel. If the ultrasound beam uniformly insonates the vessel then all the velocity components will be equally represented in the Doppler signal. Non-uniform insonation has been studied using computer simulations for the case of a coaxial beam and vessel by Evans (1982), and for the case of misalignment between the beam and vessel by Cobbold et al (1983). For alignment of the vessel and beam, non-uniform insonation leads to reduction of the low frequency components of the Doppler signal, which is the case for figure 1.4c. For misalignment of the beam and vessel there is some loss of high frequency componenents. If non-uniform insonation was the only physical effect occuring a sharp cut-off in $\Psi_u(\delta F)$ would be expected at the maximum frequency. $\Psi_u(\delta F)$ is not sharp due to intrinsic spectral broadening. This arises due to the finite size of the transducer, which results in the velocity vector of each red cell in the ultrasound beam subtending a range of angles, hence producing a range of Doppler shifts. This has been investigated over a number of years by Newhouse's group. Early papers used simple geometrical models of the beam pattern (Newhouse et al 1980). In a recent publication using diffraction methodology (Censor et al 1988) they showed that the bandwidth δF_d of the spectral broadening will be;

$$\delta F_d = \frac{2v\ D}{R\ \lambda} \sin(\theta) \qquad \text{eqn. 1.3}$$

where R is the focal distance, v is the blood velocity, D is the transducer diameter, and λ is the wavelength. The sin θ dependence of δF_d should be contrasted to the cos θ dependence of the main Doppler shift component (equation 1.1). This makes intrinsic spectral broadening of most importance for angles near 90^o.

Commonly a continuous wave non-imaging system is used for acquisition of umbilical artery Doppler waveforms. With this system the operator has no independent knowledge of the beam-vessel angle, vessel depth or the degree of

alignment between the beam and the vessel. The question then arises as to how these factors affect the calculated RI and PI values.

A number of other characteristics of the Doppler spectrum can be attributed to the instrument. Figure 1.4c shows that no signal is present for low frequencies. This is due to the high pass filter in the Doppler detector, which is necessary to remove low frequency large amplitude components arising as a result of vessel wall pulsation. The received Doppler power will vary, depending on such factors as the number of red cells in the sample volume and the thickness of the tissue between the vessel and the transducer. In order to display the waveforms at the correct intensity levels the user has control over the amplifier gain. If the signal strength is low, the high gain necessary for display leads to the appearance of amplifier noise on the spectrum. If the signal strength is higher, then a high gain will lead to saturation of the amplifier output. This produces additional spectral components which appear as a 'ghosting' of the original signal. This effect is most noticeable when high amplitude low frequency components are produced by fetal movement or transducer movement across the skin. The resulting distortion can completely obliterate the desired arterial waveforms. Other vessels may also intersect the Doppler beam giving rise to masking of the desired arterial signal.

All of the above factors can influence the identification of the maximum frequency envelope of the umbilical artery Doppler waveforms. Commercial instruments provide 2 different methods for calculation of RI and PI. Firstly the operator manually defines the waveform envelope, or particular points of the envelope such as the peak systolic and end diastolic frequencies, and the RI and PI are calculated from this data. The second method is automatic calculation of the indices by the Doppler machine. This requires the following steps;

i) Adjustment of the amplifier gain to display the waveform; this step is performed by the operator,

ii) Calculation of the maximum frequency envelope,

iii) Calculation of the start and end points of each waveform,

iv) Calculation of the RI and PI values for each waveform,

v) Display of the RI and PI.

For each of these 2 methods the operator should have an appreciation of what constitutes an acceptable quality Doppler waveform, so that indices of RI and PI are not in error. In our institution we have favoured the manual method as this forces the operator to make a conscious decision as to the location of the maximum frequency envelope, which should engender an appreciation of waveform quality. The automatic method is more likely to be prone to abuse as it allows the operator to simply read the RI and PI values off the screen, and to a greater or lesser extent ignore the quality of the waveforms and the envelope from which these values arose. The possibility then arises of inaccurate calculation of RI and PI, with the consequent scenario of management of the patient by clinical staff based upon incorrect data. At best, in the wrong hands this could lead to the Doppler test being discredited. At worst it could lead to inappropriate obstetric management. It would therefore seem desirable to give an indication to the operator of when the waveform quality is acceptable, with the implication that the indices of RI and PI are reliable.

1.4.3. Overall variability of waveform indices obtained in clinical practice.

In the previous 2 sections the sources of variability of Doppler waveforms and of RI and PI have been considered. In clinical practice these factors will combine. The descriptors of the error in RI and PI which are relevant are the reproducibility and the accuracy. In order to judge the accuracy it is necessary to have a gold standard for RI and PI. In clinical practice this would be difficult if not impossible to obtain, so that in the literature studies on overall variability have concentrated on the reproducibility of waveforms, (Spencer et al 1989, Maulik et al 1989a, Gudmundsson et al 1990, Murrels 1987). These studies, performed during fetal apneoa, show inter-observer coefficients of variation of 8.4 to 14.3%, and intra-

observer coefficients of 8.5 to 10.9% for PI.

1.5 Aims of thesis.

The discussion in section 1.4 of the factors influencing the calculated RI and PI values generated 2 questions which will form the aims of this thesis. These are;

i) What is the effect of physical parameters such as beam-vessel angle and beam-vessel alignment on the waveform quality, as characterised by the maximum frequency envelope and the calculated RI and PI values, of umbilical artery Doppler waveforms?

ii) Is it possible to produce waveform quality indices which could be calculated by a Doppler machine in order to indicate to the operator the degree of reliability of the RI and PI values obtained from the umbilical artery Doppler waveforms?

The thesis is arranged as follows to try and answer these questions;

Chapters 2 and 3: In order to investigate the effect of physical parameters on umbilical artery Doppler waveforms in a well controlled manner it is necessary to devise a source of reproducible velocity waveforms. Chapter 2 describes the construction of a physiological flow phantom, and chapter 3 considers the effect of the artificial blood on the Doppler signal.

Chapter 4: In this chapter is described the effect of physical parameters on the calculated maximum frequency envelope, and on RI and PI.

Chapters 5 and 6: These chapters are concerned with methods for improvement of the estimation of the maximum frequency envelope and on the RI and PI. The first method is noise reduction of the Doppler spectrum. The development of a suitable image processing algorithm is described in chapter 5. The second method is filtering the maximum frequency envelope. These methods are tested fully in chapter 6.

Chapters 7 and 8: In these chapters waveform quality indices are described and tested using the set of waveforms acquired from the flow phantom. In this way the quality indices could be compared with the quantitative errors in the envelope and in the PI.

Chapter 9: The performance of the 2 most promising quality indices is tested on 450 sets of real umbilical artery waveforms. In this trial waveform quality was assessed subjectively.

Chapter 2. Design and evaluation of a physiological flow phantom.

2.1 Introduction.

In order to systematically study the effect of physical parameters on the RI and PI, and on the waveform quality indices it is neccessary to produce a source of reproducible velocity waveforms in a vessel which simulates the umbilical artery.

Desirable features of a physiological flow phantom are to generate reproducibly a wide variety of waveform shapes in such a manner that the waveform shape can easily be changed. Many of the early systems described lack these facilities. These are described in Law et al (1987). Flow phantoms with the ability to change waveform shape are described by a number of authors (Issartier et al 1978, Wemeck et al 1984, Peterson 1984, McCarty and Locke 1986, Law et al 1987, Shortland et al 1989). The ability of the phantom to generate a variety of waveform shapes is discussed only in the recent paper by Shortland et al (1989). The flow phantom described in this chapter is an extension of a steady flow phantom described by McDicken (1986).

2.2 Flow phantom.

It would be difficult and time consuming to physically model the physiological circulation consisting of a beating heart and a system of bifurcating tubes (however an approximation to this approach has recently been reported (Shortland et al 1989)). The chosen approach was the commonly used one whereby the waveform shape is controlled by a variable flow pump. The pump used was a gear pump (model 120-040, Micropump Corp, Concord, California, USA). This model delivers 0.316 ml/revolution. Previously we had used a larger gear pump delivering 1.73 ml/revolution however it was found that for the smallest of the vessels of interest, at the desired flow rates the pump was unstable, producing a ripple on the Doppler signal associated with the action of the teeth (figure 2.1). No such problems existed with the smaller pump.

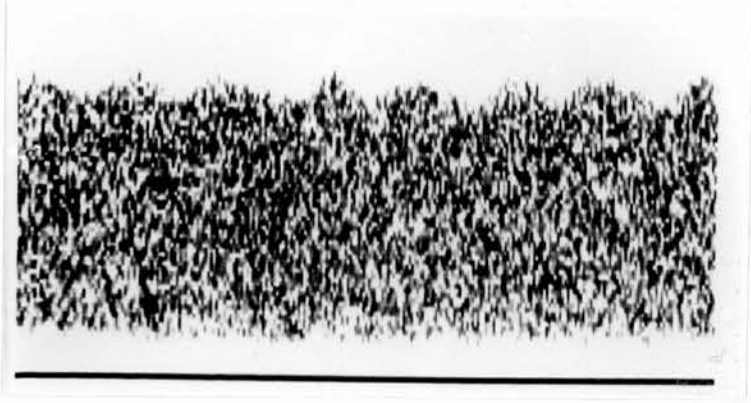

Figure 2.1 Unstable flow at low flow rates for a high output gear pump. The ripple is caused by the action of the teeth of the gears.

The tubing used must be relatively stiff. If very elastic tubing is used there are problems of kinking. We have also observed that there are large changes in waveform shape along the length of an elastic tube. This is thought to be due to reflected pressure waves from the end of the tube. This is discussed later. For the tubing which was insonated transparent heat shrink tubing was used. This was moulded around rods of known diameter as described in McDicken (1986). Pipes of 3 mm internal diameter were made to simulate the umbilical artery. These had a wall thickness of 0.36 mm. Other connecting pieces of tubing were made of PVC. There was no visible change in diameter of the tubing as assessed during pulsatile flow with an Acuson 128 scanner. The length of the insonation vessel was made large enough to produce stable flow conditions at the point of insonation. The inlet length L for pulsatile flow is quoted as

$$L = 0.04\ d\ Re \qquad \text{(McDonald 1974)} \qquad \text{eqn. 2.1}$$

where L is the pipe length

d is the pipe diameter

Re is the Reynolds number

L can also be expressed in terms of the mean flow rate Q. This expression is independent of the tube diameter d.

$$L = \frac{0.16\,\rho\,Q}{\pi\,\eta} \qquad \text{eqn. 2.2}$$

where ρ is the fluid density

η is the viscosity

For the solution used, $\rho = 1.1 \times 10^{3}$ kgm $^{-3}$ and $\eta = 0.004$ kgm^{-1}s^{-1}.

If Q is expressed in ml min $^{-1}$, this gives

$$L = 1.7507 \times 10^{-2}\ Q \qquad \text{eqn. 2.3}$$

If the upper value of Q is for example 1000 ml min^{-1}, L is 17.5 cm; for Q = 2000 ml min^{-1}, L is 35 cm. The pipes used in this study were all 35 cm or more long.

The acoustic properties of the prepared heat shrink material were estimated (table 2.1). The speed of sound was measured by timing 3.5MHz ultrasound pulses from transmission by one transducer to reception by a second 3.5MHz transducer. The pulses passed through water in which a block had been inserted. The block consisted of layers of flat prepared heat shrink material giving a total thickness of 1.0 to 1.35 cm. The estimated speed of sound through the heat shrink material was 1850 m/s. This is higher than the speed of sound in water (1480 m/s) or in tissue

(1450 m/s to 1650 m/s), (data from Wells 1977). This will lead to refraction of the sound as it travels through the tubing. Using Snell's law, at a water/heat shrink interface the Doppler angle at which total reflection occurs is approximately 37^{o}. In chapter 4 the effect of beam-vessel angle on waveforms is considered, and in that chapter it will be noted that no waveforms can be acquired for Doppler angles less than 40^{o}, which is consistent with the 37^{o} critical angle. In a second experiment the attenuation coefficient of the material was measured by observing the change in received ultrasonic peak height occuring on insertion of a 3.5 mm block of the material into ultrasonic gel. The same transmit and receive transducers were used as before. The estimated attenuation coefficient was 18dB/cm. For the simulated umbilical artery, which had a wall thickness of 0.36mm, there is approximately 97% transmission of ultrasound which is normally incident. Law et al (1989) review the design of flow phantoms. They report longitudinal velocities in typical vessel materials such as polyethylene (1950 m/s), perspex (2750 m/s) and pyrex glass (5040 m/s). These velocities are all higher than the velocity of 1850 m/s measured for the heat shrink material used in this study. In chapter 4 the effect of a number of physical parameters on the Doppler waveforms is considered. Further discussion of the influence of diffraction of the ultrasound beam by the tubing used will be considered in relation to the results obtained in that chapter.

Physical parameter	Value	Units
Density	940 ± 45	kgm^{-3}
Speed of sound	1850 ± 10	ms^{-1}
Attenuation coefficient	18 ± 2	$dBcm^{-1}$
Characteristic impedance	$1.74\times10^{6} \pm 0.10\times10^{6}$	$kgm^{-2}s^{-1}$

Table 2.1. Physical properties of prepared heatshrink material. Errors given are 1 standard deviation of 3 separate measurements.

The blood substitute used was a suspension of Sephadex particles (type G25, Pharmacia, Uppsala, Sweden) in a mixture of glycerol and water, as described by McDicken (1986). Blood is a non-Newtonian fluid, however McDonald (1974) states that the effects of non-Newtonian behaviour at high shear rates are important only in small vessels of arteriolar dimension. Following Pedley (1980) blood is taken to be a Newtonian fluid of viscosity 0.004 $kgm^{-1}s^{-1}$. A mixture of 42%/58% glycerol/water by mass gives a viscosity of 0.004 $kgm^{-1}s^{-1}$ at $20^{o}C$ (CRC handbook of chemistry and physics 1985). It is known that gear pumps will cause damage to the sephadex particles; however this damage as observed by a microscope is small after several hours use. A magnetic stirrer was used to keep the particles in suspension. Further consideration of the sephadex suspension is given in chapter 3.

A block diagram of the system is shown in figure 2.2 The pump was powered using a stepping motor. The stepping motor speed was controlled using a microcomputer (BBC master 128, Acorn Computers, Cambridge, England) to produce the desired waveform. The waveform shapes used were generated by hand using a tracker ball and stored to disc. The control digital output from the microcomputer could be varied over the range 0 to 4095. A new value of the waveform shape was sent every 5 ms, and the waveform was repeated once the endpoint had been reached. This was converted to an analogue signal by a combination of a D/A converter and a voltage/frequency converter. It was necessary to smooth the output of the voltage/frequency converter in order to avoid discontinuous jumps in the output which the stepping motor could not follow. This smoothing did not affect the waveform shape. The system could support both forward and reverse flow. Reverse flow was indicated by a control bit sent from the microcomputer with each new value.

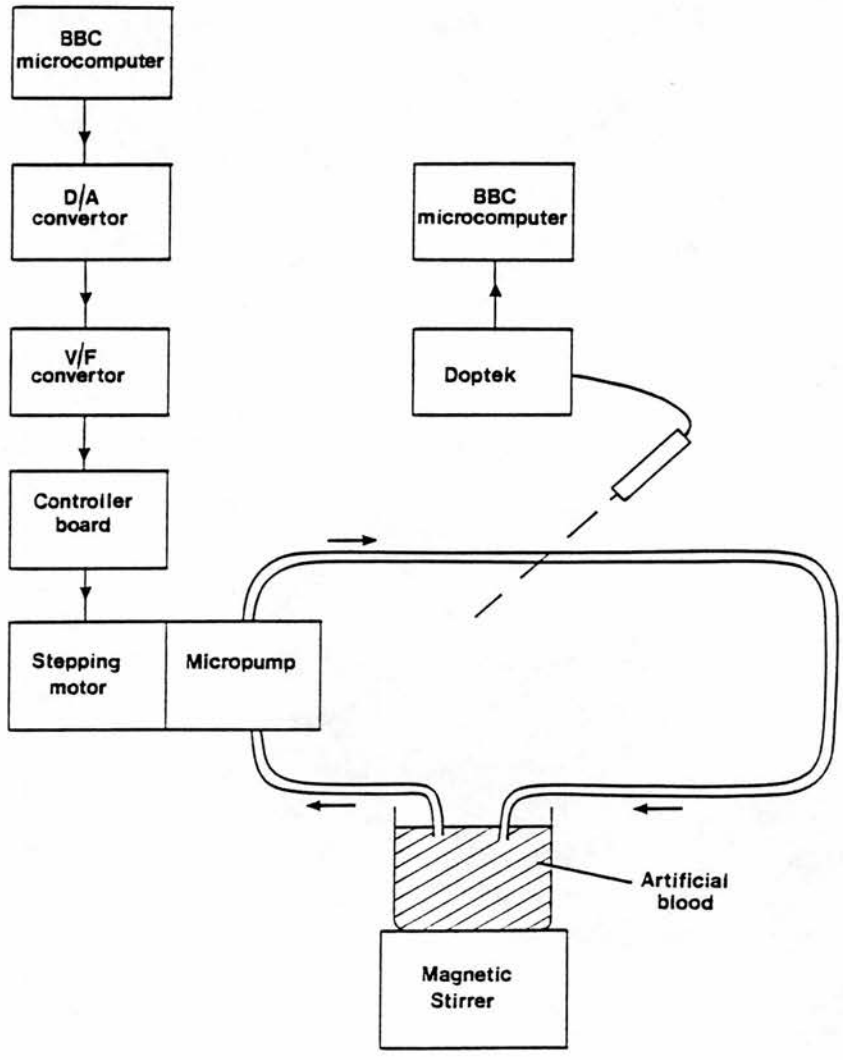

Figure 2.2. Block diagram of the flow phantom.

Waveforms were acquired using a Doptek 4 MHz continuous wave Doppler unit. The maximum frequency envelope or the entire Doppler spectrum could be sent to the microcomputer for storage. Analysis of the Doppler waveforms was performed using the microcomputer.

Typical waveforms acquired using the final system are shown in figure 2.3. The beam-vessel angle was 45^{o}. The pump speed was adjusted to give a maximum velocity of approximately 0.8 ms^{-1}. Simulated umbilical artery waveforms are shown in figure 2.3a and 2.3b. In order to demonstrate the flexiblity of the phantom simulated uterine artery waveforms using the 6 mm tube are shown in figure 2.3c and 2.3d.

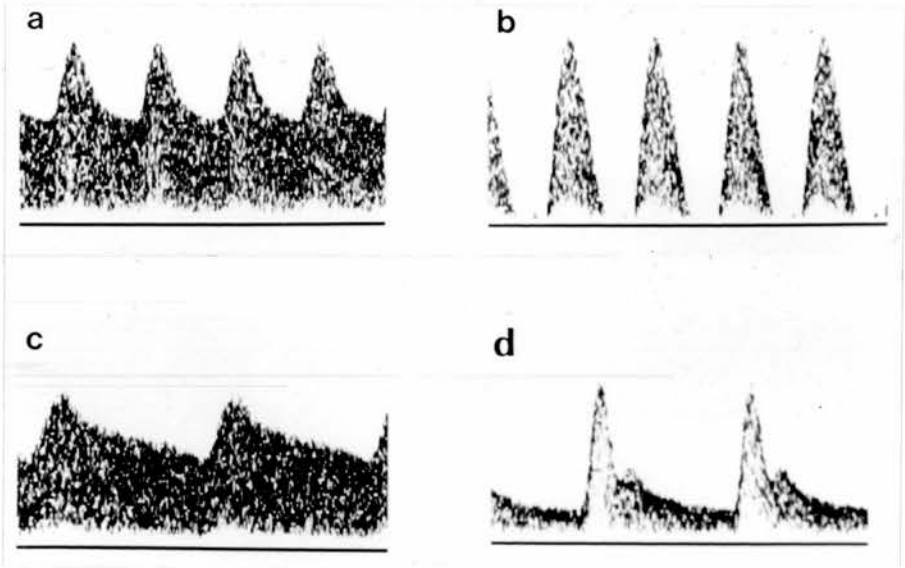

Figure 2.3. Waveforms produced using the flow phantom. a) and b); umbilical waveforms using the 3 mm tube, c) and d); uterine waveforms using the 6 mm tube.

2.3 Evaluation.

2.3.1 Flow calibration

Constant flow levels were generated by the microcomputer. Flow was measured using a measuring cylinder and stopwatch. This was done for both forward and reverse flow over the range of interest (figure 2.4a).

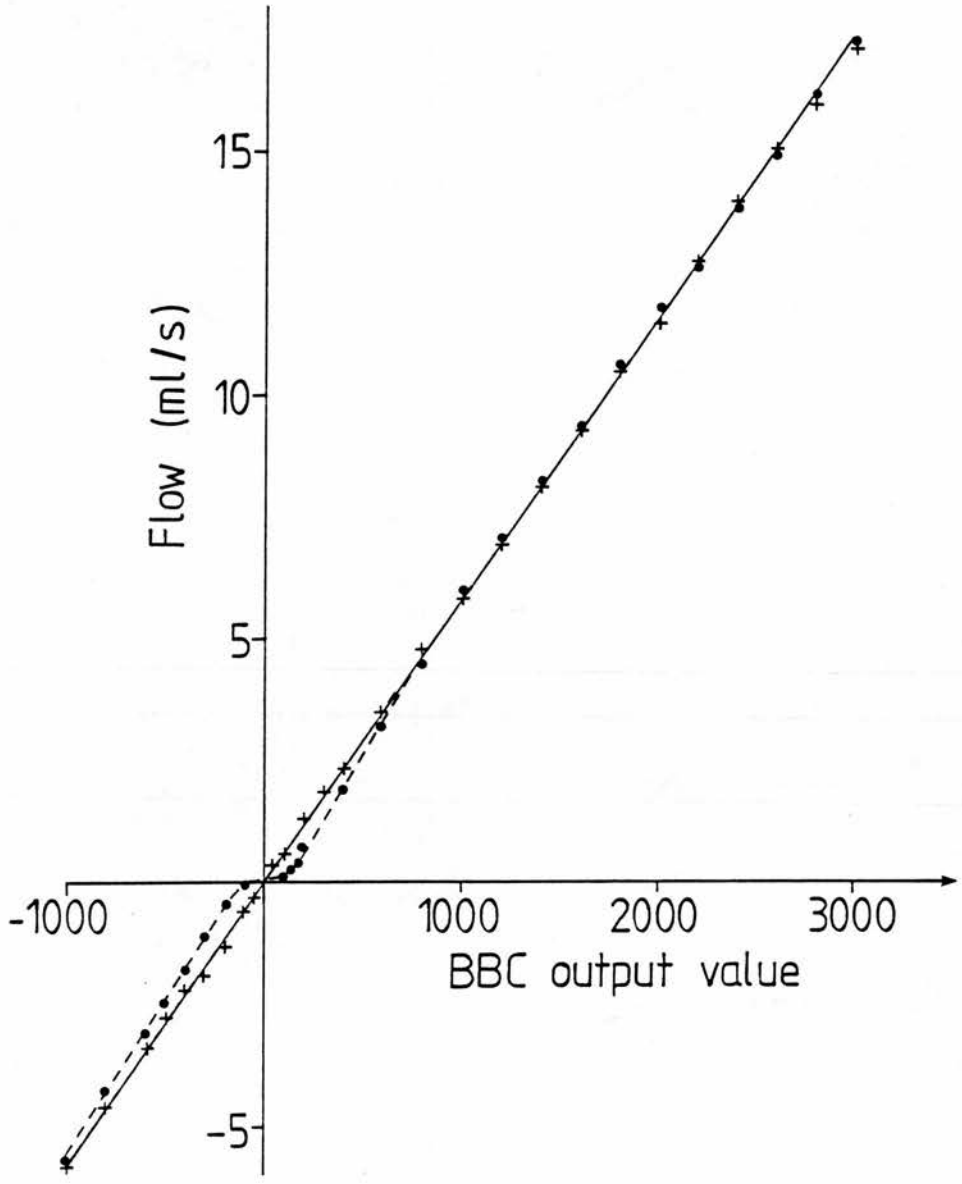

Figure 2.4. Relationship between the control output value from the micrcomputer and the flow rate. a) before correction (points), b) after correction (crosses).

At low flows the curve of microcomputer control value versus volume flow is non-linear. This is a combination of non-linearity in the control board electronics, and in pump efficiency. In particular, when the microcomputer output value is zero there is a residual flow of 0.0017 mls^{-1}. For a 3 mm tube this gives a maximum Doppler shift of about 1.2 Hz which is much smaller than the filter level of 70 Hz. This small flow will however affect the accuracy of volume flow measurement performed using a measuring cylinder and stopwatch when very pulsatile flow is used. This was overcome by reversing the direction of flow of the pump every 5 ms when the microcomputer output was zero. By using the curve of figure 2.4a, correction factors were calculated from which the microcomputer output was corrected to increase the stepping motor speed for the low flow region. Correction was performed by linear interpolation over 14 regions between the values -1000 and 1000. This results in the more linear curve of figure 2.4b.

2.3.2 Distortion of the waveform shape

The tubing which is connected to the pump outflow had its other end in the reservoir of sephadex suspension. If the tube is very elastic there are obvious distortions in the recorded Doppler waveform, such as the presence of a second peak, which can be reduced by increasing the resistance to flow at the end of the pipe arising from a mismatch between the impedance of the pipe and that of the sephadex solution. This suggests that the distortion is due to reflected pressure waves from the end of the pipe. This type of distortion was also present when the relatively stiff pipes of moulded heat shrink tubing were used. A number of methods were tried to remove these effects. Basically these methods attempted to match the impedance between the tubing and the sephadex syspension. The methods tried included drilling holes in the tubing wall for several centimetres from the end, shaping the end to be a slanted cut instead of a blunt cut, and tying a piece of foam tightly around the end. The first two of these methods had no effect. The third method did cause a reduction in waveform distortion. This,

however, is not a desirable method as pieces of foam fray off and could damage the gear teeth. The distortion was reduced when the heat shrink tubing was of reduced diameter for the last 20-30 cm of its length before entering the reservoir. A diameter reduction of a half was used. The reduction in distortion achieved was greater as the length of the narrow tube was increased (figure 2.5). The reasons for the removal of the distortion using this method are not entirely clear. One possible explanation is that the mismatch in impedance at the interface between the insonation tube and the narrow tube causes reflected pressure waves which cancel out the distorting effects of the pressure waves reflected from the end of the tube. Another possible explanation is that, as the speed of the fluid in the narrow pipe is a factor of four greater than in the insonation tube, this impedes the progress of the reflected waves from the end of the pipe. Though empirical this method does give some reduction in distortion.

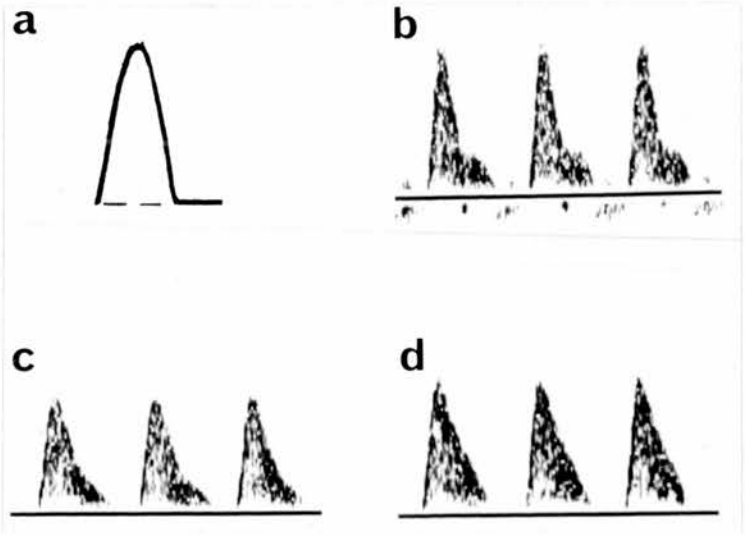

Figure 2.5. Reduction in waveform distortion using an adjoining narrow bore tube a) control waveform, b) narrow bore length = 0 cm, c) narrow bore length = 18 cm, d) narrow bore length = 31 cm.

2.3.3 Comparison of control waveforms and Doppler waveforms.

Waveforms with a wide range of pulsatility, including reverse flow, were generated at a pulse rate of 120 per minute. RI values were calculated for the control waveform and for the maximum frequency envelope of 5 Doppler waveforms. The results are presented in figure 2.6. The RI of the Doppler waveforms is in general lower than that of the control waveforms, but only by a

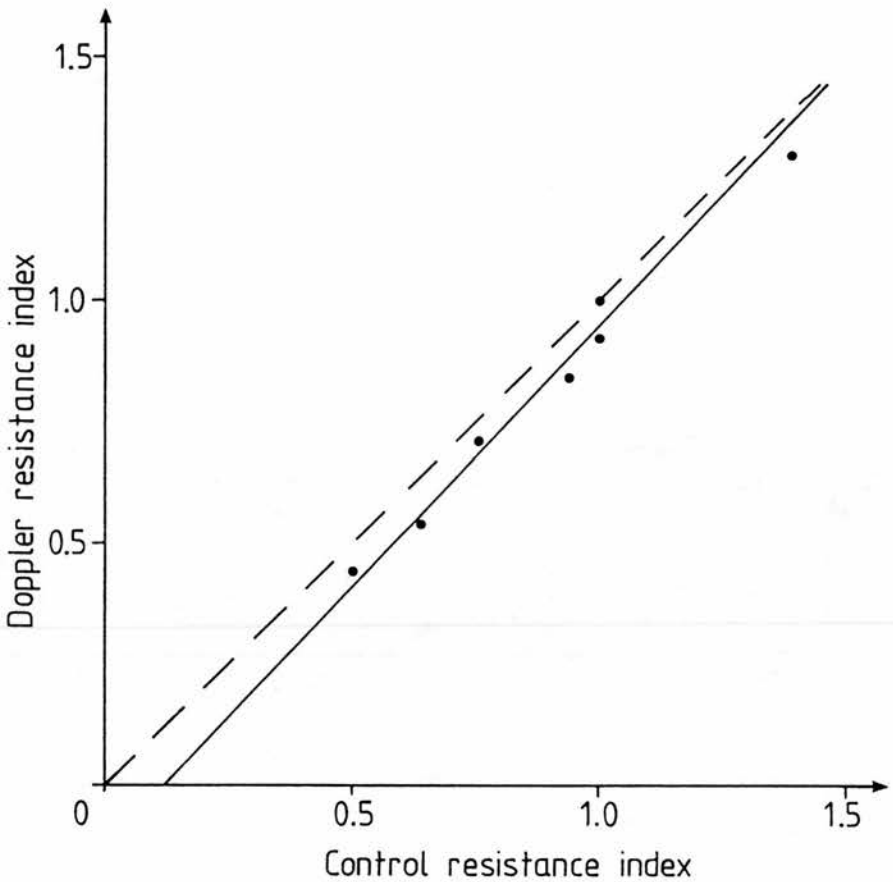

Figure 2.6. Comparison of the control waveforms and Doppler waveforms using the resistance index. The solid line is the line of best fit; the dotted line is the line of identity.

small amount (<0.1). Perfect agreement would not be expected since the control waveform influences the mean velocity, and it is known that the velocity profile and hence the relationship between the mean and maximum velocity changes over the waveform cycle. In some cases there was obvious disagreement between the control waveform and the Doppler waveform. Figure 2.7a shows a case where there is diastolic flow when the control waveform has absent end diastolic flow. Figure 2.7b shows a case where there is a tertiary Doppler peak which is not present on the control waveform. This distortion could be caused by residual reflected waves within the system.

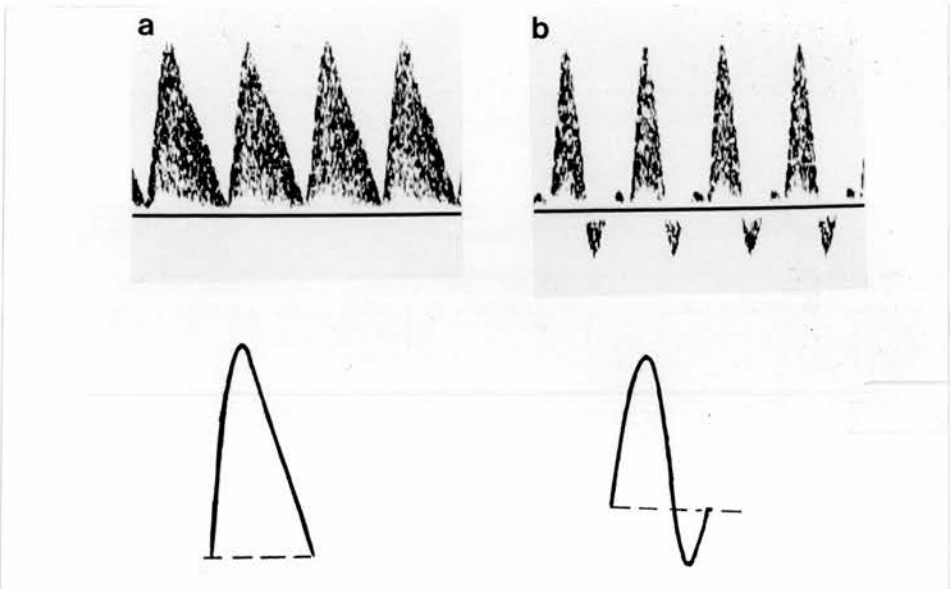

Figure 2.7. Cases where there is obvious disagreement between the control and Doppler waveforms. a) the control waveform has no end diastolic flow whereas the Doppler waveform does have end diastolic flow, b) the Doppler waveform possesses a tertiary peak which is absent in the control waveform.

2.4 Conclusion.

A flow phantom based upon microcomputer control of a stepping motor/gear pump combination has been described. The system works well and is able to generate a wide variety of physiological waveforms.

Chapter 3. A comparison of the Doppler spectra from human blood and artificial blood used in the flow phantom.

3.1 Introduction.

The Doppler signal from blood results from the combination of the ultrasound scattered from each red cell. The average distance between two red cells is about 10% of its diameter for a haematocrit of 45% (Shung et al 1976). In this situation the red cells must be considered as interacting. Theoretical modelling of the Doppler signal from blood taken as a suspension of interacting scatterers has been performed by a number of authors (Atkinson and Berry 1974, Shung 1982, Mo and Cobbold 1986a). Angelson (1980) treated blood as a continuum and therefore bypassed the interaction. For blood the Doppler shifted signal arises from fluctuations in red cell concentration in the sample volume. The fluctuating nature of this signal gives rise to the characteristic speckle pattern of the Doppler spectrum from discrete Fourier transform based spectrum analysers.

The use of blood as a scattering medium is inconvenient - the red cells are easily damaged, it is difficult not to introduce air bubbles into the blood, stringent microbiological safety precautions are necessary, and a large supply can be difficult to obtain. It is much more convenient to use a blood substitute. The blood substitute used was Sephadex G25 superfine particles (Pharmacia, Uppsala, Sweden) in a glycerol solution. These particles have a swollen diameter of 20-70 μm which is much larger than the red cell dimensions of approximately 2.4 by 8.5 μm. The question then arises as to whether the backscattered Doppler power and the statistics of the Doppler spectrum are similar for human blood and for a suspension of the Sephadex particles. It is the purpose of this chapter to investigate these aspects.

3.2 Method.

3.2.1 Experimental set up.

The artificial blood was a suspension of Sephadex particles in a mixture of 42%

glycerol to 58% water. This has a viscosity of 0.004 $kgm^{-1}s^{-1}$ at $20^{o}C$, identical to the viscosity of blood at $37^{o}C$. The flow phantom and artificial blood were kept at $20^{o}C$ for the duration of the study. The artificial blood was prepared in such a manner as to remove air bubbles. Boiling water was added to the glycerol to remove the dissolved air.

The Sephadex was prepared by adding a weighed amount of dry Sephadex to the glycerol solution and heating for 2-3 hours at $85^{o}C$. This swells the particles to their final volume and removes dissolved air. As a precautionary measure the glycerol solution and the Sephadex suspension were placed in an evacuated chamber of pressure less than 50 mmHg for 1-2 minutes to remove any final air bubbles. No air was observed to come off from the solution and suspensions. The flow phantom was flushed with water degassed by boiling and by exposing it to low pressure. Special care was taken to remove air trapped within the gear pump. This

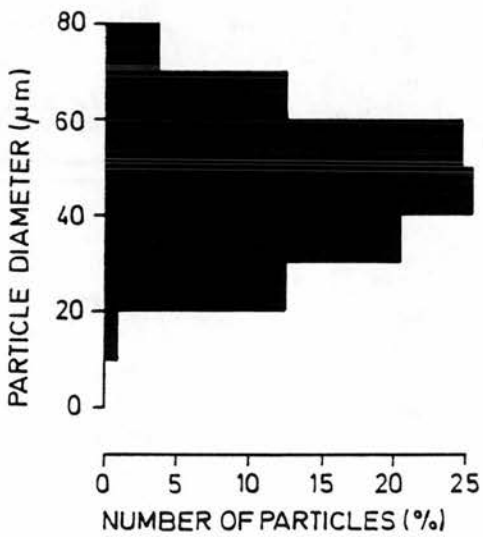

Figure 3.1: Diameter distribution of swollen Sephadex particles. This was calculated from diameter measurements made on 500 particles.

could be done by inverting the gear pump and running it at high speed. The presence of microbubbles was monitored using Doppler ultrasound. A microbubble produced a very high intensity Doppler signal. Flushing was repeated until no recirculating bubbles were observed. The flow phantom was further flushed with glycerol solution, then the Sephadex suspension introduced. Dilution of the original Sephadex suspension was performed using degassed glycerol solution carefully added to the Sephadex. Figure 3.1 shows the distribution of the swollen particle diameters. Diameter measurements were made using a microscope with a calibrated eyepiece. The mean and 2 standard deviations of the diameter was 46 $\pm$ 26 μm, which gives a range of approximately 20 to 70 μm.

Human blood was taken from a willing volunteer. This was withdrawn slowly through a 19 gauge butterfly into 50 ml syringes to prevent bubble formation. This was emptied carefully into a beaker. 0.25 ml of heparin at a concentration of 1000 units per ml were used with each 50 ml of blood to prevent clotting.

Gear pumps are known to cause damage to particulate suspensions. During the course of the experiments the damage to the Sephadex particles was minimal as observed through a microscope. The red blood cells are more fragile and so were not recirculated. The blood was sucked through the system so that the blood did not encounter the gear pump until after it had passed the insonation site.

Doppler spectra were acquired using the Doptek continuous wave unit. The transducer-vessel distance was 7.4 cm, the beam-vessel angle was 47^{o} and the vessel inner diameter was 4 mm. This set up is similar to that which occurs in practice when Doppler waveforms are acquired from vessels in the body. A 1 cm layer of tissue equivalent attenuator (reticulated foam) was placed between the vessel and the transducer to avoid saturation of the Doppler signal when the higher concentrations of Sephadex were used. A 4 MHz transducer focused at 5 cm was used with the transducer face submerged under water.

3.2.2 Measurement of statistical parameters.

The initial Sephadex concentration was 50% by volume. The flow rate of the pump was set to a constant value which gave a 3 kHz maximum frequency shift. This corresponds to a maximum velocity of about 0.8 ms^{-1}. The suspension was allowed to circulate for 15-20 seconds to give a uniform concentration of particles. The Doptek frequency range was 4 kHz; that is the highest displayed frequency was 4 kHz. A new spectral line was produced every 10 ms. The Doppler gain was adjusted to keep pixel saturation to a minimum. A spectrum of 240 lines (2.4 seconds) was transferred to the BBC microcomputer. Dilution of the Sephadex was performed taking care not to create air bubbles. This procedure was repeated until the Sephadex concentration was between 1 and 8%.

Without touching the transducer, attenuator or vessel, the Sephadex was flushed from the flow phantom using degassed water. Blood was introduced and spectra were acquired. All spectra were transferred to the BBC microcomputer and then to an Archimedes microcomputer for analysis.

For each spectrum the 240 consecutive spectral profiles were used to generate data on the standard deviation of pixel values as a function of the mean pixel value. A single data point was derived by calculating the mean and standard deviation of the 240 values corresponding to a particular frequency. This was repeated for all frequencies from 100 to 2850 Hz. The mean and standard deviation are parameters describing the first order statistics of the Doppler spectrum. Second order statistics refer to the relationship between the value of a pixel and that of the surrounding pixels. This can be described by the normalised autocovariance function NAF(k).

$$NAF(k) = \frac{1}{N - k} \frac{\sum_{i=1}^{N-k} [P(i) - \overline{P}][P(i+k) - \overline{P}]}{\sum_{i=1}^{N} [P(i) - \overline{P}]^2} \qquad \text{eqn. 3.1}$$

where P(i) is an array of N elements, $\overline{P}$ is its mean value and k = 0, 1, 2 ..... is the lag variable.

If this function has a simple shape it can be characterised by its full width at half maximum height (FWHM). This values gives an indication of the size of the speckle seen on the image. The NAF was calculated in both the time and the frequency direction. Calculation along the time axis was performed over a period of 2.4 seconds (240 points) for each frequency from 1000 Hz to 2850 Hz. The average NAF along the time axis, NAF_t was then calculated. Calculation of the NAF along the frequency axis, NAF_f, was performed over the interval from 1900 to 2850 Hz (20 points). This was performed for each of the 10 ms spectral lines and the average value taken. For calculation of NAF_f ideally the region should be uniform; that is the mean pixel value should not be a function of frequency. Along the frequency direction the mean pixel value increases as the frequency increases. This is a consequence of the relative geometry of the beam and velocity profile of the vessel. The maximum variation of average/pixel values over the region 1900 to 2850 Hz was $\pm$13%. Along the time axis the mean pixel value does not change. Normalisation removes any dependency of the autocovariance function on the mean value for that line hence the requirement for uniformity in the frequency direction is not so strict.

3.2.3 Measurement of relative Doppler power.

The measurement of relative power can be explained with the help of figure 3.2. The Doppler signal is a fluctuating signal $V_1(t)$. $V_1(t)$ is the Doppler signal after directional demodulation. The upper channel only was used. The power of the signal is related to the average value of $V_1^2(t)$. In figure 3.2 R_{out} is the output resistance of the Doptek unit. R_A is a digital attenuator reading from 0 to 1000. R_{in} is the input resistance of an RMS voltmeter. After the introduction of the Sephadex of 50% concentration the attenuation value was set to 100,

corresponding to a high attenuation, and the RMS voltage noted. Subsequent dilution of the Sephadex suspension produced a different output power. The attenuation resistance was adjusted so that the RMS voltage level returned to its baseline value. From the equivalent circuit the ratio M of V_1 to V_2 is

$$M = \frac{V_1}{V_2} = \frac{(R_1 + R_{out})(R_{in} + R_2)}{(R_{in}R_2)} + 1 \qquad \text{eqn. 3.2}$$

Using this the power P of the Doppler measurement relative to the first measurement can be calculated

$$\frac{P_n}{P_1} = \frac{M_n^2}{M_1^2} \qquad \text{eqn. 3.3}$$

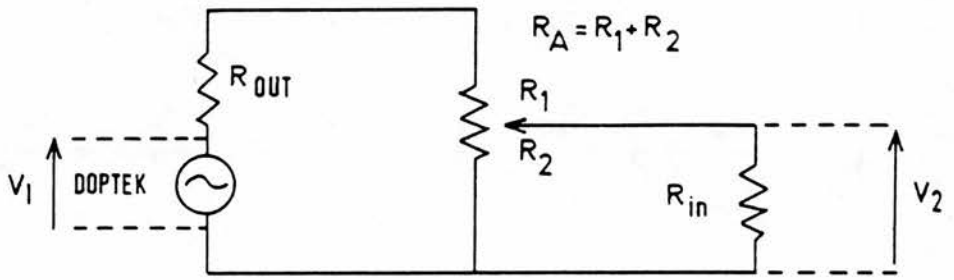

Figure 3.2: Circuit for the calculation of relative Doppler power. R_{out} is the Doptek output impedance and R_{in} the input impedance of the RMS voltmeter. R_A is an attenuator. R_A is split into R_1 and R_2. The values of R_1 and R_2 depend on the attenuation needed to maintain V_2 constant.

The attenuation values R_1 and R_2 were measured directly using an ohmeter. The input and output impedances were measured using the standard electrical techniques. An alternative method of power measurement is to use the power readings direct from the RMS meter. Non-linearities in the calibration of the meter could be present which would affect the measurements. Using the meter as a null device meant that the meter was being used at fixed point hence non-linearities were not relevant.

The measurement of the relative power of blood using the flow phantom was found to be difficult. This was due to the limited time available as the blood could not be recirculated. An alternative approach was devised. A 60 ml syringe was connected to a 1 metre length of silicon rubber tubing whose outlet was placed in a beaker. Blood or Sephadex suspension at a concentration of 20% by volume was introduced. Doppler measurements from the fluid in the silicon rubber tubing could be taken by emptying and refilling the syringe. The beam-vessel angle and transducer-vessel distance were identical to the values used in the previous measurements. It was possible to pass blood then Sephadex, after flushing, through the tubing without disturbing the beam-vessel geometry. Maximum frequencies of 2.8 to 3.2 kHz were produced by this method which gave a stable power reading for a sufficient length of time to enable the measurements to be performed. Using this method the relative power of blood and Sephadex at 45% concentration by volume was measured.

3.3 Results.

The relative Doppler power is plotted as a function of Sephadex concentration by volume in figure 3.3. The relative power peaks at approximately 40% concentration and falls as the concentration increases. A similar effect has been shown to occur for blood, where the backscattering coefficient reaches a peak for a haematocrit between 12 and 25% (Shung et al 1976, Mo and Cobbold 1986a). Newhouse et al (1982) measured backscattered power as a function of the

concentration of cellulose MN300 particles and demonstrated that the power plateaus, rather than peaks. It was suggested that this effect was caused by settling out of the powder at higher concentrations; so that the concentration of suspended powder approaches an almost constant value. The plateau concentration of suspended powder was suggested to be dependent on stirrer speed and geometry, so that for example at higher speeds the concentration of suspended powder would be higher, as would the plateau power. In our apparatus we attempted to keep all of

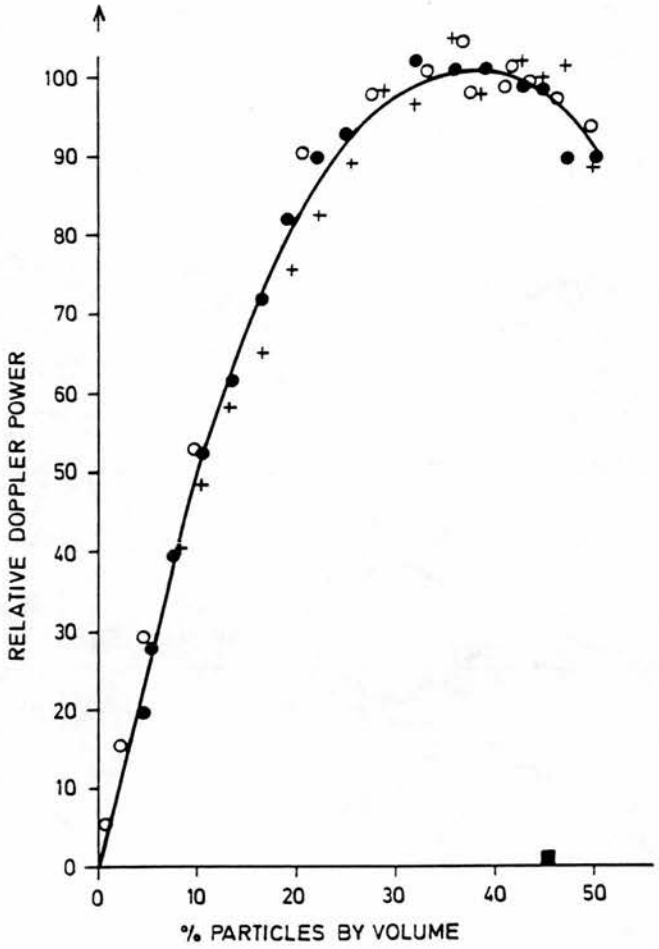

Figure 3.3: Doppler power for Sephadex as a function of concentration, and for blood. Three series of measurements are shown for Sephadex indicated by o , ● and +. The measurement for blood is shown as ■ . The solid line is a line of best fit.

the Sephadex in suspension by using a high stirrer speed. No deposition of Sephadex was observed in the tubing or beaker. The power of blood was less than the power of Sephadex of similar concentration by a factor of approximately 150-250. It should be noted that the power readings for blood were still difficult to make so that the factor of 150 may represent a lower limit. In practice the relative power may be higher than this.

Figure 3.4 shows the standard deviation of pixel values for a given frequency plotted against the mean pixel value. The points represent measurements taken from four blood spectra (224 points in all). For Sephadex, measurements from 46 spectra were taken resulting in a total number of 2576 points. Because of the very large number of points only two solid curves showing the spread of the results (average $\pm$ 2 x standard deviation) are displayed in figure 3.4. There was no dependence of this data on Sephadex concentration. Nearly all the points for the blood spectra lie within the two solid curves, indicating that the first order statistics of blood and Sephadex are identical.

Previous work has provided evidence that the amplitude level of any particular Doppler frequency obtained from blood follows a Rayleigh distribution (Mo and Cobbold 1986b, Luckman et al 1988). Consequently the points of figure 3.4 for blood should lie in a straight line passing through the origin of the axes, since the mean of a Rayleigh random variable is proportional to its standard deviation. In an attempt to explain the discrepancy between the theoretically expected and experimental results it was assumed that the deviation from Rayleigh statistics is due to a signal processing operator applied to the spectral data. One such operator, which can be used before displaying the spectral information in order to reduce the background noise, is known as baseline shift. This operator subtracts an amount C from each signal amplitude. If the resulting signal level is less than zero it is set to zero. The broken curve of figure 3.4 was obtained using the first-order statistics of a Rayleigh variable after baseline shift by a level C which represents 5% of the

available dynamic range (see section 3.6). This value provides good agreement with the experimental results, as can be seen from figure 3.4.

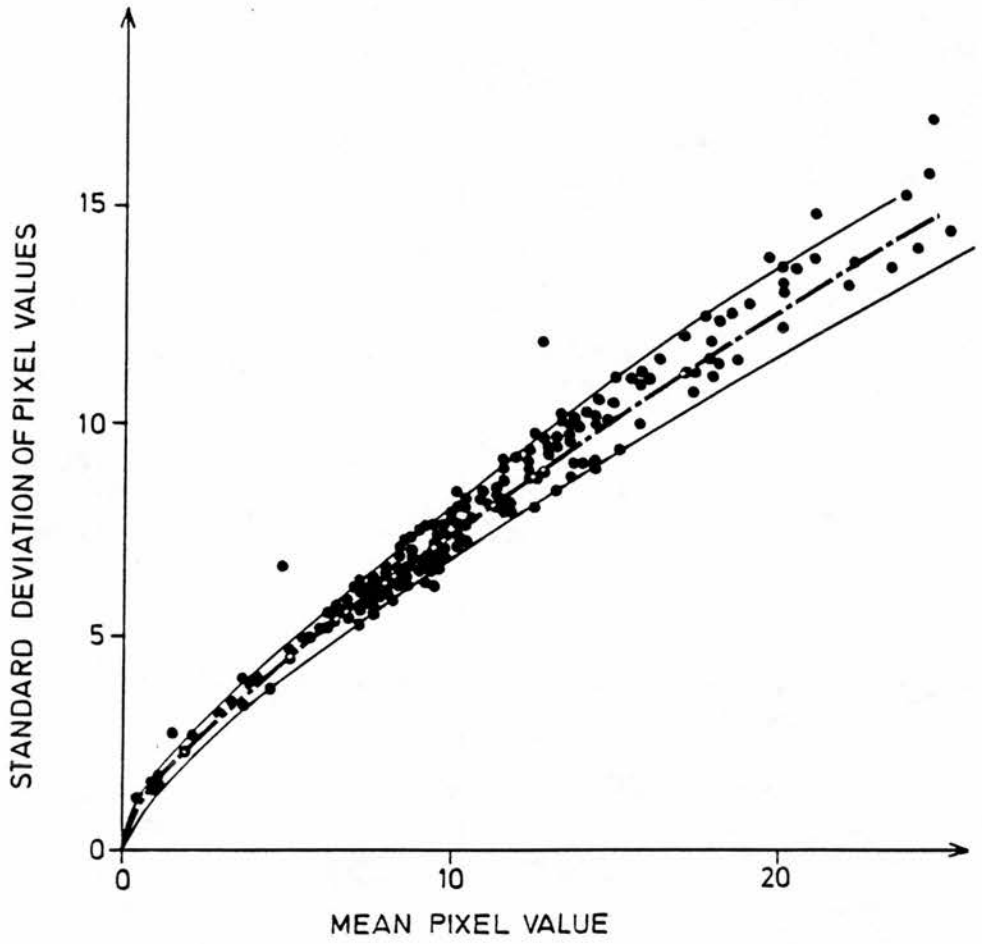

Figure 3.4: Standard deviation of pixel values is plotted as a function of mean pixel value. The solid curves represent the average $\pm$ 2 x standard deviation for the Sephadex spectra. The broken curve is that from theoretical modelling when there is a baseline shift of 5%. The data for blood is shown as ● .

A typical example of NAF_t is shown in figure 3.5a. NAF_t drops to the noise level after 10 ms (1 pixel) indicating no correlation between the value of neighbouring points along the time axis. This was the case for all the Sephadex spectra and for blood. With the frequency range used the frequency resolution was 50 Hz and the length of the data sweep 20 ms. Overlapping of adjacent data by 50% is employed in order to generate a new profile every 10 ms. With this degree of overlap the measured lack of correlation along the time axis warrants further investigation. A possible explanation is that the autocovariance function is proportional to the square of the overlap between data in the time domain. In order to test this hypothesis the whole process was simulated by computer. This involved generation of Doppler signals in the time domain using the speckle model of Mo and Cobbold (1986a), calculation of the Fourier transform of the time domain data, calculation of the sample autocovariance function (128 of them) and averaging in order to obtain an estimate of the ensemble autocovariance function. For a rectangular window with 50% overlap the value of the NAF_t for lag one was 0.23, whereas for a Hanning window NAF_t for lag one was 0.04. The Doptek uses a Hanning window and the value of 0.04 is consistent with the experimental observation that NAF_t drops to the noise level after one pixel. On the other hand NAF_f drops to the noise level after 100 Hz (2 pixels). If it is assumed that the Doppler signal is a Gaussian process the autocovariance of the spectrum would be expected to behave like a delta function (Jenkins and Watts, 1968). The spread observed in the experimentally measured NAF_f (figure 3.5b) is consistent with the use of a Hanning window by the Doptek instrument before spectral analysis; an operation which increases the width of the autocovariance of the spectrum of a random process (Jenkins and Watts 1968). The FWHM was estimated by linear interpolation from the NAF_f values at 0 and 50 Hz. These are plotted as a function of concentration in figure 3.6. There is no dependence of the FWHM on concentration of Sephadex. The mean FWHM is 41.5 $\pm$ 0.8 Hz for Sephadex and

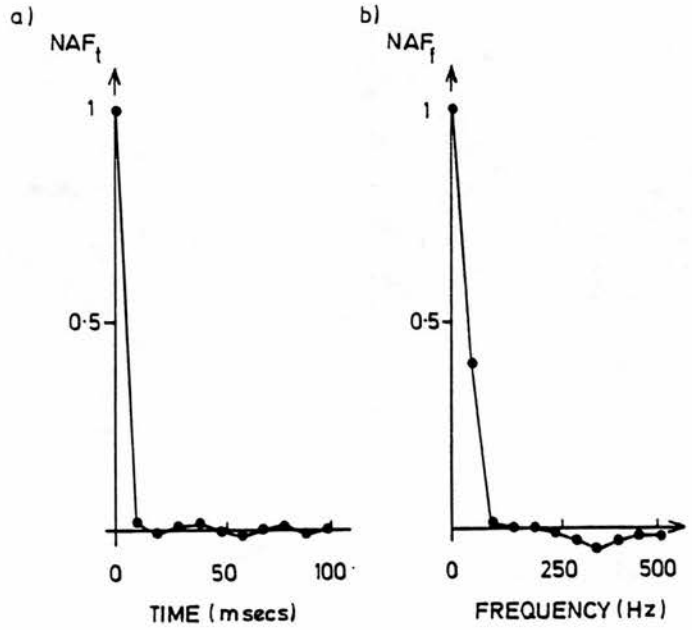

Figure 3.5: Typical examples of the normalised autocovariance function along the time axis (a) and frequency axis (b).

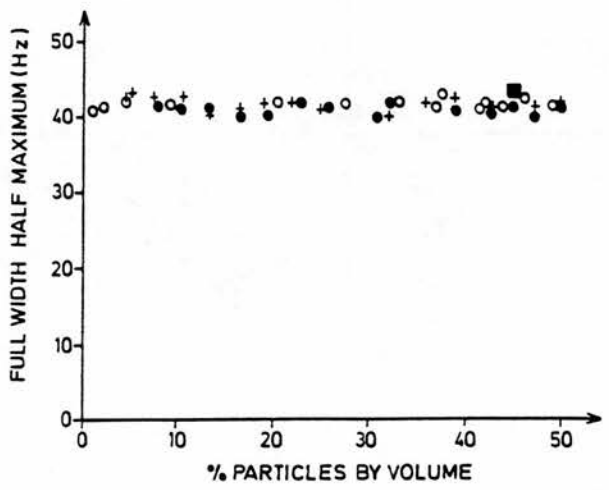

Figure 3.6: FWHM of the NAF_f as a function of Sephadex concentration. Three series of measurements are shown indicated by o , ● and +. The measurement for blood is shown as ■.

42.8 $\pm$ 0.7 Hz for blood. These values are significantly different ($p < 0.001$) however the difference is still small.

3.4 Discussion.

Under the conditions that have been used in this experiment it has been shown that the first and second order statistics of blood and a Sephadex suspension are very similar. Two factors are discussed below where care is needed before implementation of these conclusions. The first is the time resolution of the device used. A 10 ms time resolution has been used in this study as that is commonly used in our hospital. Measurements of NAF_t demonstrated a δ - correlation; that is no correlation for lags of 1 pixel or greater. If a lower time resolution was used it is possible that there would be correlation at shorter time intervals. The second factor is the frequency of the transducer. If the particle size is much less than the wavelength it is known that Rayleigh scattering occurs. In this experiment, with a 4 MHz transducer, the wavelength was 380 μm. The Sephadex particle diameters were 20-70 μm; that is 5-18% of the wavelength which is a small proportion. The similarity of the first and second order statistics of blood and Sephadex, and the agreement between the measured first order statistics and the mathematical model gives support to the validity of assuming Rayleigh scattering in this case. At higher frequencies the particle diameters will be a larger fraction of the wavelength and there may come a point where Rayleigh scattering can be no longer assumed to apply.

3.5 Conclusion.

Under the conditions in which these measurements have been made it has been shown that the first and second order statistics of blood and a suspension of Sephadex particles in a glycerol solution are very similar. This suggests that investigations in which Doppler speckle plays an important role may be performed in the laboratory using the flow phantom. This is particularly important for the investigations described in the subsequent chapters of this thesis. The statistical

parameters are also independent of Sephadex concentration, so no special measures need to be taken to ensure a suspension of the correct concentration. The relative Doppler power from blood is much lower than the power from the Sephadex suspension.

3.6 Appendix. First order statistics of a Rayleigh variable after baseline shift

The probability density function $f_x(x)$ of a Rayleigh random variable x is given by

$$f_x(x) = \begin{cases} (x/\alpha)\exp(-x^2/2\alpha) & x \geq 0 \\ 0 & x < 0 \end{cases}$$

Baseline shift subtracts an amount C from each signal amplitude, and if the resulting signal amplitude is less than zero the value is set to zero. This can be expressed as a transformation of the form $y = g(x)$ where

$$y = g(x) = \{|x - C| + x - C\}/2 = \begin{cases} x - C & x \geq C \\ 0 & x < C \end{cases}$$

Using a theorem which provides the probability density function $f_y(y)$ of the random variable y in terms of $f_x(x)$ (Papoulis 1981) it can be shown that

$$f_y(y) = \begin{cases} \{(y + C)/\alpha\}\exp\{-(y + C)^2/2\alpha\} & y > 0 \\ 1 - \exp(-C^2/\alpha) & y = 0 \\ 0 & y < 0 \end{cases}$$

Based on $f_y(y)$ the first two moments of y can be calculated.

$$m_1 = \int_{-\infty}^{+\infty} y f_y(y)dy = (\pi\alpha/2)^{1/2}\{1 - \mathrm{erf}[C/(2\alpha)^{1/2}]\}$$

and

$$m_2 = \int_{-\infty}^{+\infty} y^2 f_y(y)dy$$

$$= 2\alpha \exp(-C^2/2\alpha) + 2C(\pi\alpha/2)^{1/2}\{\text{erf}[C/(2\alpha)^{1/2}] - 1\}$$

where erf(z) is the error function (Abramowitz and Stegun 1964). The mean m_y and variance α_y^2 of y are then equal to $m_y = m_1$ and $\alpha_y^2 = m_2 - m_1^2$ respectively. Of course for C = 0 the mean and variance of the Rayleigh distribution are obtained.

Chapter 4. Accuracy of estimation of the maximum frequency envelope and pulsatility index of simulated umbilical artery waveforms as a function of 3 physical parameters.

4.1 Introduction.

In chapter 1, section 1.4, the sources of variability of RI and PI values calculated from umbilical artery waveforms were considered. It was noted that there had been no systematic study of the effect of physical parameters on umbilical artery waveforms; specifically, of the effect of physical parameters on the maximum frequency envelope and on the RI and PI derived from the envelope. It is the purpose of this chapter to perform such a systematic study with simulated umbilical artery waveforms from the flow phantom described in chapters 2 and 3.

The identification of the maximum frequency envelope of a Doppler waveform is an edge detection problem. The relevant literature to this problem will be considered first.

4.2 Literature concerning the detection of the maximum frequency envelope of the Doppler waveform.

Edge detection is important in other image processing areas such as computer vision and there is a large literature on the subject. Early studies used differential techniques of edge detection (Ballard and Brown 1982). These techniques calculate the first derivative of pixel values in a window about the central element. The points where local maxima of the first derivative occur are declared to be the edge points. Differential methods are known to be highly sensitive to noise. A second class of edge detection techniques involves convolution with the first or second order derivative of a Gaussian operator. First order derivative Gaussian operators have been described by Canny (1983), and Torre and Paggio (1984). Second order operators have been described by Marr and Hildreth (1980). The result of the convolution is an image which has high values where there are edges. These

techniques are relatively insensitive to noise but are computationally demanding. Other more complex edge detectors have also been described including methods based on surface fitting (Haralick 1984).

For Doppler waveforms in which the region above the waveform is either devoid of any other signal or is filled with uniform electronic noise, the problem of maximum frequency envelope identification should be simpler than the general problem of edge detection. Note that this may not be true when there are other sources of noise such as substantial interference from overlying vessels, however these are not considered in this chapter. A number of maximum frequency followers have been described in the past. Early methods used the analogue Doppler signal (Sainz et al 1976, Skidmore and Follet 1978). More recently digital maximum frequency followers applied to the Doppler spectrum have been described. These followers can be split into percentile and threshold-based techniques.

In the percentile method the total value T of pixel values of a single spectral line is calculated. The maximum frequency is the point where the sum of pixel values below that frequency just exceeds a specified percentage of T, typically $\frac{7}{8}$ or $\frac{15}{16}$ expressed in percentage terms. The percentile method is known to be sensitive to background noise however it is still widely used.

In the threshold method the maximum frequency follower algorithm starts from the high frequency end of a spectral line and works to the lower frequencies comparing each pixel value with the threshold value. The highest frequency at which the pixel value exceeds the threshold value is called the maximum frequency. The underlying principle of this method is that a threshold value can be chosen which lies above the majority of the noise pixel values, but is less than the pixel values corresponding to the maximum frequency envelope. For systems which utilise a fixed threshold value the performance of the system will start to deteriorate when the noise level exceeds the threshold level. Adjustment of the

threshold level with background noise can be either performed manually (Prytherch and Evans 1985) or automatically on the basis of measurements of the background noise level (D,Alessio 1985, Mo et al 1988b). Mo et al (1988b) compared a percentile follower, threshold followers adaptive to the level of background noise, and a hybrid follower combining features of the threshold and percentile methods. They found the best performance given equally by the hybrid follower and an optimised adaptive threshold follower. In this study an adaptive threshold maximum frequency follower was used which was similar to that described by Mo et al (1988b). This is discussed further in section 4.3.2.2.

4.3. Method

A brief description of the methodology is given here. Detailed description is given in the sections following. The use of a flow phantom allowed the production of a large number of identical velocity waveforms in a vessel which simulated the typical diameter and depth of an umbilical artery. Doppler waveforms could then be obtained with knowledge of the beam-vessel angle, beam-vessel axial misalignment, and the thickness of attenuating material. Series of waveforms were acquired with alteration of one of these physical parameters at a time. For each measurement a cohort of 16 consecutive waveforms was acquired. A microcomputer was used to calculate the maximum frequency envelope of each waveform and perform subsequent analysis.

In order to investigate the effect of each physical parameter on the maximum frequency envelope it was necessary to define a 'gold standard' or ideal envelope with which subsequent envelopes could be compared. The gold standard for each series of measurements was taken in each case from the cohort of 16 Doppler waveforms obtained with a beam-vessel angle of 50^{o}, no offset between beam axis and vessel axis, and 2 cm of attenuator. Visually these waveforms had a clearly defined outline and no background noise. Ensemble averaging of these 16 waveforms was performed in order to reduce Doppler speckle, which would

otherwise affect the maximum frequency envelope. The gold standard maximum frequency envelope obtained from the ensemble averaged waveform was compared with subsequent envelopes, allowing calculation of bias and variability of the envelope as a whole, and also bias and variability of the PI derived from the envelope.

4.3.1 Acquisition of Doppler waveforms.

Doppler waveforms were acquired from the flow phantom. The tubing diameter was 3 mm which was chosen as being representative of the diameter of the umbilical artery. A Doptek 4 MHz continuous wave unit was used for waveform acquisition. In each case the amplifier gain was adjusted to allow the best possible display of waveforms. Doppler spectra of 2.4 seconds of data or 240 spectral lines could be transferred from the Doptek to the BBC microcomputer. Subsequent analysis was performed using a second microcomputer (Archimedes 440, Acorn Computers Ltd, Cambridge).

Waveforms were acquired for the conditions listed below. Simulated umbilical artery waveforms were used of 500 millisecond duration. In each case 3 pulsatilities were used of PI values of 0.8, 1.4 and 2.3 (figure 4.1). For each measurement a cohort of 16 consecutive waveforms (4 screens of data) was acquired.

4.3.1.1 Beam-vessel angle

A simple transducer holder was constructed which could be clipped on to the side of the flow tank and which enabled the beam-vessel angle θ to be adjusted manually. The angle was altered about a fixed centre of rotation which was positioned to coincide with the centre of the 3 mm tubing. In this way the transducer - vessel distance was fixed at 5 cm. The tubing was positioned so that the vessel and beam axes were coincident. Reticulated foam was fixed to the transducer giving a fixed path length of 2 cm of attenuating material. Doppler waveforms were acquired for values of θ from 90^{o} to 40^{o} in 5^{o} steps.

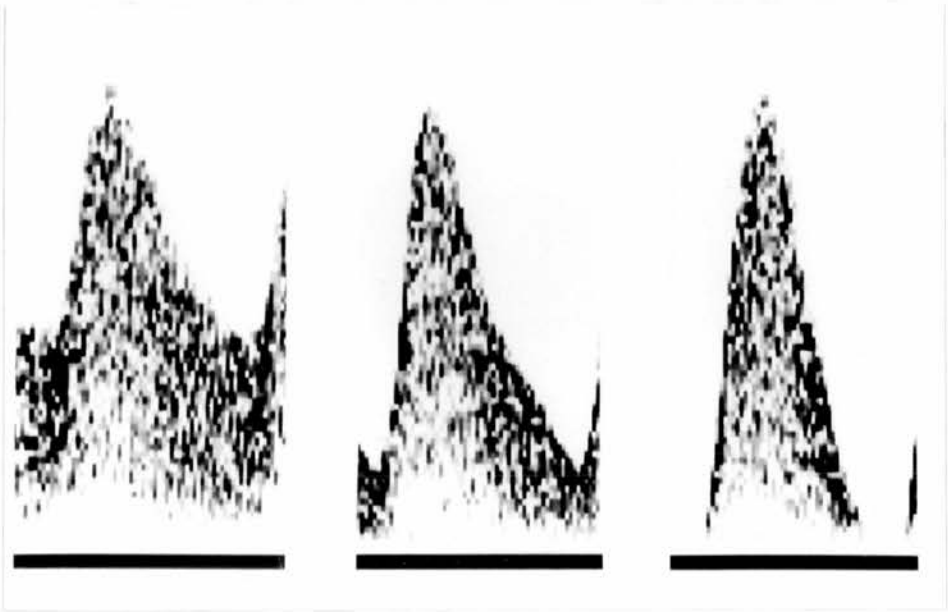

Figure 4.1: Examples of the 3 waveform pulsatilities used in the study.
a) PI = 0.8, b) PI = 1.4, c) PI = 2.3

4.3.1.2 Misalignment between beam and vessel axes.

A second simple transducer holder was constructed which could be clipped across the top of the flow tank enabling the transducer to be moved across the vessel. The transducer was held at a fixed angle of 50^{o} with respect to the vessel. Sideways movement was produced using a screw thread. Reticulated foam giving an ultrasound path length of 2 cm of attenuating material was used. Doppler waveforms were acquired for values of the offset d between the beam and vessel

axes from d = 0 to 18 mm in 1.5 mm steps. At the highest value of d the waveforms were only just visible through the background noise.

4.3.1.3 Thickness of attenuating material.

A beam-vessel angle of 50^{o} was used. The beam axis and vessel axis were coincident. The path length of attenuating reticulated foam was adjusted between 2 and 5 cm and Doppler waveforms acquired.

4.3.2 Processing of Doppler waveforms

4.3.2.1 Ensemble averaging of Doppler waveforms.

Ensemble averaging of the cohort of waveforms from each series of measurements with 2 cm of attenuator, 50^{o} beam-vessel angle and no misalignment of beam and vessel axes was performed. The cohort of 16 waveforms was composed of 4 screens of 4 waveforms each. For the first screen the position of the start of the waveform was entered manually. The registration of subsequent waveforms was calculated automatically as follows. For the first screen ensemble averaging of the waveforms was performed on the basis of the manually entered point and the 500 millisecond period between waveforms. For subsequent screens the approximate start position was entered manually. This position was then refined by calculating the correlation between the current averaged waveform and the current Doppler waveform for waveform start values up to 5 pixels on either side of the manual guess. The true start of the waveform was calculated as the point where the correlation was maximum. The ensemble averaged waveform was displayed and the maximum frequency envelope calculated (see section 4.3.2.2). If the manually entered first point was not actually the start point of the waveform this showed up clearly on the envelope. The new start point of the ensemble averaged waveform was entered manually and the waveform was redisplayed correctly then saved to disc along with its envelope. Figure 4.2 shows a typical ideal envelope.

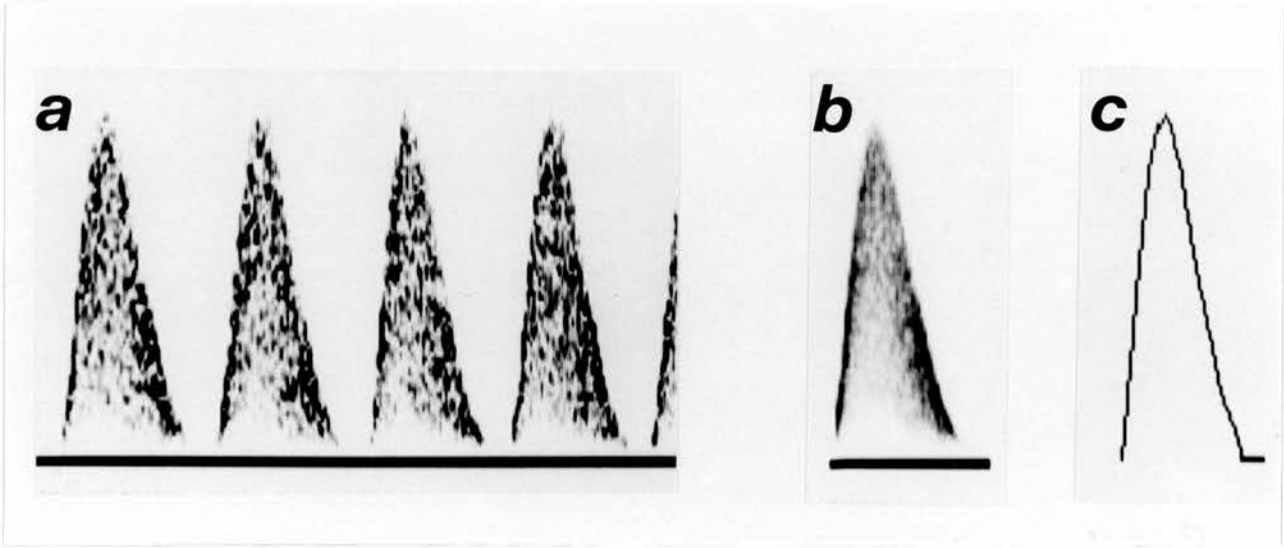

Figure 4.2: The gold standard maximum frequency envelope is obtained from the ensemble averaged waveform of 16 individual waveforms. a) 4 of the 16 waveforms, b) ensemble averaged waveform, c) gold standard maximum frequency envelope.

For investigation of bias and variability produced by axial offset and by attenuator thickness the ideal maximum frequency envelope could be used directly as the angle in these measurements was fixed. For investigation of bias produced by beam-vessel angle the height of the ideal envelope must be corrected as the angle will substantially affect the height of the envelope from individual waveforms, and therefore from the ensemble averaged envelope. The height of the envelope was adjusted using the assumption that correction by cos θ was sufficient. A direct result of this assumption is that when the transducer is normal to the vessel there should be no detected Doppler shift. This correction is described in equation 4.1 below.

$$\hat{M}_C(\theta) = \hat{M}(\theta) \frac{\cos(\theta)}{\cos(50^\circ)} \qquad \text{eqn. 4.1}$$

where $\hat{M}(\theta)$ and $\hat{M}_C(\theta)$ are the ideal maximum frequency envelopes before and

after correction respectively.

4.3.2.2 Maximum frequency follower.

The maximum frequency envelope was calculated using a threshold method where the threshold value was adaptive to the level of background noise. The reasons for the choice of this maximum frequency follower are outlined in section 4.2. The equation relating the threshold level THR and the mean background noise level BG will depend upon the first order statistics of the noise; that is on the relationship between the mean pixel value and the standard deviation of pixel values. This relationship is influenced by smoothing introduced by windowing the Doppler signal and any baseline shift used in the display of the spectrum. Mo et al (1988b) in their mathematical model assumed that a Hanning window was used and that there was no baseline shift. The equation relating the threshold level and the background noise level they used was:

$$THR = \lambda BG \qquad \text{eqn. 4.2}$$

where λ was 3 for a signal to noise ratio (SNR) between 5 and 13dB, and 4.5 for a SNR between 13 and 20dB.

For the Doppler instrument used in this study measurements of the first order statistics (chapter 3) suggest that there is a baseline shift of 5% of the dynamic range. A Hanning window function is used by this device. This indicates that equation 4.2 cannot be used for this machine. Suitable threshold values were chosen for a wide variety of signal to noise ratios for waveforms obtained from a flow phantom. The background noise level in each case was measured using a 6 x 5 window at the high frequency end. The threshold values and background values were used to derive an empirical equation relating the threshold level and the background noise level. This relationship is shown in figure 4.3. It should be noted

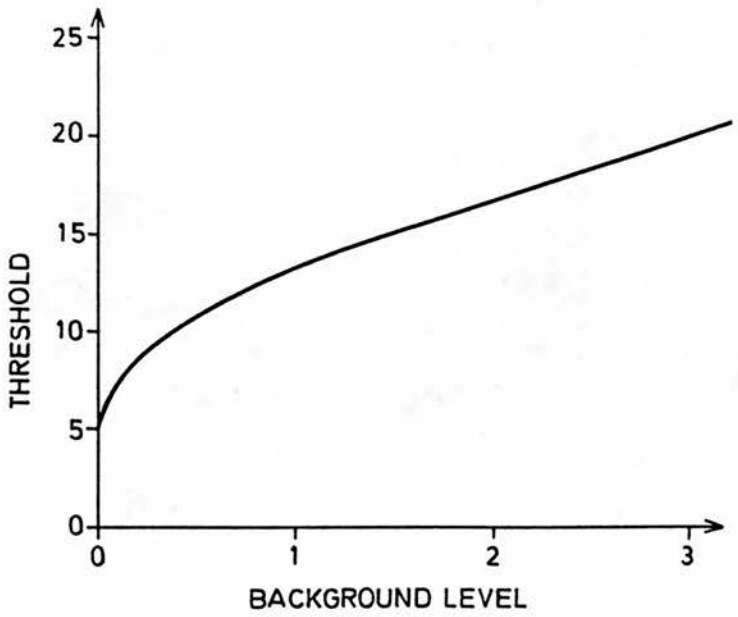

Figure 4.3: Relationship between the threshold level used by the maximum frequency follower and the measured background level. For the ensemble averaged Doppler waveforms there was no background noise so a fixed threshold of 5 was used.

that, due to the variable nature of the noise, there may be background noise present in some pixels for a particular spectral line when the measured background value for that line is zero. An offset threshold value of 5 for a background value of 0 was necessary to ensure that the maximum frequency follower was not erroneously influenced by noise in that case.

4.3.2.3 Bias and variability of the maximum frequency envelope.

For each series of measurements made one of the three physical parameters was altered. In each case this resulted in a series of waveforms ranging from waveforms with a clearly defined outline and no background noise to waveforms with an ill defined outline sometimes with substantial background noise. Each

cohort of maximum frequency envelopes obtained was assessed in terms of the overall bias in comparison with the 'ideal' envelope and in terms of the variability. The indices of bias and variability described below apply to the whole envelope, not a particular point of the envelope.

$$BS(\%) = \left(\frac{1}{N} \sum_{I=1}^{N} B(I)\right)^{1/2} \left(\frac{100}{\hat{M}_M}\right) \qquad \text{eqn. 4.3}$$

where $$B(I) = (\hat{M}(I) - \overline{M}(I))^2 \qquad \text{eqn. 4.4}$$

$$SD(\%) = \left(\frac{1}{N} \sum_{I=1}^{N} V(I)\right)^{1/2} \left(\frac{100}{\hat{M}_M}\right) \qquad \text{eqn. 4.5}$$

where $$V(I) = \frac{1}{N^1} \sum_{J=1}^{N^1} (M_J(I) - \overline{M}(I))^2 \qquad \text{eqn. 4.6}$$

where N is the number of points of the maximum frequency envelope,

N^1 is the number of envelopes of the cohort; $N^1 = 16$,

M is the individual envelope from a cohort,

$\hat{M}$ is the 'ideal' envelope,

$\hat{M}_M$ is the maximum height in Hz of the ideal envelope,

$\overline{M}$ is the ensemble averaged envelope.

B(I) is the squared difference between the ensemble averaged maximum frequency envelope and the ideal envelope for point I of the envelope. This is averaged over the whole waveform. The square root is taken and normalisation by $\hat{M}_M$ performed to give BS(%) which is a measure of bias in relationship to the maximum height of the ideal envelope. V(I) is the variance for point I of the envelope calculated over the cohort of 16 envelopes. This is averaged over the whole waveform. The square root is taken and normalisation by $\hat{M}_M$ performed to

give SD(%) which is a measure of the variability in relationship to the maximum height of the ideal envelope. Indices of bias and variance used in a similar manner to this have been described by Vaitkus et al (1988a).

A parameter which gives a single estimate of the overall accuracy of estimation of the maximum frequency envelope is the normalised root-mean square error, MFE_{er}

$$MFE_{er} = (SD(\%)^2 + BS(\%)^2)^{\frac{1}{2}} \qquad \text{eqn. 4.7}$$

Calculation of BS(%) and SD(%) over a cohort of maximum frequency envelopes in this manner assumes that the start of the waveforms are aligned. This had been performed by correlating individual envelopes with the ideal envelope for that cohort (see section on maximum frequency followers). However because of the coarse size of the pixels in the time direction (10ms), a difference of one pixel produced by slightly different correlation conditions will give a large difference in the envelope values in the frequency direction, particularly at the leading edge of the waveform. The question arises as to whether this will affect the indices BS(%) and SD(%). To investigate this linear interpolation of the envelope points was performed for individual envelopes and for the ideal envelope. Waveforms were realigned and the indices BS(%) and SD(%) calculated. This was performed for 3 cohorts of waveforms and the average value of the indices BS(%) and SD(%) calculated. Interpolation had no effect upon BS(%), but did affect SD(%). As the interpolation factor increased SD(%) tended to a value of about 3.7, which was a 25% decrease from the starting value of 5.0. An interpolation factor of 3 gave a 22.5% decrease in SD(%). This factor was chosen as a suitable compromise between reduction in SD(%) and increase in computational time.

4.3.2.4 Bias and variability of pulsatility index.

Another way of examining the performance of a maximum frequency follower is to consider the bias and variability of typically calculated indices of the maximum frequency envelope such as resistance index (RI) and pulsatility index (PI). In this study only PI was considered (equation 4.8). For each individual waveform the start and end point had been found as described previously. The minimum (MIN) and maximum (MAX) values were found by searching all maximum frequency envelope values between the waveform start and end points. The mean (MEAN) value was also calculated.

$$PI = \frac{MAX - MIN}{MEAN} \qquad \text{eqn. 4.8}$$

The PI was calculated from the gold standard maximum frequency envelope (PI_I) and compared with the average PI value (PI_{av}) from a particular cohort, to give the bias δPI for that cohort

$$\delta PI = PI_I - PI_{av} \qquad \text{eqn. 4.9}$$

The standard deviation (PI_{sd}) of PI values from a cohort is a measure of the variability of PI.

In a similar manner to the calculation of MFE_{er}, a parameter can be derived relating to the accuracy of calculation of PI for a particular cohort of maximum frequency envelopes. PI_{av} and PI_{sd} are estimates of the average PI value and standard deviation of PI values for the maximum frequency envelopes of waveforms obtained with a particular set of values of beam-vessel angle, attenuator thickness etc. If from a similar ensemble of waveforms n are chosen to measure PI, then the 90% confidence interval for the measured PI value will be

$$PI_{av} - \frac{1.96}{\sqrt{n}} PI_{sd} < PI_{ms} < PI_{av} + \frac{1.96}{\sqrt{n}} PI_{sd} \qquad \text{eqn. 4.10}$$

The measured PI value, PI_{ms}, will in general not be an unbiased estimator of the true PI. The absolute error in estimation of PI from n waveforms is then:

$$PI_{er} = \left| PI_{true} - PI_{ms} \right| \qquad \text{eqn. 4.11}$$

Taking the 90% limit, and taking absolute values, this gives

$$PI_{er} = \left| PI_{true} - PI_{av} \right| + 1.96 \frac{PI_{sd}}{\sqrt{n}} \qquad \text{eqn. 4.12}$$

or

$$PI_{er} = \left| \delta PI \right| + \frac{1.96}{\sqrt{n}} PI_{sd} \qquad \text{eqn. 4.13}$$

PI_{er} is a measure of the overall error of estimation of PI taking into account both the bias and variability components. If the number of waveforms used to estimate PI is large ($n \rightarrow \infty$) then the error PI_{er} will be determined only by the bias component. In the more realistic case where n is small, say n = 5, PI_{er} is determined by roughly equal quantities of the bias and variability components.

In some situations knowledge of the start and end points of the waveform can be found from the ECG. The start point can also be found directly from the Doppler waveform for example by searching for a steep rising edge. It would be expected that the performance of such a waveform-start detector would be dependent upon the design of that detector and on the physical factors which are being investigated in this study. Hence the indices of the maximum frequency envelope and PI would be influenced by the chosen waveform-start detector and by the physical parameter being investigated. In this study a knowledge of the waveform start and end points was imposed so that the effects of the physical parameters could be investigated independently of any waveform start-detector.

4.4. Results.

For each of the physical parameters studied graphs are presented showing indices describing the accuracy of estimation of the maximum frequency envelope as a whole, and of the accuracy of estimation of PI. These graphs only consider one of the three waveform pulsatilities - where the correct PI value was 1.4. The accompanying tables give numerical values of these indices, averaged over the three waveform pulsatilities, for selected values of each physical parameter.

4.4.1 Effect of beam-vessel angle.

The results are shown in figures 4.4 and 4.5 and table 4.1. Indices of PI and of the maximum frequency envelope are smallest at an angle of 45^{o} and increase by only a small amount up to about 70^{o}. Beyond this point all indices rise sharply. There are two effects which are relevant to these results. Firstly the calculation of BS(%) has been performed on the assumption of a simple cos θ dependence of the Doppler shift. Censor et al (1988) demonstrated that the maximum observed

	Indices of MFE			Indices of PI		
Angle (degrees)	BS(%)	SD(%)	MFE_{er}	δPI	PI_{sd}	PI_{er}
45	0.9	5.9	6.0	0.039	0.021	0.058
65	2.9	12.0	12.4	0.126	0.059	0.177
85	55.4	65.0	87.4	0.570	0.226	0.766

Table 4.1: Results for variation of beam-vessel angle. Each value is the average of measurements from 3 waveform pulsatility. (Note MFE is short for maximum frequency envelope).

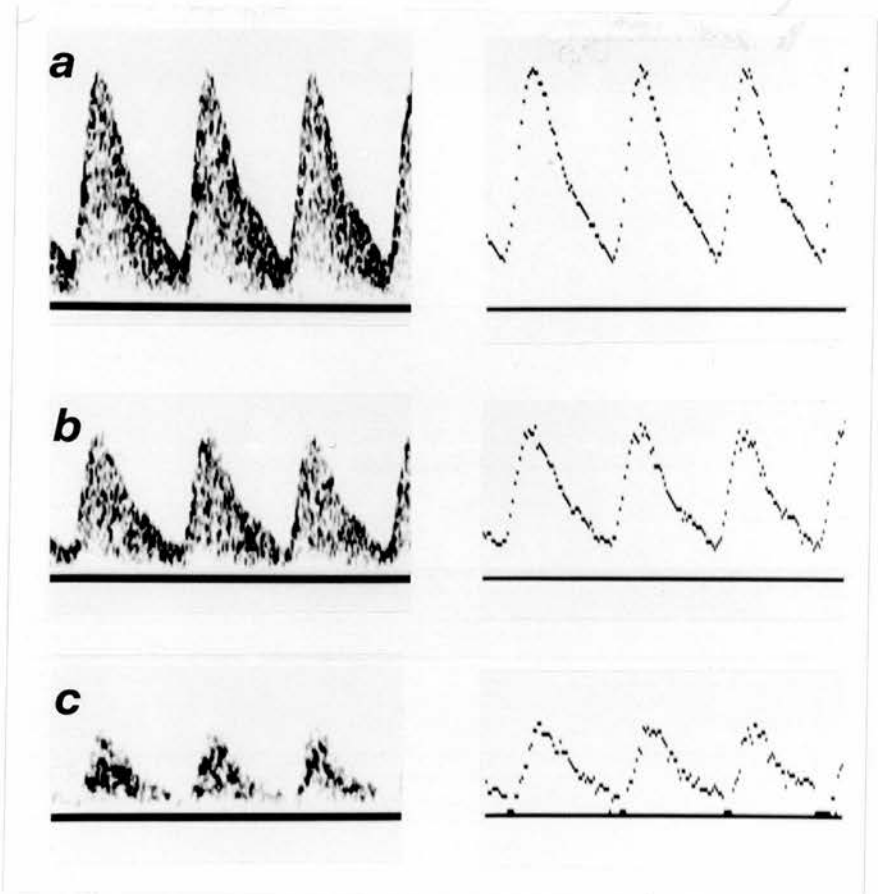

Figure 4.4: Waveforms and maximum frequency envelopes of correct PI = 1.4 for beam - vessel angles of a) 45^{o}, b) 65^{o} and c) 85^{o}.

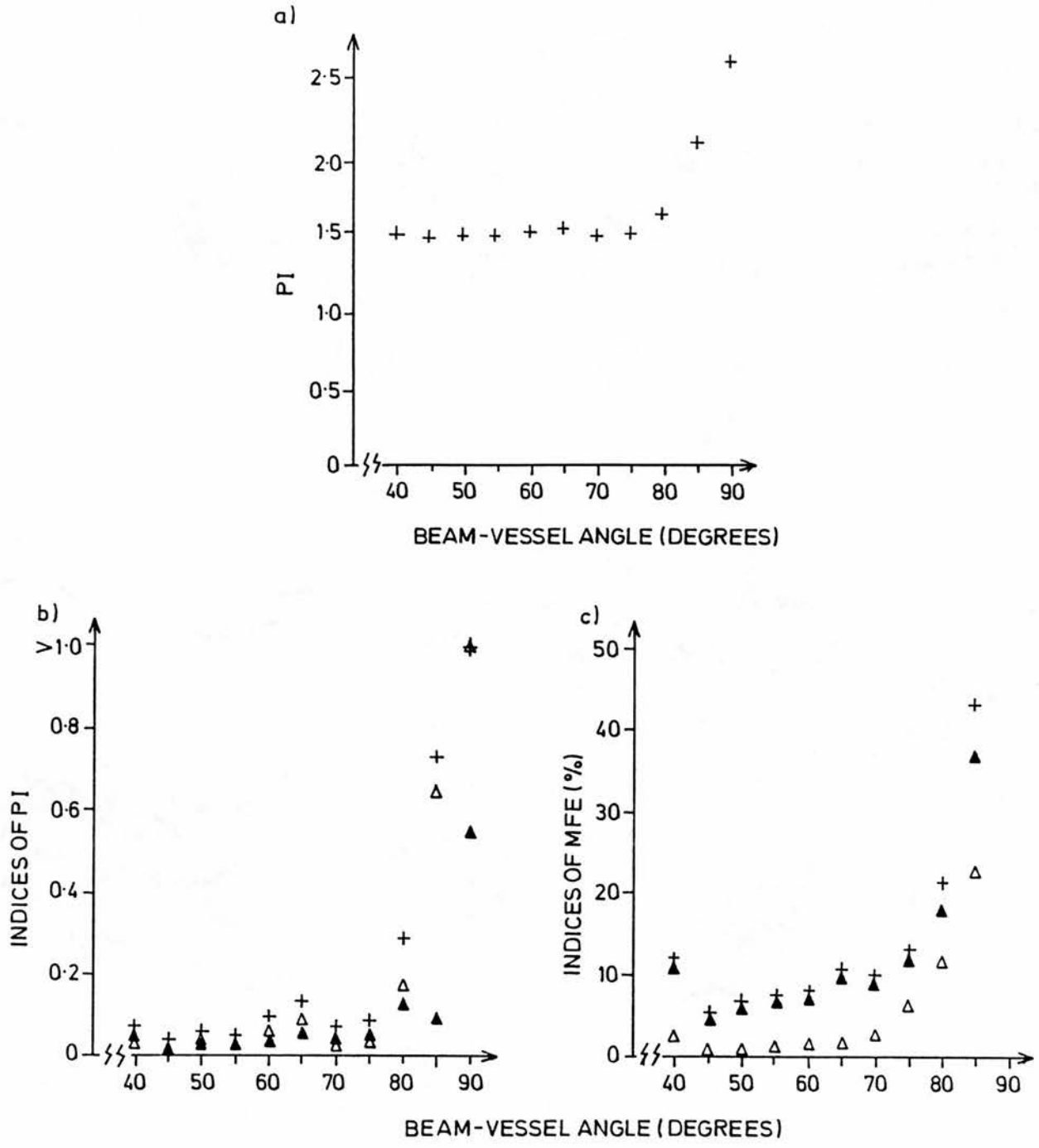

Figure 4.5: Results for variation of beam-vessel angle are shown for waveforms with a correct PI value of 1.4. a) Average PI value, b) Indices of PI; + PI_{er}, △ δPI and ▲ PI_{sd}, c) Indices of the maximum frequency envelope; + MFE_{er}, △ BS% and ▲ SD(%).

Doppler frequency is the result of two effects - a simple Doppler effect with a cos θ dependence, and intrinsic spectral broadening due to finite transducer size with a sin θ dependence (section 1.4.2). The results obtained show that the effects of spectral broadening increase with angle, but are most significant for angles greater than about 70^{o}. The second effect is the loss of end diastolic frequencies for angles near to 90^{o} which also serves to increase BS(%), but manifests itself mainly by an increase in the average PI value.

In this study no waveforms could be acquired for angles less than 40^{o}. This is probably due to the effects of refraction by the wall of the tubing used, and this is further discussed in section 4.5.

4.4.2 Effect of beam-vessel misalignment.

The results are shown in figures 4.6 and 4.7 and table 4.2. The main point to note from this data is that PI_{er} and MFE_{er} have small values and change little over a large range of offsets; from zero offset to 10.5mm. These measurements were made at a transducer-vessel depth of 5cm. Measurements were made of the transmission directivity pattern at 5cm depth in a direction bisecting the orientation of the 2 split D crystals of the transducer and in a second direction orthogonal to the first direction. In each case the half width at half peak pressure amplitude height was 3mm, and the half width at one tenth peak pressure amplitude height was 7.5mm. Therefore the maximum frequency envelope and the PI are estimated with little change in accuracy over most of the significant field of the transducer. The degree of alignment of the vessel and the beam had been increased until Doppler waveforms were only just visible on the spectral display. Beyond 10.5mm the low return power of the Doppler signal necessitated the use of a high amplifier gain which resulted in increasing degrees of background noise. The maximum frequency follower performs less well in the presence of such noise so that the indices PI_{er} and MFE_{er} have increasingly large values for offsets beyond 10.5mm.

It was noted in section 2.2 that there will be refraction of the ultrasound beam

as it passes through the vessel wall. This is further discussed in section 4.5 of this chapter, where it is argued that the maximum frequency may not be unduly affected by this effect. However it is best to be cautious when performing interpretation of the more subtle features of the results of this section. Two observations fall into this category. Firstly the general trend of increase in PI_{er} and MFE_{er} for offsets greater than 10.5 mm is modulated by a reduction in these parameters at 9 to 10.5 mm and at 13.5 mm. This could be due to the directivity pattern of the transducer; that is the presence of side lobes of diminishing amplitude. Secondly, figure 4.7 shows that the bias BS(%) increases linearly from 0.5% at zero offset to 5% at 6mm offset. Examination of the calculated envelope reveals that this is due to a progressive overall reduction in the height of the maximum frequency envelope with increasing offset. Although this effect occurs it appears that the overall shape of the envelope is preserved as the δPI values are constant. This is consistent with loss of high frequency components due to non uniform insonation as described by Cobbold et al (1983). In both of these cases the effects of refraction cannot be discounted.

	Indices of MFE			Indices of PI		
Offset (mm)	BS(%)	SD(%)	MFE_{er}	δPI	PI_{sd}	PI_{er}
0.0	0.8	6.5	6.6	0.054	0.034	0.084
7.5	9.7	9.7	13.8	0.108	0.058	0.158
15.0	17.5	40.4	44.3	0.549	0.217	0.738

Table 4.2: Results for variation of beam-axis offset. Each value is the average of measurements from 3 waveform pulsatilities. (Note MFE is short for maximum frequency envelope).

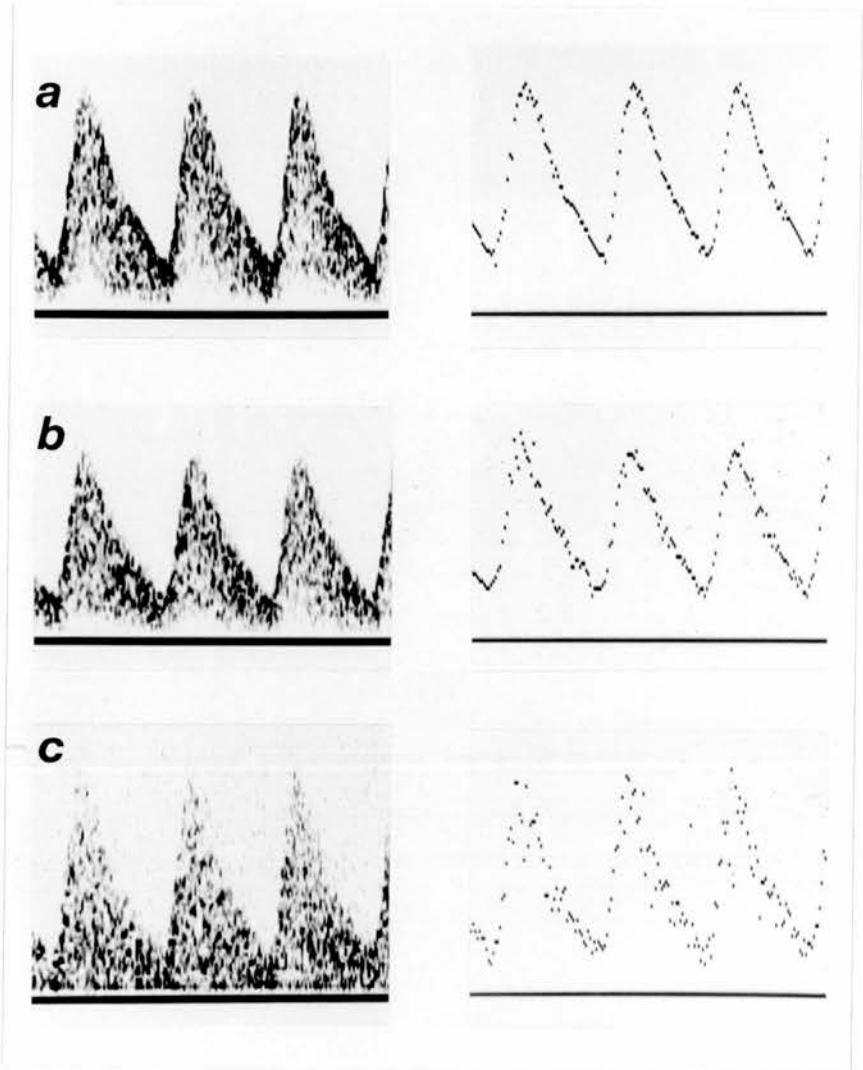

Figure 4.6: Waveforms and maximum frequency envelopes of correct PI = 1.4 for beam - vessel axial offsets of a) 0 mm, b) 7.5 mm and c) 15 mm.

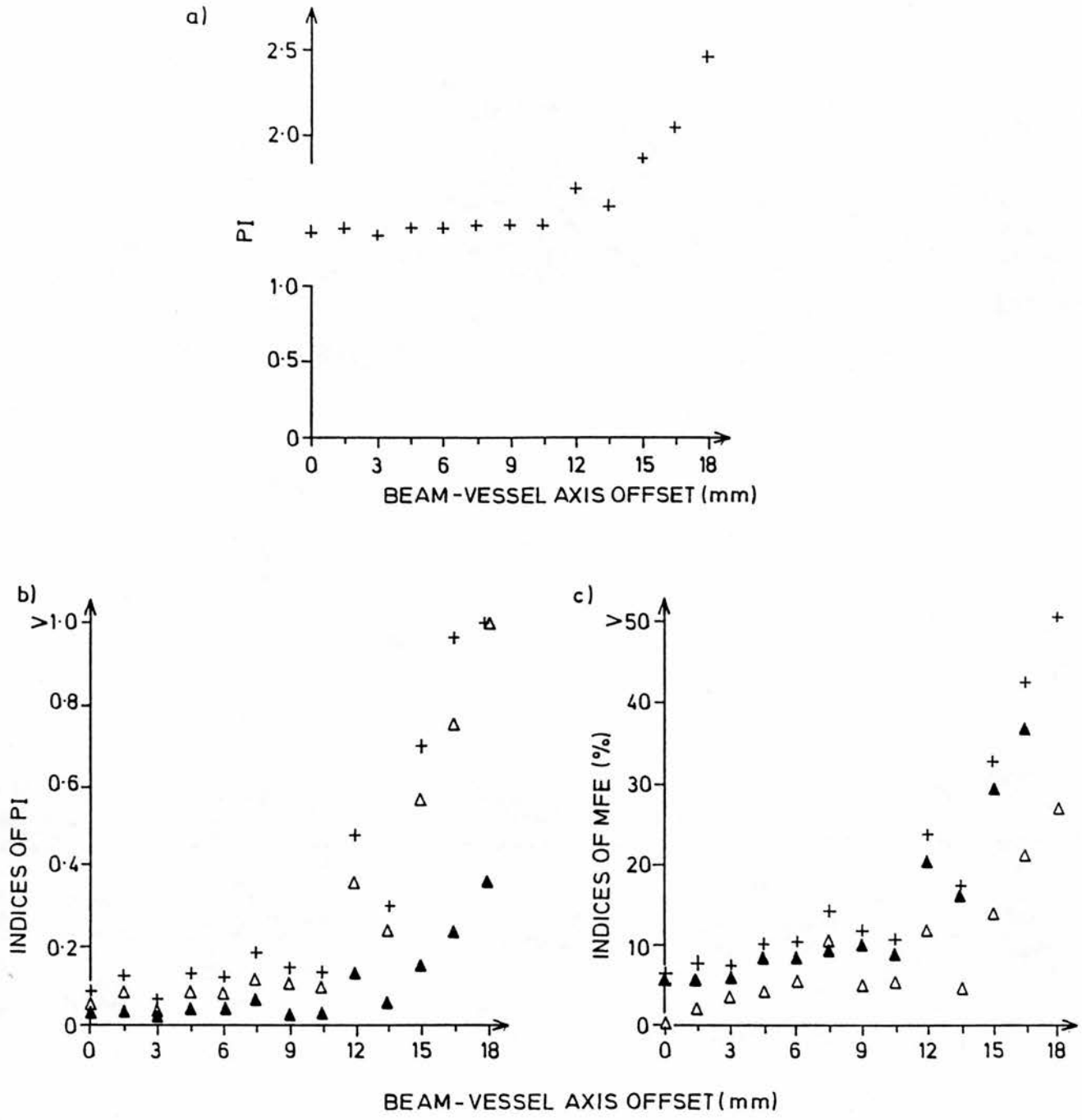

Figure 4.7: Results for variation of beam-vessel axial offset for waveforms with a correct PI value of 1.4. a) Average PI value, b) Indices of PI; + PI_{er}, △ δPI and ▲ PI_{sd}, c) Indices of the maximum frequency envelope; + MFE_{er}, △ BS% and ▲ SD(%).

4.4.3 Effect of attenuation.

The results are shown in figures 4.8 and 4.9 and table 4.3. All indices are roughly constant for thicknesses of attenuator up to 3.5-4 cm. Beyond this point all indices rise sharply. In this case the relative geometry of the beam and vessel are fixed so there is little change in the underlying spectral profile. Background noise is present to an increasing degree from 3 cm of thickness. The background noise is insufficient to cause changes in the shape of the maximum frequency envelope up to 3.5 cm, but beyond this point the high threshold levels employed by the maximum frequency follower due to background noise lead to more underestimation of the maximum frequency envelope and elevated indices of the envelope and of PI.

	Indices of MFE			Indices of PI		
Attenuator Thickness (cm)	BS(%)	SD(%)	MFE_{er}	δPI	PI_{sd}	PI_{er}
2.0	1.1	5.7	5.8	0.053	0.028	0.078
3.5	2.5	8.3	8.7	0.070	0.039	0.104
5.0	9.1	49.9	50.9	0.465	0.249	0.682

Table 4.3: Results for variation of attenuator thickness. Each value is the average of measurements from 3 waveform pulsatilities. (Note MFE is short for maximum frequency envelope).

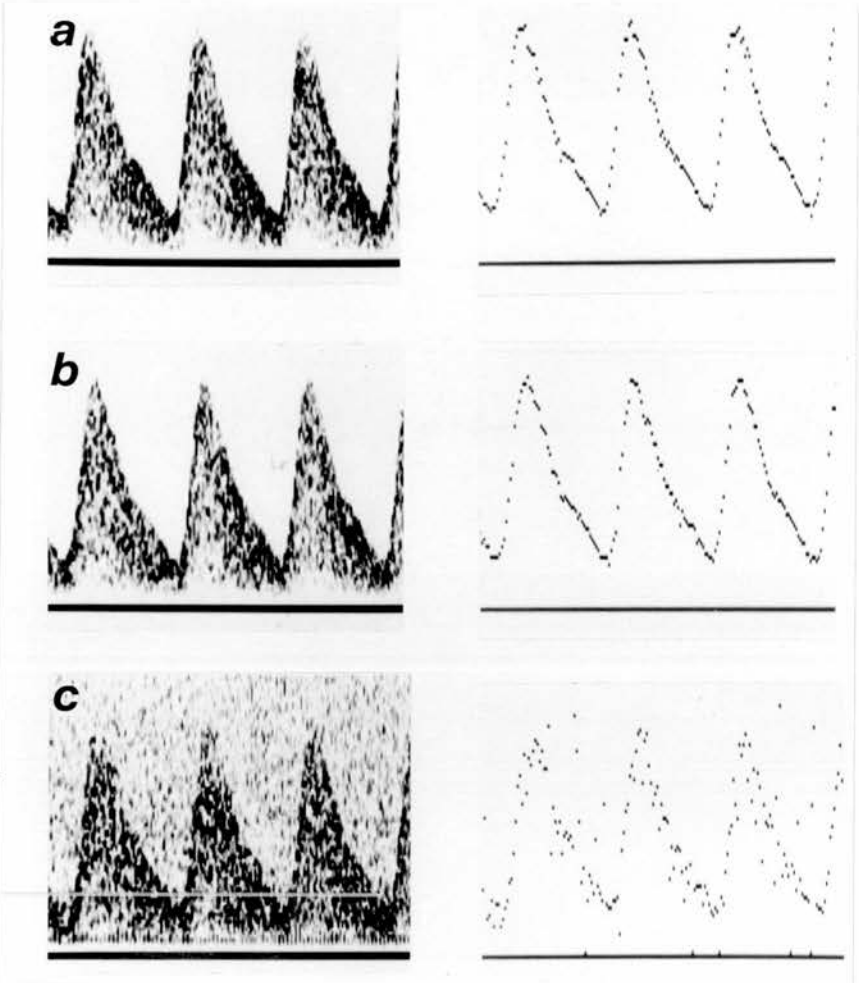

Figure 4.8: Waveforms and maximum frequency envelopes of correct PI = 1.4 for attenuator thickness of a) 2 cm, b) 3.5 cm and c) 5 cm.

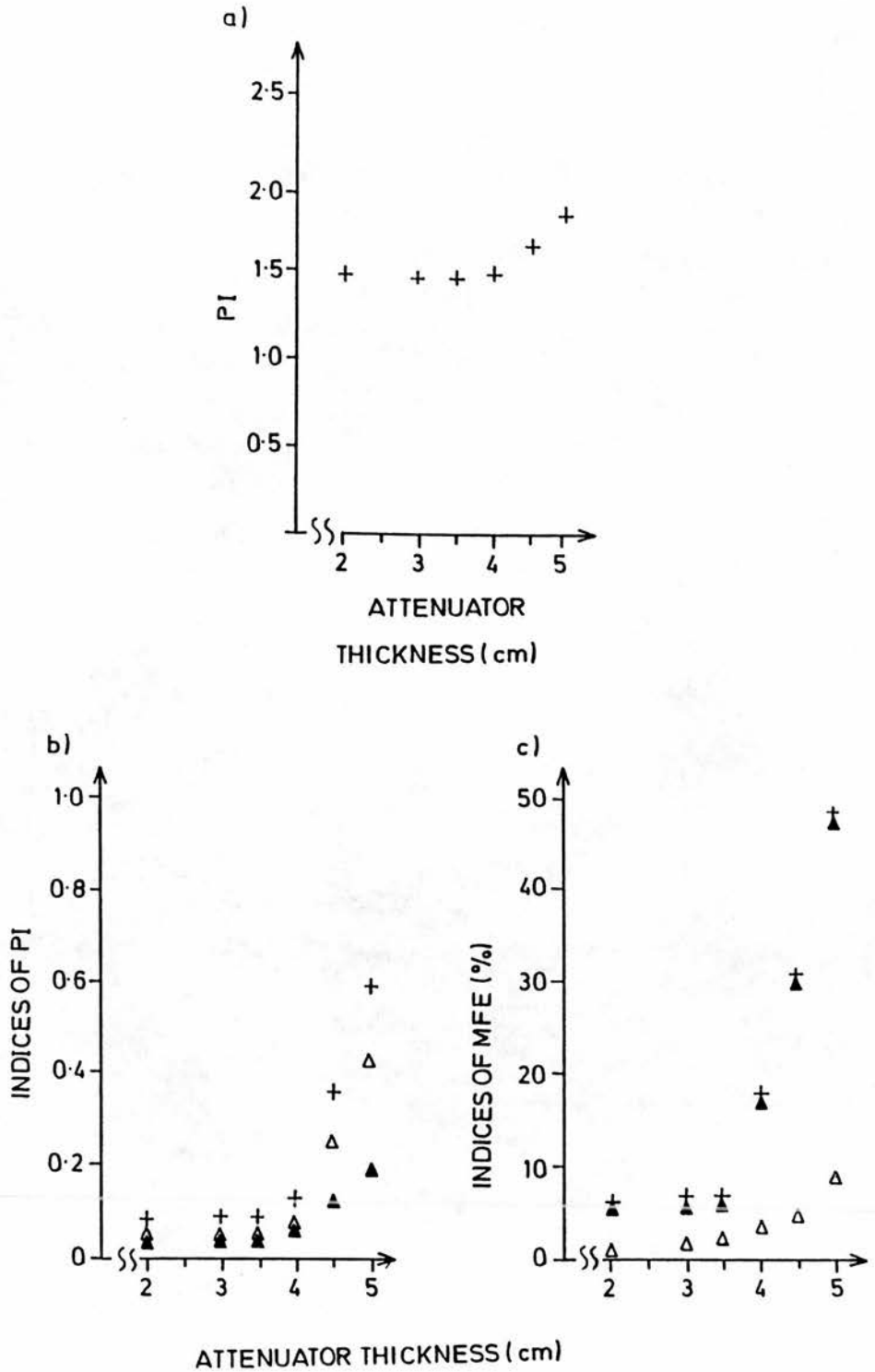

Figure 4.9: Results for variation of attenuator thickness for waveforms with a correct PI of 1.4. a) Average PI value, b) Indices of PI; + PI_{er}, △ δPI and ▲ PI_{sd}, c) Indices of the maximum frequency envelope; + MFE_{er}, △ BS(%) and ▲ SD(%).

4.5 Discussion.

In this study simulated umbilical artery Doppler waveforms have been obtained from a stiff walled vessel which had the typical diameter and depth of an umbilical artery. In the true umbilical artery, the arterial tissue has almost the same acoustic properties as blood and the surrounding tissue. For the heat-shrink material used for vessels in this study the speed of sound at 1850 m/s is higher than that in the surrounding water (section 2.2). This leads to refraction of the ultrasound beam at the water/heat-shrink interface. Using Snell's law the incident angle above which total reflection occurs is 53^{o}, which gives a Doppler angle of 90^{o}-53^{o} or 37^{o}. This is consistent with the observation in this study that no Doppler waveforms were obtained for Doppler angles less than 40^{o}. The Doppler angle used to investigate the effect of beam-vessel misalignment and attenuator thickness was fixed at 50^{o}. For insonation of the centre of the vessel the incident angle to the vessel wall will be 90^{o}-50^{o} or 40^{o}. At the extreme edges of the vessel the incident angle is 90^{o}. This increasing angle of incidence gives rise to an increasing degree of diffraction of the beam, with total reflection occuring for angles greater than 53^{o}. This effect and the further refraction which occurs as the ultrasound beam passes from the tube into the Sephadex suspension will lead to underestimation of the amplitude of lower frequency components associated with low velocities near the vessel wall. In this study it is the maximum frequency envelope that is of most interest, so the effects of low frequencies should be of small importance. However, it would be difficult to study the detailed effects of refraction therefore it is advisable to exercise caution in the interpretation of the more subtle features of the results. This is of relevance mainly to section 4.4.2 where the effect of beam-vessel misalignment is investigated. A second factor worthy of consideration is the received power of Doppler signals from blood in umbilical arteries compared to the power of signals from Sephadex in heat shrink tubing. It is known that the backscattered power from a Sephadex suspension of similar particle concentration

to blood is greater than the power from blood by a factor greater than 150 (chapter 3). This is relevant since, when the Doppler signal strength is low, increase of the amplifier gain for adequate spectral display gives rise to background noise on the spectrum which leads to inaccurate estimation of the maximum frequency envelope and PI. As the degree of background noise is dependent on backscattered Doppler signal strength it may be that in practice background noise will start to appear at different values of tissue thickness and beam-vessel axial offsets than occur in this study. These factors indicate that the range of physical conditions giving rise to similar indices of the maximum frequency envelope and PI may therefore be different to that observed in this study.

4.5. Conclusion.

The effect of 3 physical parameters on the maximum frequency envelope and pulsatility index has been studied using simulated umbilical artery Doppler waveforms. The maximum frequency envelope and pulsatility index are estimated most accurately when there is minimal attenuation between transducer and vessel, when the beam and vessel axes are aligned and when the beam-vessel angle is minimum. Physical conditions away from the optimal conditions give estimates of the maximum frequency envelope and pulsatility index which change little over a wide range of physical conditions indicating that in practice it is not essential to obtain waveforms with a critical set of physical conditons. The inaccurate estimation of pulsatility index and of the maximum frequency envelope associated with larger values of each physical parameter should be avoided.

Chapter 5. A comparison of three different filters for speckle reduction of Doppler spectra.

5.1 Introduction

In the last chapter the accuracy of calculation of the maximum frequency envelope and of the pulsatility index was considered. The envelope was calculated from Fourier transform (FT) based Doppler spectra. These Doppler spectra will be inherently noisy due to the presence of Doppler speckle (chapter 3), and for low power Doppler signals will exhibit a background electronic noise due to the high amplifier gain necessary for display of the waveforms. These factors will cause the envelope to be noisy. The removal of this noise may improve the estimation of the envelope and of the RI and PI. Two approaches can be considered. Firstly envelope noise suppression using a Double Window Modified Trimmed Mean (DWMTM) filter (Lee and Kassam 1985), and secondly spectral noise suppression.

Other spectral estimation techniques have been described (Kay and Marple, 1981) some of which are less sensitive to Doppler speckle than the FT. For example, Vaitkus et al (1988 a,b) have shown using simulated Doppler signals that autoregressive (AR) and autoregressive-moving average (ARMA) algorithms produce consistently smooth spectra which are closer to the theoretical spectral density than the ones obtained from the FT. However, although a real-time autoregressive analyser has very recently been described (Schlindwein and Evans, 1989), all of the current commercial Doppler analysers rely on FT based spectral analysis. Ensemble averaging of waveforms has been shown to be a viable technique of speckle reduction for very regular waveforms produced by a flow phantom (Luckman et al 1988). However the large number of regular waveforms required will put limitations on its use in routine clinical practice where for example physiological changes such as heart rate variation are occurring, or where the artery or patient is moving quickly such as in paediatric cases or in the fetus. The

approach to noise reduction developed in this chapter is to treat the Doppler spectrum as a grey scale image and to use image processing methods. The remainder of this chapter compares 3 different filtering methods which can be applied to all current FT based spectra.

As stated above two types of noise which are present in the Doppler spectrum are Doppler speckle and extraneous background noise. The background noise is electronic in origin and manifests itself when the gain of the Doppler amplifier needs to be high in order to display low power Doppler signals. In the context of Doppler ultrasound, a noise smoothing filter should possess the following desirable properties:

a) Give maximum reduction of extraneous noise above the Doppler waveform,

b) Give maximum reduction of Doppler speckle for those areas of the Doppler waveform which are relatively uniform,

c) Introduce as little distortion as possible to the underlying true spectrum by preserving, for example, the edge content in the vicinity of the maximum frequency envelope.

The performance of the filters proposed here was evaluated in terms of their ability to satisfy the three requirements listed above. In order to achieve this, the filters were applied to a variety of spectra obtained from the physiological flow phantom. Because of the regular nature of the data produced by the phantom, ensemble averaging of a large number of unfiltered spectra enabled the underlying Doppler spectrum, after speckle had been eliminated, to be revealed. This served as a "gold standard", i.e. as the output of an ideal filter which is capable of suppressing speckle completely without introducing any distortion to the true signal. Comparison of the filters' output with the "gold standard" allowed the noise reduction, bias and distortion of the maximum frequency envelope introduced by filtering to be examined. These procedures are described in detail in the Methods Section below. Note that throughout this chapter, the term "Doppler waveform" is

used to describe those parts of the spectrum which lie below the maximum frequency envelope, and the term spatial frequency spectrum refers to the two-dimensional Fourier transform of an image, (in this case the image is the greyscale spectrogram and should not be confused with the Doppler frequency spectrum).

5.2 Filtering techniques

Filtering of an image involves replacement of a central pixel value by a combination of the pixel values in a region (or window) surrounding the central pixel. Early methods of noise filtering involved so-called linear filters. These filters are based upon the concept of the frequency spectrum. Suppression of noise is achieved by filtering if the noise frequencies and the true signal frequencies are separated in the frequency domain. In most types of image there are sharply defined edges which are described by very high frequencies. Suppression of high frequency noise by low pass filtering therefore leads to blurring of the true edge details. For this reason linear filters are not generally useful in image processing. This is discussed further by Loupas (1988). In recent years non-linear filters have been described which attempt to overcome the limitations of linear filters. In general the mathematical analysis of such filters is extremely complex, so that filter design is based upon empirical principles. The three non-linear filters used in this study are described below.

5.2.1 Double Window Modified Trimmed Mean (DWMTM) Filter

The DWMTM filter is a combination of a median and a running mean filter. This was first described by Lee and Kassam (1985). In median filtering the pixels in a window surrounding the central pixel are ordered and the median value is taken as the filter output. In contrast the output of the running mean filter is the average value of the pixels in the window. The median filter tends to perform well in suppressing noise consisting of 'spikes', ie large excursions from the surrounding values, and also at preserving edges. The running mean filter performs worse in these respects causing blurring of edges and smearing out of spikes. These features

are demonstrated in figure 5.1. However in a uniform area corrupted by noise the running mean gives very good noise reduction compared to the median. The DWMTM filter attempts to combine the properties of both the median and running mean filter by using two windows. The median of the terms inside a small window provides a first estimate of the 'true' image value. Then from the larger second window those elements which are within a specified limit of the median are included in a running mean, which is the filter output. In this way a compromise is reached between the edge preserving properties of the median and the noise reduction properties of the mean. The amount of each property is controlled by the choice of the specified limit. If this limit is large there will be substantial noise reduction in the image at the expense of edge preservation, but if the limit is small the opposite is true.

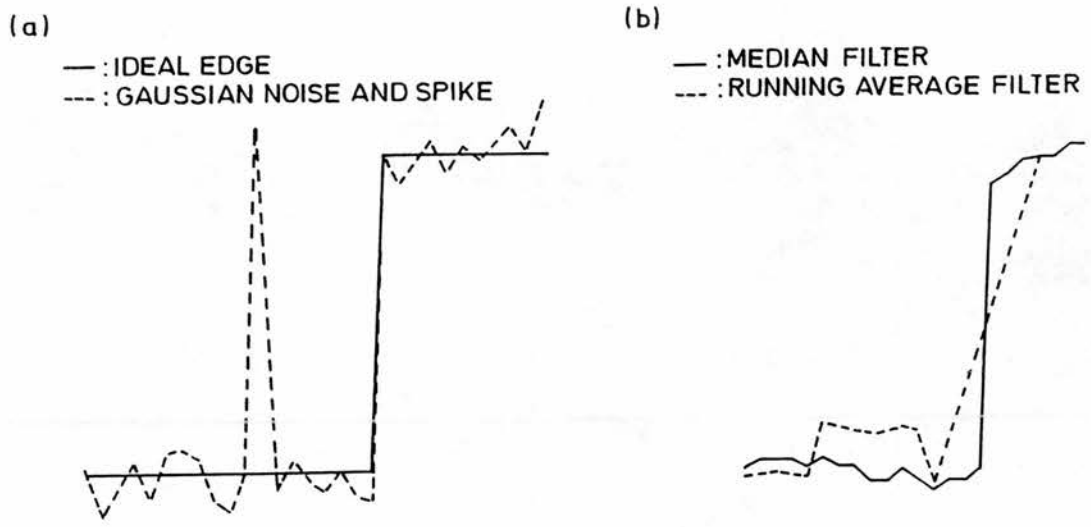

Figure 5.1: Noise reduction by the median and running mean filters. (a) An ideal edge is corrupted by Gaussian noise and a spike. (b) The median filter gives good edge preservation and removes the spike, whereas the running mean filter blurs the edge and smears out the spike. (From Loupas (1988) with permission).

The DWMTM filter is an example of a non-adaptive non-linear filter. The next two filters are examples of adaptive filters whereby the proportion of edge preservation or smoothing at each point of the image is controlled by the value of some local image measure at that point. For adaptive filters the local image measure must be calculated at each point. This makes these filters computationally more complex than non-adaptive filters.

5.2.2 Lee's filter.

This filter is described in equation 5.1 and was suggested by Lee (1980).

$$O(x,y) = m(x,y) + C[I(x,y) - m(x,y)] \qquad \text{eqn. 5.1}$$

where I(x, y) is the value of the central pixel

m(x, y) is the local mean of terms inside the filter window

O(x, y) is the filter output

C is a controlling parameter which depends on a local image measure

The value of C determines the amount of smoothing performed at each point. The local image measure should be formulated to give values of C near zero in a uniform area, resulting in maximum smoothing (O(x, y) = m(x, y) for C = 0), and values of C near 1 at an edge, so that little smoothing is performed and edges are preserved (O(x,y) = I(x,y) for C = 1). Filters based on equation 5.1 have been used for general noise reduction (Lee 1980, Chan and Lim 1985), synthetic aperture radar speckle suppression (Lee 1981, 1986; Kuan et al 1987) and ultrasonic B-scan speckle suppression (Bamber and Daft 1986, Bamber and Cook-Martin 1987).

5.2.3 Directional filtering.

The 2 filters described above take no account of the 2 dimensional nature of the image. The filter output would be the same if the window contents were distributed along a single line. Directional filters take into account the 2 dimensional nature of the image by calculating along a number of separate directions. Methods for image enhancement which utilise directional information have been described by Chan and Lim (1985), Kim and Jung (1987) and Peli

(1987). Loupas (1988) described a directional two stage filter which gave combined smoothing and sharpening of ultrasonic B-scan images. In this paper only the smoothing stage is used, where the filter output O(x,y) is given by equation 5.2 below.

$$O(x,y) = \frac{\sum_{d=1}^{8} m(d)[C(d)]^k}{\sum_{d=1}^{8} [C(d)]^k} \qquad \text{eqn. 5.2}$$

where m(d) is the mean value of elements in a window aligned along the direction d,

C(d) is the local image measure along the same direction,

k is a parameter which determines the relative contributions of the directional means m(d) to the final output.

The values of the local image measure C(d) determine the amount of smoothing performed by the filter. C(d) should be formulated so that in a uniform area the values C(d) for d = 1, ..., 8 are all comparable so that maximum smoothing is achieved. However, in the presence of an edge C(d) should become maximum along the edge direction so that only smoothing parallel to the edge axis is performed. This should improve its definition without introducing much blurring.

5.3 Local image measures.

The aggressiveness of smoothing of Lee's filter and the directional filter are controlled by the local image measure C or C(d) respectively. The local image measure is calculated from the values in a predefined neighbourhood around the central pixel. Three possibly useful types of image content from which the local image measure can be formulated are considered below.

5.3.1 Local statistics.

Firstly consider the local statistics of the image. The expression for a local image measure based upon local statistics will depend upon the characteristics of the

image noise. For synthetic aperture radar images multiplicative noise is present, and the speckle can be characterised by σ/m where σ is the local standard deviation and m is the local mean (Lee 1981). Ultrasonic speckle has square-root noise, as shown by Loupas (1988), and this can be characterised by σ^2/m. Measurements of spectra obtained from a commercial Doppler device (Doptek, Chichester) suggest that for this device Doppler speckle falls somewhere between the cases of multiplicative noise and square-root noise mentioned above (chapter 3). For this reason both the σ/m and σ^2/m image measures were applied to Doppler spectra in order to determine which one is the most suitable.

5.3.2 Slope

A second approach is to use the slope SL(d) of the least-squares-fit line passing through the data points along a specific direction d. The use of this quantity as a local image measure is justified by the argument that for a uniform area the slope should have a low value but near an edge it should become higher.

The slope SL(d) was calculated along 8 directions spaced at equal intervals of 22.5^{o}. A set of 9 values was used in the calculation of a particular slope SL(d), with each value corresponding to the average of the 3 adjacent pixels lying perpendicularly to the direction of interest.

5.3.3 Edge parameter.

Consider figure 5.2 and equation 5.3. The directional mean is shown aligned along a direction d with two background areas, one on either side of the directional mean window. A parameter R(d) can be formed, (equation 5.3), which gives high values when the directional mean window lies along an edge.

$$R(d) = m(d) - \lambda \frac{2.B1(d).B2(d)}{B1(d)+B2(d)} \qquad \text{eqn. 5.3}$$

where m (d) is the mean value of elements in the directional mean window,

B1 (d) is the mean value of elements in the background region B1,

B2 (d) is the mean value of elements in the background region B2, and

λ is a factor controlling the amount of background subtracted.

R(d) represents a directional edge detection operator. In relatively uniform areas, for any given direction d the directional mean m(d) will be similar to the background means B1(d) and B2(d), so that all the edge parameters R(d) will have small and very similar values. The presence of an edge will give rise to a value of R(d) along the edge axis which is considerably larger than the rest. The maximum value of R(d) at a particular point is called RMAX. In order to reduce the sensitivity of R(d) to noise, a value of λ = 1.5 was chosen and negative values of R(d) were set to zero.

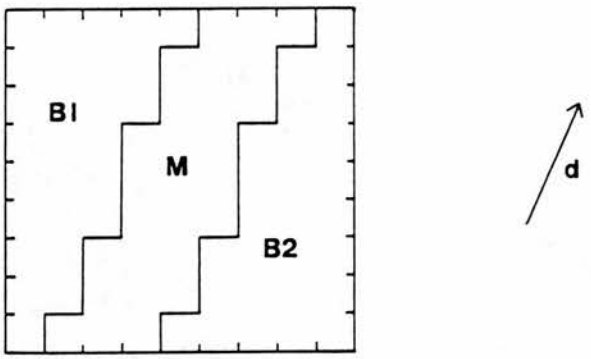

Figure 5.2: Windows used for the calculation of the edge parameter R(d). M is the 3 x 9 directional mean window, B1 is a background window above M and B2 is a background window below M.

5.4 Methods.

5.4.1 Data acquisiton.

Doppler waveforms were acquired from the flow phantom. The tubing diameter was 3 mm which was chosen as being representative of the diameter of the umbilical artery. A Doptek 4 MHz continuous wave unit was used for waveform acquisition. Three examples of 'good' waveforms were acquired, each having different pulsatility. Three examples of 'poor' waveforms were also acquired, corresponding to a high beam-vessel angle, a large offset between the

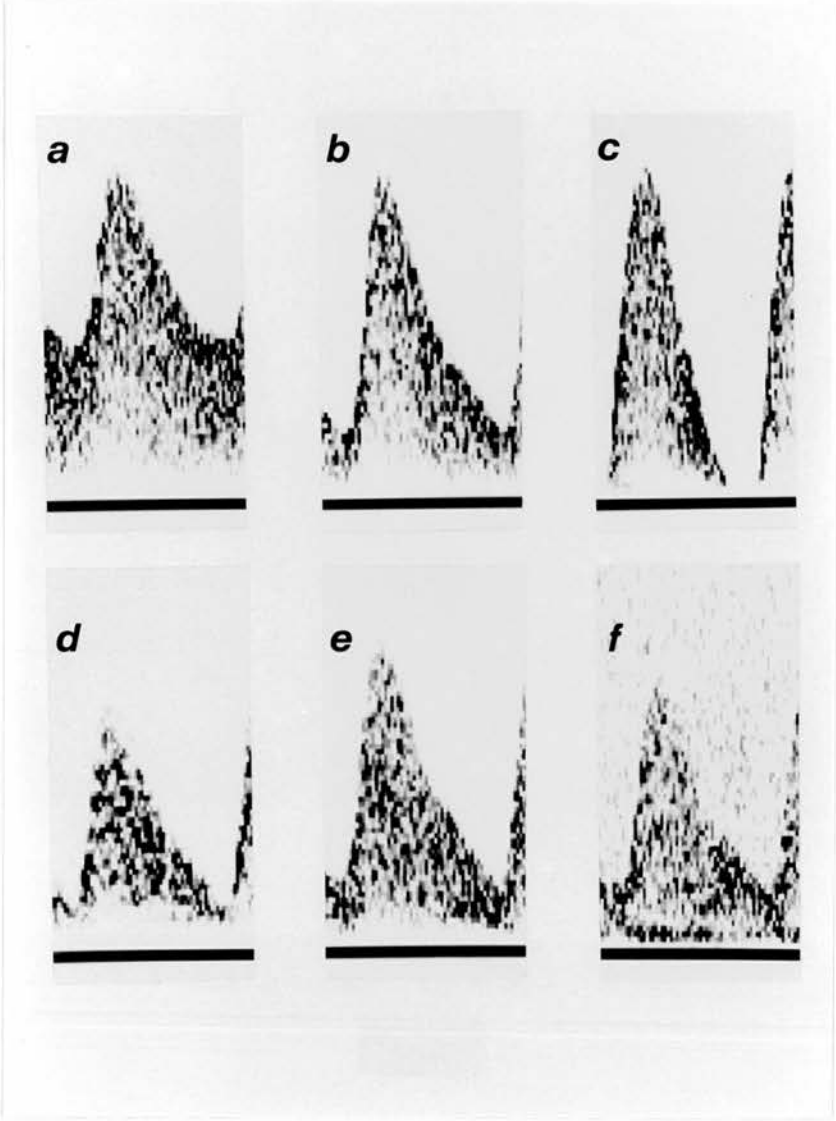

Figure 5.3: Doppler waveforms used for filter development. Waveforms are given in the table below; (θ is the beam-vessel angle, d is the transducer-vessel depth (cm), b is the beam-vessel axial offset (cm), a is the thickness of attenuating material between the vessel and transducer (cm), and RI is the resistance index).

waveform	θ	d	b	a	RI
(a)	45	5	0	1	0.6
(b)	45	5	0	1	0.85
(c)	45	5	0	1	1.0
(d)	75	5	0	1	0.85
(e)	45	5	1.1	1	0.85
(f)	45	8	0	6	0.85

beam axis and vessel axis, and a large amount of overlying tissue. These are shown in figure 5.3. In each of the six cases, 42 screens of data corresponding to 168 waveforms were acquired, transferred from the Doptek to the microcomputer (BBC Master, Acorn Computers, Cambridge) in a serial pixel-by-pixel fashion and stored on disk. The BBC microcomputer was used as a data logger only. Subsequent analysis of the Doppler spectra was performed by a second microcomputer (Archimedes 440, Acorn Computers, Cambridge) which was approximately 25 times faster than the BBC microcomputer during image processing. The waveforms corresponding to figures 5.3a-c and 5.3e-f were acquired using a time resolution of 10 ms and a frequency resolution of 50 Hz. For the waveform of figure 5.3d the time and frequency resolution were 10 ms and 25 Hz respectively. A Hanning window was employed by the Doptek analyser in all cases. The overlap between windowed data segments used to generate adjacent spectral profiles was 50% for a frequency resolution of 50 Hz and 75% for a frequency resolution of 25 Hz.

5.4.2 Filtering.

All filtering programmes were written in interpreted Basic. Filtering 2.4 seconds of data, which was 4 waveforms or 240 x 80 pixels, took between 25 minutes and 160 minutes depending on the filter complexity. Batch processing programmes were written which enabled filtering of many screens of data to be performed without operator intervention.

For the DWMTM filter the large window size was 9 x 9 and the small window was a 5 pixel cross. For Lee's filter and the directional filter a 9 x 9 window was used. The directional means were calculated using a 3 x 9 window within the 9 x 9 window. A value k = 1 was used for the directional filter.

5.4.3 Ensemble averaged waveforms.

This was performed on the unfiltered and the filtered waveforms in order to examine the noise reduction offered and the bias introduced by the filters. This

technique is fully described in section 4.3.2.1. The averaged waveform was saved to disc. Calculation of the ensemble averaged standard deviation at each point in the Doppler waveform was performed using the same registration technique.

5.4.4 Assessment of filter performance.

Comparison of the filters was performed in terms of the filter's ability to satisfy the three desirable requirements listed in the introduction.

A number of parameters were calculated from the ensemble averaged waveforms to examine bias and noise reduction produced by filtering. These parameters are described below. In all cases subscript f indicates ensemble averaged filtered waveform and subscript r indicates ensemble averaged unfiltered waveform.

The coefficient of variation (CV) at a particular location of the waveform was calculated from the values of the ensemble averaged standard deviation (σ) and mean at that location (CV = 100σ/mean). Three regions from the waveform were chosen to allow comparison of the noise reduction properties of different filters. The first region was a relatively uniform 9 x 9 area in the centre of the waveform (CA: central area). The mean coefficient of variation CV_{CA} was calculated over the 81 locations for this central area. The second region was the leading edge of the waveform (LE: leading edge). This is a highly non-uniform region. The coefficient of variation of pixels in this region gives an indication of the noise reduction properties of the filter in the presence of an edge. The coefficient of variation was calculated for locations along the leading edge between 1000 and 1500 Hz and from them the mean value CV_{LE} was derived.* The third region was a 9 x 9 area above the Doppler waveform, which was chosen to examine the smoothing of extraneous electronic noise produced by filtering (UR: upper region). The mean coefficient of variation CV_{UR} was calculated only for the Doppler spectrum of figure 5.3f as this is the only case with extraneous noise. Having calculated the mean coefficients of variation for both raw and filtered data, their ratio could then

be derived (5.4, 5.5 and 5.6 below). These quantities indicate the factor by which noise, as measured by the coefficient of variation, has been reduced by filtering.

$$RCV_{CA} = CV_{CA(r)}/CV_{CA(f)} \qquad \text{eqn. 5.4}$$

$$RCV_{LE} = CV_{LE(r)}/CV_{LE(f)} \qquad \text{eqn. 5.5}$$

$$RCV_{UR} = CV_{UR(r)}/CV_{UR(f)} \qquad \text{eqn. 5.6}$$

The bias produced by filtering in each of the three regions was also examined. In each case, the average height of pixel values in the region of the ensemble averaged filtered waveform and the ensemble averaged raw waveform was calculated and the change in height produced by filtering derived (5.7, 5.8 and 5.9 below).

$$RH_{CA} = \sum_{CA(f)} A(x,y) \,/\, \sum_{CA(r)} A(x,y) \qquad \text{eqn. 5.7}$$

$$RH_{LE} = \sum_{LE(f)} A(x,y) \,/\, \sum_{LE(r)} A(x,y) \qquad \text{eqn. 5.8}$$

$$RH_{U} = \sum_{UR(f)} A(x,y) \,/\, \sum_{UR(r)} A(x,y) \qquad \text{eqn. 5.9}$$

The 'smearing' of the edges produced by filtering was examined further by considering the maximum frequency envelope of the ensemble averaged waveform. A threshold maximum frequency follower with a threshold value of 5 was used.

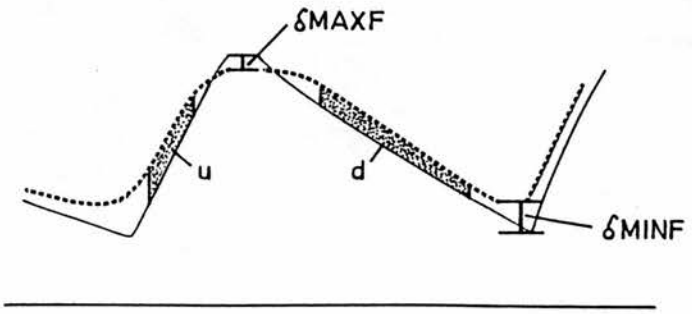

Figure 5.4: The effect of filtering on the maximum frequency envelope. Envelopes are shown for the ensemble averaged unfiltered waveform (solid line) and for the ensemble averaged filtered waveform (dashed line). The differences have been exaggerated for clarity.

For a particular Doppler profile the maximum frequency is defined as that point at which the pixel value first exceeds the threshold value of 5, starting from the high frequency end. A number of parameters (equations 5.10 to 5.12) were calculated which describe differences between the maximum frequency envelopes of the ensemble averaged filtered and unfiltered waveforms; (see also figure 5.4).

$$\delta MAXF = MAXF(PS)_f - MAXF(PS)_r \qquad \text{eqn. 5.10}$$

where MAXF(PS) is the maximum frequency at peak systole for a threshold of 5.

$$\delta MINF = MINF(ED)_f - MINF(ED)_r \qquad \text{eqn. 5.11}$$

where MINF(ED) is the maximum frequency at end diastole for a threshold of 5.

δMAXF and δMINF indicate the average amount of distortion of the maximum frequency envelope produced at peak systole and end diastole. These are two commonly used points from which indices such as resistance index (Pourcelot 1974) are calculated.

$$\delta MFE = \sum_{upslop} [MAXF(U)_f - MAXF(U)_r] + \sum_{dwnslop} [MAXF(D)_f - MAXF(D)_r] \qquad \text{eqn. 5.12}$$

where MAXF is the maximum frequency at a threshold of 5

U is the upslope of the waveform excluding the peak and trough,

D is the downslope of the waveform excluding the peak and trough.

δMFE indicates the average amount of distortion of the maximum frequency envelope produced by the filter at the downslope and upslope of the waveform.

5.5 Results.

5.5.1 Parametric images.

Local image measures were generated using a 9 x 9 window from one of the 'good' waveforms of RI=0.85. These are shown as parametric images in figure 5.5a-e. A parametric image is an image where the pixel value at a point is proportional to the value of the parameter under consideration at that point.

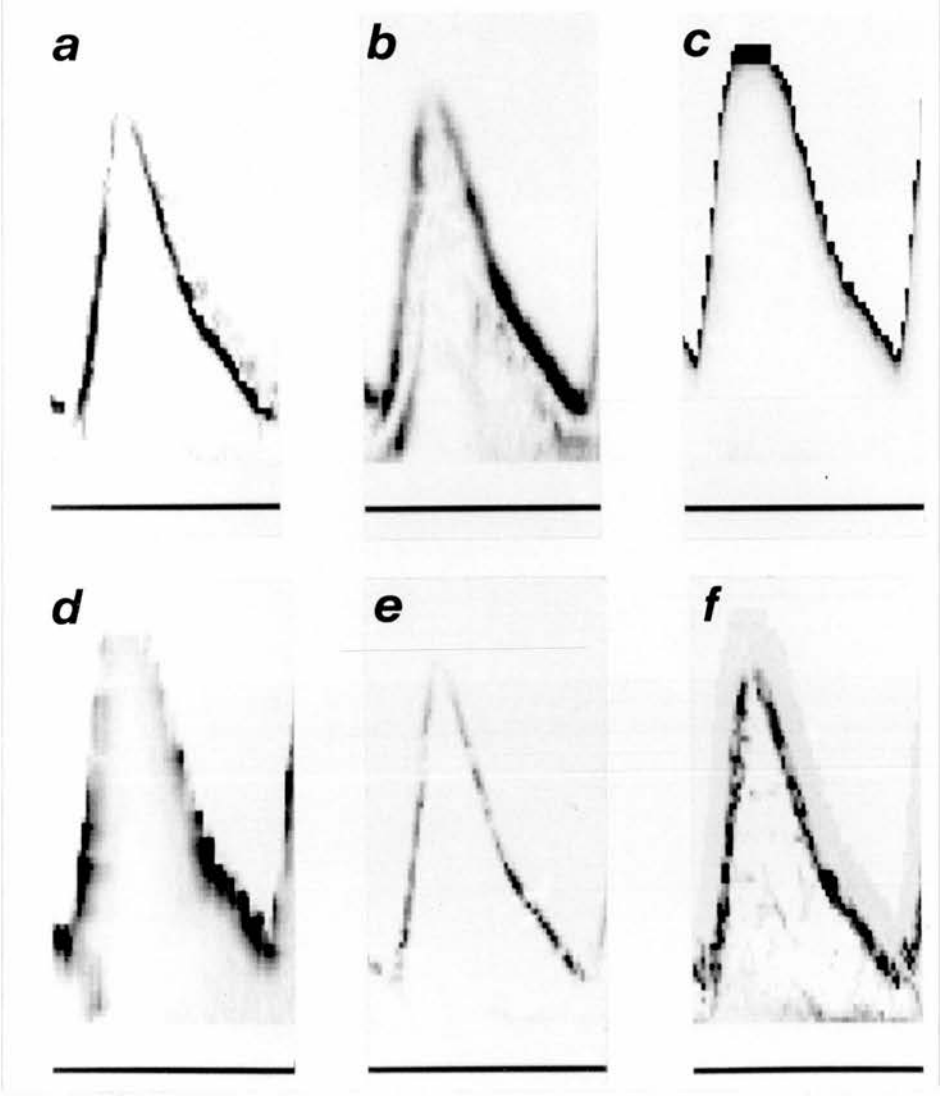

Figure 5.5: Parametric images generated using waveform (b) of figure 5.3. a to e were produced using a 9 x 9 window. (a) Edge parameter RMAX, (b) $\sum$SL(d), (c) σ/m, (d) σ^2/m, (e) (R(d)/SL(d))max, (f) was generated using equation 5.13 where C (d) = 1 + R(d)/SL(d).

It is the purpose of the local image measure to 'tell' the adaptive filter where a true structure is, so that the filter can apply minimum smoothing there. In this respect a parametric image which has high pixel values in the region of the edges of the waveform and low values elsewhere is desirable. Examination of these images will help to choose which local image measure may be useful in Lee's filter. The edge detection parameter RMAX gives a strong peak at the waveform outline with a small amount of noise above the outline [figure 5.5a]. The maximum directional slope was relatively noisy, however the sum $\sum SL(d)$ of the directional slopes was better [figure 5.5b]. This parameter peaks just above, and for the leading edge, just below the waveform outline. The parameter standard-deviation/mean (σ/m) peaked well above the waveform outline [figure 5.5c]. This parameter also gives extremely large values in the presence of a small amount of background noise above the waveform and is therefore not useful. The parameter variance/mean (σ^2/m) gives some peaking just above the waveform outline [figure 5.5d)] however this is inferior to that of the sum of slopes $\sum SL(d)$, so it will not be considered further. The parameter R(d)/SL(d) can be calculated for each direction and the maximum value $[R(d)/SL(d)]_{max}$ found. This gives an image very similar to that of RMAX except that the noise above the outline has been removed [figure 5.5e].

For the directional filter it is not possible to display a single parametric image because the filter's action is controlled by eight normalised directional image measures (see equation 5.2). However by using the parameter P, defined below in equation 5.13, it is possible to visualise those parts of the image where one of the directional image measures C(d) is dominant.

$$P = \frac{\sum_{d=1}^{8} [C(d)]^2}{[\sum_{d=1}^{8} C(d)]^2} \qquad \text{eqn. 5.13}$$

Figure 5.5f shows the parametric image for P when C(d) = 1 + R(d)/SL(d). This shows that there is a dominant directional value of C(d) around the edge of the waveform with noise directly above this.

5.5.2 Comparison of filters.

A comparison between the filters with associated local image measures chosen from above was performed using the 'good' waveform with a resistance index of 0.85. Examples of this waveform after a variety of filters have been applied are shown in figure 5.7. Table 5.1 shows the indices of maximum frequency envelope distortion, bias and noise reduction calculated from the ensemble of waveforms. The ensemble averaged waveform constructed from 168 unfiltered waveforms is shown in figure 5.6. This can be considered to be the waveform that would result if a perfect filter was applied to an individual waveform. This should be compared to the waveforms in figure 5.7.

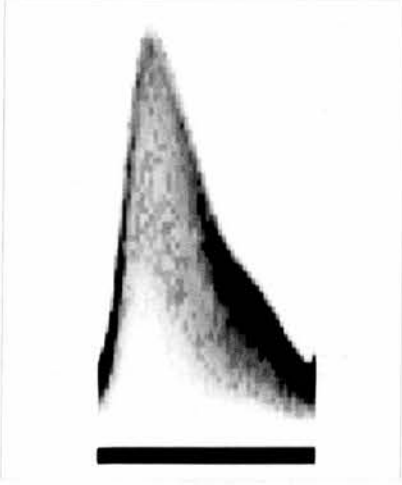

Figure 5.6: Ensemble averaged waveform derived from 168 waveforms of RI value equal to 0.85.

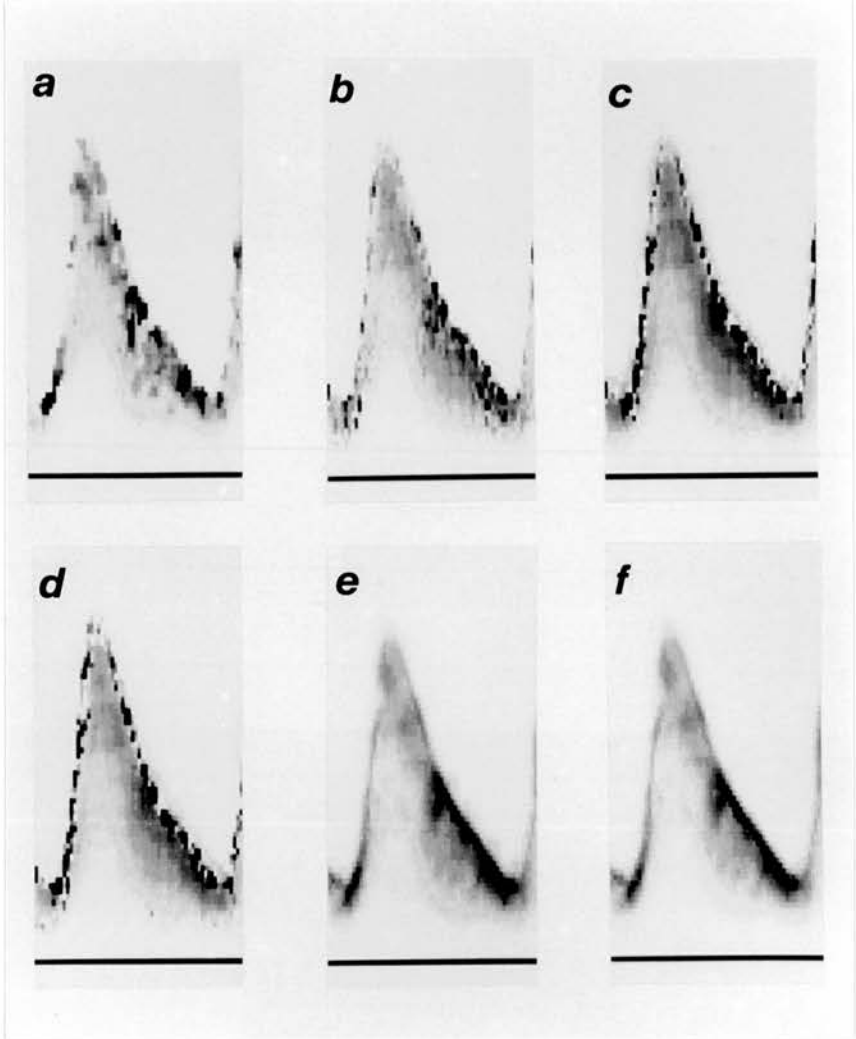

Figure 5.7: Processing using different filters. Waveform (b) of figure 5.3 was used in each case. (a) DWMTM, (b) Lee filter with sum of slopes parameter $\sum SL(d)$, c) Lee filter with edge parameter RMAX, (d) Lee filter with $[R(d)/SL(d)]_{max}$, (e) Directional filter with parameter C(d) = R(d), (f) Directional filter with parameter C(d) = 1 + R(d)/SL(d).

From table 5.1 it can be seen that all the filters perform very well in the uniform central area. They offer considerable noise reduction, by a factor varying between 4.06 and 5.75, and also introduce almost negligible bias as indicated by the values of RH_{CA} which are very close to 1. However, as far as the leading edge region is concerned significant differences in performance can be found. Filters (a) and (b) reduce the edge height considerably, by 46 and 43% respectively, while offering only moderate noise reduction. Filters (c) and (d) preserve the edge height but at the expense of no noise reduction. On the other hand the directional filters (e) and (f) offer a reasonable compromise between noise reduction and edge preservation. This is due to the fact that in the vicinity of an edge smoothing is performed only along the edge axis; something which improves its definition without introducing excessive blurring.

		MFE indices			Leading Edge		Central area	
Filter	Parameter C or C(d)	δMAXF (Hz)	δMINF (Hz)	δMFE (Hz)	RH_{LE}	RCV_{LE}	RH_{CA}	RCV_{CA}
a) DWMTM	-	-100	0	-46	0.54	1.37	0.95	4.06
b) Lee	$\sum SL(d)$	-50	0	40	0.57	1.70	1.04	5.31
c) Lee	RMAX	-50	200	81	1.00	1.02	1.05	5.75
d) Lee	$\left(\frac{R(d)}{SL(d)}\right)_{max}$	-50	0	70	0.94	1.00	1.05	5.31
e) Direc	R(d)	-50	150	104	0.72	3.15	1.03	4.31
f) Direc	$1 + \frac{R(d)}{SL(d)}$	-50	100	70	0.74	3.15	1.04	4.30

Table 5.1: Indices of bias and variance for the filtered data. Waveform (b) of figure 5.3 was used in each case. (MFE stands for maximum frequency envelope).

The same conclusions about the superiority of filters (e) and (f) can be drawn by visual examination of the images in figure 5.7. The filtered spectra (a) to (d) are composed of smooth areas together with very noisy edges and overall have a very unbalanced appearance. On the other hand, the spectra (e) and (f) are much more balanced. There is very little to choose between (e) and (f). However on the basis of the maximum frequency envelope indices and especially δMFE (see table 5.1), the directional filter (f) which is controlled by the local image measure C(d) = 1 + R(d)/SL(d) is preferable.

The effectiveness of speckle suppression is demonstrated by figure 5.8 where it

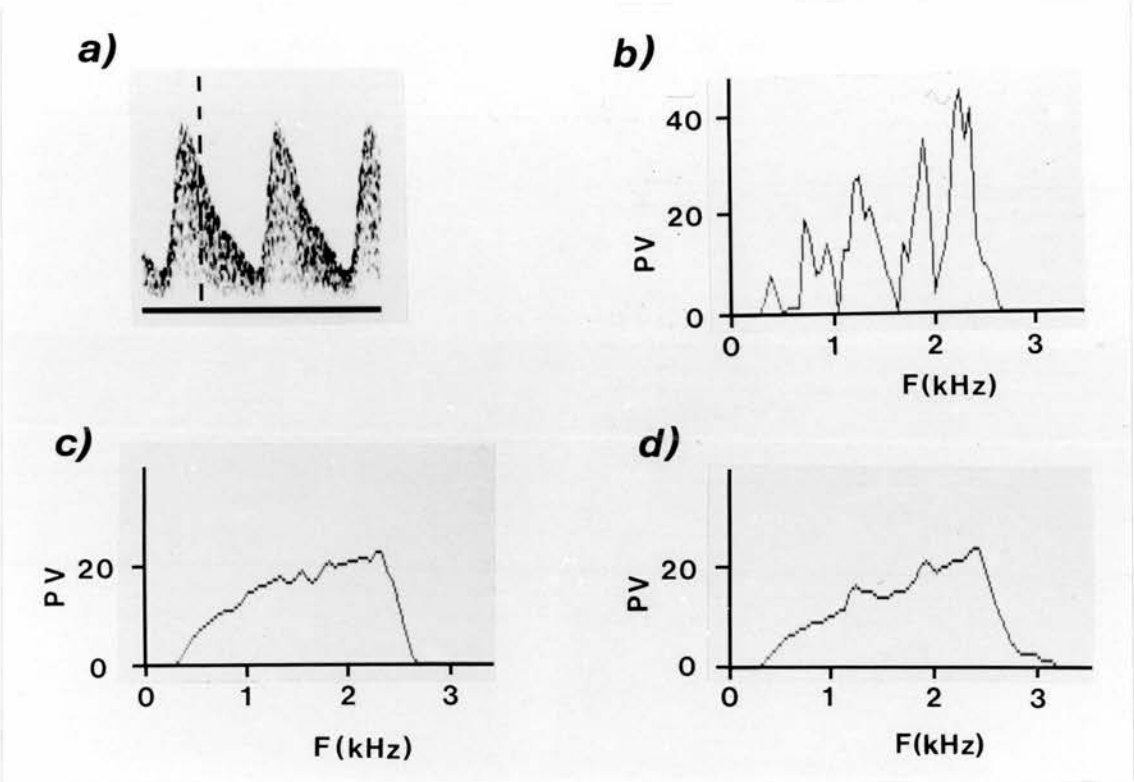

Figure 5.8: Profiles from waveform (b) of figure 5.3. a) Single unfiltered waveform; the profile position is indicated by the dashed line, b) Profile from a single unfiltered waveform, (c) Profile from ensemble averaging of 168 unfiltered waveforms, (d) Profile from a single filtered waveform.

can be seen that the spectral profile obtained from ensemble averaging of 168 raw waveforms is very similar to the profile of a single waveform smoothed by filter (f).

Figure 5.9 shows the application of this filter to the six different waveforms of figure 5.3, and table 5.2 lists the quantitative indices related to each waveform type. The upper region (UR) indices are presented only for waveform (f) because it is the only one with background noise above the waveform outline. There are differences in each of the other indices for the six waveforms, however these are small. Since the waveforms used were chosen to represent the range of shapes encountered in practice, this suggests that the directional filter controlled by the parameter C(d) = 1 + R(d)/SL(d) will perform similarly over a wide range of waveform types.

Wave-form	δMAXF (Hz)	δMINF (Hz)	δMFE (Hz)	RH_{LE}	RCV_{LE}	RH_{CA}	RCV_{CA}	RH_{UR}	RCV_{UR}
a)	0	50	53	0.78	3.81	0.98	5.03	-	-
b)	-100	100	70	0.74	3.15	1.04	4.31	-	-
c)	-50	0	82	0.65	3.10	1.03	5.65	-	-
d)	-50	50	38	0.80	2.52	1.06	4.36	-	-
e)	-50	100	28	0.84	4.13	1.03	5.19	-	-
f)	-50	100	82	0.78	4.57	1.04	4.82	1.05	4.18

Table 5.2: Indices of bias and variance for the six different waveforms of figure 5.3 when the directional filter with parameter 1 + R(d)/SL(d) was used.

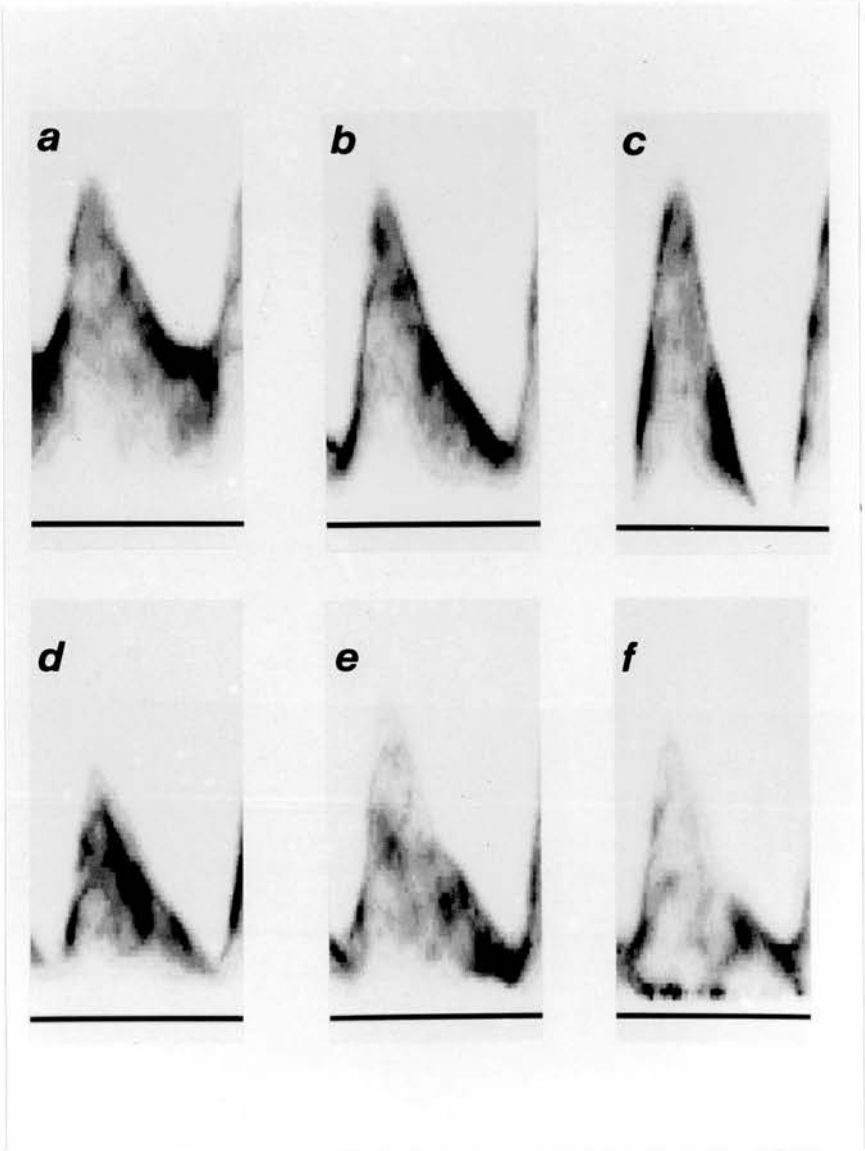

Figure 5.9: Examples of individual filtered waveforms. These are the filtered versions of the waveforms shown in figure 5.3. The filter was the directional filter with parameter 1 + R(d)/SL(d) in each case.

Table 5.3 presents the mean values of the quantitative indices for the six waveforms. These can be considered as a measure of the filter's average performance. The indices describing the distortion introduced by the filter to the maximum frequency envelope have small values, indicating a small yet systematic bias in threshold maximum frequency calculations. The performance in edge preservation described by RH_{LE} shows a 23% average loss of height for the leading edge. The bias introduced by the filter in the uniform central area and the upper region with background noise is very small (RH_{CA} = 1.03, RH_{UR} = 1.05). Filtering has resulted in noise reduction varying between a factor of 3.4 at the leading edge and 5.0 at the central area.

Location	Index	Value
Maximum Frequency Envelope	δMAXF	-50Hz
	δMINF	67Hz
	δMFE	59Hz
Leading Edge	RH_{LE}	0.77
	RCV_{LE}	3.40
Central Area	RH_{CA}	1.03
	RCV_{CA}	5.00
Upper Region	RH_{UR}	1.05
	RCV_{UR}	4.20

Table 5.3: Indices of bias and variance averaged over the six waveforms of figure 5.9.

5.6 Discussion.

In this chapter it has been demonstrated that Doppler speckle reduction can be performed to reveal the underlying Doppler spectrum. The filtered spectrum will have a degree of bias in those regions of the spectrum containing edges. However this is a natural consequence of performing noise reduction by averaging over a finite area.

5.7 Conclusion.

The filter giving the best performance, in terms of compromise between bias introduced and noise reduction offered, was the directional filter with the parameter 1 + R(d)/SL(d).

Chapter 6. The effect of noise reduction algorithms on the maximum frequency envelope and on the pulsatility index.

6.1 Introduction.

In chapter 5 it was suggested that reduction of the maximum frequency envelope noise would lead to improved estimation of the envelope and of RI and PI. Two methods based upon filtering were considered. These methods were filtering of the envelope itself using a DWMTM filter, and secondly filtering of the spectrum using the directional filter developed in chapter 5. It is the purpose of this chapter to determine whether these 2 methods improve the estimation of the maximum frequency envelope and PI.

6.2 Methods.

The waveforms acquired for chapter 4 will also be used in this chapter. These waveforms will be referred to as 'unprocessed waveforms'. The methodology leading to calculation of the bias and variability of the maximum frequency envelope and PI is described for the unprocessed Doppler waveforms in chapter 4. Much of this methodology is used unchanged in this chapter. Those aspects of methodology peculiar to this chapter are described below separately for each of the two noise reduction techniques.

6.2.1 Filtering of the maximum frequency envelope from unprocessed waveforms.

When there was a high background noise level the maximum frequency envelope from the unprocessed waveforms was in general noisy. A double window modified trimmed mean (DWMTM) filter (Lee and Kassam 1985) was applied to the maximum frequency envelope from the unprocessed waveforms in an attempt to reduce the noise. The action of the DWMTM filter in this case is to remove spikes by finding the median of a 5 element window, then to provide smoothing by calculating the mean within the same window of elements whose value lies within a band of $\pm$ 10 on either side of the median. For the calculation of the PI for the

unprocessed waveforms, the algorithm for finding MAX and MIN (the maximum systolic and end diastolic frequencies respectively) is relatively unintelligent in that, for example, it searches for the MIN value where it is known that the systolic peak of the waveform will be present. This may not be important where the waveform quality is high and the maximum frequency follower performs well, however if the maximum frequency envelope is noisy a more intelligent algorithm may perform better. For the envelopes calculated after DWMTM filtering a semi-intelligent algorithm was used which searched for MAX in an interval 50 to 150 ms after the waveform start, and which searched for MIN in an interval 70 to 0 ms before the waveform end.

6.2.2 Filtering of the Doppler spectra from unprocessed waveforms.

All Doppler waveforms were filtered using the optimal directional filter developed in chapter 5. The maximum frequency envelope was found using the adaptive threshold technique described in section 4.3.2.2. In this case the fluctuations of the background noise have been substantially reduced compared with the unprocessed spectra, so that a lower threshold value can be used for the same measured mean background level. The relationship between the mean background level and the threshold level used by the maximum frequency follower is shown in figure 6.1. The PI of the maximum frequency envelope from the filtered waveforms was calculated using the semi-intelligent algorithm of section 6.2.1. For the calculation of the bias in the estimated envelope and PI from the directionally filtered waveforms, it was necessary to compare the ensemble averaged envelope with a gold standard envelope. For the filtered waveforms the gold standard envelope was derived from the appropriate ensemble averaged waveform obtained from the individual filtered waveforms. This should be contrasted with the use of the ensemble averaged waveform obtained from the individual unprocessed waveforms in section 6.2.1 and in chapter 4. The reasons for this are explained in section 6.4.

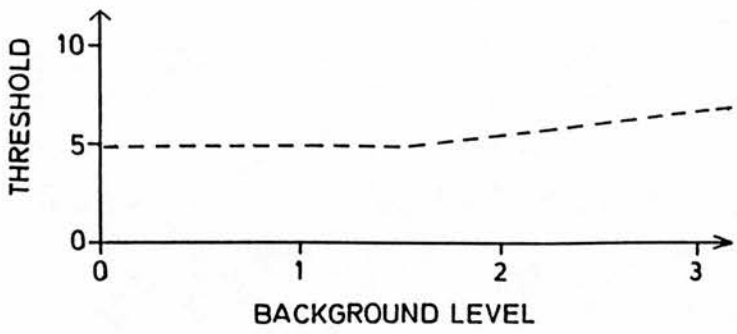

Figure 6.1. Relationship between the threshold level used by the maximum frequency follower and the measured background level for waveforms which have been directionally filtered.

6.3 Results.

Tables 6.1, 6.2 and 6.3 show the bias and variability of the maximum frequency envelope and PI for selected values of each physical parameter. In each case averaging over the 3 waveforms pulsatilities has been performed. Figures 6.2 and 6.3 illustrate these results for variation of beam-vessel axis offset for waveforms of correct PI = 1.4. The relationship between MFE_{er}, PI_{er} and each physical parameter is broadly comparable to that for the unfiltered waveforms in that MFE_{er} and PI_{er} are similar over a wide range of physical parameters, but at higher values of each physical parameter there is increasingly inaccurate estimation of the maximum frequency envelope and PI. MFE_{er} and PI_{er} are lower in all cases for the processed waveforms compared to the unprocessed waveforms, particularly for higher values of each physical parameter. At the highest values for each physical parameter filtering of the spectra gives the highest accuracy of estimation of the maximum frequency envelope and PI.

		Indices of MFE			Indices of PI		
	Angle (degrees)	BS(%)	SD(%)	MFE_{er}	δPI	PI_{sd}	PI_{er}
DWMTM filtered MFE	45	1.0	4.6	4.7	0.027	0.015	0.039
	65	2.6	7.0	7.5	0.036	0.035	0.068
	85	47.6	48.1	68.7	0.248	0.126	0.358
MFE from filtered waveforms	45	0.6	5.8	5.8	0.009	0.018	0.025
	65	2.9	7.2	7.9	0.020	0.039	0.055
	85	38.4	38.1	54.8	0.433	0.086	0.509

Table 6.1. Indices showing the accuracy of estimation of the maximum frequency envelope (MFE) and PI for variation of the beam-vessel angle. Each value is the average of 3 waveform pulsatilities.

		Indices of MFE			Indices of PI		
	Offset (mm)	BS(%)	SD(%)	MFE_{er}	δPI	PI_{sd}	PI_{er}
DWMTM filtered MFE	0	1.2	4.8	4.9	0.015	0.018	0.031
	7.5	9.9	6.5	11.9	0.014	0.032	0.041
	15.0	17.6	24.1	29.9	0.145	0.165	0.288
MFE from filtered waveforms	0	1.1	6.0	6.1	0.016	0.021	0.034
	7.5	10.7	5.4	12.1	0.024	0.027	0.047
	15.0	10.4	21.8	24.4	0.099	0.115	0.200

Table 6.2. Indices showing the accuracy of estimation of the maximum frequency envelope (MFE) and PI for variation of the beam-vessel axial offset. Each value is the average of 3 waveform pulsatilities.

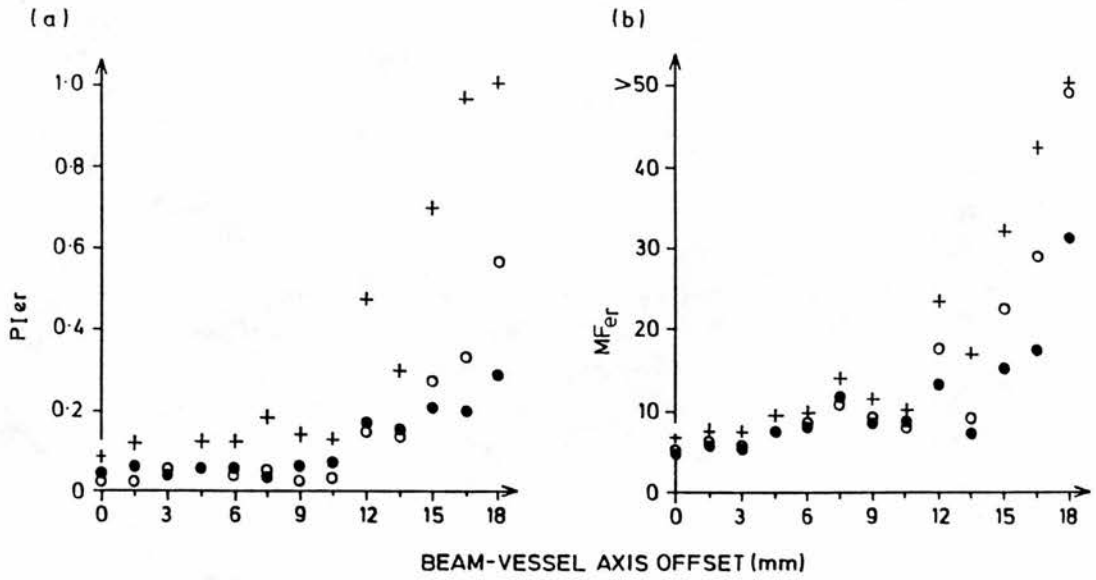

Figure 6.2. The effect of the 2 noise reduction algorithms on a) PI_{er}, and b) MFE_{er}. + maximum frequency envelope from unprocessed waveforms, o DWMTM filtered envelope, • envelope from filtered waveforms.

		Indices of MFE			Indices of PI		
	Attenuator Thickness (cm)	BS(%)	SD(%)	MFE_{er}	δPI	PI_{sd}	PI_{er}
DWMTM filtered MFE	2.0	1.2	4.5	4.7	0.010	0.018	0.026
	3.5	2.6	5.8	6.3	0.011	0.024	0.032
	5.0	8.4	27.7	29.1	0.044	0.119	0.148
MFE from filtered waveforms	2.0	0.8	5.7	5.8	0.020	0.024	0.072
	3.5	2.0	6.8	7.1	0.033	0.021	0.050
	5.0	5.1	19.4	20.1	0.093	0.092	0.174

Table 6.3. Indices showing the accuracy of estimation of the maximum frequency envelope (MFE) and PI for variation of the attenuator thickness. Each value is the average of 3 waveform pulsatilities.

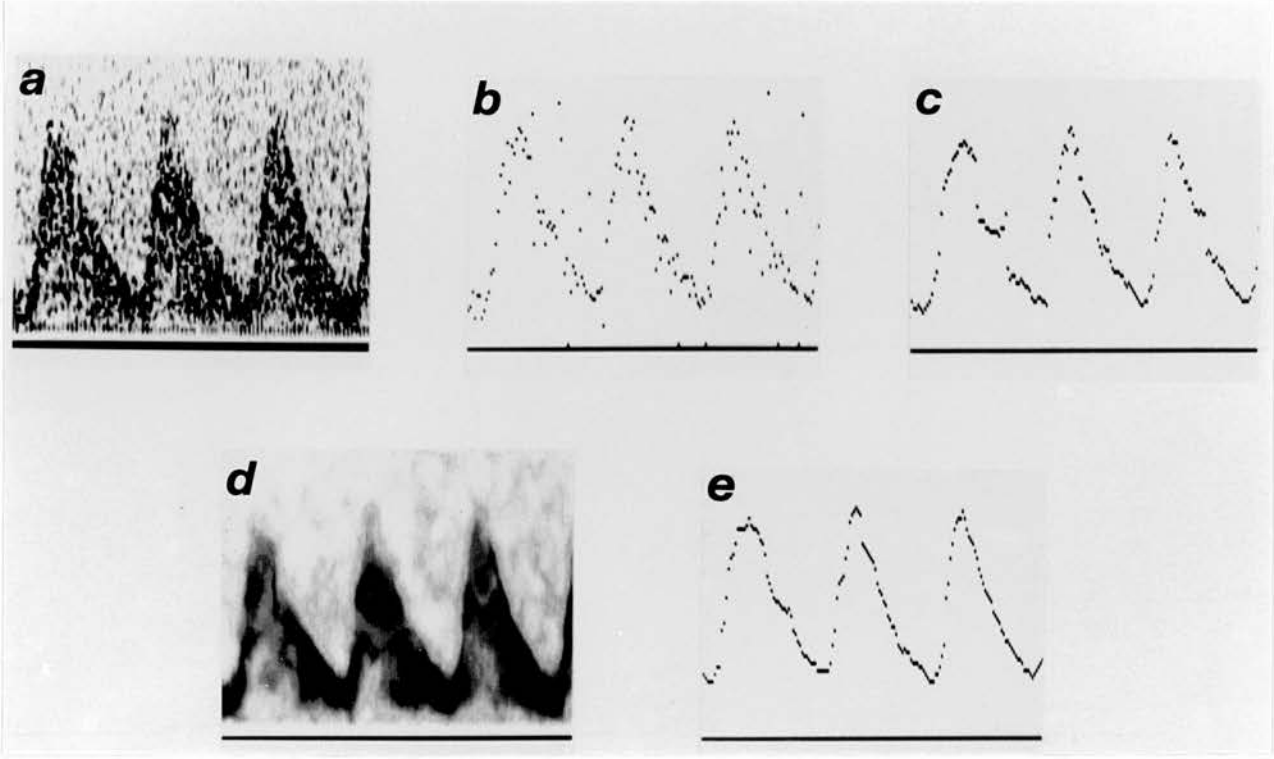

Figure 6.3. Examples of waveforms and maximum frequency envelopes (MFEs) after further processing (for waveforms of correct PI=1.4 when the beam-vessel axial offset was 16.5mm). a) Unprocessed waveforms, b) MFE from unprocessed waveforms, c) MFE from unprocessed waveforms after DWMTM filtering, d) filtered waveforms, e) MFE from filtered waveforms.

6.4 Discussion.

In the unprocessed Doppler waveforms the presence of Doppler speckle always produces a degree of noise of the maximum frequency envelope. The small underestimation of the minimum value, MIN, which this will produce explains the consistent overestimation of the PI values, by 3-4%, for the unprocessed

waveforms. Application of the DWMTM filter, by smoothing the noise of the maximum frequency envelope, leads to better estimation of MIN and MAX, and hence gives a relatively unbiased estimate of PI (figure 6.2 and tables 6.1 to 6.3). Background noise acts to produce noise spikes on the maximum frequency envelope. The DWMTM filter substantially reduces this noise leading to improved estimation of the maximum frequency envelope and PI. This effect is shown in figure 6.2 where background noise is present for waveforms with offset values greater than 10.5 mm.

Maximum frequency envelopes with a generally smooth shape are produced from filtered Doppler waveforms. This is due to speckle reduction which gives smooth outlines to the Doppler waveform, and to background noise smoothing which, by obviating the effect of high amplitude noise pixels on the maximum frequency follower, reduces the number of positive going noise spikes. A natural consequence of the filtering process used is to produce smoothing of the waveform at peak systole and end diastole leading to consistent overestimation of the end diastolic maximum frequency, MIN, and consistent underestimation of the peak systolic maximum frequency, MAX. This leads to PI values which are consistently low by about 0.1 (3-4%) for the waveforms of this study. This is a consistent effect so has been treated as part of the spectral estimation process in this study. Using this approach the gold standard maximum frequency envelope for filtered waveforms was obtained from the appropriate ensemble-averaged filtered waveform rather than the ensemble-averaged unfiltered waveforms.

The accuracy of estimation of the maximum frequency envelope and PI is similar for both methods of further processing of waveforms with no background noise, whereas when background noise is present filtering of the waveforms is superior. This is shown in figure 6.2 where background noise is present for offsets greater than 10.5 mm. Figure 6.3 shows waveforms and maximum frequency envelopes obtained when the offset was 16.5 mm.

6.5 Conclusion.

Further processing of the waveforms improves the estimation of the maximum frequency envelope and of PI. On balance DWMTM filtering of the maximum frequency envelope from unprocessed Doppler waveforms is likely to be preferred to filtering of the Doppler spectra as the DWMTM approach is computationally less demanding and gives only a small bias for the calculation of PI.

Chapter 7. A comparison of three Doppler waveform quality indices.

7.1 Introduction.

In section 1.4 the sources of variability of RI and PI were considered, and it was pointed out that Doppler systems which provided automatic calculation of the RI and PI could be prone to abuse as the possibility arose of management of the patient by clinical staff based upon incorrect data. Further it was argued that it would seem desirable for a Doppler machine to indicate to the operator when the waveform quality is acceptable, with the implication that the indices of RI and PI are reliable. This chapter is concerned with the development and testing of 3 waveform quality indices.

A number of levels of approach can be taken in tackling this problem. At one extreme there would be complete reliance on the operator to obtain the waveforms and calculate the indices. At the other extreme would be the performance of the test by a robot which would also judge the waveform quality, calculate the indices and display these. This latter approach would require substantial development work, something which is beyond the scope of this thesis. Two intermediate levels of approach can be considered which involve software analysis of the waveforms. In this respect it is important that the software be sufficiently simple that it can perform real time analysis of the waveforms.

Approach 1. Acquisition of the waveforms by the operator, with the machine performing the following:

- identifies that the waveforms are from the umbilical artery,
- identifies that the waveforms are of appropriate quality,
- calculates and displays the RI and PI values.

Approach 2. Acquisition of waveforms by the operator <u>including</u> identification that the waveforms are from the umbilical artery, with the machine performing the

following,

- identifies that the waveforms are of appropriate quality,
- calculates and displays the RI and PI values.

There is only a small difference between these 2 intermediate approaches, the difference being the identification of the waveforms as being from the umbilical artery by the machine in the first approach, and by the human operator in the second approach. However this difference could have a very large difference in the sophistication of the software used to assess quality. In other areas of medical imaging automatic interpretation of images is being attempted. In general medical images are complex, being 2 or 3 dimensional arrays containing information from many different tissues types, so that work on image analysis is performed by teams of reseach people over many years. For Doppler waveforms the shape of the waveform envelope, as well as other features such as the heartrate and the presence of venous signals in the opposite Doppler channel give clues as to the artery from which the signal arose. In this case it may be possible to automatically identify umbilical artery waveforms, in real time, from the shape of the envelope using pattern recognition techniques such as template matching. This represents an additional level of complexity which has not been pursued in this study. The approach adopted is the second one above, that is; it is the job of the operator to identify the umbilical artery waveform, and it is the job of the quality index to tell the operator whether these umbilical waveforms are acceptable or not.

7.2 Method.

The set of waveforms used in chapter 4 were used to investigate the relationship between quality indices and the 3 physical parameters. In addition waveforms were acquired to investigate the dependence of each quality index on physiological variables (see section 7.2.2). Chapter 4 gives a full description of the methodology leading to the calculation of the indices of bias and variability of the

maximum frequency envelope as a whole, and of the PI.

7.2.1 Waveform quality indices.

In chapter 4 it was observed that the variability and the degree of noise of the maximum frequency envelope increased as the value of each physical parameter increased. It would then be expected that an assessment of the degree of noise of the envelope from individual waveforms or pairs of waveforms would be related to the waveform quality. Each of the quality indices described below is based on an assessment of the degree of noise of the envelope. In this context envelope noise is associated specifically with the fluctuations which may occur in poor quality waveforms between adjacent points of the maximum frequency envelope. This should not be confused with noise associated with the spectrum, such as Doppler speckle or background electronic noise.

7.2.1.1 Correlation of the maximum frequency envelope of successive waveforms (QI1).

$$QI1 = \frac{50}{N} \quad \frac{2}{FMAX_1 + FMAX_2} \quad \sum_{i=1}^{N} \left| F_{1,i} - F_{2,i} \right| \qquad \text{eqn. 7.1}$$

where

$F_{1,i}$ and $F_{2,i}$ are the value of the maximum frequency envelope at position i for waveform 1 and waveform 2 respectively,

$FMAX_1$ AND $FMAX_2$ are the maximum values of the envelope for waveforms 1 and 2 respectively,

N is the number of points of the envelope.*

If adjacent waveforms produce identical maximum frequency envelopes then, for all i, $F_{1,i} - F_{2,i}$ will be zero, and QI1 will be zero. Noise of the envelope will lead to dissimilarity between adjacent envelopes and hence give a non-zero value of QI1, so that QI1 is a measure of the correlation between successive waveforms. Normalisation of the quality index for the overall height of the waveform was performed by dividing by the average maximum frequency of the two adjacent

waveforms. For each waveform the peak frequency was found by searching in an interval 50-150 ms after the waveform start. To reduce the problem of spurious high values for the peak frequency, which may be present when there is substantial background noise, the maximum frequency was taken as the average value of 5 elements surrounding and including the peak value. Normalisation of the quality index by the mean frequency was considered however the mean frequency would be dependent on waveform pulsatility in that its value would fall as the waveform becomes more pulsatile. The maximum frequency is not dependent on pulsatility and hence is preferred for normalisation. Initial investigations on the dependency of a quality index based upon this method showed an approximately linear dependence on waveform length; hence in the above formulation normalisation by waveform length has been performed.

7.2.1.2 Measure of local linearity (QI2).

$$QI2 = \frac{50}{N} \quad \frac{1}{FMAX} \quad \sum_{i=2}^{N-1} S_i \qquad \text{eqn. 7.2}$$

where $$S_i = \left| \frac{1}{2}(F_{i-1} + F_{i+1}) - F_i \right| \qquad \text{eqn. 7.3}$$

If the waveform outline is smooth the value F_i will change slowly with respect to i, and the term S_i and hence the sum $\sum S_i$ will be small. If there is noise which causes larger changes in F_i as a function of i, S_i and hence $\sum S_i$ will have larger values. S_i can be considered as a measure of the local linearity of elements in the region of i as S_i takes on larger values when there is an increasing degree of non-linearity. Normalisation by the maximum frequency FMAX and waveform length was performed in the same way as for QI1.

7.2.1.3 Frequency content by the Fourier transform of the maximum frequency envelope (QI3).

The frequency content of the maximum frequency envelope was calculated for

each waveform by performing a 111 point discrete Fourier Transform. For waveforms whose length was less than 111 points or 1.11 seconds, zero padding was performed to increase their length to 111 points. A Hanning window was used to avoid spectral leakage. Noise of the envelope would be expected to introduce higher frequency components (figure 7.1). A fixed threshold frequency was

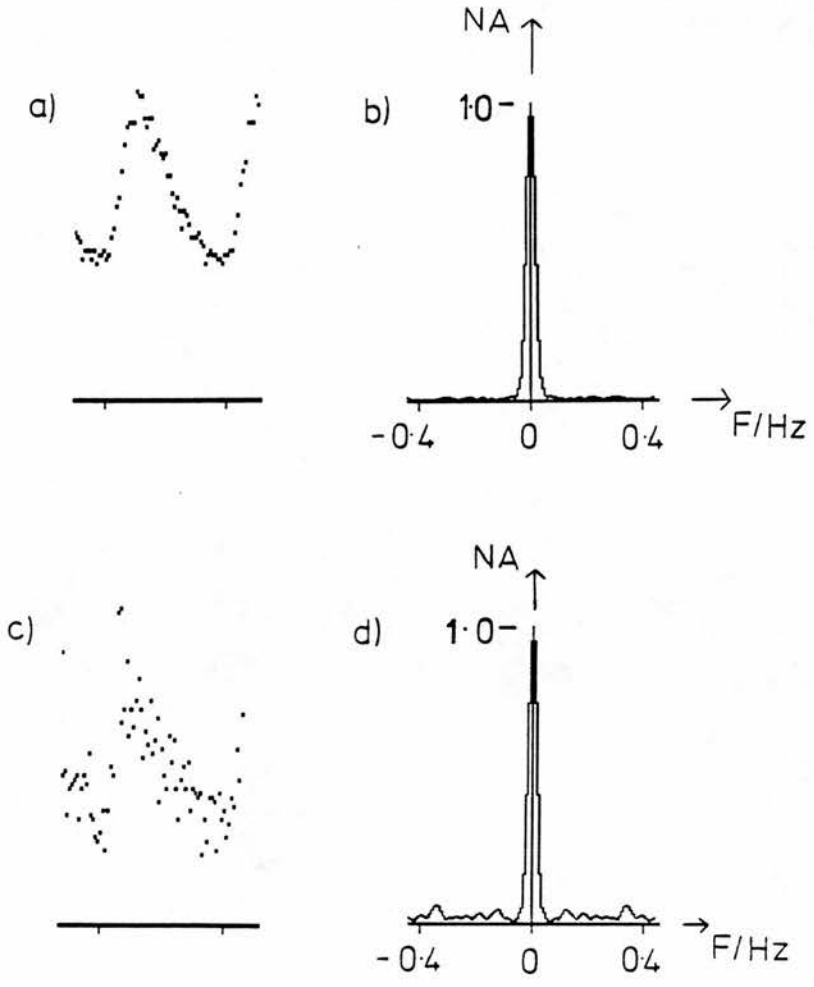

Figure 7.1. Maximum frequency envelope and associated Fourier transform frequency amplitude plots are shown for a) an envelope with a smooth outline, b) envelope with a noisy outline.

defined above which there was little signal present when the waveform outline was smooth. From preliminary experiments in which waveforms with a clearly defined outline were used, the threshold frequency was defined as being the tenth spectral component of the Fourier transform frequencies. The sum of the amplitudes of frequencies above this threshold was calculated and expressed as a percentage of the total sum of amplitudes. Normalisation of waveform length was performed as for QI1. Characterisation of time varying signals in this way has been described in other fields such as seismic acoustic waveform analysis (Chen 1986).

7.2.2 Dependence of the quality indices on physiological variables.

Ideally each quality index should be sensitive only to noise of the maximum frequency envelope however it is important to assess the dependence of each quality index on physiological variables. This was performed using good quality simulated umbilical artery waveforms from the flow phantom as described below. In each case the beam and vessel axes were aligned, the beam-vessel angle was 50^{o}, the transducer vessel distance was 5 cm, and 2 cm of attenuator were used.

7.2.2.1 Pulsatility.

Waveforms of different pulsatility at a length of 500 ms were acquired. The PI values varied between 0.8 and 2.7.

7.2.2.2 Waveform length.

Waveforms of length between 300 and 700 ms were acquired at a PI value of 1.0 ± 0.1. This range of waveform lengths represents the range occurring in the umbilical artery in practice.

7.2.2.3 Fetal breathing.

The effect of fetal breathing is to cause variability of the waveform shape of consecutive waveforms; the degree of variability depending upon the strength of breathing actions. The flow phantom is mostly used to produce identical velocity waveforms by means of a single repeated control waveform. If instead of a single control waveform, a set of 3 consecutive dissimilar control waveforms are used,

then the resulting velocity waveforms will vary in a similar manner to real umbilical artery velocity waveforms when there is fetal breathing. Waveforms of 500 ms length and an average PI value of 0.75 were acquired simulating different degrees of fetal breathing; specifically, no-breathing, light-breathing and strong-breathing.

7.2.3 Comparison of quality indices with estimates of the accuracy of the maximum frequency envelope and PI.

In chapter 4 it was shown how the percentage root mean square error of the maximum frequency envelope MFE_{er} and the PI error (PI_{er}) were single parameters indicating the accuracy with which the envelope and PI respectively are estimated for particular values of each physical parameter. In order to compare MFE_{er} and PI_{er} with each quality index, a test group was formed consisting of all of the waveforms acquired with variation of each physical parameter. This test group will not be identical to a test group of umbilical artery waveforms in clinical practice, however the group covers waveforms acquired with the range of physical parameters, and also the range of pulsatilities, which would be encountered in practice.

In order to perform the analysis it is necessary to specify the number of waveforms averaged for calculation of each quality index, and for the specification of PI_{er}. 5 waveforms were taken as this represents the number used in our hospital for the calculation of RI and PI for umbilical artery waveforms in clinical practice. Hence for each cohort of 16 waveforms, 3 separate groups of 5 waveforms were taken allowing the calculation of 3 values for each quality index for that cohort.

7.2.3.1 Correlation of each quality index with MFE_{er} and PI_{er}.

A least square regression line was calculated between each quality index and MFE_{er}, and each quality index and PI_{er}. The correlation coefficient was calculated as a measure of the degree of linearity.

7.2.3.2 Performance of each quality index when maximum acceptable values of MFE_{er} and PI_{er} are specified.

In clinical practice the quality index would be used in a decision making process whereby quality index values above a threshold would be assessed as being low quality and therefore unacceptable. For the waveforms of this study the division of waveforms into low and high quality can be performed by choosing threshold values for PI_{er} and MFE_{er}. A threshold value for each quality index can then be calculated to give for example 90% sensitivity for detection of low quality waveforms based upon a greater than threshold quality index value. Calculation of the specificity for detection of high quality waveforms can then be performed and used to compare the quality indices.

7.2.4 Assessment of computational efficiency of each quality index.

The calculation time was calculated for a single waveform for QI2 and QI3, and a waveform pair for QI1.

7.3 Results.

7.3.1 Dependence of quality indices on physiological variables.

The results are given table 7.1. In each case the degree of dependence of a quality index on the physiological variable has been quantitated by calculating the

	QI1	QI2	QI3
Waveform pulsatility ($QI_{PI=2.6}/QI_{PI=0.8}$)	95	72	105
Waveform length (QI_{700ms}/QI_{300ms})	115	85	69
Fetal breathing (QI_{strong}/QI_{none})	600	106	102

Table 7.1: Dependence of each quality index on physiological variables. The ratio (%) of the quality index values from the maximum and minimum physiological condition is shown.

ratio of the quality index value from the maximum and minimum physiological conditions. In clinical practice a degree of dependency of a quality index on a physiological variable may be tolerated so it is difficult at this stage to specify threshold ratio values indicating an acceptable degree of dependence of a value on a physiological parameter. In 6 out of 9 cases the ratio value deviates by 15% or less from the perfect value of 100%. The highest ratio value of 600% is given by QI1 for fetal breathing. A high ratio value is to be expected since QI1 is a measure of the difference in waveform shape of consecutive waveforms and takes no account of the origin of that difference, be it due to gross changes caused by fetal breathing or to noise of the maximum frequency envelope. QI2 gives a ratio value of 72% for waveform pulsatility. Examination of the data reveals that QI2 is constant to within 5% for PI values between 0.8 and 2.1, but for a PI of 2.6 QI2 drops by 27% giving the ratio value of 72% (see figure 7.2). This suggests that the dependence of QI2 on pulsatility in clinical practice may be less significant than the ratio value indicates.

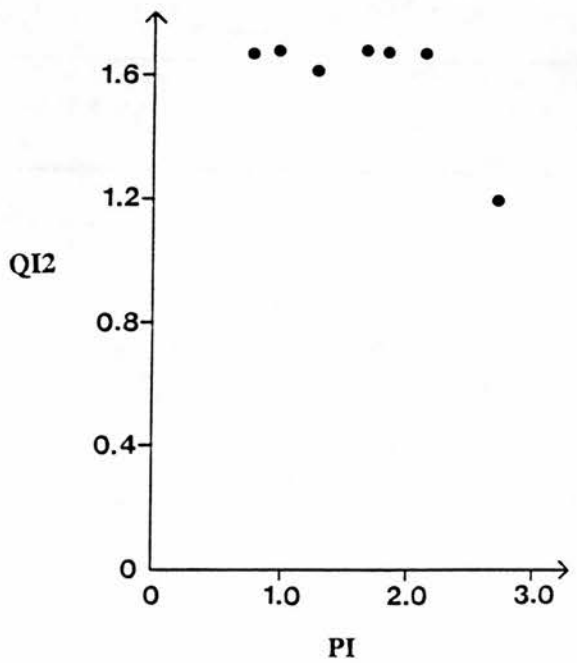

Figure 7.2. Dependence of QI2 on waveform pulsatility.

7.3.2 Dependence of quality indices on physical parameters.

Figure 7.3 shows the dependence of QI2 on each of the physical parameters considered for waveforms of correct PI = 0.8. In each case QI2 increases as the physical parameter increases. Similar results were obtained for QI1 and QI3, and for waveforms of correct PI = 1.4 and 2.3. Tables 7.2, 7.3 and 7.4 show the quality index values averaged over the waveform pulsatilities for selected values of the 3 physical parameters.

Angle (degrees)	QI1	QI2	QI3
45	1.13	1.53	0.059
65	2.06	3.12	0.114
85	6.06	7.39	0.238

Table 7.2: Results for variation of beam-vessel angle. Each value is the average of measurements from 3 waveform pulsatilities.

Offset (mm)	QI1	QI2	QI3
0	1.17	1.66	0.069
7.5	1.96	3.05	0.116
15	8.69	13.1	0.347

Table 7.3: Results for variation of beam-axis offset. Each value is the average of measurements from 3 waveform pulsatilities.

Attenuator thickness(cm)	QI1	QI2	QI3
2.0	1.12	1.48	0.064
3.5	1.39	1.99	0.085
5.0	8.06	12.32	0.349

Table 7.4: Results for variation of attenuator thickness. Each value is the average of measurements from 3 waveform pulsatilities.

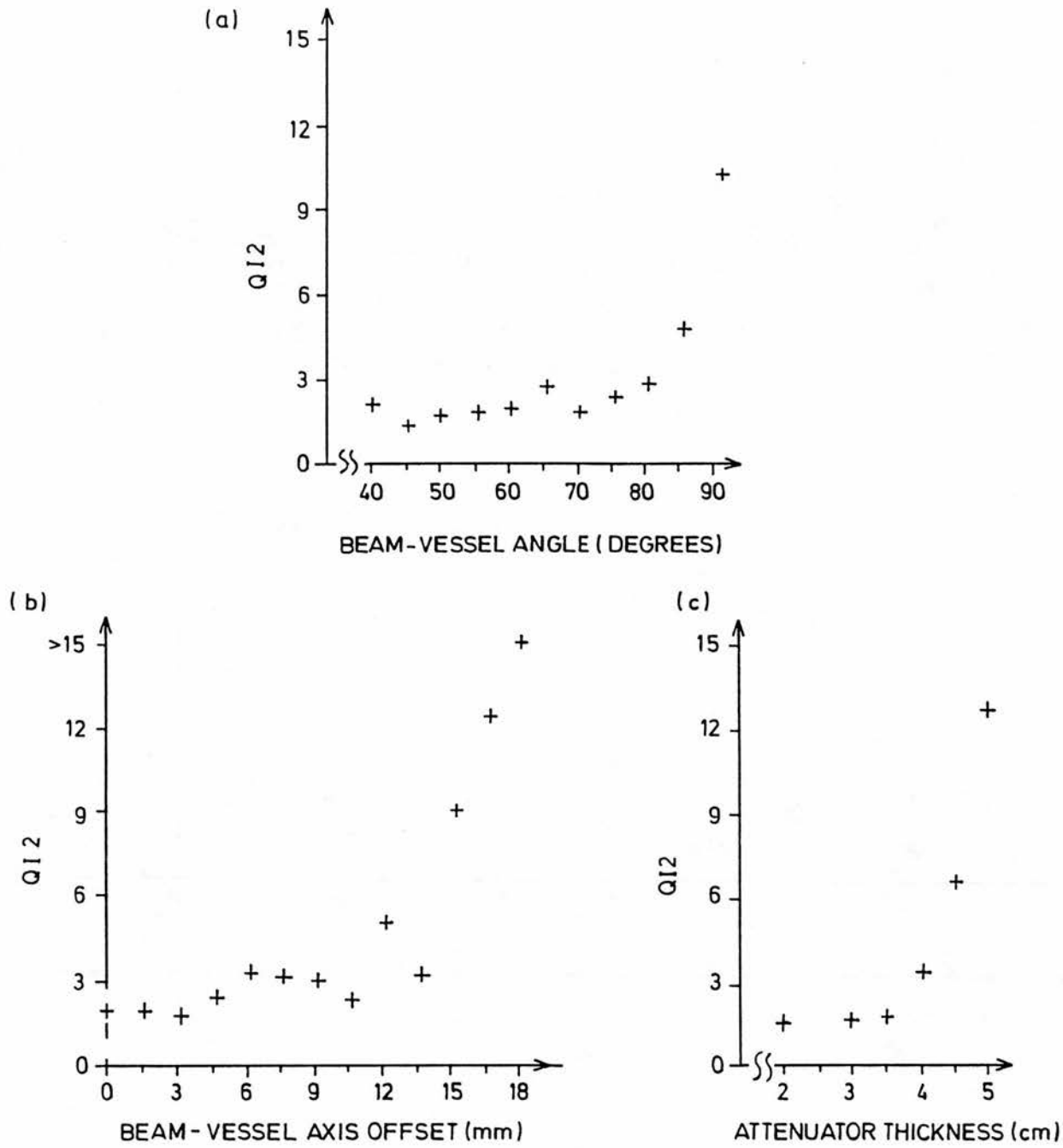

Figure 7.3 Dependence of QI2 for waveforms of correct PI = 0.8 on each of the 3 physical parameters. a) Beam-vessel angle, b) Beam-vessel axis offset, c) attenuator thickness.

7.3.3 Relationship between quality indices and MFE_{er}.

Table 7.5 shows the correlation coefficients for linear regression between each quality index and MFE_{er}. Figure 7.4 shows a plot of QI2 versus MFE_{er}. The correlation coefficients are high at 0.90 or greater in all cases. This seems to indicate that all of these quality indices can be used as indices of waveform quality since there is a good linear relationship between quality indices and the overall accuracy of estimation of the maximum frequency envelope as characterised by

QI1	QI2	QI3
0.94	0.90	0.96

Table 7.5: Correlation coefficients for linear regression between each quality index and MFE_{er}.

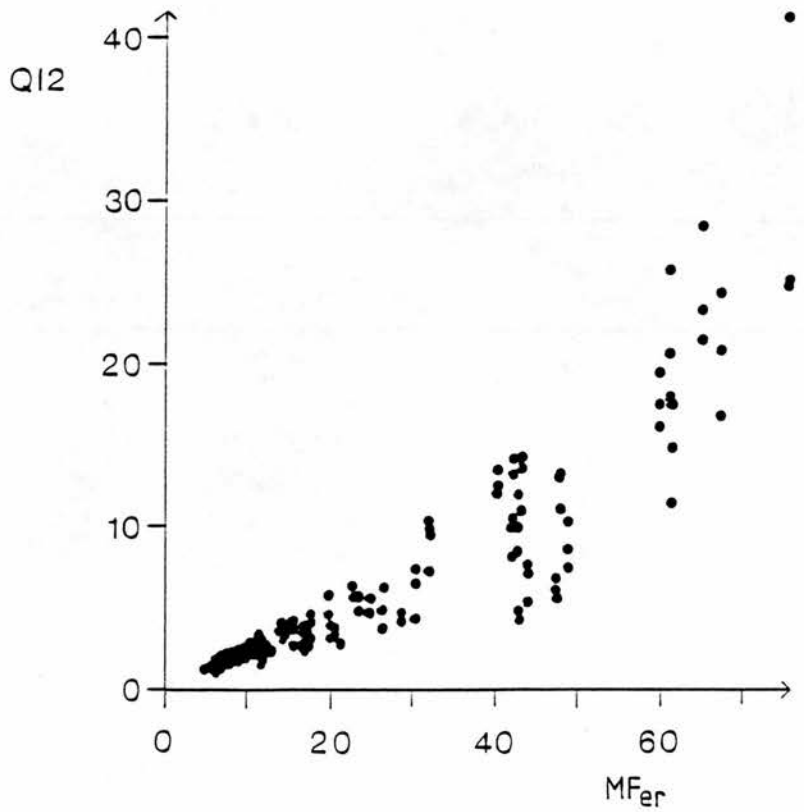

Figure 7.4. Plot of QI2 versus MFE_{er}.

MFE_{er}. The correlation coefficient is a measure of the overall linearity between 2 quantities, and although it is encouraging that the correlation coefficients are high it is of more relevance to consider the performance at low values for each quality index, for it is in this region that a decision must be made as to accept or reject the waveforms acquired.

Table 7.6 shows the specificity for detection of good quality waveforms when the sensitivity for detection of poor quality waveforms is set to 90%. In this case good quality was defined as MFE_{er} less than 10%. In each case the specificities are high at 94 to 98%. Specificities were also calculated for each waveform pulsatility separately. The specificities were calculated for the same threshold of quality index as for the data as whole. There is a small dependence of the specificity on PI for each quality index however in all cases the specificities are high at 89% or greater.

	All data (n=261)			Data by PI (n=87)		
				Specificity (%)		
	QI threshold	% with MFE_{er} <10	Specificity(%)	PI=0.8	PI=1.4	PI=2.3
QI1	1.68	38	96	93	97	97
QI2	2.46	38	94	89	94	97
QI3	0.10	38	98	96	97	100

Table 7.6: Specificities at 90% sensitivity for detection of poor waveforms based upon a threshold value of MFE_{er} of 10%. The test population is considered as a whole (n = 261), and also by PI (n = 87 in each case). Note that the data for a beam-vessel angle of 90^{o} has been excluded as MFE_{er} is infinite.

7.3.4 Relationship between quality indices and PI_{er}.

Table 7.7 shows the correlation coefficients for linear regression between each quality index and PI_{er}. Figure 7.5 shows a plot of QI2 versus PI_{er}. The correlation coefficients are high at 0.89 - 0.91.

QI1	QI2	QI3
0.91	0.89	0.89

Table 7.7: Correlation coefficients for linear regression between each quality index and PI_{er}.

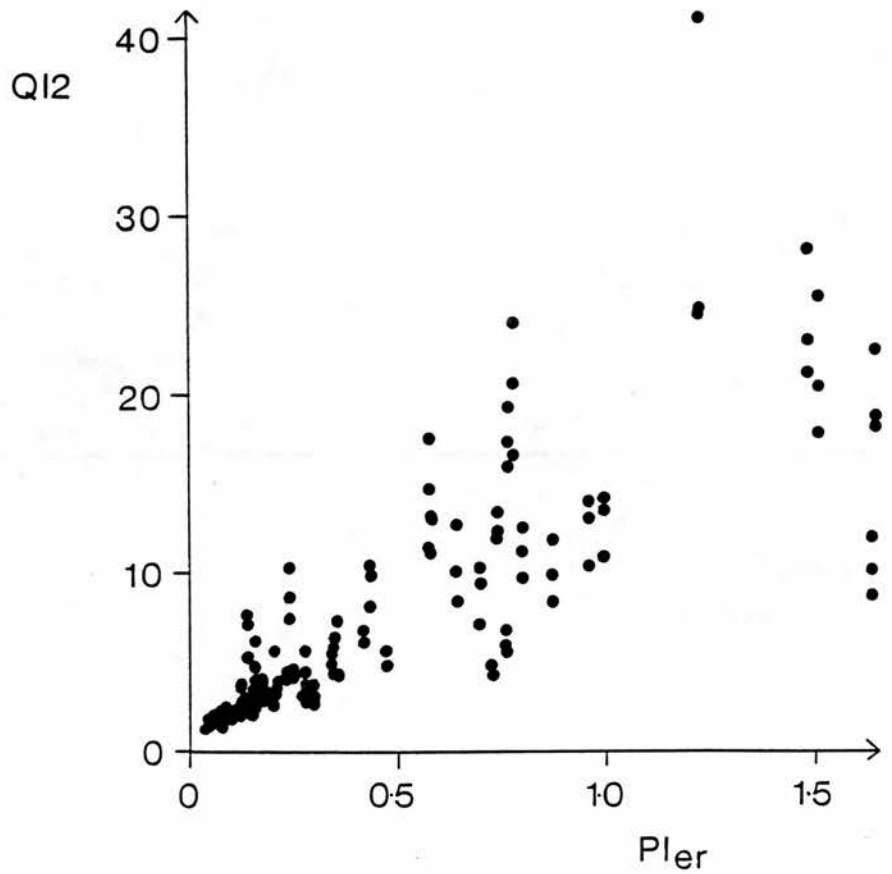

Figure 7.5 Plot of QI2 versus PI_{er}.

Table 7.8 shows the specificities for detection of good quality waveforms when the sensitivity for detection of poor quality waveforms is set to 90%. Good quality was defined as PI_{er} less than 0.15. The specificities for the data considered as a whole are high at 90-93% (Figure 7.6). There is no obvious dependence of the specificities on PI, and in all cases the specificity is high at 86% or greater.

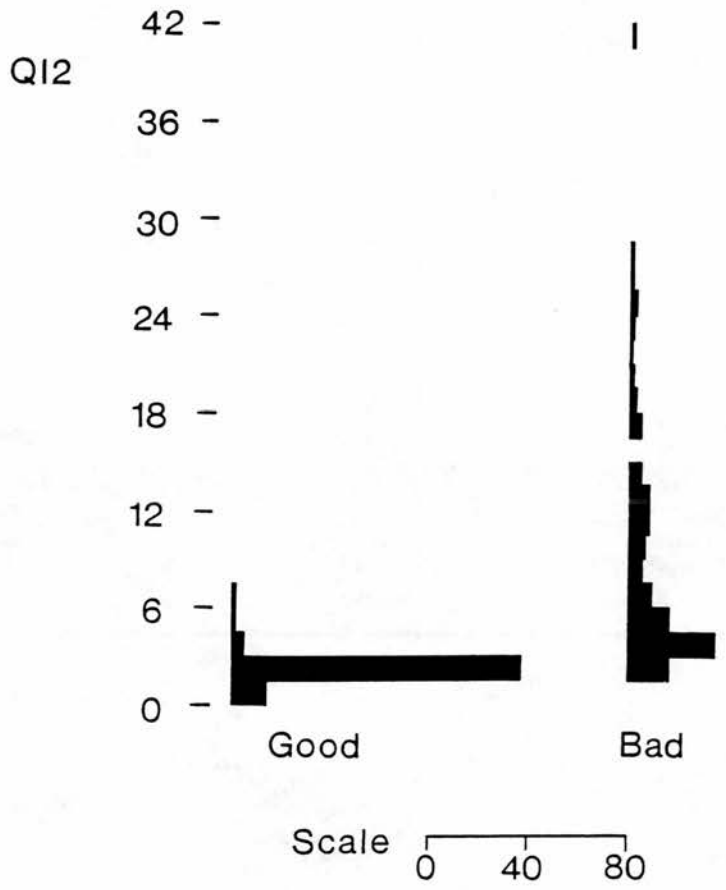

Figure 7.6 QI2 values for good and bad waveforms based upon a threshold of 0.15 for PI_{er}.

		All data (n=270)		Data by PI (n=90)		
	QI threshold	% with PI_{er} <0.15	Specificity(%)	Specificity (%) PI=0.8	PI=1.4	PI=2.3
QI1	1.99	51	93	97	91	94
QI2	2.92	51	91	94	88	94
QI3	0.114	51	90	94	86	92

Table 7.8: Specificities at 90% sensitivity for detection of poor waveform based upon a threshold value of 0.15 for PI_{er}. The test population is considered as a whole (n = 270), and also by PI (n = 90 in each case).

7.3.5 Computational efficiency of each quality index.

Table 7.9 shows the relative time taken for calculation of each QI, where the time has been normalised to 1 for QI2. QI1 and QI2 are comparable in their computational efficiency but QI3 takes 280 times longer than QI2 to calculate. This is due to the length of time necessary to calculate the Fourier transform for QI3.

QI1	QI2	QI3
0.60	1.00	280

Table 7.9: Computational time for each quality index normalised to 1 for QI2.

7.4 Discussion.

The errors in the PI considered in this study arise from the physical variables and the way in which the envelope and PI have been calculated. The error PI_{er} was formulated in order to give a single index to compare with the quality indices. This error is composed of the bias plus 1.96 times the standard deviation. High and low

quality waveforms were defined according to a threshold error of 0.15 for PI_{er}. For PI values in clinical practice of 0.8 to 3.0 this corresponds to a percentage error of 18 to 5%. The question arises as to whether this would be an acceptable error for clinical usage. The only comparable clinical data derives from inter and intra observer reproducibility studies (see section 1.4.3). These studies include the effects of physiological variables as well as physical parameters and envelope calculation. They also consider only the reproducibility and take no account of bias. The nearest comparable error from these studies is 1.96 times the coefficient of variation, which gives 16 to 27%. Though not strictly comparable it can be seen that the pecentage threshold errors in PI for acceptable waveforms of 5 to 18% in this study are comparable with the clinical errors of 16 to 27%, indicating that a threshold value of 0.15 for PI_{er} is a realistic value.

This study has demonstrated the feasibility of using an assessment of the noise of the maximum frequency envelope of umbilical artery Doppler waveforms to classify the waveforms in terms of high and low quality based upon the accuracy of estimation of the envelope and PI. In general strong dependence of a quality index on a physiological variable will count against the use of such a quality index in clinical practice. In some cases, such as the linear dependence of a quality index on waveform length, it may in practice be possible to correct the quality index. All 3 quality indices were similar in their ability to discriminate high and low quality waveforms from a test population where physical variables had been altered to produce waveforms of different quality.

7.5 Conclusion.

The quality index with the best performance in terms of its independence from physiological variables, its ability to discriminate high and low quality waveforms, and its computational efficiency is QI2, the local linearity measure. QI1, the correlation between successive envelopes, may be of interest for waveforms obtained during fetal apnoea.

Chapter 8. The use of quality indices for waveforms on which noise reduction algorithms have been applied.

8.1. Introduction.

In chapter 7 it was shown that Doppler waveform quality indices could be formulated based upon quantitation of the noise of the maximum frequency envelope (MFE) of individual waveforms or pairs of waveforms, and these quality indices gave very good separation of high and low quality waveforms categorised according to the errors in envelope and PI calculation. In this chapter these quality indices will be tested on waveforms on which noise reduction algorithms have been applied. The two noise reduction methods are filtering of the maximum frequency envelope itself using a double window modified trimmed mean (DWMTM) filter, and secondly filtering of the spectrum using the directional filter developed in chapter 5.

8.2. Methods.

The sets of waveforms used in chapter 6 were also used in this chapter. The methodology leading to calculation of the bias and variability of the maximum frequency envelope and PI, and of the calculation and testing of the waveform quality indices, is described for the Doppler waveforms in chapters 4, 6 and 7.

8.3. Results.

8.3.1. Dependence of quality indices on physiological variables.

The results are given in table 8.1. In each case the dependence of a quality index on the physiological variable has been quantitated by calculating the ratio of the quality index value from the maximum and minimum physiological conditions. There is a greater degree of dependence of the quality indices on physiological variables for the processed waveforms compared to the unprocessed waveforms. The ratio value deviates by 15% or less from 100% in only 2 out of 9 cases for the DWMTM filtered envelopes, and 3 out of 9 cases for the directionally filtered spectra. The dependence of each quality index on waveform pulsatility is

particularly high; this is discussed further in section 8.4.

	QI1	QI2	QI3
a) DWMTM filtered MFE.			
Waveform pulsatility ($QI_{PI=2.6}/QI_{PI=0.8}$)	148	152	254
Waveform length (QI_{700ms}/QI_{300ms})	76	72	125
Fetal breathing (QI_{strong}/QI_{none})	800	92	114
b) MFE from filtered waveforms.			
Waveform pulsatility ($QI_{PI=2.6}/QI_{PI=0.8}$)	230	207	405
Waveform length (QI_{700ms}/QI_{300ms})	77	68	104
Fetal breathing (QI_{strong}/QI_{none})	1000	97	105

Table 8.1: Dependence of each quality index on physiological variables. The ratio (%) of the quality index values from the maximum and minimum physiological conditions is shown.

8.3.2 Dependence of quality indices on physical variables.

The results are given in tables 8.2, 8.3 and 8.4 for selected values of the 3 physical parameters. In each case the average of 3 pulsatilities has been taken. The dependence of the 3 quality indices on each physiological parameter is broadly comparable for the unprocessed and processed waveforms, with each quality index increasing in value as the physical parameters increase in value.

	Angle (degrees)	QI1	QI2	QI3
DWMTM filtered MFE	45	0.87	0.74	0.026
	65	1.20	0.96	0.039
	85	3.98	1.97	0.095
MFE from filtered waveforms	45	0.89	0.83	0.030
	65	1.09	0.98	0.036
	85	3.30	2.19	0.101

Table 8.2: Quality index values for variation of beam-vessel angle. Each value is the average of measurements from 3 waveform pulsatilities.

	Offset (mm)	QI1	QI2	QI3
DWMTM filtered MFE	0	0.87	0.74	0.026
	7.5	1.17	1.02	0.041
	15	4.91	3.32	0.166
MFE from filtered waveforms	0	0.94	0.77	0.030
	7.5	1.02	0.84	0.035
	85	3.68	2.33	0.121

Table 8.3: Quality index values for variation of beam-axis offset. Each value is the average of measurements from 3 waveform pulsatilities.

	Attenuator thickness (cm)	QI1	QI2	QI3
DWMTM filtered MFE	2.0	0.88	0.74	0.026
	3.5	1.00	0.90	0.033
	5.0	3.85	2.62	0.130
MFE from filtered waveforms	2.0	0.89	0.81	0.031
	3.5	1.11	0.92	0.037
	5.0	2.72	1.69	0.086

Table 8.4: Quality index values for variation of attenuator thickness. Each value is the average of measurements from 3 waveform pulsatilities.

8.3.4 Relationship between the quality indices and MFE_{er}.

Table 8.5 shows the correlation coefficients for linear regression between each quality index and MFE_{er}. The correlation is high at 0.90 to 0.93 for the processed waveforms, which is similar to the values of 0.85 to 0.90 for the unprocessed waveforms. Table 8.6 shows the specificities for detection of good quality waveforms when the sensitivity for detection of poor quality waveforms is set to 90%. Good quality was defined as occuring when MFE_{er} was less than 10%. The specificities for the data considered as a whole are high at 88 to 91% for DWMTM filtered envelopes, but lower at 66 to 74% for the envelopes from the filtered waveforms. If the specificities are considered for each pulsatility separately it can be seen that where the quality index is strongly dependent on waveform pulsatility (see table 8.1) the quality index performs significantly worse for waveforms with high PI values. This is particularly noticeable for the filtered waveforms where the strong dependence of each quality index on pulsatility has resulted in extremely low values of specificity of 0 to 18% for waveforms of PI = 2.3.

	QI1	QI2	QI3
MFE from unprocessed waveforms	0.94	0.90	0.96
DWMTM filtered MFE	0.93	0.89	0.92
MFE from filtered waveforms	0.90	0.92	0.91

Table 8.5: Correlation coefficients for linear regression between each quality index and MFE_{er}.

		All data (n=261)		Data by PI (n=87)		
	QI thresh-old	% with MFE_{er} <10	Specif-icity(%)	Specificity (%) PI=0.8	PI=1.4	PI=2.3
a) DWMTM filtered MFE						
QI1	1.28	57	88	94	88	82
QI2	1.00	57	81	98	72	76
QI3	0.041	57	90	96	91	78
b) MFE from filtered waveforms						
QI1	1.18	57	72	90	86	18
QI2	0.91	57	66	97	72	0
QI3	0.04	57	74	93	91	18

Table 8.6: Specificities at 90% sensitivity for detection of good waveforms based upon a threshold value of MFE_{er} of 10%. The test population is considered as a whole (n = 261), and also by PI (n = 87 in each case).

8.3.4 Relationship between the quality indices and PI_{er}.

Table 8.7 shows the correlation coefficients for linear regression between each quality index and PI_{er}. The values at 0.70 to 0.82 for processed waveforms are lower than the corresponding values of 0.85 to 0.90 for the unprocessed waveforms. For the unprocessed waveforms of chapter 7 a threshold PI_{er} value of 0.15 was taken as the criterion to define good quality waveforms as this was a reasonable value which was achievable in practice. The noise reduction methods have led to lower achievable values of PI_{er} so that a threshold value of 0.10 for PI_{er} can now be used. Table 8.8 shows the specificities for detection of good quality waveforms when the sensitivity for detection of poor quality waveforms was set to 90%. The specificities for the data considered as a whole are high at 88-96% for the DWMTM filtered envelope (see figure 8.1), but low at 76 to 81% for the envelopes from the filtered waveforms. The effect of the dependency on pulsatility is less pronounced for the filtered waveforms for PI_{er} than for MFE_{er} however the specificities for detection of good quality waveforms with PI = 2.3 are low at between 39-67%. This improved performance of PI_{er} over MFE_{er} for high pulsatility filtered waveforms is due to the lower values of the threshold quality index giving 90% sensitivity used for PI_{er}. With a lower threshold quality index value a larger number of the waveforms have a quality index value greater than the threshold for PI = 2.3. This is a further reflection of the dependence of quality index on pulsatility.

	QI1	QI2	QI3
MFE from unprocessed waveforms	0.90	0.85	0.88
DWMTM filtered MFE	0.82	0.80	0.81
MFE from filtered waveforms	0.70	0.78	0.79

Table 8.7: Correlation coefficients for linear regression between each quality index and PI_{er}.

		All data (n=270)		Data by PI (n=90)		
	QI threshold	% with PI_{er} <0.10	Specificity(%)	Specificity (%) PI=0.8	PI=1.4	PI=2.3
a) DWMTM filtered MFE						
QI1	1.88	72	96	100	91	97
QI2	1.24	72	88	100	87	79
QI3	0.061	72	94	100	93	89
b) MFE from filtered waveforms						
QI1	1.33	72	76	84	88	50
QI2	1.12	72	77	92	89	39
QI3	0.047	72	81	87	88	67

Table 8.8: Specificities at 90% sensitivity for detection of good waveform based upon a threshold value of 0.1 for PI_{er}. The test population is considered as a whole (n = 290), and also by PI (n = 90 in each case).

8.4 Discussion.

This study has investigated the feasibility of using an assessment of the maximum frequency envelope noise to assess waveforms in terms of high and low quality based upon accuracy of estimation of PI and the envelope. At first sight it might appear that this approach would give best results for envelopes from unfiltered waveforms as these have the most noise, however results for each quality index are comparable in terms of the correlation coefficient and specificity for envelopes from unfiltered waveforms and for DWMTM filtered envelopes. Results are more disappointing for the envelopes from the directionally filtered waveforms. The low values of specificity obtained for high pulsatility waveforms would make this approach unviable in practice for these envelopes. This could be due to the

lower noise level of the envelopes which arises as a natural result of filtering of the Doppler spectra.

Ideally a quality index should be independent of physiological variables so that it is influenced only by noise of the maximum frequency envelope due to physical variables. It has been seen in the study population how strong dependence of a quality index on pulsatility led to inadequate performance at high pulsatilities.

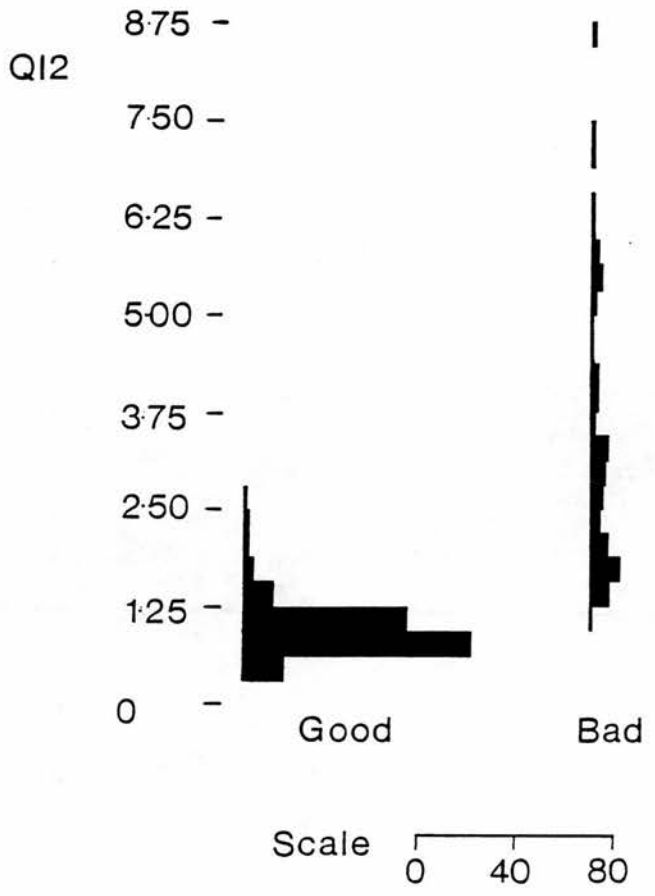

Figure 8.1. QI2 values for good and bad waveforms when the envelope has been DWMTM filtered. A threshold value of 0.10 for PI_{er} was used to separate waveforms into good and bad.

Similar inadequate performance will certainly arise in practice if a quality index is strongly dependent on other physiological variables such as heartrate (waveform length) and fetal breathing. QI1 is strongly dependent on fetal breathing so will be of interest in practice only if waveforms are obtained when there is fetal apnoea, whereas QI2 and QI3 show no significant dependence on fetal breathing.

For the DWMTM filtered waveforms all 3 quality indices show a degree of dependency on pulsatility. Correction of each quality index for dependence on pulsatility could be attempted by directly using the calculated PI. For such a quality index strongly dependent on pulsatility, no judgement could be made on the acceptability of a waveform until the quality index had been corrected for PI. However the PI must be accurate which requires knowledge of the quality index. This is a circular argument so direct correction of such a quality index by PI is unlikely to be useful. Indirect correction for pulsatility by, for example, use of the width of the waveform has been tried and this procedure does substantially reduce dependence of the quality index on PI. However such a procedure increases to a large extent the dependence of each quality index on waveform length, hence such a method is inadvisable. Although there is some dependency on PI, the specificities for detection of good waveforms for the population considered was high for all 3 quality indices. This suggests that in practice some degree of dependence of a quality index on physiological variables would be tolerated.

The approach to identification of waveforms of suitable quality in this study has relied upon the noise of the maximum frequency envelope. An alternative approach is the investigation of the spectral profile, which is known to be dependent on physical variables. This approach may be more relevant to filtered Doppler waveforms where speckle reduction gives a good estimation of the underlying spectral profile.

8.5 Conclusion.

For the DWMTM filtered maximum frequency envelope, this study has

demonstrated the feasibility of using an assessment of the noise of the envelope of simulated umbilical artery Doppler waveforms to assess the waveforms in terms of high and low quality based upon the accuracy of estimation of the envelope and PI. For the directionally filtered waveforms the strong dependence of each quality index on pulsatility makes this approach untenable. The best performance in terms of independence from physiological variables, ability to categorise high and low quality waveforms, and computational simplicity was by QI2. QI1 may also be of interest for studies of the umbilical artery during fetal apnoea. It is important to note that these waveforms have been acquired from a flow device. In a clinical setting other sources of noise may be important and a full assessment needs to be performed of the use of quality indices derived from filtered envelopes.

Chapter 9. A clinical trial of umbilical artery Doppler waveform quality indices.

9.1 Introduction.

In chapter 7 umbilical artery waveform quality indices were described. These were tested using simulated umbilical artery Doppler waveforms acquired with variation of a number of physical parameters including beam-vessel angle and beam-vessel axial misalignment. The results from that chapter were very encouraging in that, firstly there was a high correlation between the quality indices and the errors in estimation of the maximum frequency envelope (MFE_{er}) and in estimation of the pulsatility index (PI_{er}), and secondly there were high specificities and sensitivities for detection of high and low quality waveforms categorised according to threshold values of PI_{er} and MFE_{er}. In clinical practice there will be additional sources of noise present in the Doppler spectrum which cannot easily be investigated using the physiological flow phantom. Some of these features are mentioned in section 1.4.1, and include interference by overlying vessels and saturation of the Doppler amplifier input by large amplitude signals caused by fetal movement. It is therefore important to investigate the performance of the quality indices using umbilical artery waveforms obtained from patients. In this chapter such an assessment is performed.

9.2. Methods.

A brief description of the methodology will be given here. A detailed description is given in the sections following. 500 sets of waveforms were used for the trial. These were divided into 427 sets of waveforms from patients, 17 sets of waveforms from the flow phantom and 56 duplicates. Hardcopy of each set of 5 waveforms was taken. The quality indices were calculated using a microcomputer. The waveform quality of each waveform was subjectively assessed from the hardcopy by an observer and these scores compared with the calculated waveform quality indices.

9.2.1. Acquisition of data.

In our maternity unit umbilical artery Doppler waveforms have been obtained for a number of years using a 4 MHz continuous wave unit (Doptek Ltd, Chichester). This has a low pass filter of 80 Hz, and all waveforms are recorded onto audio cassette. In this study about 300 sets of waveforms obtained recently were used. The operators who had acquired this data were all fully trained hence the overall quality of the waveforms was good. In order to fully test the waveform quality indices portions of recordings from earlier studies were used which were deliberately selected to give waveforms of varying degrees of poor quality. In all 427 sets of waveforms from patients were obtained. 17 sets of waveforms from the flow phantom were also used. These were waveforms obtained for the study of chapter 4. These waveforms are 'calibrated' in the sense that they have known errors in envelope and PI estimation (MFE_{er} and PI_{er}). These were used to compare the operators subjective scores with the calibrated errors. There is obviously no umbilical vein signal for the waveforms from the flow phantom. This could have lead the observer to guess that these were not from patients. In order to counter this an umbilical vein signal was fed into the lower channel of the spectrum analyser from a second tape recorder synchronously with the simulated arterial waveforms.

Waveforms were displayed on a Doptek spectrum analyser and the total spectrum of five of these transferred to a microcomputer (Archimedes 440, Acorn Computers, Cambridge) for analysis. Hardcopy of each set of 5 waveforms was taken using a thermal printer (Sony UP850). For 56 sets of waveforms duplicate pictures were taken for the purpose of assessing the reproducibility of subjective assessment.

9.2.2 Calculation of waveform parameters.

Quality indices and other parameters were calculated from the spectra which had been transferred into the microcomputer. The analysis was performed as

follows:-

i) The maximum frequency envelope was calculated using a follower adaptive to the level of background noise. This follower is described in section 4.3.2.2.

ii) The waveform start and end locations were calculated using an algorithm described by Evans (1988). This algorithm operates in four stages. Firstly the envelope is filtered using a 5-point DWMTM filter described in chapter 6, secondly the maximum height of each waveform is detected, thirdly the point of maximum gradient on the upslope of the waveform is found, and fourthly the maximum rate of change of the gradient at the foot of the waveform is found. This final position is declared to be the waveform start. Only slight modification to the original algorithm was made. The algorithm parameters used in this study are shown in table 9.1.

iii) The quality indices QI1 and QI2 described in chapter 7 were calculated for the interval between each pair of start and end locations. Also calculated were the waveform length (end location - start location) and the PI.

iv) As part of the waveform start detector the envelope was filtered using the 5-point DWMTM filter. The quality indices etc. were also calculated for this filtered envelope.

v) The envelope in its unprocessed form and the DWMTM filtered envelope were saved to disc along with the estimated start and end locations of the waveforms, the quality index, PI and waveform length values.

Parameter	Evans (1988)	This study
Digitisation Time.	12.5ms	10ms
Smoothing filter for detection of maximum height.	5 point weighted mean	5 point DWMTM (theshold=10)
No. points for slope calculation.	5 (62.5ms)	7 (70ms)
No. points per bin (N).	15-20 (187.5-250ms)	30 (300ms)
No. points for search window of peak first derivative (M).	10-15 (125-187.5ms)	19 (190ms)
No. points for search window of peak second derivative.	8 (100ms)	10 (100ms)

Table 9.1. Parameters used in the waveform start detector.

9.2.3 Subjective assessment of waveforms.

The 500 sets of pictures of waveforms were randomised by shuffling. Each set was assessed subjectively by the author in terms of the waveform outline clarity (1 score for each waveform), in terms of the degree of interference in the region of the spectrum above the outline (1 score for each set of waveforms), and in terms of the degree of variability of the waveforms caused by fetal breathing (1 score for each set of waveforms). The scoring criteria are detailed in table 9.2. Waveforms illustrating each score are shown in figures 9.1, 9.2 and 9.3.

a) Clarity of waveform outline.

Score	Criterion
0	Envelope clearly defined over the whole waveform.
1	Envelope is less clear for at least part of the waveform.
2	Envelope is very unclear.

b) Interference above the waveform.

Score	Criterion
0	No interference.
1	Small amount of interference.
2	Large amount of interference.

c) Variability of waveforms as a result of fetal breathing.

Score	Criterion
0	No significant variability.
1	Small variability.
2	Large variability.
3	No assessment possible.

Table 9.2. Criteria for assessment of umbilical artery waveforms.

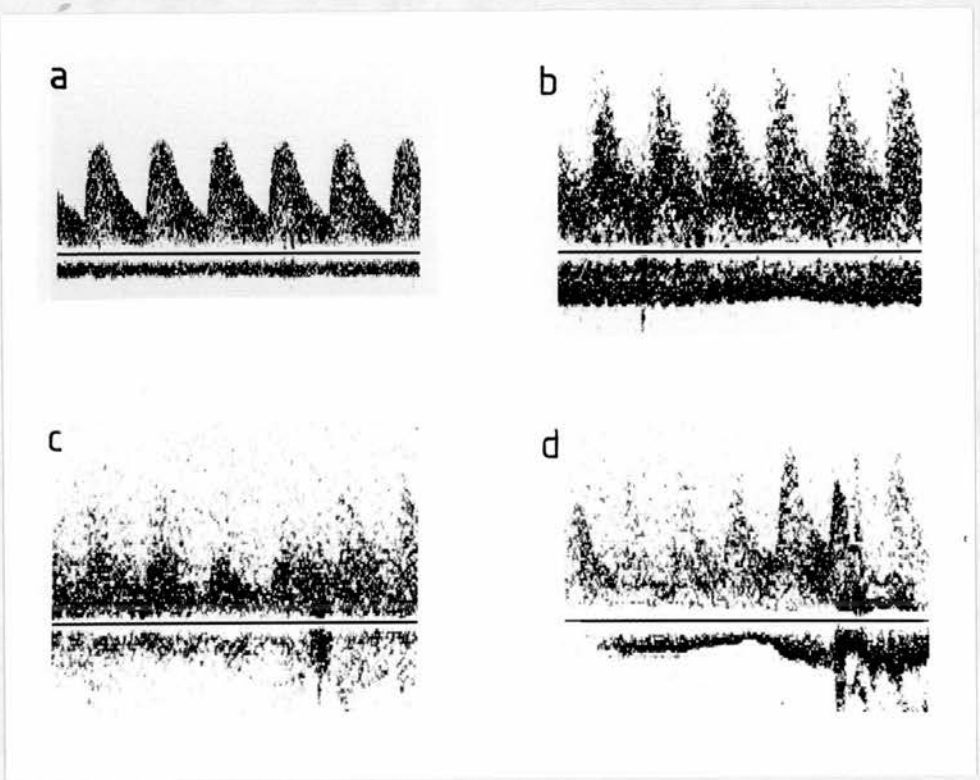

Figure 9.1. Waveforms illustrating the scoring system used for assessment of envelope clarity. a) score 0, b) score 1, c) and d) score 2.

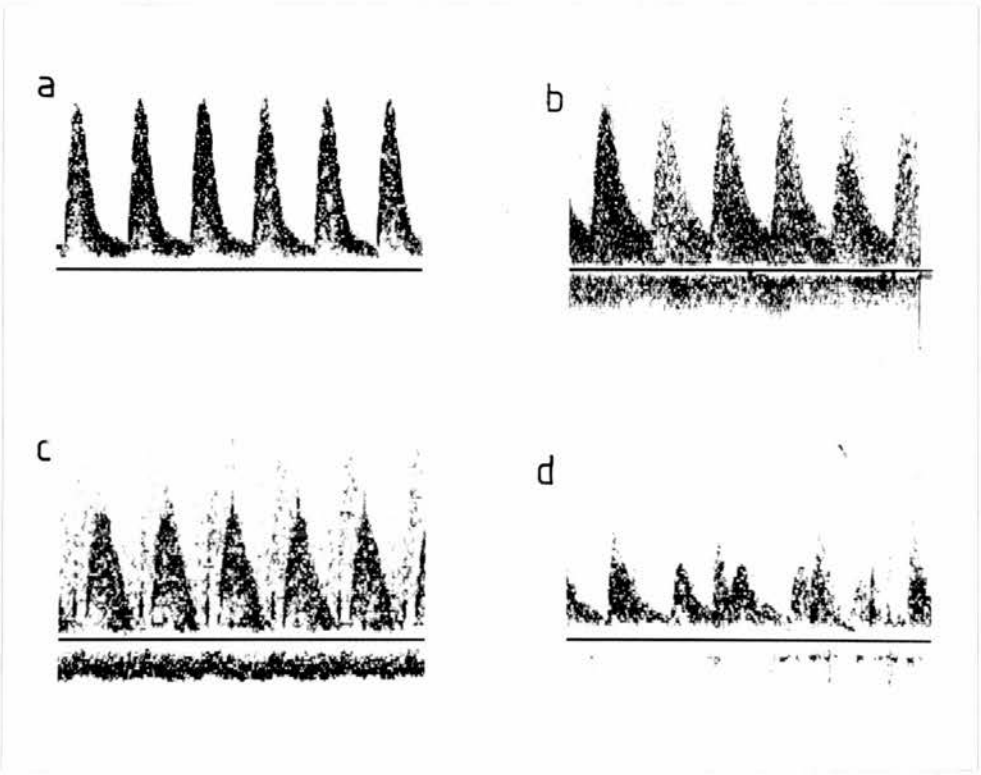

Figure 9.2. Waveforms illustrating the scoring system used for assessment of envelope interference. a) score 0, b) score 1, c) and d) score 2.

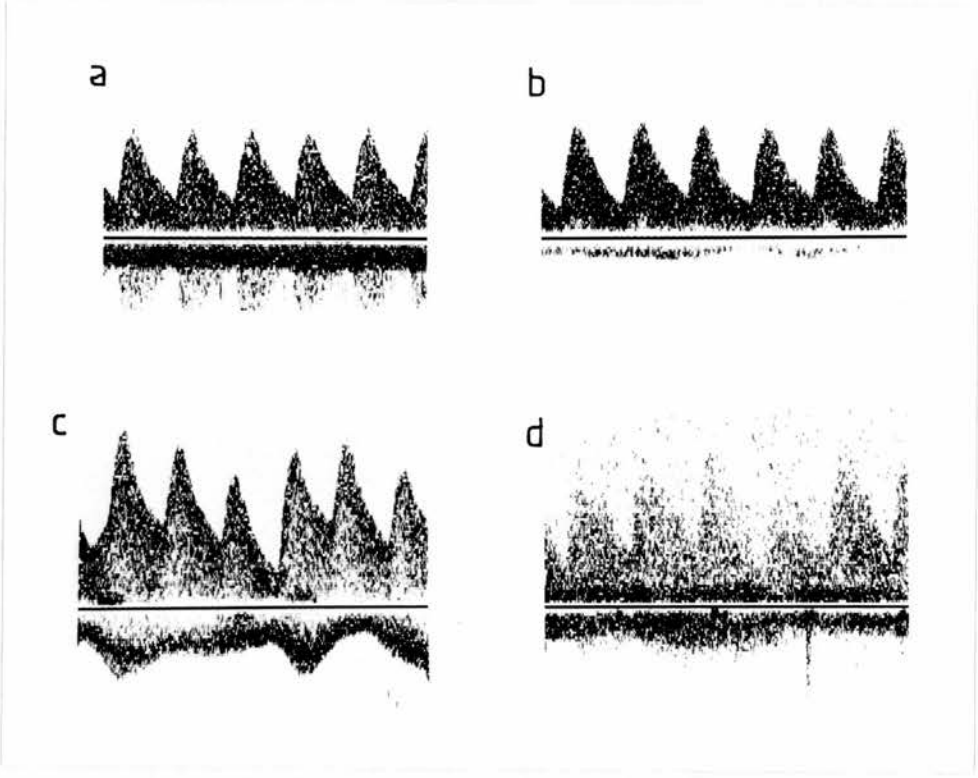

Figure 9.3. Waveforms illustrating the scoring system used for assessment of variability due to fetal breathing. a) score 0, b) score 1, c) score 2, d) score 3.

9.3 Results.

9.3.1 Reproducibility study.

Table 9.3 shows the results for the assessment of envelope clarity, envelope interference and variability due to fetal breathing. The percentage of waveforms scored identically on 2 occasions is high in all cases; 95% for envelope clarity, 100% for envelope interference and 89% for variability due to breathing. The remainder of the waveforms differed by only one group on reassessment.

a) Envelope score (first waveform)

2	0	3	28
1	4	116	0
0	118	10	0
	0	1	2

Envelope score (second waveform)

b) Interference score (first set)

2	0	0	19
1	0	5	0
0	32	0	0
	0	1	2

Interference score (second set)

c) Variability score (first set)

3	0	0	0	5
2	0	2	6	0
1	2	5	1	0
0	34	1	0	0
	0	1	2	3

Variability score (second set)

Table 9.3. Results for assessment of waveforms on 2 occasions a) envelope clarity, b) envelope interference, c) variability due to fetal breathing.

9.3.2 Quality index values and envelope scores from the calibrated waveforms.

Figure 9.4 shows a plot of PI_{er} versus the envelope clarity score. The Spearman rank correlation coefficient for this data at 0.76 is highly significant ($p < 0.001$). Only one of the set of waveforms with zero envelope score has a high value for PI_{er}. The waveforms and the estimated envelopes for this set are shown in figure 9.5. There is a small but definite amount of end-diastolic flow which is just above the filter level. In this region the maximum frequency follower occasionally gives zero values ('dropout') which give rise to the high value for PI_{er}.

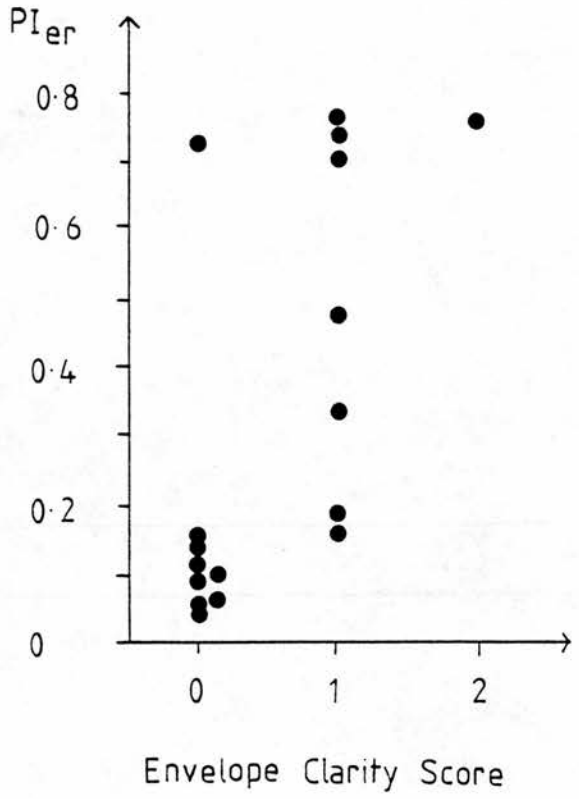

Figure 9.4. Plot of PI_{er} versus the average envelope clarity score for the 17 sets of waveforms obtained from the flow phantom.

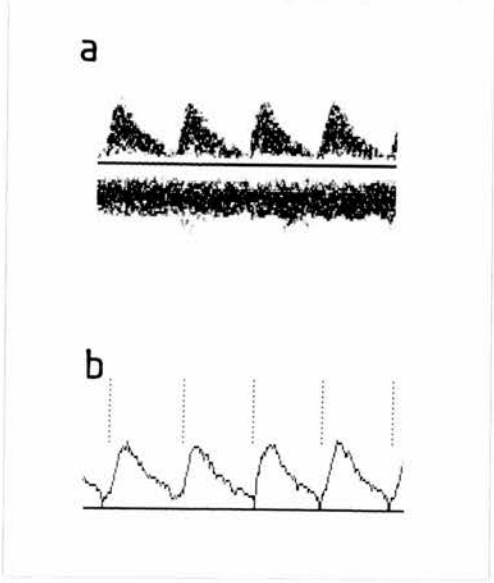

Figure 9.5. Doppler waveforms and estimated envelopes with an average envelope clarity score of zero and a PI_{er} of 0.73.

9.3.3 Results for waveforms from patients.

9.3.3.1. Assessment of envelope clarity for the data as a whole.

Each waveform had been given an envelope score, giving a total of 2135 individual scores. Figure 9.6 shows the distribution of individual waveform values for one of the quality indices; QI2. There is an overall increase in the QI2 values as the envelope score increases. Similar results were found for QI1. For comparative purposes the mean value of parameters for each set of waveforms was taken. Assessment was performed in terms of the ability of the parameters to distinguish between high and low quality waveforms. High quality was defined as a mean envelope score of zero. The sensitivity for detection of good quality waveforms was set at 90% and the specificity for detection of poor quality waveforms calculated. The results are shown in table 9.4. Also included in this table are a

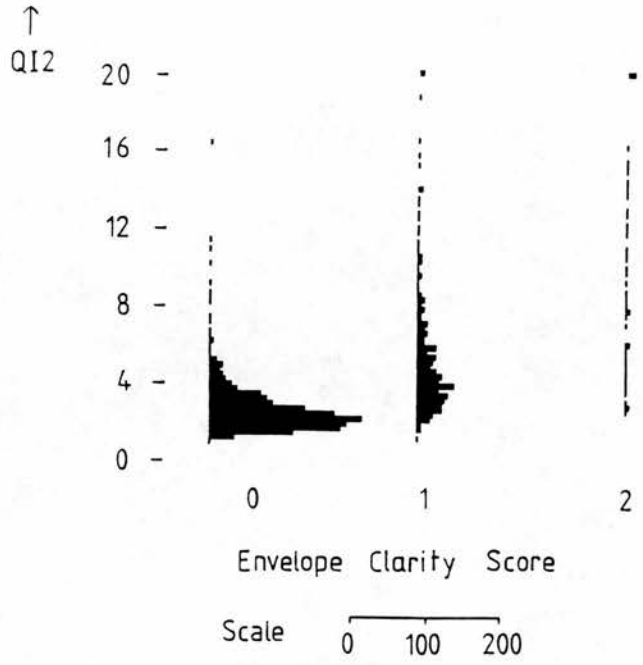

Figure 9.6. Distribution of individual waveform values of QI2 categorised according to envelope clarity score.

Parameter	Threshold	Specificity(%)	Sensitivity(%)	p value
Fmax	1241Hz	2.9	89.9	<0.001
Waveform length	0.412s	9.6	88.8	<0.001
CV_{wl}	1.1%	20.9	89.9	<0.001
CV_{PI}	4.8%	39.3	88.8	<0.001
QI1	2.37	52.7	89.9	<0.001
QI2	2.57	68.2	89.9	-

Table 9.4. Specificities for detection of good quality sets of waveforms based upon a threshold average envelope score of 0. The sensitivity for detection of poor quality waveforms was set at 90%. p values (McNemars test) are given for the difference in specificities compared to QI2. The number of sets of waveforms in each case is 427.

number of other parameters which would be expected to be influenced by waveform quality and hence which could be useful as waveform quality indices. These are average systolic peak frequency (Fmax), average waveform length, coefficient of variation of length values (CV_{wl}) and the coefficient of variation of PI (CV_{PI}). QI2 has the highest specificity at 68.2% and this is significantly greater than the specificities for the other parameters (McNemars test, Armitage and Berry 1987). QI1 has a slightly lower specificity at 52.7%. The other parameters are not useful individually in the categorisation of these waveforms, however further examination of CV_{wl} and mean waveform length show that large values are only associated with the low quality waveforms. These high values reflect the poor performance of the waveform start detector when the envelope is very noisy. The possibility arises of the use of combinations of parameters in order to detect poor quality waveforms. Examination of the mean QI1 and QI2 values for those sets of waveforms reveals that these are greater than the threshold values given in table 9.4. In this case the waveforms have already been categorised correctly as poor quality waveforms so these additional parameters will not be useful.

9.3.3.2 Dependence of quality indices on various factors.

In chapter 4 it was explained that the quality index should be related to the degree of clarity of the envelope but not on other factors such as physiological variables. The influence of other factors for the set of waveforms of this chapter which were obtained from patients can be assessed by considering the sets of waveforms with an average envelope score of 0. Four factors will be considered as detailed below.

- Interference above the waveform outline. The scores obtained previously were used. Sets of waveforms were eliminated where the fetal breathing score was greater than 0.

- Fetal breathing. The scores obtained previously were used. Sets of waveforms were eliminated where the interference score was greater than 0.

- Pulsatility index. The PI values were separated into 3 groups. Score 0, PI < 1.2; score 1, 1.2 ≤ PI < 2.0; score 2, PI ≥ 2. All waveforms with fetal breathing or interference scores greater than zero were eliminated.

- Waveform length. The waveform length values were separated into 3 groups. Score 0, length < 420ms; score 1, 420ms ≤ length < 480ms; score 2, length ≥ 480ms. These correspond to the length values which are approximately 1 standard deviation either side of the mean length value for this group. All waveforms with fetal breathing or interference scores greater than zero were eliminated.

In each case the specificities for detection of good quality waveforms were calculated using the threshold values established in table 9.4. Tables 9.5a and 9.5b show the results for QI1 and QI2 respectively. The dependence of QI1 and QI2 on the score for each factor was statistically tested using the χ^2 test for trends in proportion (Armitage and Berry 1987). If there is a significant trend this will lead to a low p value. A significant result was defined as one where p was less than 0.05.

There is a highly significant ($p < 0.001$) fall in specificity for both QI1 and QI2 for increasing degrees of interference. Figure 9.7 demonstrates 2 sets of waveforms for which there is interference above the envelope. Of the other factors only the effect of fetal breathing on QI1 is significant. This is consistent with the observations of chapter 7 where it was noted that the dependence of QI1 on breathing was to be expected since QI1 is a measure of the degree of variability between adjacent envelopes, regardless of whether the variability arises from envelope noise or gross changes in waveform shape. The effect of waveform length on QI2 is worthy of further consideration. The p value is not significant however at 0.09 it is only slightly higher than 0.05. The cutoff waveform lengths defined above to subdivide that data were 0.42s and 0.48s, corresponding to the positions for 1 standard deviation either side of the mean. If 2 standard deviations are used (approximately 0.40 and 0.50s), the specificities for scores 0,1 and 2 are 100%, 77%

and 54% respectively which gives a significant trend with a p value just under 0.025. Examination of the raw data (figure 9.8) reveals that the highest and lowest values for the waveform length are associated with high and low values for QI2 respectively. This is considered further in the discussion.

a) QI1		Score			
	N	0	1	2	p
Interference	141	87	60	35	<0.001
Fetal breathing	205	87	35	2	<0.001
PI	119	86	94	71	>0.50 (NS)
Waveform length	119	89	86	90	>0.90 (NS)

b) QI2		Score			
	N	0	1	2	p
Interference	141	77	50	14	<0.001
Fetal breathing	205	77	71	76	>0.90 (NS)
PI	119	75	79	86	>0.25 (NS)
Waveform length	119	100	72	75	>0.05 (NS)

Table 9.5. Specificities (%) for detection of good quality waveforms for various subgroups. p values (χ^2 test) are given indicating the significance of a trend in the specificities going from score 0 to score 2. N is the number of sets of waveforms in each subgroup. a) QI1, b) QI2.

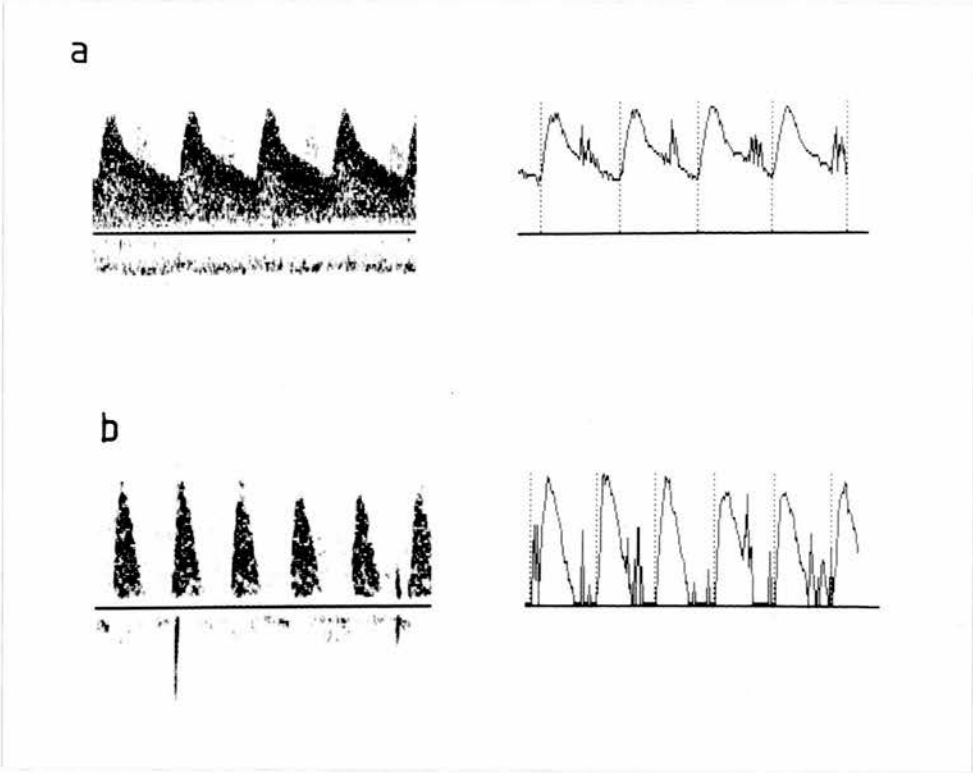

Figure 9.7. Waveforms and associated envelopes for 2 cases where the average envelope clarity score is 0, but where the QI1 and QI2 values are high as a result of the spectral interference above the envelope.

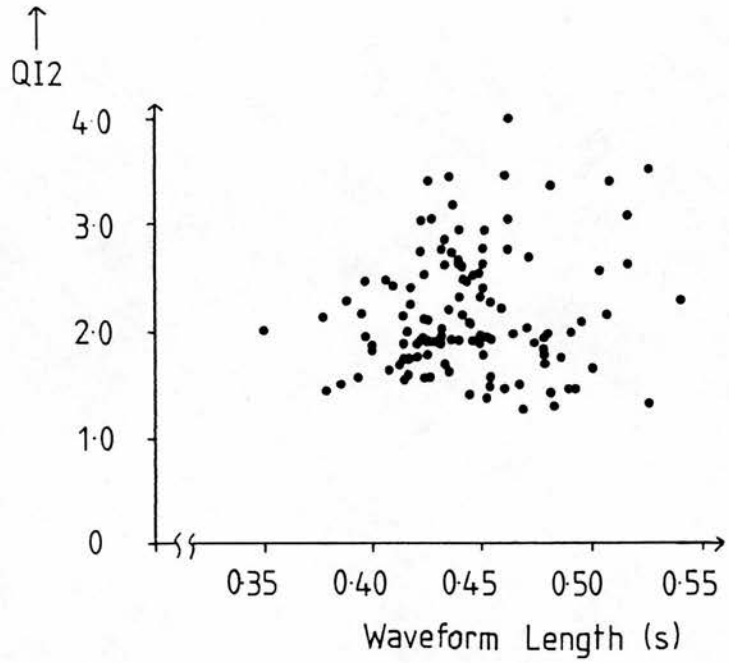

Figure 9.8. Plot of mean waveform length value versus the mean QI2 value for the subgroup where the average envelope score was 0, and where waveforms with non-zero scores for fetal breathing and envelope interference have been removed.

9.3.3.3. Results for the DWMTM filtered envelopes.

In chapter 8 it was shown that the quality indices from the DWMTM filtered envelope could be used to classify waveforms in terms of high and low quality based upon accuracy of estimation of the envelope and of PI. Tables 9.6 and 9.7 show the results for quality indices derived from the DWMTM filtered envelopes when good quality was defined as an average envelope score of 0. These tables were derived in a similar manner to tables 9.4 and 9.5. QI2 has the highest specificity at 46.2%. This is not significantly greater than the specificity for QI1 of

46.0%, but is significantly greater than the specificities for the other parameters (McNemars test, Armitage and Berry 1987). The specificities for QI1 and QI2 are very low. The main point to note from table 9.7 is that QI1 and QI2 are strongly dependent on PI. This is consistent with the observations of chapter 8 (table 8.1) where it was noted that both QI1 and QI2 were dependent on PI.

Parameter	Threshold	Specificity(%)	Sensitivity(%)	p value
Fmax	1098Hz	1.3	89.9	<0.001
Waveform length	0.412s	9.6	88.8	<0.001
CV_{wl}	1.1%	20.9	89.9	<0.001
CV_{PI}	3.8%	32.6	89.9	<0.001
QI1	1.67	46.0	89.9	>0.8 (NS)
QI2	0.99	46.2	89.4	-

Table 9.6. Specificities for detection of good quality sets of waveforms based upon a threshold average envelope score of 0 for DWMTM filtered envelopes. The sensitivity for detection of poor quality waveforms was set at 90%. p values (McNemars test) are given for the difference in specificities compared to QI2. The number of sets of waveforms in each case is 427.

a) QI1

	N	Score 0	1	2	p
Interference	141	81	40	0	<0.001
Fetal breathing	205	81	17	0	<0.001
PI	119	84	75	40	<0.025
Waveform length	119	89	78	83	>0.50 (NS)

b) QI2

	N	Score 0	1	2	p
Interference	141	46	35	0	>0.10 (NS)
Fetal breathing	205	46	55	53	>0.25 (NS)
PI	119	57	21	0	<0.001
Waveform length	119	61	39	63	>0.05 (NS)

Table 9.7. Specificities (%) for detection of good quality waveforms for various subgroups for DWMTM filtered envelopes. p values (χ^2 test) are given indicating the significance of a trend in the specificities going from score 0 to score 2. N is the number of sets of waveforms in each subgroup. a) QI1, b) QI2.

9.4 Discussion.

In this study waveform quality indices calculated from the maximum frequency envelope have been tested using umbilical artery waveforms from patients. In order to do this the sets of waveforms were assessed subjectively in terms of envelope clarity, envelope interference and variability due to fetal breathing. The assessment in this chapter was performed by the author. The author recognises that this is not ideal as the same person that formulated the indices also performed the assessment, and there could be a temptation to categorise the waveforms inappropriately, however every attempt was made to give an unbiased subjective assessment.

Originally the sets of waveforms were given to a colleague physicist to score. Examination of these scores and discussion with the colleague revealed a difference in approach, most importantly all waveforms with absent end diastolic flow were given a score of 2 for envelope clarity on the grounds that if the envelope fell below the filter level then it was impossible to say with confidence exactly where the envelope lay. This approach would lead to the conclusion that most clinically abnormal waveforms, which have absent end diastolic flow, would not be of sufficiently high technical quality to be usable. This is clearly inappropriate for clinical usage. Also it was noted that there were clear cases where mistakes in assessment had been made. These 2 factors tended to obscure the relationship between the quality indices and the subjective scores, and also between the quality indices and the various subgroups such as fetal breathing, making both the results and the interpretation of the results not useful. As the author was primarily interested in finding out under what conditions the quality indices worked, and under what conditions they failed, he performed the assessment himself.

For the unprocessed waveforms both quality indices perform poorly when there is spectral interference above the envelope, even when the envelope is clearly defined (score 0) according to the observer. The observer has the ability to 'see through' the noise to some extent. However the maximum frequency follower does not have the same ability as the human brain to follow the waveform outline in the presence of interference hence gives high QI values. This emphasises that the quality index is inherently bound in with the maximum frequency follower and when this performs poorly large quality index values may arise. In this respect the presence of high values for the quality indices when there is substantial interference is consistent with the poor estimation of the envelope in that the PI values derived from the envelope will be in error.

The other main factor influencing the quality indices, and this is only relevant for QI1, is fetal breathing. QI1 is strongly dependent on fetal breathing which is

probably the reason for its poorer performance compared to QI2 for the data considered as a whole (52.7% specificity for QI1 compared with 68.2% for QI2). When the effects of interference and fetal breathing are removed these specificities rise to 87% and 77% for QI1 and QI2 respectively. These are high specificities and are probably as good as can be expected bearing in mind the inevitable percentage of envelopes which will have been misclassified due to the observers variabilty in scoring, and also the close similarity between for example a set of waveforms with envelope scores of (0,0,0,0,0), which was defined as acceptable, and a set with scores (0,0,0,0,1), which was defined as unacceptable.*

For QI1 the other factors considered, that is waveform length and PI, had no effect. For QI2 PI had no effect. The effect of length on QI2 is a small effect as was mentioned in the results section. QI2 is based upon a sum of local linearity measures. Early work using this approach revealed a dependence of the sum on the waveform length, so that in the formulation of QI2 normalisation by waveform length was performed. As there appears to be a further dependence of QI2 on length it could be argued that in the formulation of QI2 normalisation by $(\text{length})^2$ should be performed. This was tried and the residual dependence of the new index on length is low however the overall performance in detection of normal waveforms is poorer. It may be that it is best to stick to a simple linear normalisation for QI2 and accept that for a small percentage of the waveforms QI2 may perform poorly.

For the DWMTM filtered envelopes the specificities are low at 46% for both QI1 and QI2. For the subgroup in which removal of the waveforms exhibiting fetal breathing and spectral interference was performed the specificities are 81% and 46%. These values should be compared with the specificities from the same subgroup for the unprocessed envelopes of 87% and 77%. In chapters 7 and 8 it was shown using the flow phantom that QI1 and QI2 gave very high specificities for detection of high quality waveforms for both the unprocessed and the DWMTM filtered envelopes. Two question are then raised for the quality indices when

applied to the DWMTM filtered envelopes. Firstly, why does QI1 perform better than QI2 for the no-breathing and no-interference subgroup? Secondly, why is there poor performance for QI2 for the waveforms in the patient study compared with the flow phantom study? The first point to make in trying to answer these questions is that, even the highest quality waveforms will exhibit a degree of envelope noise due to Doppler speckle. The degree of noise between adjacent pixels will be suppressed to a very large extent on application of the DWMTM filter. When there is a large degree of noise on the original envelope, arising from for example uniformly distributed spectral noise of electronic origin, the filter does not fully suppress the noise. The residual noise of adjacent pixels for the filtered envelope gives rise to large values of QI2; this quality index being a measure of the degree of noise of adjacent pixels. In the flow phantom studies a large proportion of the low quality waveforms exhibited this electronic noise, which produced noisy envelopes, filtered envelopes with residual noise, and high values for QI2. For the study of this chapter the proportion of low quality waveforms exhibiting electronic noise was less. Hence for the low quality waveforms as a whole it is probably the case that the DWMTM filter was effective at suppressing the envelope noise hence QI2 is not able to distinguish to any degree the high and low quality waveforms. For the subgroup where the effects of interference and fetal breathing have been removed one would expect the DWMTM filter to be highly effective in suppressing envelope noise which would explain the poor specificity of 46% for QI2 in this subgroup. For the same subgroup for the unprocessed envelopes; the envelopes have a degree of noise due to Doppler speckle so that QI2 performs well. QI1 is a measure of the degree of correlation between successive envelopes. This may be less sensitive to noise suppression than QI2 in that the filtered envelope may be smooth but estimated incorrectly, so that envelope values for successive waveforms may vary in height. A second factor which may be relevant here is that QI2 is strongly dependent on PI whereas QI1 is less dependent. These factors may explain why

QI1 gives a high specificity for the no-breathing and no-interference subgroup for the DWMTM filtered envelopes whereas QI2 does not. In summary for the discussion of this paragraph, the quality indices are based upon an assessment of the degree of noise of the envelope, and for the waveforms of this chapter acquired from patients it appears that suppression of the envelope noise by filtering substantially affects the quality index performance. There is also dependence of each of these indices on PI. This and the low specificities above make these quality indices not useful for DWMTM filtered envelopes.

In chapter 6 it was shown that improved estimation of the PI was produced by DWMTM filtering of the envelope. This would be a desirable thing to do however in this chapter it has been demonstrated that the quality indices only work well for the unprocessed waveforms. One approach which could be attempted in clinical practice is to assess waveform quality using the unprocessed envelope, and to calculate PI for each waveform from the filtered envelope.

In clinical practice criteria are defined for both the envelope clarity and the degree of variability due to fetal breathing. Many reports in the literature claim to acquire waveforms with a clearly defined envelope during fetal apneoa. In our hospital we have taken the more pragmatic approach, as regards the fetal breathing criteria, of acquiring waveforms during fetal apneoa if possible and if this is not possible then accepting waveforms with a small amount of variability due to breathing. In order for the quality indices to follow this approach there would need to be a high degree of separation of the fetal breathing groups. QI2 is not sensitive to breathing and for QI1 and also for the coefficient of variation of PI there is considerable overlap between the groups, so that in practice none of these parameters could be used as fetal breathing detectors. The criteria used for fetal breathing in clinical practice arises from a need to acquire waveforms with an acceptably low coefficient of variation for PI (or resistance index). An alternative approach to fetal breathing detection is the specification of an upper limit for the

coefficient of variation of PI. In clinical practice therefore a twofold approach could be adopted consisting of a threshold average quality index value, and a threshold value for the coefficient of variation of PI.

9.5 Conclusion.

The best overall performance of the quality indices when applied to the unprocessed waveforms is by QI2. This shows good independence from waveform pulsatility and fetal breathing, and also reasonable independence from waveform length. Both QI1 and QI2 perform poorly when there is a large degree of noise in the region of the spectrum above the envelope, however this poor performance is often related to the inability of the maximum frequency follower to estimate correctly the maximum frequency envelope in these conditions so that the high waveform quality values reflect the erroneous calculation of the PI in these cases. In practice it appears that the suppression of envelope noise produced by the DWMTM filter is sufficient to give rise to unacceptably poor quality index performance.

The approach adopted in the detection of waveform quality has been relatively simple in that the degree of noise of the envelope has been used as an indicator of quality. No consideration has been given to the underlying Doppler spectrum, and the complex techniques of pattern recognition and artificial intelligence have not been used. Bearing this in mind the results from this clinical study are encouraging. The indices are sufficiently simple to be calculated in real time, and this approach to the assessment of waveform quality should be useful for Doppler systems with automated calculation of waveform indices such as pulsatility index from the umbilical artery. Waveform quality detectors with improved performance could possibly be generated using the Doppler spectrum, along with the appropriate pattern recognition and artificial intelligence tools however it is unlikely that the algorithms so generated would be sufficiently simple to be operated in real time.

Chapter 10. Future work.

This thesis has been concerned with the development and testing of indices of waveform quality which can be used with umbilical artery Doppler waveforms. The approach adopted has been to quantitate the degree of noise of the maximum frequency envelope, and it has been shown using flow phantom studies that these indices are related to the error in estimation of the envelope and in the pulsatility index. Further it has been shown using waveforms from patients that these indices give reasonable separation of high and low quality waveforms classified subjectively. The analysis in all cases was performed off-line using a microcomputer. In clinical usage the quality indices could be used in a real time system which would have automated calculation of waveform parameters such as pulsatility index. Clearly an assessment of the performance of the quality indices in a real time system would be desirable. This assessment has not been performed in this thesis as it would have meant duplicating in real time many of the features of a commercial Doppler system on the microcomputer or in hardware, such as spectral estimation, envelope identification etc. This would have involved a very considerable amount of development work, something which is beyond the scope of the present work.

It is possible that superior performance in waveform quality assessment would be produced from more complex quality indices based upon the envelope noise. An alternative approach would be to use the underlying Doppler spectrum. In a small pilot study performed in the early days of this thesis simple quality indices based upon the whole spectrum were investigated (Hoskins et al 1988c). In that study speckle suppression was performed using a 9×9 DWMTM filter. The results from that study were not encouraging hence that approach was not followed. However the field of image analysis is a large one and the more complex techniques of pattern recognition and artificial intelligence may be useful in the differentiation of high and low quality waveforms. As mentioned in chapter 9 the algorithms

developed using these methods are unlikely to be usable in real time with the current processing power of Doppler machines. Also the desirability of following this approach should be balanced against its possible usefulness.

This study has been restricted to umbilical artery Doppler waveforms acquired using a continuous wave Doppler device. The use of quality indices has been relevant since acquisition of these waveforms can be difficult even using a duplex system. Continuous wave devices have also been used to acquire waveforms from the lower limb and the cerebrovascular circulation. Increasingly continuous wave systems are being replaced by, or used in conjunction with, duplex or colour flow systems. Duplex and colour flow systems enable the operator to obtain Doppler waveforms from many vessels in the body. These waveforms can often be acquired free from interference by overlying vessels and with a known beam-vessel angle and location of the sample volume within the vessel. For such vessels the use of waveform quality indices is unlikely to be useful. For the smaller vessels of interest in the body, such as the placental arcuate arteries, visualisation using a duplex system can be difficult hence for the waveforms obtained from these vessels quality indices may be useful. The smaller vessels can often be identified using colour flow systems. This may provide sufficient localisation to enable high quality waveforms to be acquired, however it is only relatively recently that colour flow systems able to detect flow in small vessels have been commercially available, and this area is still being assessed. Of course quality indices could be useful where the more expensive duplex and colour flow systems are not available and continuous wave systems are used. Quality indices applied to waveforms other than the umbilical artery would certainly need to be fully assessed.

References.

Abramawicz J S, Warsof S L, Arrington J and Levy D L (1989) Doppler analysis of the umbilical artery: the importance of choosing the placental end of the cord. Journal of Ultrasound in Medicine 8 219-221

Abramowitz M and Stegun I A. (1964) Handbook of mathematical functions. US Government Printing Office, Washington D C.

Adamson S L, Morrow R J, Bascom P A J, Mo L Y L and Ritchie J W K (1989) Effect of placental resistance, arterial diameter and blood pressure on the uterine arterial velocity waveform: a computer modelling approach. Ultrasound in Medicine and Biology 15 437-442

Adamson S L, Morrow R J, Langille B L, Bull S B and Ritchie J W K (1990) Site dependent effects of increases in placental vascular resistance on the umbilical arterial velocity waveform in fetal sheep. Ultrasound in Medicine and Biology 16 19-27

D'Alessio T (1985) 'Objective' algorithm for maximum frequency follower estimation in Doppler spectral analysers. Medical and Biological Engineering and Computing 23 63-68

Angelson B A J (1980) A theoretical study of the scattering of ultrasound from blood. IEEE Transactions on Biomedical Engineering BME 27 61-67

Arduini D, Rizzo G, Romanini C and Mancuso S (1987) Utero-placental blood flow velocity waveforms as predictors of pregnancy-induced hypertension. European Journal of Obstetrics, Gynecology and Reproductive Biology 26 335-341

Armitage P and Berry G (1987) Statistical methods in medical research. Blackwell Scientific Publications, Oxford.

Atkinson P and Berry M V (1974) Random noise in ultrasonic echoes diffracted by blood. Journal of Physics 7 1293-1302

Ballard D H and Brown C M (1982) Computer Vision. Prentice Hall, New Jersey.

Bamber J C and Cook-Martin G (1987) Texture analysis and speckle reduction in medical echography. SPIE Proceedings 768 120-127

Bamber J C and Daft C (1986) Adaptive filtering for reduction of speckle in ultrasonic pulse echo images. Ultrasonics 24 41-44

Beattie R B and Dornan J C (1989) Antenatal screening for intrauterine growth retardation with umbilical artery ultrasonography. British Medical Journal 1298 631-635

Bewley S, Campbell S and Cooper D (1989) Uteroplacental Doppler flow velocity waveforms in the second trimester: a complex circulation. British Journal of Obstetrics and Gynaecology 96 1040-1046

Bilardo C M, Nicolaides K H and Campbell S (1990) Doppler measurements of fetal and uteroplacental circulations: Relationship with umbilical venous blood gases measured at cordocentesis. American Journal of Obstetrics and Gynecology 162 115-120.

Brar H S, Medeoris A L, De Vore G R and Platt L D (1988) Fetal umbilical

velocimetry using continuous wave and pulsed wave Doppler ultrasound in ultrasound in high risk pregnancies: a comparison of systolic to diastolic ratios. Obstetrics and Gynecology 72 607-610

Campbell S, Diaz-Recasens J, Griffin D R, Cohen-Overbeck T E, Pearce J M, Willson K and Teague M J (1983) New Doppler technique for assessing utero-placental blood flow. Lancet i 675-677

Campbell S, Pearce J M F, Hackett G, Cohen-Overbeck T and Hernandez C (1986) Qualitative assessment of uteroplacental blood flow: early screening test for high risk pregnancies. Obstetrics and Gynecology 68 649-653

Canny J F (1983) Finding edges and lines in images. M S thesis, MIT.

Censor D, Newhouse V L, Vantz T and Ortega H V (1988) Theory of ultrasound Doppler-spectra velocimetry for arbitrary beam and flow configuration. IEEE Transactions on Biomedical Engineering BME 35 740-751

Chambers, S E, Johnstone, F D Muir, B B, Hoskins, P R Haddad, N G and McDicken, W N (1988) The effects of placental site on the arcuate artery flow velocity waveform. Journal of Ultrasound in Medicine 7 671-673

Chambers S E, Hoskins P R, Haddad N G, Johnstone F D, McDicken W N and Muir B B (1989) A comparison of fetal abdominal circumference measurements and Doppler ultrasound in the prediction of small-for-dates babies and fetal compromise. British Journal of Obstetrics and Gynaecology 96 803-808

Chan P and Lim JS (1985) One dimensional processing for adaptive image

restoration. IEEE Transactions on Acoustics, Speech and Signal Processing 33 117-126

Chen C H (1986) Seismic and underwater acoustic waveform analysis. In, Handbook of pattern recognition and image processing, (edited by Young T Y and Fu K S), pp 527- 544. Academic Press, London.

Chen H Y, Chang F M, Huang H C, Hsieh F J and Lu C C (1988) Antenatal fetal blood flow in the descending aorta and in the umbilical vein in normal pregnancy. Ultrasound in Medicine and Biology 14 263-268

Clewell W H, Hackett G, McCooke H B, Hanson M A and Campbell S (1988) Phsiological interpretation of the Doppler waveform in the uterine artery of the sheep. In, Fetal and Neonatal Development, (edited by C T Jones). Perinatology press.

Cobbold R S C, Veltink P H and Johnston K W (1983) Influence of beam profile and degree of insonation on the CW Doppler ultrasound spectrum and mean velocity. IEEE Transactions on Sonics and Ultrasonics SU 30 364-370

Cohen-Overbeek T, Pearce J M and Campbell S (1985) The antenatal assessment of utero-placental and feto-placental blood flow using Doppler ultrasound. Ultrasound in Medicine and Biology 11 329-339

CRC Handbook of chemistry and physics (1985) The Chemical Rubber Company, Cleveland, Ohio.

Eik-Nes S H, Marsal K and Kristofferson K (1984) Methodology and basic

problems related to blood flow studies in the human fetus. Ultrasound in Medicine and Biology 10 329-337

Erskine R L A and Ritchie J W K (1985) Umbilical artery blood flow characteristics in normal and growth-retarded fetuses. British Journal of Obstetrics and Gynecology 92 605-610

Evans D H (1982) Some aspects of the relationship between instantaneous volumetric blood flow and continuous wave Doppler ultrasound recordings. I. The effect of ultrasonic beam width on the output of maximum frequency, mean frequency and RMS processors. Ultrasound in Medicine and Biology 8 605-609

Evans D H (1986) Can ultrasonic scanners really measure volumetric blood flow? In, Physics in Medical Ultrasound, (edited by J A Evans), pp 145-154. York, IPSM.

Evans D H (1988) A Pulse foot seeking algorithm for Doppler ultrasound waveforms. Clinical Physics and Physiological Measurement 9 267-271

Evans D H, McDicken W N, Skidmore R and Woodcock J P (1989) Doppler ultrasound: physics, instrumentation and clinical applications. John Wiley and Sons, Chichester.

van Eyck J, Wladimiroff J W, van der Wijgaard J A G W, Noordam M J and Prechtl H F R (1987) The blood flow velocity waveform in the fetal internal carotid and umbilical artery; its relation to fetal behavioural states in normal pregnancy at 37-38 weeks. British Journal of Obstetrics and Gynaecology 94 736-741

van Eyck J, Wladimiroff J W, Noordam M J, van der Wijgaard J A G W and Prechtl H F R (1988) The blood flow velocity waveform in the fetal internal carotid and umbilical artery; its relation to fetal behavioural states in the growth retarded fetus at 37-38 weeks gestation. British Journal of Obstetrics and Gynaecology 95 473-477

Fairlie F M and Lang G D (1988) The ralation between fetal heart rate and Doppler flow velocity waveform A/B ratio. British Journal of Obstetrics and Gynecology 95 312-314.

Fisk N M, MacLachlan N, Ellis C, Tannirandorn Y, Tonge H M and Rodeck, C H (1988) Absent end-diastolic flow in first trimester umbilical artery. Lancet i 1256-1257

Fitzgerald, D E and Drumm, J E (1977) Non-invasive measurement of the fetal circulation using ultrasound; a new method. British Medical Journal 2 1450-1451

Fitzgerald D E, Stuart B, Drumm J E and Duignan N M (1984) The assessment of the feto-placental circulation with continuous wave Doppler ultrasound. Ultrasound in Medicine and Biology 10 371-376

Fleischer A, Schulman H, Farmakides G, Bracero L, Blattner P and Randolph G (1985) Umbilical artery velocity waveforms and intra-uterine growth retardation. American Journal of Obstetrics and Gynecology 151 502-505

Fouron J, Korcaz Y and Leduc B (1975) Cardiovascular changes associated with fetal breathing. American Journal of Obstetrics and Gynecology 123 868-876

Giles W B, Trudinger B J and Baird P J (1985) Fetal umbilical artery flow velocity waveforms and placental resistance: pathological correlation. British Journal of Obstetrics and Gynaecology 92 31-38

Gill R W, Kossoff G, Warren P S and Garrett (1984) Umbilical venous flow in normal and complicated pregnancy. Ultrasound in Medicine and Biology 10 349-363.

Gosling R C and King D H (1974) Continuous wave ultrasound as an alternative and complement to X-rays. In, Cardiovascular applications of ultrasound, (edited by R S Reneman), pp 266-282. North Holland, Amsterdam.

Griffin D R, Bilardo K, Masini L, Diaz-Recasens J, Pearce J M, Willson K and Campbell S (1984) Doppler blood flow waveforms in the descending thoracic aorta of the human fetus. British Journal of Obstetrics and Gynaecology 91 997-1006

Gudmundson S and Marsal K (1988) Umbilical and uteroplacental blood flow velocity waveforms in pregnancies with fetal growth retardation. European Journal of Obstetrics and Gynecology and Reproductive Biology 27 187-196

Gudmundsson S, Fairlie F, Lingman G and Marsal K (1990) Recording of blood velocity waveforms in the uteroplacental and umbilical circulation: Reproducibilty study and comparison of pulsed and continuous wave Doppler ultrasonography. Journal of Clinical Ultrasound 18:97-101

Haddad N G, Johstone F D, Hoskins P R, Chambers S E, Muir B B and McDicken

W N (1988) Umbilical artery Doppler waveforms in pregnancies with uncomplicated intra-uterine growth retardation. Gynecological and Obstetric Investigations 26 206-210

Hanretty K P, Primrose M H, Neilson J P and Whittle M J (1989) pregnancy screening by Doppler uteroplacental and umbilical artery waveforms. British Journal of Obstetrics and Gynaecology 96 1163-1167.

Haralick R M. (1984) Digital step edges from zero-crossings of second directional derivative. IEEE Transactions on Pattern Analysis and Machine Intelligence PAMI-6 58-68.

Hendricks S K, Sorensen T K, Wang K Y, Bushnell J M, Seguin E M and Zingheim R W (1989) Doppler umbilical artery waveform indices - Normal values from fourteen to forty - two weeks. American Journal of Obstetrics and Gynecology 161 761-765

Hill C R (Ed) (1986) Physical principles of medical ultrasonics. Ellis Horwood, Chichester.

Hoskins P R, McDicken W N, Johnstone F D, Chambers S E and Haddad N G (1988a) The practical consequences of fetal breathing on umbilical artery Doppler waveform acquisition (abstract). British Journal of Radiology 61 541

Hoskins P R, McDicken W N, Johnstone F D, White G, Haddad N G and Chambers S E (1988b) Determination of the presence of fetal apnoea using umbilical artery and umbilical vein Doppler waveforms Ultrasound in Medicine and Biology 14 589-592

Hoskins P R, Loupas T and McDicken W N (1988c) Characteristics of umbilical artery Doppler waveforms in relation to waveform quality (abstract). Clinical Physics and Physiological Measurement 9 278

Hoskins P R, Johnstone F D, Chambers S E, Haddad N G, White G and McDicken W N (1989a) Heartrate variation of umbilical artery Doppler waveforms. Ultrasound in Medicine and Biology 15 101-105

Hoskins P R, Haddad N G, Johnstone F D, Chambers S E and McDicken W N (1989b) The choice of index for umbilical artery Doppler waveforms. Ultrasound in Medicine and Biology 15 107-111

Issartier P, Siouffi M and Pelissier R (1978) Simulation of blood flow by a hydrodynamic generator. Med Prog Technol 6 39-40

Jenkins G M and Watts D G. (1968) Spectral analysis and its applications. Holden-May, San Francisco.

Johnstone F D, Haddad N G, Hoskins P R, McDicken W N, Chambers S E and Muir B B (1988) Umbilical artery Doppler flow velocity waveform: the outcome of pregnancies with absent end diastolic flow. European Journal of Obstetrics, Gynecology and Reproductive Biology 28 171-178

Johnstone F D, Greer I A, Haddad N G and Hoskins P R (1989) Antenatal screening with umbilical artery Doppler ultrasonography (letter). British Medical Journal 298 1097

Johnstone F D, Haddad N G, Steel J M, Hoskins P R, Greer I A, Chambers S E and McDicken W N Doppler umbilical and arcuate artery measurements in diabetic pregnancy (In press).

Joupilla P and Kirkinen P (1984) Increased vascular resistance in the descending aorta of the human fetus in hypoxia. British Journal of Obstetrics and Gynaecology 91 853-856

Kay S M and Marple S L Jr (1981) Spectrum analysis - a modern perspective. Proceedings of the IEEE 69 1380-1419

Kim N C and Jung S H (1987) Adaptive image restoration using local statistics and directional gradient information. Electronics letters 23 610-611

Kofinas A D, Penry M, Greiss F C M, Meis P J and Nelson L H (1988) The effect of placental location on uterine artery flow velocity waveforms. American Journal of Obstetrics and Gynecology 159 1504-1508

Kofinas A D, Espeland M, Swain M, Penry M and Nelson L H (1989) Correcting umbilical artery flow velocity waveforms for fetal heart rate is unnecessary. American Journal of Obstetrics and Gynecology 160 704-707

Kuan D T, Sawchuck A A, Strand T C and Chavel P (1987) Adaptive restoration of images with speckle. IEEE Transactions on Acoustics, Speech and Signal Processing 35 373-383

Lang G D, Levene M I, Dougall A, Shortland D and Evans D H (1988) Direct measurements of fetal cerebral blood flow velocity with duplex Doppler ultrasound.

European Journal of Obstetrics, Gynecology and Reproductive Biology 29 15-19

Laurin J, Marsal K, Persson P H and Lingman G (1987) Ultrasound measurement of fetal blood flow in predicting fetal outcome. British Journal of Obstetrics and Gynaecology 94 940-948

Law Y F, Cobbold R S C, Johnston K W and Bascom P A J (1987) Computer controlled pulsatile pump system for physiological flow simulation. Medical and Biological Engineering and Computing 25 590-595.

Law Y F, Johnston K W, Routh H F and Cobbold R S C (1989) On the design of a steady flow model for Doppler ultrasound studies. Ultrasound in Medicine and Biology 15 505-516

Lee J S (1980) Digital image enhancement and noise filtering by use of local statistics. IEEE Transactions on Pattern Analysis and Machine Intelligence 2 165-168

Lee J S (1981) Speckle analysis and smoothing of synthetic aperture radar images. Computer Graphics and Image Processing 24 255-269

Lee J S (1986) Speckle suppression and analysis for synthetic aperture radar images. Optical Engineering 25 636-643

Lee Y H and Kassam S A (1985) Generalised median filtering and related nonlinear filtering techniques. IEEE Transactions on Acoustics Speech and Signal Processing 33 672-683

Loquet P, Pipkin F B, Symonds E M and Rubin P C (1988) Blood velocity waveforms and placental vascular formation. Lancet i 1252-1253

Loupas T (1988) Digital image processing for noise reduction in medical ultrasonics. PhD thesis, University of Edinburgh

Luckman N P, Skidmore R, Evans J M, Jenkins D and Wells P N T (1988) The effect of acoustic speckle on ultrasonic Doppler studies of blood flow. In, Physics in Medical Ultrasound II, (edited by DH Evans and K Martin). IPSM, York.

Marr D and Hildreth E C (1980) Theory of edge detection. Proceedings of the Royal Society of London 207 187-217

Maulik D, Yarlagadda A P, Youngblood J P and Willoughby L (1989a) Components of variability of umbilical arterial Doppler velocimetry - A prospective study. American Journal of Obstetrics and Gynecology 160 1406-1412

Maulik D, Yarlagadda P, Nathanielsz P W and Figueroa J P (1989b) Hemodynamic validation of Doppler assessment of fetoplacental circulation in a sheep model Journal of Ultrasound in Medicine 8 177-181

McCarty K and Locke D J (1986) Test objects for the assessment of the performance of Doppler shift flowmeters. In, Physics in Medical Ultrasound, (edited by J A Evans), pp 94-106. IPSM, York.

McCowan L M, Mullen B M and Ritchie K (1987a) Umbilical artery flow velocity waveforms and the placental vascular bed. American Journal of Obstetrics and Gynecology 157 900-902

McCowan L M, Erskine L A and Ritchie K (1987b) Umbilical artery Doppler blood flow studies in the preterm, small for gestational age fetus. American Journal of Obstetrics and Gynecology 156 655-659

McDicken W N (1986) A versatile test-object for the calibration of ultrasonic Doppler flow instruments. Ultrasound in Medicine and Biology 12 245-249

McDicken W N (1981) Diagnostic ultrasonics: principles and use of instruments. Wiley, New York.

McDonald D A (1974) Blood flow in arteries. Edward Arnold, London.

Mehalek K E, Rosenberg J, Berkowitz G S, Chitkara V and Berkowitz R L (1989) Umbilical and uterine artery flow velocity waveforms; effect of the sampling site on Doppler ratios. Journal of Ultrasound in Medicine 8 171-176

Mires G, Dempster J, Patel N B and Crawford J W (1987) The effect of fetal heart rate on umbilical artery flow velocity waveforms. British Journal of Obstetrics and Gynaecology 94 665-669

Mo L Y L and Cobbold R S C (1986a) A stochastic model of the backscattered Doppler ultrasound from blood. IEEE Transactions of Biomedical Engineering BME 33 20-27

Mo L Y L and Cobbold R S C (1986b) "Speckle" in continuous wave Doppler ultrasound spectra: A simulation study. IEEE Transactions on Ultrasonics, Ferroelectrics and Frequency Control, UFFC 33 747-753

Mo L Y L, Bascom P A J, McCowan L M E and Ritchie K A (1988a) Transmission line modelling approach to the interpretation of uterine Doppler waveforms. Ultrasound in Medicine and Biology 14 365-376

Mo L Y L, Yun L C M and Cobbold R S C. (1988b) Comparison of four digital maximum frequency estimates for Doppler ultrasound. Ultrasound in Medicine and Biology 14 355-363

Morrow R J, Adamson S L, Bull S B and Ritchie J W K (1989) Effect of placental embolisation on the umbilical arterial velocity waveform in fetal sheep. American Journal of Obstetrics and Gynecology 161 1055-1060.

Mulders L G M, Jongsma H W, Hein P R (1989) Uterine and umbilical artery blood flow velocity waveforms and their validity in the prediction of fetal compromise. European Journal of Obstetrics, Gynecology and Reproductive Biology 31 143-154

Murrils D, Yarlagadda A P, Youngblood J P and Willoughby L (1989) Reproducibility in umbilical artery blood velocity waveforms. In, Obstetric and Neonatal Blood Flow, (edited by Sheldon C D, Evans D H and Savage J R). Biological Engineering Society, London.

Neilson J P (1987) Doppler ultrasound. British Journal of Obstetrics and Gynaecology 94 929-934

Newhouse V L, Furgason E S, Johnston G F and Wolf D A (1980) The dependence of ultrasound Doppler bandwidth on beam geometry. IEEE Transactions on Sonics

and Ultrasonics SU-27:50-59

Newhouse VL, Nathanhan RS and Hertyler LW (1982) A proposed standard target for ultrasound Doppler gain calibration. Ultrasound in Medicine and Biology 8 313-316

Nimrod C, Clapp J, Larrow R, D'Alton M and Persaud D (1989) Simultaneous use of Doppler ultrasound and electromagnetic flow probes in fetal flow assessment. Journal of Ultrasound in Medicine 8 201-205

Noordam M J, Wladimiroff J W, Lotgering F K, Struijk and Tonge H M (1987) Fetal blood flow velocity waveforms in relation to changing peripheral vascular resistance. Early Human Development 15 119-127

Papoulis A. (1981) Probability, Random Variables and Stochastic Processes. McGraw-Hill, New York.

Patrick J, Natale R and Richardson B (1978) Patterns of human fetal breathing at 34-35 weeks gestation. American Journal of Obstetrics and Gynecology 132 507-513

Patrick J, Campbell K, Carmichael L, Natale R and Richardson B (1980) Patterns of human fetal breathing during the last 10 weeks of pregnancy. Obstetrics and Gynecology 56 24-30

Pearce J M and McParland P (1988) Doppler uteroplacental waveforms. Lancet i 1287

Pearce J M, Campbell S, Cohen-Overbeek T, Hackett, Hernandez J and Royston J P (1988) Reference ranges and sources of variation for indices of pulsed Doppler flow velocity waveforms from the uteroplacental and fetal circulation. British Journal of Obstetrics and Gynaecology 95 248-256

Pedley T J (1980) The fluid mechanics of large blood vessels. Cambridge University Press, Bristol.

Peli E (1987) Adaptive enhancement based on a visual model. Optical Engineering 26 655-660

Peterson J N (1984) Digitally controlled system for reproducing blood flow waveforms in vitro. Medical and Biological Engineering and Computing 22 277-280

Pourcelot L (1974) Applications cliniques de l'examen Doppler transuctane Velocimetrie Ultrasonore Doppler (Paris, Seminaire INSERM) pp 213-240

Prytherch D R and Evans D H. (1985) Versatile microcomputer-based system for the capture, storage and processing of spectrum-analysed Doppler ultrasound blood flow signals. Medical and Biological Engineering and Computing 23 445-452

Redman C W G (1989) Examination of the placental circulation by Doppler ultrasound: its place in management still to be defined. British Medical Journal 298 621-622

Reuwer P J H M, Bruinse H W, Stautenbeck P and Haspels A A (1984) Doppler assessment of the fetoplacental circulation in normal and growth retarded

fetuses. European Journal of Obstetrics, Gynecology and Reproductive Biology 18 199-205

Reuwer P J H M, Sijmons E A, Rietman G W, van Tiel M W M and Bruinse H W (1987) Intrauterine growth retardation prediction of perinatal distress by Doppler ultrasound. Lancet ii 415-418

Rochelson B, Schulman H, Farmakides G, Bracero L, Ducey J, Fleischer A, Penny B and Winter D (1987) The significance of absent end-diastolic velocity in umbilical artery waveforms. American Journal of Obstetrics and Gynecology 156 1213-1218

Sainz A, Roberts V C and Pinardi G (1976) Phase-locked loop techniques applied to ultrasonic Doppler signal processing. Ultrasonics 14 128-132

Schlindwein F S and Evans D H (1989) A real-time autoregressive spectrum analyser for Doppler ultrasound signals. Ultrasound in Medicine and Biology 15 263-272

Shortland A P and Cochrane T (1989) Doppler spectral waveform generation in vitro: an aid to diagnosis of vascular disease. Ultasound in Medicine and Biology 15 737-748

Shung K K, Sigelman R A and Reid J M (1976) Scattering of ultrasound by blood. IEEE Transactions Biomedical Engineering BME 23 460-467

Shung K K (1982) On the ultrasound scattering from blood as a function of haematocrit. IEEE Transactions on Sonics and Ultrasonics SU 29 327-331

Skidmore R and Follett D H (1978) Maximum frequency follower for the processing of ultrasonic Doppler shift signals. Ultrasound in Medicine and Biology 4 145-147

Spencer J A D and Price J P (1989) Intraobserver variation in Doppler ultrasound indices of placental perfusion derived from different numbers of waveforms. Journal of Ultrasound in Medicine 8 197-199

Steel S A, Pearce J M F, Nash G, Christopher B, Dormandy J and Bland J M (1988a) Maternal blood viscosity and uteroplacental blood flow velocity waveforms in normal and complicated pregnancies. British Journal of Obstetrics and Gynaecology 95 747-752.

Steel S A, Pearce J M and Chamberlain G (1988b) Doppler ultrasound of the uteroplacental circulation as a screening test for severe pre-eclampsia with intra-uterine growth retardation. European Journal of Obstetrics, Gynecology and Reproductive Biology 28 279-287

Steel S A, Pearce J M F, Nash G, Christopher B, Dormandy J and Bland J M (1989) Correlation between Doppler flow velocity waveforms and cord blood viscosity. British Journal of Obstetrics and Gynaecology 96 1168-1172.

Stuart B, Drumm J E, Fitzgerald D E and Duignan N M (1980) Fetal blood velocity waveforms in normal pregnancy. British Journal of Obstetrics and Gynaecology 87 780-786

Thomson R S, Trudinger B J and Cook C M (1986) A comparison of Doppler

ultrasound waveform indices in the umbilical artery - I. Indices derived from the maximum velocity waveform. Ultrasound in Medicine and Biology 12 835-844

Thomson R S and Stevens R J (1989) Mathematical model for interpretation of Doppler velocity waveform indices. Medical and Biological Engineering and Computing 27 269-276

Tonge H M, Wladimiroff J W, Noordam M J and van Kooten C (1986) Blood flow velocity waveforms in the descending fetal aorta: comparison between normal and growth retarded pregnancies Obstetrics and Gynecology 67 851-855

Torre V and Paggio T (1984) On edge detection, MIT AI Memo 768

Trudinger B J, Giles W B, Cook C M, Bombardieri J and Collins J (1985a) Fetal umbilical artery flow velocity waveforms and placental resistance: clinical significance. British Journal of Obstetrics and Gynaecology 92 23-30

Trudinger B J, Giles W B and Cook C M (1985b) Flow velocity waveforms in the maternal uteroplacencental and fetal umbilical placental circulation. American Journal of Obstetrics and Gynecology 152 155-163

Trudinger B J, Cook C M, Giles W B, Connelly A and Thompson R S (1987a) Umbilical artery flow velocity waveforms in high risk pregnancy: randomised controlled trial. Lancet i 188-190

Trudinger B J, Stevens D, Connelly A, Hales J R, Alexander G, Bradley L, Fawcett A and Thompson R S (1987b) Umbilical artery flow velocity waveforms and placental resistance: the effects of embolisation of the umbilical circulation.

American Journal of Obstetrics and Gynecology 157 1443-1448

Tyrrell S, Obaid A H and Lilford R J (1989) Umbilical artery Doppler velocimetry as a predictor of fetal hypoxia and acidosis at birth. Obstetrics and Gynecology 74 332-336

Vaitkus P J and Cobbold R S C (1988a) A comparative study and assessment of Doppler ultrasound spectral estimation techniques. Part I: estimation methods. Ultrasound in Medicine and Biology 14 661-672

Vaitkus P J, Cobbold R S C and Johnston K W (1988b) A comparative study and assessment of Doppler ultrasound spectral estimation techniques. Part II: methods and results. Ultrasound in Medicine and Biology 14 673-688

Veille J C and Cohen I (1990) Middle cerebral artery blood flow in normal and growth-retarded fetuses. American Journal of Obstetrics and Gynecology 162 391-396.

Vyas S, Nicolaides K H and Campbell S (1989) Renal artery flow velocity waveforms in normal and hypoxemic fetuses. American Journal of Obstetrics and Gynecology 161 168-172

Warren P S, Gill R W and Garret W J (1988) Doppler assessment of fetal blood flow. In, Fetal and neonatal neurology and neurosurgery, (edited by Levene M I, Bennett M J and Punt J). Churchill-Livingstone, Edinburgh.

Wells P N T (1977) Biomedical ultrasonics. Academic Press, London.

Wemeck M M, Jones N B and Morgan J (1984) Flexible hydraulic simulator for cardiovascular studies. Medical and Biological Engineering and Computing 22 86-89

Wladimiroff J W, Tonge H M and Stewart P A (1986) Doppler ultrasound assessment of cerebral blood flow in the human fetus. British Journal of Obstetrics and Gynecology 93 471-475

Wladimiroff J W, Noordam M J van der Wijngaard J A G W and Hop W C J (1988) Fetal internal carotid and umbilical artery blood flow velocity waveforms as a measure of fetal well-being in intrauterine growth retardation. Pediatrics Research 24 609-612

Woo J S K, Liang S T, Lo R L S, Chan F Y (1987) Middle cerebral artery Doppler flow velocity waveforms. Obstetrics and Gynecology 70 613-616

Yarlgooda P, Willoughby L, Maulik D (1989) Effect of fetal heartrate on umbilical arterial Doppler indices. Journal of Ultrasound in Medicine 8 215-218

Appendix 1. Listings of selected computer programs.

	page
Pump speed and direction control code. . . .	181
Doptek to BBC micro spectrum transfer code. . .	184
Calculation of envelope and PI values. . . .	186
Quality index calculation.	188
Directional filter for Doppler waveforms. . . .	190

```
 10REM  **********     PUMP SPEED AND DIRECTION CONTROL CODE          ********
 20
 30REM  This machine code is used within a main basic programme, which loads
 40REM  a control waveform from disc and converts this to the appropriate
 50REM  input for the machine code. The inputs to the machine code are:-
 60REM      - control waveform data pair values (locations &3000 to end pair)
 70REM      - the end location of the control data pairs (&8A and &8B)
 80REM      - step interval update rate (&85 and &86).
 90REM  The output is a 2 byte number sent every 5ms containing the pump
100REM  speed (top 12 bits) and direction (bottom bit). The output sequence
110REM  is an initial acceleration from zero pump speed to the waveform start
120REM  value, then a repetitive output of the waveform. The programme is
130REM  interrupted by pressing the BREAK key.
140
150
160
170 CLEAR
180LOMEM=&4300
190
200DIMG(500):DIMH(500):DIMCODE% 1200
210IND=&81        :REM index for windup
220INDEX=&78      :REM  memory pointer for data pairs
230FINH=&79       :REM  end of data pairs , set by &8B and &8A from basic prog
240FINL=&80
250ISTH=&70       :REM  start of data pairs
260ISTL=&71
270HINC=&73       :REM intermediate start values for pointer update loop
280LINC=&72
290HVAL=&74       :REM  data pair values;time(us) of step interval (for timer1
300LVAL=&75
310TTWH=&76       :REM  time in us of update of step interval (for timer 2)
320TTWL=&77
330LSTA=&84       :REM  intermediate data pair values for windup loop
340HSTA=&83
350LZER=&8E
360
370FOR C=0TO3 STEP 3
380P%=&2D00
390[OPT C
400               \**************   SETUP   ***********************************
410
420SEI            \inhibit interrupts
430.setup
440LDA #&FF       \set IRB data lines to output
450STA &FE62
460LDA #&0        \disable timer 1, set  timer 2 timed interrupt
470STA &FE6B
480
490LDA #&30       \start of waveform data pairs at &3000
500STA ISTH
510LDA #&0
520STA ISTL
530
540LDA &8B        \set end location of waveform data pairs (&8A and &8B
550STA FINL       \determined from control waveform )
560LDA &8A
570STA FINH
580
590LDA &86        \set step interval update (&86 and &85 determined from
600STA TTWL       \basic programme (nominally set to 5ms)
610LDA &85
620STA TTWH
630
640.windup        \***********  WINDUP PUMP SPEED TO INITIAL VALUE    ******
650
660LDA &3000      \set desired waveform start data pair values
```

```
 670STA HVAL
 680LDA &3001
 690STA LVAL
 700
 710LDA &3001       \make initial output zero (note lowest bit is control bit
 720AND #1          \for direction which is preserved by anding with 1
 730STA LSTA
 740LDA #0
 750STA HSTA
 760
 770LDA LSTA
 780STA LZER
 790
 800LDA HSTA        \if hi byte start value is zero, skip windup loop
 810CMP HVAL
 820BEQ start
 830.winloop
 840
 850LDA #&FF        \start timer 2 (step interval update rate set to &20FF)
 860STA &FE68
 870LDA #&20
 880STA &FE69
 890
 900.readout
 910LDA #224        \set CB2 high
 920STA &FE6C
 930LDA HSTA
 940STA &FE60       \send data pair hi byte
 950LDA #192        \set CB2 low
 960STA &FE6C
 970LDA LSTA
 980STA &FE60       \send data pair lo byte
 990
1000.f1             \look for timer2 timeout, indicating end of interval
1010LDA &FE6D
1020AND #&20
1030BEQ f1
1040
1050LDA LSTA        \load next data pair; increase low data byte by 16
1060ADC #&10         \add 16 to LSTA
1070STA LSTA
1080LDA LSTA
1090CMP LZER
1100BNE f3
1110
1120INC HSTA        \increment hibyte if necessary
1130.f3
1140
1150LDA HSTA
1160CMP HVAL
1170BNE winloop
1180
1190LDA LSTA
1200CMP LVAL
1210BNE winloop
1220
1230                \******** WAVEFORM OUTPUT ***********
1240
1250.start
1260
1270LDA #0          \set index to 0
1280STA INDEX
1290
1300LDA ISTH        \transfer start of data location to HINC,LINC
1310STA HINC
1320LDA ISTL
1330STA LINC
1340
1350.memloop
```

```
1360
1370
1380LDA TTWL       \set timer 2 running (5ms update)
1390STA &FE68
1400LDA TTWH
1410STA &FE69
1420
1430.readout
1440LDA #224       \set CB2 high
1450STA &FE6C
1460LDY INDEX      \load next data pair to control pulse rate on PB7
1470LDA(LINC),Y
1480STA &FE60      \send out hi byte to pump
1490INY
1500LDA #192       \set CB2 low
1510STA &FE6C
1520LDA(LINC),Y
1530STA &FE60      \send out low byte to pump
1540
1550INC INDEX:INC INDEX
1560INY
1570CPY #0
1580BNEgd
1590INC HINC       \increment hibyte location if Y=0
1600.gd
1610
1620.flag2
1630LDA &FE6D      \look for timer 2 timeout,if set end that 5ms batch
1640AND #&20
1650BEQ flag2
1660
1670LDA FINL       \check to see whether end of data pairs is reached- if
1680CMP INDEX      \they have then repeat from start of waveform; else move to
1690BNE memloop    \next data pair
1700LDA FINH
1710CMP HINC
1720BNE memloop
1730
1740JMP start
1750CLI            \reenable interrupts
1760RTS
1770]
1780NEXT
```

```
 10REM*******     DOPTEK TO BBC MICRO SPECTRUM TRANSFER CODE      *******
 20
 30REM  The Doptek spectrum is sent out as sequential spectral lines from
 40REM  an 8 bit parallel port with the following format for each line -
 50REM           byte 0  - marker byte   (&9F)
 60REM           byte 1  - zero line     (&9F)
 70REM           byte 2  - zero line     (&9C)
 80REM           byte 3  - lower channel bin 1
 90REM           byte 4  - upper channel bin 1
100REM           byte 5  - lower channel bin 2
110REM           byte 6  - upper channel bin 2
120REM             :         :       :       :
130REM             :         :       :       :
140REM           byte 158- lower channel bin 79
150REM           byte 159- lower channel bin 79
160REM
170REM  The data is sent out continuously with no hand shaking to the micro
180REM  user port. The machine code routine below stores every alternate byte
190REM  so that only the upper channel is stored. Note that the first byte is
200REM  a marker byte and that the zero line starts with the second stored
210REM  byte. 307 sequential spectral lines are stored in the micro. The
220REM  machine code is called from  a control BASIC program which divides
230REM  each pixel value by 4 giving a range of spectral pixel values from
240REM  0 to 63 (the Doptek has 64 grey levels from 0 to 252 in increments
250REM  of 4). The first 250 sequential lines are saved to disc.
260
270
280FOR C=0 TO 3 STEP 3
290P%=&0E06
300[OPT C
310                \*****************      SETUP       ****************
320LDA #00         \set up user port side B as data input
330LDX #&62
340JSR write
350
360LDA #&10        \disable CB1 interrupt (bit 4 in IER)
370LDX #&6E
380JSR write
390
400LDA #&80
410STA &FE6C
420LDA #&10        \CB1 flag in IFR set on positive edge of CB! input
430STA &FE6C
440
450LDX #&6B        \enable latch on side B (bit 2 in ACR)
460JSR read
470AND #&FD
480ORA #&02
490JSR write
500AND #&60
510JSR read
520
530LDA #&10        \start of data location at &1000
540STA &74
550LDA #&00
560STA &73
570
580LDY #&00        \set up pointers
590LDA #&01
600STA &72
610SEI
620LDY #&00
630                \************     DATA IN LOOP       *****************
640.cbwait
650LDA &FE6D       \wait for CB1 flag to be set by positive input edge on
660AND #&10        \CB1.
670BEQ cbwait
680
690LDA &FE60       \read data on port B - this resets CB1 flag
700STA (&73),Y     \store data
710
```

```
720INC &72          \return for every alternate data point (this ensures
730LDA &72          \that only the upper spectrum is acquired)
740AND #&01
750BNE cbwait
760
770INY              \increment hi and lo byte data pointers and return. Exit
780BNE cbwait
790INC &74
800LDA &74
810CMP #&70
820BNE cbwait
830
840CLI
850RTS
860                 \**************     READ   DATA   SUBROUTINE      ********
870.read
880STX &72          \preserve registers
890STY &71
900LDA #&96         \read from VIA
910JSR &FFF4        \using OSBYTE
920TYA
930LDY &71
940LDX &72          \retrieve registers
950RTS
960                 \**************     WRITE  DATA   SUBROUTINE      ********
970.write
980STA &70          \preserve registers
990STY &71
1000STX &72
1010TAY
1020LDA #&97        \write to VIA
1030JSR &FFF4       \using OSBYTE
1040LDX #&72
1050LDY #&71
1060LDA #&70        \retrieve registers
1070RTS
1080]
1090NEXT
```

```
 10REM   CALCULATION OF ENVELOPE, RI AND PI VALUES FOR CHAPTER 4,6 AND 8.
 20
 30REM   This program estimates the maximum frequency envelope using a
 40REM   threshold method adaptive to the level of background noise. RI
 50REM   and PI are calculated. The envelope is filtered using a DWMTM
 60REM   filter and RI and PI recalculated.
 70
 80
 90
100LOMEM=&30000              :REM  Top of user defined memory space
110
120FMEM%=&20000              :REM  start of spectral data
130PROCdimension             :REM  dimension arrays
140PROCmaxf                  :REM  calculate maximum frequency envelope
150PROCriraw                 :REM  calculate RI and PI for unfiltered envelope
160PROCdwmtm                 :REM  apply DWMTM filter to envelope
170PROCrifilt                :REM  calculate RI and PI for filtered envelope
180END
190
200DEFPROCdimension          :REM  dimension arrays
210DIMSORT%(10)              :REM  intermediate storage array for DWMTM filter
220DIMRI(10)                 :REM  array for RI from unfiltered data
230DIMPi(10)                 :REM  array for PI from filtered data
240DIMRIF(10)                :REM  array for RI from unfiltered data
250DIMPiF(10)                :REM  array for PI from filtered data
260DIM ENV% 250              :REM  array for envelopes
270DIM ENT% 250              :REM  intermediate storage array for DWMTM filter
280DIMB% 10                  :REM  array for waveform start locations
290ENDPROC
300
310DEFPROCbg                 :REM  calculate mean background noise level in a
320BL%=0                     :REM  6*5 window at the high frequency spectrum
330FORN%=75TO79:FORM%=-5 TO 0
340LM%=FMEM%+(L%+M%)*80+N%
350BL%=BL%+?LM%
360NEXT:NEXT
370BL=BL%/30
380ENDPROC
390
400DEFPROCmaxf               :REM  calculate maximum frequency using a
410                          :REM  threshold method adaptive to the level
420                          :REM  of background noise
430GCOL0,0 TINT 0:MOVE0,0:MOVE630,0:PLOT85,0,1023:PLOT85,630,1023
440GCOL0,63
450FORL%=0 TO 240
460LMEM%=FMEM%+L%*80         :REM  240 spectral lines
470PMAX%=1
480PROCbg                    :REM  find mean background noise level
490THR=BL*3.3333+10          :REM  adaptive threshold
500IF BL<1 THR=8*SQR(BL)+5
510FORN%=79TO1STEP-1         :REM  find maximum frequency for line L%
520MEM%=LMEM%+N%
530IF?MEM%>THR PMAX%=N%:N%=1
540NEXT
550?(ENV%+L%)=PMAX%-1:PLOT69,?(ENV%+L%)*8+648,1023-L%*4
560NEXT
570ENDPROC
580
590DEFPROCriraw              :REM  calculate RI and PI for unfiltered envelope
600FORE%=0TO(NW%-1)          :REM  number of waveforms is NW%
610ST%=(255-?(B%+E%))        :REM  start location of waveform envelope
620MAX=0:MIN=32000:MEAN=0
630FORI%=0TOLAN%             :REM  LAN% is number of points
640IF ?(ENV%+I%+ST%)>MAX:MAX=?(ENV%+I%+ST%)
650IF ?(ENV%+I%+ST%)<MIN:MIN=?(ENV%+I%+ST%)
660MEAN=MEAN+?(ENV%+I%+ST%)
670NEXT
680MEAN=MEAN/(LAN%+1)
690RI(E%)=(MAX-MIN)/MAX
700Pi(E%)=(MAX-MIN)/MEAN
710NEXT
720ENDPROC
```

```
730
740DEFPROCdwmtm              :REM  apply 5 point DWMTM filter to envelope
750FORI=0TO245:?(ENT%+I)=?(ENV%+I):NEXT
760THR=10                    :REM  threshold is 10
770FORI%=2TO240              :REM  spectral lines 2 to 240
780
790G%=0
800SORT%(1)=?(ENT%+I%-2)     :REM  store current values in array (5 point)
810SORT%(2)=?(ENT%+I%-1)
820SORT%(3)=?(ENT%+I%)
830SORT%(4)=?(ENT%+I%+1)
840SORT%(5)=?(ENT%+I%+2)
850
860FORK%=1 TO 3              :REM calculate median
870MIN%=32000
880FORL%=K% TO 5
890IF SORT%(L%)<MIN% MIN%=SORT%(L%):MINPOS%=L%
900NEXT
910SORT%(MINPOS%)=SORT%(K%):SORT%(K%)=MIN%
920NEXT
930MED%=SORT%(3)
940
950ISUM=0:ICOUNT=0           :REM  find mean value of elements in range
960FORL%=1TO5                :REM  median-threshold to median+threshold
970IPIX%=SORT%(L%)
980IDIF=ABS(MED%-IPIX%)
990IF IDIF>THR GOTO1020
1000ISUM=ISUM+IPIX%
1010ICOUNT=ICOUNT+1
1020NEXT
1030VC=ISUM/ICOUNT           :REM  filter output
1040?(ENV%+I%)=VC+0.5        :REM  store including 0.5 for rounding
1050NEXT
1060ENDPROC
1070
1080DEFPROCrifilt            :REM  calculate RI and PI for DWMTM filtered
1090                         :REM  envelope
1100FORE%=0TO(NW%-1)         :REM  number of waveforms is NW%
1110
1120STP%=(255-?(B%+E%))+5
1130EN%=STP%+15
1140MAX=0
1150FORI%=STP% TO EN%
1160IF ?(ENV%+I%)>MAX:MAX=?(ENV%+I%)
1170NEXT
1180ST%=(255-?(B%+E%))
1190MEAN=0
1200FORI%=0TOLAN%
1210MEAN=MEAN+?(ENV%+I%+ST%)
1220NEXT
1230MEAN=MEAN/(LAN%+1)
1240
1250MIN=3200000
1260EN%=ST%+LAN%
1270FORI%=EN%-7 TO EN%
1280IF ?(ENV%+I%)<MIN MIN=?(ENV%+I%)
1290NEXT
1300
1310RI(E%)=(MAX-MIN)/MAX
1320Pi(E%)=(MAX-MIN)/MEAN
1330NEXT
1340ENDPROC
```

```
 10REM          QUALITY INDEX CALCULATION
 20
 30REM  This programme calculates the quality indices from the estimated
 40REM  envelope and is used in chapters 7,8 and 9.
 50
 60
 70LOMEM=&30000                :REM  top of user defined memory space
 80FMEM%=&20000                :REM  start of spectral data
 90
100PROCdimension               :REM  dimension arrays
110PROCqual1                   :REM  calculate first quality index (QI1)
120PROCqual2                   :REM  calculate second quality index (QI2)
130PROCqual3                   :REM  calculate third quality index (QI3)
140END
150
160DEFPROCdimension                :REM  dimension arrays
170DIMQI3(20)                      :REM  array for spectral ratio (QI3)
180DIMQI1(20)                      :REM  array for paired correlation (QI1)
190DIMQI2(20)                      :REM  array for linearity measure (QI2)
200DIMH1(120):DIMR(120):DIMC(120)  :REM  arrays used in Fourier transform
210DIM ENV% 250                    :REM  array for envelope
220DIMWST%(20)                     :REM  array for waveform starts
230ENDPROC
240
250DEFPROCqi1                      :REM  calculate first quality index (QI1)
260FORJ%=0TO(NW%-2)                :REM  no. pairs waveforms is NW%-1
270ST1%=WST%(J%):EN1%=WST%(J%+1)
280N1%=EN1%-ST1%+1                 :REM  no. points for first waveform
290ST2%=WST%(J%+1):EN2%=WST%(J%+2)
300N2%=EN2%-ST2%+1                 :REM  no. points for second waveform
310N%=N1%:IFN2%<N1%:N%=N2%        :REM  correlate over smallest of N1% and N2%
320MAAX%=0:MAAX2%=0:PMAAX%=0:PMAAX2%=0:MMX=0:MMX2=0
330
340FORI%=5TO15                   :REM  find peak values at 50-150ms from start
350X1=?(ENV%+ST1%+I%)            :REM  for each of the pair of waveforms
360X2=?(ENV%+ST2%+I%)
370IF X2>MAAX2%:MAAX2%=X2:PMAAX2%=I%
380IF X1>MAAX%:MAAX%=X1:PMAAX%=I%
390NEXT
400FORI%= (PMAAX%-2) TO (PMAAX%+2)  :REM  max value of first waveform taken
410MMX=MMX+?(ENV%+ST1%+I%)          :REM  as mean of 5 elements around peak
420NEXT
430FORI%= (PMAAX2%-2) TO (PMAAX2%+2):REM  max value of second waveform taken
440MMX2=MMX2+?(ENV%+ST2%+I%)        :REM  as mean of 5 elements around peak
450NEXT
460MMX=MMX/5:MMX2=MMX2/5
470MENX=(MMX+MMX2)/2                :REM  max value for normalisation taken
480                                 :REM  as average of maxima of the pair
490DSUM=0
500FORI%=0TO(N%-1)                  :REM  sum all residual paired differences
510DSUM=DSUM+ABS(?(ENV%+ST1%+I%)-?(ENV%+ST2%+I%))
520NEXT
530QI1(J%)=(DSUM/MENX)*(50/N%)      :REM  calculate QI1 normalising for the
540                                 :REM  max height and waveform length
550NEXT
560ENDPROC
570
580DEFPROCqi2                       :REM  calculate second quality index QI2
590FORJ%=0TONW%-1
600ST%=WST%(J%):EN%=WST%(J%+1):N%=EN%-ST%+1 :REM  no. points of envelope
610MAAX=0:PMAAX=0:MMX=0
620FOR I%=5 TO 15                   :REM  find peak as for QI1
630X2=?(ENV%+ST%+I%)
640IF X2>MAAX:MAAX=X2:PMAAX=I%
650NEXT
660FORI%=(PMAAX-2) TO (PMAAX+2)     :REM  find max as mean of 5 elements
670MMX=MMX+?(ENV%+ST%+I%)
680NEXT
690MMX=MMX/5
700
```

```
710CDIF=0:SDIF=0:SSM=0
720FORI%=1TO(N%-2)                    :REM  QI1 calculated from point 1 to N%-2
730X1=?(ENV%+ST%+I%-1)               :REM  sum local linearity measures
740X2=?(ENV%+ST%+I%)
750X3=?(ENV%+ST%+I%+1)
760SSM=SSM+X2
770PDIF=ABS(X1+X3-2*X2)
780SDIF=SDIF+PDIF
790NEXT
800SSM=SSM+?(ENV%+ST%)+?(ENV%+ST%+N%-1)
810QI2(J%)=(SDIF/MMX)*(50/N%)         :REM  calculate QI1 normalising for max
820                                   :REM  and for waveform length
830NEXT
840ENDPROC
850
860DEFPROCqi3                         :REM  calculate third quality index (QI3)
870NF%=111                            :REM  111 points for transform (1.11 secs)
880FORJ%=0 TO NW%-1
890ST%=WST%(J):EN%=WST%(J+1)
900FORG%=0TOLAN%:H1(G%)=?(ENV%+ST%+G%):NEXT   :REM transfer data to work array
910FORH%=G%TONF%:H1(H%)=0:NEXT                :REM and perform zero padding
920PROCwindow                                 :REM apply Hanning window to
930                                           :REM reduce spectral leakage
940PROCfortran                                :REM calculate Fourier transform
950PROCpower                                  :REM calculate spectral ratios
960NEXT
970ENDPROC
980
990DEFPROCwindow          :REM apply Hanning window to reduce spectral leakage
1000NPT%=EN%-ST%+1
1010MP%=NPT%/2
1020NT%=NPT%-1:NM=NT%DIV2+0.5
1030NM%=NT%/2
1040FORI=-MP%TO(NT%-MP%)
1050H1(I+MP%)=0.5*(1-COS(2*PI*(I-MP%)/NT%))*H1(I+MP%)
1060NEXT
1070ENDPROC
1080
1090DEFPROCfortran        :REM  calculate Fourier transform
1100NPT%=NF%
1110MP%=NPT%/2
1120NT%=NPT%-1:NM=NT%DIV2+0.5
1130NM%=NT%/2
1140T=2*PI/NPT%
1150FORK%=-MP% TO (NT%-MP%)
1160R=0:C=0
1170Q=T*K%
1180FORN%=-MP% TO (NT%-MP%)
1190P=Q*N%
1200R=R+H1(N%+MP%)*COS(P)
1210C=C+(-1)*H1(N%+MP%)*SIN(P)
1220NEXT
1230R(K%+MP%)=R                               :REM  real part
1240C(K%+MP%)=C                               :REM  complex part
1250NEXT
1260FORI=0TONF%:H1(I)=SQR(R(I)^2+C(I)^2):NEXT   :REM power spectrum
1270ENDPROC
1280
1290DEFPROCpower                  :REM  calculate spectral ratio
1300THR=10                        :REM  threshold is 10th harmonic
1310LSUM=0:USUM=0
1320FORI=0TONPT%
1330T=ABS(I-MP%)
1340IF T<=THR LSUM=LSUM+H1(I)
1350IF T>THR USUM=USUM+H1(I)
1360NEXT
1370TT=LSUM+USUM
1380QI3(J%)=(USUM/TT)             :REM  store spectral ratio
1390ENDPROC
```

```
 10REM***********     DIRECTIONAL FILTER FOR DOPPLER WAVEFORMS      *******
 20
 30REM  This is the optimal directional filter described in chapter 5 and
 40REM  used in chapters 6 and 8. The filter parameter C(d) is 1+R(d)/SL(d)
 50REM  This filter acts on a Doppler spectrum of 240 lines to give a
 60REM  spectrum of 230 lines. The raw spectrum is stored as a sequential
 70REM  byte array in memory from &22000 and the filtered spectrum from
 80REM  &15000.
 90
100
110LOMEM=&30000                :REM   top of user defined memory space
120PROCdimension               :REM   dimension arrays
130PROCsetup                   :REM   setup data files etc.
140PROCload                    :REM   load waveform from disc
150PROCdisp                    :REM   display waveform
160PROCadfilt                  :REM   filter waveform
170PROCsave                    :REM   save filtered waveform
180END
190
200
210DEFPROCdimension            :REM   dimension arrays
220DIMMAT%(9,9)                :REM   intermediate array for raw data
230DIMP(64)                    :REM   pallette, for video output to B/W monitor
240DIMT(64)                    :REM   through combined colour video adaptor.
250DIMSL(8)                    :REM   directional slope - 8 directions
260DIMSF(8)                    :REM   directional sum - 8 directions
270DIMCR(6)                    :REM   cfs for slope calc
280DIMX(8):DIMY(8)             :REM   cfs for slope calc
290DIMRA(8)                    :REM   local image measure - 8 directions
300DIMFW%(80)                  :REM   window size along frequency
310DIMTW%(80)                  :REM   window size along time
320DIMN(10)                    :REM   cfs for slope calc
330DIMD(10)                    :REM   cfs for slope calc
340DIMR(8)                     :REM   edge parameter - 8 directions
350ENDPROC
360
370DEFPROCsetup                :REM setup data files etc.
380MODE10                      :REM graphics mode
390@%=&20204                   :REM printer format
400CLOSE #0                    :REM close any open files
410LMEM%=&15000                :REM start of 2 blocks of memory for
420HMEM%=&22000                :REM raw data and filtered data
430PROCdata                    :REM angular correction factors for slope
440PROCconst                   :REM correction factors dependent on window size
450PROCconstants               :REM cfs for slope calculation
460PROCwind                    :REM window sizes as a function of frequency
470PROCloadpalet               :REM load 64 level pallette for B/W display
480ENDPROC
490
500DEFPROCdata                  :REM    angular correction factors for slope
510X(1)=1
520X(2)=COS(22.5*PI/180)        :REM    Factors account for increased distance
530X(3)=X(2)                    :REM    between adjacent pixels moving not
540X(4)=COS(45*PI/180)          :REM    horizontally or vertically.
550X(5)=X(4)
560X(6)=COS(77.5*PI/180)
570X(7)=X(6)
580X(8)=0
590SX=0:SXX=0
600FORI=1TO8:SX=SX+X(I):SXX=SXX+X(I)^2:NEXT
610ENDPROC
620
630DEFPROCconst                 :REM    correction factors dependent on window
640TH=22.5:TH=TH*PI/180         :REM    size (size changes at top and bottom).
650CR(1)=3*TAN(TH)+3.5          :REM    5 by 5
660CR(2)=3.5-3*TAN(TH)          :REM    5 by 5
670CR(3)=4*TAN(TH)+4.5          :REM    7 by 7
680CR(4)=4.5-4*TAN(TH)          :REM    7 by 7
690CR(5)=5*TAN(TH)+5.5          :REM    9 by 9
700CR(6)=5.5-5*TAN(TH)          :REM    9 by 9
710C3=TAN(TH)
720ENDPROC
```

```
 750DEFPROCconstants            :REM    cfs for slope calculation
 760N(1)=3                      :REM    5 by 5
 770N(2)=2.5                    :REM    5 by 5
 780N(3)=4                      :REM    7 by 7
 790N(4)=3.5                    :REM    7 by 7
 800N(5)=5                      :REM    9 by 9
 810N(6)=4.5                    :REM    9 by 9
 820D(1)=10                     :REM    5 by 5
 830D(2)=5                      :REM    5 by 5
 840D(3)=28                     :REM    7 by 7
 850D(4)=17.5                   :REM    7 by 7
 860D(5)=60                     :REM    9 by 9
 870D(6)=42                     :REM    9 by 9
 880ENDPROC
 890
 900DEFPROCwind                 :REM  window sizes as a function of frequency
 910                            :REM  bin number (to account for image edges)
 920TW%(2)=3:FW%(2)=3
 930TW%(3)=3:FW%(3)=3
 940TW%(4)=3:FW%(4)=3           :REM  reduction in window size in both
 950TW%(5)=5:FW%(5)=5           :REM  directions near baseline to preseve
 960TW%(6)=7:FW%(6)=7           :REM  details
 970
 980FORJ%=7 TO 75
 990TW%(J%)=9:FW%(J%)=9         :REM  9 by 9 window
1000NEXT
1010
1020TW%(76)=7:FW%(76)=7         :REM  reduction in window size along frequency
1030TW%(77)=9:FW%(77)=5         :REM  but high window size along time to get
1040TW%(78)=9:FW%(78)=3         :REM  maximum possible reduction of BG noise.
1050TW%(79)=9:FW%(79)=1
1060ENDPROC
1070
1080DEFPROCadfilt                      :REM  directional filter
1090TH=22.5:TH=TH*PI/180             :REM  22.5 degrees between directions
1100
1110FORI%=0TO240                     :REM  set baseline values to zero
1120?(HMEM%+I%*80)=?(HMEM%+I%*80+79)
1130?(HMEM%+I%*80)=0
1140?(HMEM%+I%*80+1)=0
1150NEXT
1160
1170                                  :REM *******     filter loop  ******
1180FOR I%=5TO235                     :REM  5 to 235 along time axis
1190
1200PRINTTAB(0,0);I%;"    "
1210FOR J%=0TO79                      :REM  0 to 79 along frequency axis
1220PRINTTAB(0,2);J%;"  "
1230IFJ%=0 L%=63:GOTO2650             :REM  no filter for J%=0 or 1
1240IFJ%=1 L%=0::GOTO2650
1250TW%=TW%(J%):FW%=FW%(J%)           :REM  set window sizes and
1260TMA%=(TW%+1)/2                    :REM  associated variables
1270FMA%=(FW%+1)/2
1280W%=FW%:MA%=FMA%
1290IFW%=5:N1=1:N2=2
1300IFW%=7:N1=3:N2=4
1310IFW%=9:N1=5:N2=6
1320                                   :REM *****    Transfer data from
1330SM=0:N=0                           :REM *****    memory to array
1340N%=HMEM%+(I%-TMA%)*80+(J%-FMA%)
1350FORK%=1 TO TW%
1360M%=N%+K%*80
1370FORL%=1 TO FW%
1380MAT%(K%,L%)=?(M%+L%)
1390SM=SM+MAT%(K%,L%):N=N+1
1400NEXT
1410NEXT
1420SM=SM/N
1430IF SM=0 L%=0:GOTO2650              :REM  if no data set ouput to zero
1440
1450IF J%<=4 OR J%>=77:L%=SM:GOTO2650  :REM  take mean at top and bottom
1460
```

```
1470                                    :REM ******   Calculate directional
1480                                    :REM ******   slope and mean for
1490SFT=0:SF=0                          :REM ******   8 directions
1500FORK%=1TOW%
1510V=(MAT%(MA%,K%)+MAT%((MA%-1),K%)+MAT%((MA%+1),K%))/3
1520SF=SF+V
1530SFT=SFT+K%*V
1540NEXT
1550SL(5)=ABS((SFT-N(N1)*SF)/D(N1))
1560SF(5)=SF/W%
1570
1580SFT=0:SF=0
1590FORL%=1TOW%
1600V=(MAT%(L%,MA%)+MAT%(L%,(MA%-1))+MAT%(L%,(MA%+1)))/3
1610SF=SF+V
1620SFT=SFT+L%*V
1630NEXT
1640SL(1)=ABS((SFT-N(N1)*SF)/D(N1))
1650SF(1)=SF/W%
1660
1670SFT=0:SF=0
1680FORK%=1TO(W%-1)
1690L%=K%
1700V=(MAT%(L%,K%)+MAT%(L%,K%+1)+MAT%(L%+1,K%))/3
1710SF=SF+V
1720SFT=SFT+K%*V
1730NEXT
1740SL(3)=X(4)*ABS((SFT-N(N2)*SF)/D(N2))
1750SF(3)=SF/(W%-1)
1760
1770SFT=0:SF=0
1780FORK%=1TO(W%-1)
1790L%=(W%+1)-K%
1800V=(MAT%(L%,K%)+MAT%(L%-1,K%)+MAT%(L%,K%+1))/3
1810SF=SF+V
1820SFT=SFT+K%*V
1830NEXT
1840SL(7)=X(4)*ABS((SFT-N(N2)*SF)/D(N2))
1850SF(7)=SF/(W%-1)
1860
1870SFT=0:SF=0
1880FORL%=1TOW%
1890K%=INT(L%*C3+CR(N2))
1900V=(MAT%(L%,K%)+MAT%(L%,K%-1)+MAT%(L%,K%+1))/3
1910SF=SF+V
1920SFT=SFT+L%*V
1930NEXT
1940SL(2)=X(2)*ABS((SFT-N(N1)*SF)/D(N1))
1950SF(2)=SF/W%
1960
1970SFT=0:SF=0
1980FORL%=1TOW%
1990K%=INT(CR(N1)-L%*C3)
2000V=(MAT%(L%,K%)+MAT%(L%,K%-1)+MAT%(L%,K%+1))/3
2010SF=SF+V
2020SFT=SFT+L%*V
2030NEXT
2040SL(8)=X(2)*ABS((SFT-N(N1)*SF)/D(N1))
2050SF(8)=SF/W%
2060
2070SFT=0:SF=0
2080FORK%=1TO W%
2090L%=INT(K%*C3+CR(N2))
2100V=(MAT%(L%,K%)+MAT%(L%+1,K%)+MAT%(L%-1,K%))/3
2110SF=SF+V
2120SFT=SFT+K%*V
2130NEXT
2140SL(4)=X(2)*ABS((SFT-N(N1)*SF)/D(N1))
2150SF(4)=SF/W%
2160
```

```
2170SFT=0:SF=0
2180FORK%=1TO W%
2190L%=INT(CR(N1)-K%*C3)
2200V=(MAT%(L%,K%)+MAT%(L%+1,K%)+MAT%(L%-1,K%))/3
2210SF=SF+V
2220SFT=SFT+K%*V
2230NEXT
2240SL(6)=X(2)*ABS((SFT-N(N1)*SF)/D(N1))
2250SF(6)=SF/W%
2260
2270
2280SL=0:SLMAX=0                          :REM  calculate sum of slopes
2290FORI=1TO8
2300SL=SL+SL(I)
2310IF SL(I)<0.5 SL(I)=0.5
2320NEXT
2330
2340SMAX=0:PMAX=0
2350FORI=1TO8
2360IF SF(I)>SMAX SMAX=SF(I):PMAX=I
2370NEXT
2380
2390                                       :REM *****  Calculate edge parameter
2400                                       :REM *****  R(I) for 8 directions.
2410FORI=1TO8
2420IF I>=3 AND I<=7 TH=(5-I)*22.5:PROCone
2430IFI=1 TH=0:PROCtwo
2440IF I=2 TH=22.5:PROCtwo
2450IF I=8 TH=-22.5:PROCtwo
2460IF B1=0 AND B2=0 B=0:GOTO2480
2470B=2*B1*B2/(B1+B2)
2480R(I)=SF(I)-1.5*B
2490IFR(I)<0 R(I)=0
2500NEXT
2510
2520FORI=1TO8                            :REM  calculate local image measures
2530RA(I)=1+R(I)/SL(I)
2540NEXT
2550
2560MD=0:MN=0                            :REM calculate filter output
2570FORI=1TO8
2580MD=MD+(RA(I)+0.001)*SF(I)
2590MN=MN+RA(I)+0.001
2600NEXT
2610L%=(MD/MN)+0.5                       :REM add 0.5 for rounding
2620
2630IFL%>63 L%=63
2640IFL%<0 L%=0
2650?(LMEM%+I%*80+J%)=L%                 :REM  store directly in memory
2660GCOL0,P(L%) TINT 0
2670YP%=1023-I%*4
2680XP%=640+J%*8
2690PLOT69,XP%,YP%                       :REM  display data point
2700FORI=1TO8:SL(I)=0:NEXT
2710NEXT:NEXT
2720ENDPROC
2730
2740DEFPROCone                        :REM  calculate edge parameter (I=3-7)
2750TH=TH*PI/180
2760SM1=0:SM2=0:NN1=0:NN2=0
2770FORK%=W%TO1 STEP -1
2780XM=INT((K%-MA%)*TAN(TH)+MA%+0.5)-1
2790XM2=XM+2
2800IF XM<1GOTO 2840
2810FORL%=1TOW%
2820IF L%<XM SM1=SM1+MAT%(L%,K%):NN1=NN1+1
2830NEXT
2840IFXM2>W% GOTO2880
2850FORL%=1TOW%
2860IF L%>XM2 SM2=SM2+MAT%(L%,K%):NN2=NN2+1
2870NEXT
2880NEXT
2890B1=SM1/NN1
2900B2=SM2/NN2
2910ENDPROC
```

```
2930DEFPROCtwo                          :REM  calculate edge parameter (I=1,2 or 8)
2940TH=TH*PI/180
2950SM1=0:SM2=0:NN1=0:NN2=0
2960FORL%=W%TO1 STEP -1
2970YM=INT((L%-MA%)*TAN(TH)+MA%+0.5)-1
2980YM2=YM+2
2990IF YM<1GOTO 3030
3000FORK%=1TOW%
3010IF K%<YM SM1=SM1+MAT%(L%,K%):NN1=NN1+1:REMPRINTTAB(K%*4);K%;" ";
3020NEXT
3030IFYM2>W% GOTO3070
3040FORK%=1TOW%
3050IF K%>YM2 SM2=SM2+MAT%(L%,K%):NN2=NN2+1:REMPRINTTAB(K%*4);K%;" ";
3060NEXT
3070REMPRINT
3080NEXT
3090B1=SM1/NN1
3100B2=SM2/NN2
3110ENDPROC
3120
3130DEFPROCdisp                    :REM  display unfiltered waveform
3140CLS
3150FORX%=0TO 240
3160PRINTTAB(0,0);X%;"  "
3170FORY%=0TO79
3180I%=?(HMEM%+X%*80+Y%)
3190GCOL0,P(I%) TINT 0
3200YP%=1023-X%*4
3210XP%=640+Y%*8
3220PLOT69,XP%,YP%
3230NEXT:NEXT
3240ENDPROC
3250
3260DEFPROCloadpalet          :REM   load 64 level pallette for B/W display
3270N$=":4.$.SPEC.COLS"
3280X=OPENIN N$
3290FORI=0TO63
3300INPUT #X,P(I)
3310NEXT
3320CLOSE #X
3330ENDPROC
3340
3350DEFPROCload                :REM    load waveform from disc
3360PRINTTAB(0,0);"LOAD"
3370INPUT TAB(0,10);"DRIVE -";D$
3380M$="*MOUNT "+D$
3390OSCLI M$
3400D$="*DRIVE "+D$
3410OSCLI D$
3420PRINTTAB(0,12);"ID - "
3430INPUTTAB(0,13);ID$
3440F$="*LOAD "+ID$+" "+STR$~(&22000)
3450 OSCLI F$
3460ENDPROC
3470
3480DEFPROCsave                :REM    save filtered data to disc
3490PRINTTAB(0,0);"SAVE"
3500INPUT TAB(0,10);"DRIVE -";D$
3510MM$="*MOUNT "+D$
3520OSCLI MM$
3530M$="*DRIVE "+D$
3540OSCLI M$
3550PRINTTAB(0,28);"ID - ";ID$
3560INPUTTAB(0,29);ID$
3570F$="*SAVE"+ID$+" "+STR$~(&15000)+" "+STR$~(&19E20)
3580OSCLI F$
3590ENDPROC
```

Appendix 2. Publications.

A2.1 Published papers.

Hoskins P R, Anderson T and McDicken W N (1989) A computer controlled flow phantom for generation of physiological Doppler waveforms. Physics in Medicine and Biology 34 1709-1717

Hoskins P R, Loupas T and McDicken W N (1990) A comparison of the Doppler spectra from human blood and artificial blood used in a flow phantom. Ultrasound in Medicine and Biology 16 141-147

Hoskins P R, Loupas T and McDicken W N (1990) A comparison of three different filters for speckle reduction of Doppler spectra. Ultrasound in Medicine and Biology 16 375-389

A2.2 Papers accepted in final form but not yet published.

Hoskins P R, Loupas T and McDicken W N An investigation of simulated umbilical artery Doppler waveforms I. The effect of 3 physical parameters on the maximum frequency envelope and on pulsatility index. Ultrasound in Medicine and Biology

Hoskins P R An investigation of simulated umbilical artery Doppler waveforms II. A comparison of three Doppler waveform quality indices. Ultrasound in Medicine and Biology

Phys. Med. Biol., 1989, Vol. 34, No 11, 1709-1717. Printed in the UK

A computer controlled flow phantom for generation of physiological Doppler waveforms

P R Hoskins, T Anderson and W N McDicken

Department of Medical Physics and Medical Engineering, Royal Infirmary, Edinburgh, UK

Abstract. A flow phantom for the generation of physiological Doppler waveforms is described. The suspension of scattering particles is driven by a gear pump powered by a stepping motor. The speed of the stepping motor is controlled by a BBC microcomputer. The waveform shape is selected from a library of waveforms from disc. Use of the microcomputer allows the waveform shape and mean flow to be easily changed. Sephadex particles suspended in a solution of glycerol were used as artificial blood. Thin walled heat shrink tubing which had been moulded around metal rods was used. Distortions in the waveforms caused by reflections from the end of the tubing were largely removed by reducing the pipe diameter to half of its value for 30 cm from the end of the pipe. There was good agreement between the control waveforms and the Doppler waveforms over a wide range of waveform pulsatility.

1. Introduction

The field of Doppler ultrasound can be split into those techniques concerned with interpretation of waveform spectra, techniques of volume flow measurement and more recently colour flow visualisation. Both the qualitative features and the quantitative measurements made in these areas will be influenced by often complex underlying physical processes. For example it is known that the spectral content of Doppler waveforms is strongly influenced by the relative geometry of the ultrasound beam and the vessel (Evans 1982, Cobbold *et al* 1983), by the vessel geometry (Philips *et al* 1983) and by disease (Walton *et al* 1984, Hames *et al* 1985a, b).

A physiological flow phantom would therefore have the following uses.

1. Waveform analysis: testing of maximum frequency followers; testing spectral broadening indices (e.g. in carotids); testing indices of waveform quality.

2. Volume flow: calibration of equipment; testing methods of volume flow measurement.

3. Quality control: monitoring changes in performance of an operator and permitting comparison of different operators.

4. Teaching: for example to allow the operator to see for himself the effect of changes in beam-vessel angle.

Desirable features of a physiological flow phantom are to generate reproducibly a wide variety of waveform shapes in such a manner that the waveform shape can easily be changed. Many of the early systems described lack these facilities. These are described in Law *et al* (1987). Flow phantoms with the ability to change waveform shape are described by a number of authors (Issartier *et al* 1978, Wemeck *et al* 1984, Peterson 1984, McCarty and Locke 1986, Law *et al* 1987). The performance of these systems in generating a wide variety of waveform shapes is however not reported. This paper describes the construction and evaluation of a computer controlled flow phantom for generation of physiological waveforms, in particular waveforms as observed in the umbilical and arcuate/uterine arteries.

0031-9155/89/111709+09$02.50

2. Flow phantom

It would be difficult and time consuming to model physically the physiological circulation consisting of a beating heart and a system of bifurcating tubes. The chosen approach was the commonly used one whereby the waveform shape is controlled by a variable flow pump. The pump used was a gear pump (model 120-040, Micropump Corp, Concord, California, USA). This model delivers 0.316 ml per revolution. Previously we had used a larger gear pump delivering 1.73 ml per revolution. However it was found that for the smallest of the vessels of interest, at the desired flow rates, the pump was unstable, producing a ripple on the Doppler signal associated with the action of the teeth (figure 1). No such problems existed with the smaller pump.

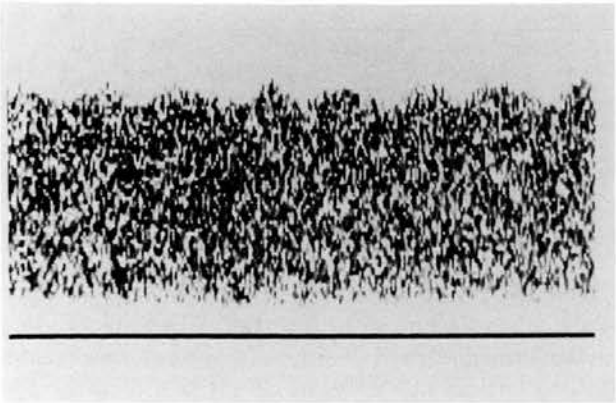

Figure 1. Unstable flow at low flow rates for a high output gear pump. The ripple is caused by the action of the teeth of the gears.

The tubing used must be relatively stiff. If very elastic tubing is used there are problems of kinking. We have also observed that there are large changes in waveform shape along the length of an elastic tube. This is thought to be due to reflected pressure waves from the end of the tube. This is discussed later. For the tubing which was insonated transparent heat shrink tubing was used. This was moulded around rods of known diameter as described in McDicken (1986). Pipes of internal diameters of 3 and 6 mm were made. These have wall thicknesses of 0.36 and 0.50 mm respectively. Other connecting pieces of tubing were made of PVC. There was no visible change in diameter of the tubing as assessed during pulsatile flow with an Acuson 128 scanner. The length of the insonation vessel was made large enough to produce stable flow conditions at the point of insonation. The inlet length L for pulsatile flow is quoted as

$$L = 0.04\, d\, Re \quad \text{(McDonald 1974)} \tag{1}$$

where L is the pipe length, d is the pipe diameter, Re is the Reynolds number.

L can also be expressed in terms of the mean flow rate Q. This expression is independent of the tube diameter d.

$$L = \frac{0.16}{\pi} \frac{\rho}{\mu} Q \tag{2}$$

where ρ is the fluid density, μ is the viscosity.

For the solution used, $\rho = 1.1 \times 10^3$ kgm^{-3} and $\mu = 0.004$ kgm^{-1} s^{-1}. If Q is expressed in ml min^{-1}, this gives

$$L = 1.7507 \times 10^{-2} Q \tag{3}$$

If the upper value of Q is for example 1000 ml min^{-1}, L is 17.5 cm; for $Q =$ 2000 ml min^{-1}, L is 35 cm. The pipes used in this study were all 35 cm or more long.

The blood substitute used was a suspension of Sephadex particles (type G25, Pharmacia, Uppsala, Sweden) in a mixture of glycerol and water, as described by McDicken (1986). Blood is a non-Newtonian fluid, however McDonald (1974) states that the effects of non-Newtonian behaviour at high shear rates are important only in small vessels of arteriolar dimension. Following Pedley (1980) we take blood to be a Newtonian fluid of viscosity 0.004 kgm^{-1} s^{-1}. A mixture of 42:58% glycerol:water by mass gives a viscosity of 0.004 kgm^{-1} s^{-1} at 20 °C (CRC Handbook of Chemistry and Physics 1985).

The sephadex particles were used to mimic the red blood cells. These particles were mixed with the water/glycerol solution and heated at 85 °C for 2 to 3 h to give complete swelling, and also to remove dissolved air. The diameter of the swollen particles is approximately 20 to 70 μm. These are large compared to red cells which have linear dimensions of 2.4 by 8.5 μm, and an average volume of 87 μm^3.

The Doppler signal from a suspension of particles results from the combination of the ultrasound scattered from each particle. If the scatterer concentration is low, the particles can be considered as point scatterers, with no volume; that is, the scatterers are non-interacting. Blood is a densely packed suspension of red cells. The average distance between two red cells is only about 10% of its diameter, for a haematocrit of 45% (Shung *et al* 1976). In this situation the red cells cannot be considered as non-interacting. Theoretical modelling of the Doppler signal from blood taken as a suspension of interacting scatterers has been performed by a number of authors (Atkinson and Berry 1974, Shung 1982, Mo and Cobbold 1986). Angelson (1980) treated blood as a continuum and therefore bypassed the interaction. For blood, the Doppler shifted signal arises from fluctuations in red cell concentration in the sample volume. The fluctuating nature of this signal gives rise to the characteristic speckle pattern of the Doppler spectrum. If work is performed using a flow phantom to investigate aspects of the Doppler spectrum connected with the speckle pattern, then a detailed comparison of the statistical properties of the test scatterer solution and blood is required. This is beyond the scope of this publication. For work concerned mainly with the waveform outline, we have found that a relatively weak suspension of 40 g in 2 l which is 10% by volume of particles, gives an adequately strong Doppler signal.

It is known that gear pumps will cause damage to the sephadex particles; however this damage as observed by a microscope is small after several hours use. A magnetic stirrer was used to keep the particles in suspension.

A block diagram of the system is shown in figure 2. The pump was powered using a stepping motor. The stepping motor speed was controlled using a microcomputer (Acorn BBC master 128) to produce the desired waveform. The waveform shapes used were generated by hand using a tracker ball and stored to disc. The control digital output from the microcomputer could be varied over the range 0 to 4095. A new value of the waveform shape was sent every 5 ms, and the waveform was repeated once the endpoint had been reached. This was converted to an analogue signal by a combination of a D/A converter and a voltage/frequency converter. It was necessary to smooth

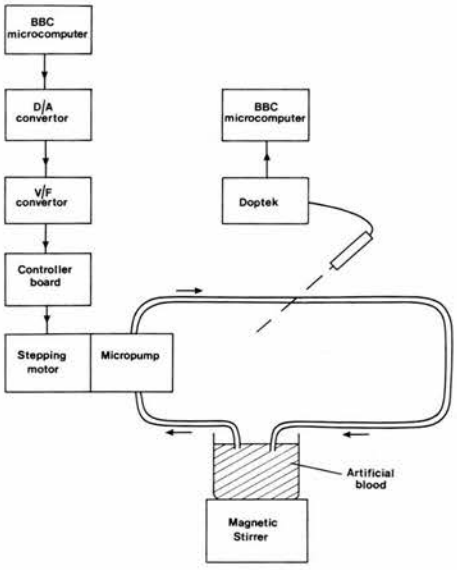

Figure 2. Block diagram of the flow phantom.

the output of the voltage/frequency converter in order to avoid discontinuous jumps in the output which the stepping motor could not follow. This smoothing did not affect the waveform shape. The system could support both forward and reverse flow. Reverse flow was indicated by a control bit sent from the microcomputer with each new value.

Waveforms were acquired using a Doptek 4 MHz continuous wave Doppler unit. The maximum frequency envelope or the entire Doppler spectrum could be sent to the microcomputer for storage. Analysis of the Doppler waveforms was performed using the microcomputer.

Typical waveforms acquired using the final system are shown in figure 3. The beam-vessel angle was 45 °. The pump speed was adjusted to give a maximum velocity of approximately 0.8 ms^{-1}. Umbilical type waveforms using the 3 mm tube are shown

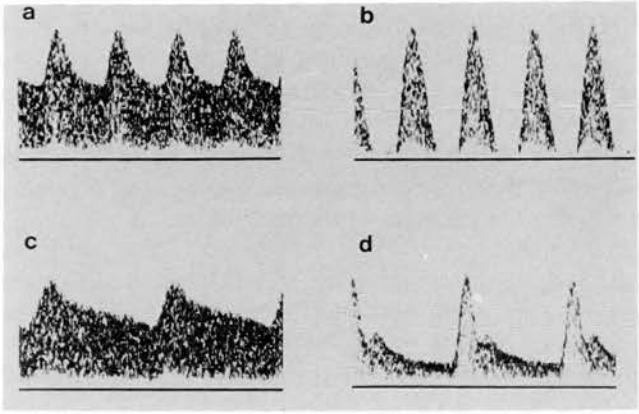

Figure 3. Waveforms produced using the flow phantom. (*a*) and (*b*); umbilical waveforms using the 3 mm tube, (*c*) and (*d*); arcuate waveforms using the 6 mm tube.

in figure 3(*a*) and (*b*). Arcuate type waveforms using the 6 mm tube are shown in figure 3(*c*) and (*d*).

3. Evaluation

3.1. Flow calibration

Constant flow levels were generated by the microcomputer. Flow was measured using a measuring cylinder and stopwatch. This was done for both forward and reverse flow over the range of interest (figure 4(*a*)). At low flows the curve of microcomputer control value versus volume flow is non-linear. This is a combination of non-linearity in the control board electronics, and in pump efficiency. In particular, when the microcomputer output value is zero there is a residual flow of 0.0017 ml s^{-1}. For a 3 mm tube this gives a maximum Doppler shift of about 1.2 Hz which is much smaller than the filter level of 70 Hz. This small flow will however affect the accuracy of volume flow measurement performed using a measuring cylinder and stopwatch when very pulsatile flow is used. This was overcome by reversing the direction of flow of the pump every 5 ms when the microcomputer output was zero. By using the curve of figure 4(*a*), correction factors were calculated from which the microcomputer output was corrected to increase the stepping motor speed for the low flow region. Correction was performed by linear interpolation over 14 regions between the values −1000 and 1000. This results in the more linear curve of figure 4(*b*).

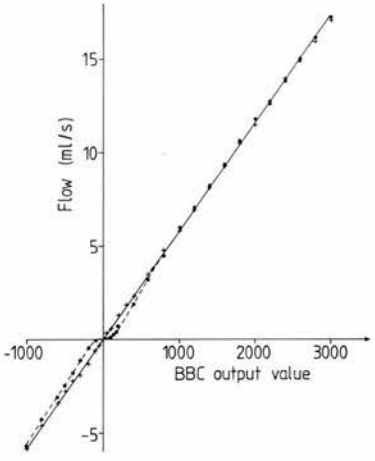

Figure 4. Relationship between the control output value from the microcomputer and the flow rate. (*a*) ●, before correction; (*b*) +, after correction.

3.2. Distortion of the waveform shape

The tubing which is connected to the pump outflow had its other end in the reservoir of sephadex suspension. If the tube is very elastic there are obvious distortions in the recorded Doppler waveform, such as the presence of a second peak, which can be reduced by increasing the resistance to flow at the end of the pipe arising from a mismatch between the impedance of the pipe and that of the sephadex solution. This

suggests that the distortion is due to reflected pressure waves from the end of the pipe. This type of distortion was also present when the relatively stiff pipes of moulded heat shrink tubing were used. A number of methods were tried to remove these effects. Basically these methods attempted to match the impedance between the tubing and the sephadex suspension. The methods tried included drilling holes in the tubing wall for several centimetres from the end, shaping the end to be a slanted cut instead of a blunt cut, and tying a piece of foam tightly around the end. The first two of these methods had no effect. The third method did cause a reduction in waveform distortion. This, however, is not a desirable method as pieces of foam fray off and could damage the gear teeth. The distortion was reduced when the heat shrink tubing was of reduced diameter for the last 20–30 cm of its length before entering the reservoir. A diameter reduction of a half was used. The reduction in distortion achieved was greater as the length of the narrow tube was increased (figure 5). The reasons for the removal of the distortion using this method are not entirely clear. One possible explanation is that the mismatch in impedance at the interface between the insonation tube and the narrow tube causes reflected pressure waves which cancel out the distorting effects of the pressure waves reflected from the end of the tube. Another possible explanation is that, as the speed of the fluid in the narrow pipe is a factor of four greater than in the insonation tube, this impedes the progress of the reflected waves from the end of the pipe. Though empirical this method does give some reduction in distortion.

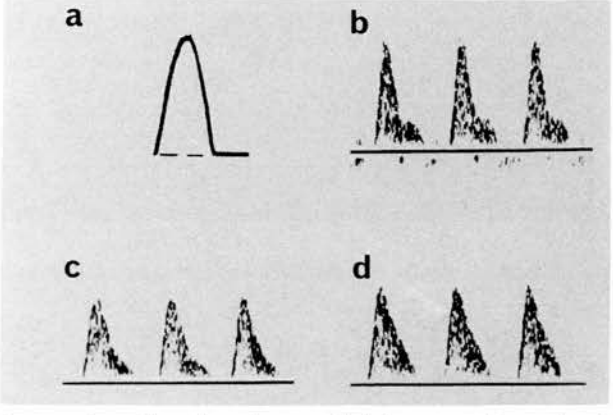

Figure 5. Reduction in waveform distortion using an adjoining narrow bore tube: (*a*) control waveform, (*b*) narrow bore length = 0 cm, (*c*) narrow bore length = 18 cm, (*d*) narrow bore length = 31 cm.

3.3. Comparison of control waveforms and Doppler waveforms

The 3 mm insonation tubing was used. Waveforms with a wide range of pulsatility, including reverse flow, were generated at a pulse rate of 120 per minute. Values of resistance index (RI) (Pourcelot 1974) were calculated for the control waveform and for the maximum frequency envelope of 5 Doppler waveforms. The results are presented in figure 6. The RI of the Doppler waveforms is in general lower than that of the control waveforms, but only by a small amount (<0.1). Perfect agreement would not be expected since the control waveform influences the mean velocity, and it is known that the velocity profile and hence the relationship between the mean and maximum velocity changes over the waveform cycle. The relationship between the control RI

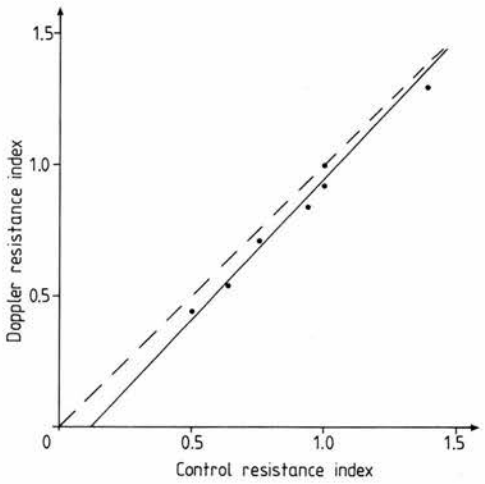

Figure 6. Comparison of the control waveforms and Doppler waveforms using the resistance index. The solid line is the line of best fit; the dotted line is the line of identity.

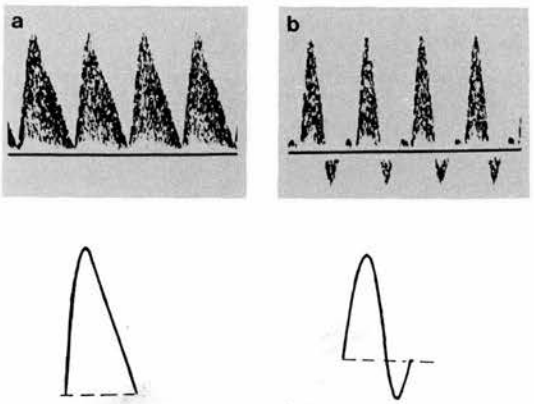

Figure 7. Cases where there is obvious disagreement between the control and Doppler waveforms. (*a*) the control waveform has no end diastolic flow whereas the Doppler waveform does have end diastolic flow. (*b*) the Doppler waveform possesses a tertiary peak which is absent in the control waveform.

and the RI derived from the intensity weighted mean Doppler frequency might be better, however the intensity weighted mean is not commonly used in Doppler waveform analysis, and it is known that it may not reflect the mean velocity if the beam width is comparable to or less than the vessel diameter (Evans 1982, Cobbold *et al* 1983). In some cases there was obvious disagreement between the control waveform and the Doppler waveform. Figure 7(*a*) shows a case where there is diastolic flow when the control waveform has absent end diastolic flow. Figure 7(*b*) shows a case where there is a tertiary Doppler peak which is not present on the control waveform. This distortion could be caused by residual reflected waves within the system.

4. Conclusion

A flow phantom based upon microcomputer control of a stepping motor/gear pump combination has been described. The system works well and is able to generate a wide

variety of physiological waveforms. Future work will consist of replacement of the current stepping motor/pump combination with a more powerful motor and higher output pump so that physiological waveforms at higher flow rates can be generated.

Acknowledgments

Thanks to Mr R Borthwick for mechanical workshop expertise, Mr A Millar for advice and comments and Miss A Faichnie and Mrs D Nicholson for secretarial work.

Résumé

Fantôme de flux contrôlé par ordinateur pour la génération d'ondes Doppler physiologiques.

Les auteurs décrivent un fantôme de flux pour la génération d'ondes Doppler physiologiques. La suspension de particules diffluantes est commandée par une pompe à engrenages entraînée par un moteur pas à pas. La vitesse du moteur pas à pas est commandée par un microordinateur BBC. La forme des ondes est choisie dans un disque-'bibliothèque' d'ondes. L'utilisation du micro-calculateur permet de changer aisément la forme de l'onde et le débit moyen. Des particules de Sephadex en suspension dans une solution de glycérine ont été utilisées pour constituer le sang artificiel. Des tubes à paroi fine et thermorétractable, prémoulés sur des tiges métalliques, ont également été utilisés. Les déformations des ondes provoquées par des réflexions à l'extrémité des tubes ont été supprimées en grande partie en réduisant le diamètre des tuyaux à la moitié de sa valeur initiale à 30 cm de leur extrémité. Les auteurs ont observé un bon accord entre les ondes de référence et les ondes Doppler dans une large gamme de pulsatilité de l'onde.

Zusammenfassung

Ein Computer-überwachtes flüssiges Phantom zur Erzeugung von physiologischen Doppler-Wellenformen.

Beschrieben wird ein flüssiges Phantom zur Erzeugung von physiologischen Doppler-Wellenformen. Die Suspension aus streuenden Teilchen wird bewegt durch eine Zahnradpumpe, angetrieben durch einen Schrittmotor. Die Geschwindigkeit des Schrittmotors wird mit einem BBC-Mikrocomputer überwacht. Die Wellenformen werden ausgewählt aus einer Bibliothek von Wellenformen auf der Platte. Duch die Verwendung eines Mikrocomputers kann die Wellenform und der mittlere Fluß leicht geändert werden. Sephadexteilchen in einer Suspension von Glyzerol, sowie dünnwandiges Wärme-empfindliches Röhrenmaterial, geformt um Metallstäbchen wurden als künstliche Blutbahnen verwendet. Verzerrungen der Wellenform, hervorgerufen durch Reflexionen vom Ende des Rohrleitungssystems wurden zum größten Teil beseitigt durch Reduzierung des Rohrdurchmessers auf die Hälfte seines Wertes 30 cm vom Rohrende. Die Uebereinstimmung zwischen den Kontrollwellenformen und den Doppler-Wellenformen war gut über einen weiten Bereich von gepulsten Wellenformen.

References

Angelson B A J 1980 A theoretical study of the scattering of ultrasound from blood *IEEE Trans. Biomed. Eng. BME* **27** 61–7

Atkinson P and Berry M V 1974 Random noise in ultrasonic echoes diffracted by blood *J. Phys.* A **7** 1293–1302

Cobbold R S C, Veltink P H and Johnston K W 1983 Influence of beam profile and degree of insonation on the CW Doppler ultrasound spectrum and mean velocity *IEEE Trans. Sonic Ultrason.* **SU-30** 364–70

CRC 1985 Handbook of Chemistry and Physics (The Chemical Rubber Company: Cleveland Ohio) p D-235

Evans D H 1982 Some aspects of the relationship between instantaneous volumetric blood flow and continuous wave Doppler ultrasound recordings. I *Ultra. Med. Biol.* **8** 605–9

Hames T K, Ratliff D A, Humphries K N, Gazzard V M, Birch S J and Chant A D B 1985 The accuracy of Duplex scanning in the evaluation of early carotid disease *Ultra. Med. Biol.* **11** 819–25

Hames T K, Humphries K N, Ratliff D A, Birch S J, Gazzard V M and Chant A D B 1985 The validation of duplex scanning and continuous wave Doppler imaging: a comparison with conventional arteriography *Ultra. Med. Biol.* **11** 827–34

Issartier P, Siouffi M and Pelissier R 1978 Simulation of blood flow by a hydrodynamic generator *Med. Prog. Technol.* **6** 39–40

Law Y F, Cobbold R S C, Johnston K W and Bascom P A J 1987 Computer controlled pulsatile pump system for physiological flow simulation *Med. Biol. Eng. Comput.* **25** 590–5

McCarty K and Locke D J 1986 Test objects for the assessment of the performance of Doppler shift flowmeters *Physics in Medical Ultrasound* ed. J A Evans (Bacardo Press: Oxford) pp 94–106

McDicken W N 1986 A versatile test-object for the calibration of ultrasonic Doppler flow instruments *Ultra. Med. Biol.* **12** 245–9

McDonald D A 1974 Blood flow in arteries (London: Edward Arnold) p 137

Mo L Y L and Cobbold R S C 1986 A stochastic model of the backscattered Doppler ultrasound from blood *IEEE Trans. Biomed. Eng. BME* **33**: 20–7

Pedley T J 1980 The fluid mechanics of large blood vessels (Cambridge University Press: Bristol) pp 30–1

Peterson J N 1984 Digitally controlled system for reproducing blood flow waveforms *in vitro. Med. Biol. Eng. Comput.* **22**: 277–80

Philips D J, Greene F M, Langlois Y, Roederer G O and Strandness D E 1983 Flow velocity patterns in the carotid bifurcations of young, presumed normal subjects. *Ultra. Med. Biol.* **9** 39–49

Pourcelot L 1974 Applications cliniques de l'examen Doppler transcutance *Veliometric Ultrasonore Doppler* ed. P Peronneau pp 625–627 vol 34 Inserm

Shung K K 1982 On the ultrasound scattering from blood as a function of haematocrit *IEEE Trans. Sonics Ultrason.* **SU-29** 327–31

Shung K K, Sigelmann R A and Reid J M 1976 Scattering of ultrasound by blood *IEEE Trans. Biomed. Eng. BME* **23** 460–7

Walton L, Martin T R P and Collins M 1984 Prospective assessment of the aorta-iliac segment by visual interpretation of frequency analysed Doppler waveforms—a comparison with arteriography *Ultra. Med. Biol.* **10** 27–32

Wemeck M M, Jones N B and Morgan J 1984 Flexible hydraulic simulator for cardiovascular studies *Med. Biol. Eng. Comput.* **22** 86–9

Ultrasound in Med. & Biol. Vol. 16, No. 2, pp. 141–147, 1990
Printed in the U.S.A.

0301-5629/90 $3.00 + .00

●*Original Contribution*

A COMPARISON OF THE DOPPLER SPECTRA FROM HUMAN BLOOD AND ARTIFICIAL BLOOD USED IN A FLOW PHANTOM

P. R. HOSKINS, T. LOUPAS and W. N. MCDICKEN
Medical Physics and Medical Engineering Department, Royal Infirmary, Edinburgh

(*Received* 26 *April* 1989; *in final form* 18 *August* 1989)

Abstract—A comparison between the Doppler signals from human blood and artificial blood used in a flow phantom is described. The artificial blood used was a suspension of Sephadex particles in a glycerol solution. The Doppler power was measured as a function of Sephadex concentration and found to peak at a concentration of about 40% by volume. The power from blood was less by a factor of 150–250 than the power from Sephadex of a similar concentration. The first and second order statistics of the Doppler spectra from Sephadex were independent of particle concentration, and were very similar to those of spectra from blood.

Key Words: **Artificial blood, Doppler ultrasound, Flow phantom.**

INTRODUCTION

The Doppler signal from blood results from the combination of the ultrasound scattered from each red cell. The average distance between two red cells is about 10% of its diameter for a haematocrit of 45% (Shung et al. 1976). In this situation the red cells must be considered as interacting. Theoretical modelling of the Doppler signal from blood taken as a suspension of interacting scatterers has been performed by a number of authors (Atkinson and Berry 1974; Shung 1982; Mo and Cobbold 1986a). Angelson (1980) treated blood as a continuum and therefore bypassed the interaction. For blood the Doppler shifted signal arises from fluctuations in red cell concentration in the sample volume. The fluctuating nature of this signal gives rise to the characteristic speckle pattern of the Doppler spectrum from discrete Fourier transform based spectrum analysers.

It is known that the underlying Doppler spectral profile is strongly influenced by beam-vessel geometry, such as misalignment of the vessel axis and the beam axis (Evans 1982; Cobbold et al. 1983) and beam-vessel angle. In the absence of turbulent flow it is generally possible to produce a Doppler spectrum with a well defined maximum frequency envelope. As the beam axis and vessel axis become increasingly misaligned, and as the beam-vessel angle approaches 90° the waveform outline becomes much less clearly defined. This will affect the performance of some maximum frequency followers which are susceptible to the noisy waveform outline present in these cases. These aspects can be investigated in the laboratory using a physiological flow phantom. The use of blood as a scattering medium is inconvenient—the red cells are easily damaged, it is difficult not to introduce air bubbles into the blood, stringent microbiological safety precautions are necessary, and a large supply can be difficult to obtain. It is much more convenient to use a blood substitute. The blood substitute used in this paper was Sephadex G25 superfine particles (Pharmacia, Uppsala, Sweden) in a glycerol solution. These particles have a swollen diameter of 20–70 μm which is much larger than the red cell dimensions of approximately 2.4 by 8.5 μm. The question then arises as to whether the backscattered Doppler power and the statistics of the Doppler spectrum are similar for human blood and for a suspension of the Sephadex particles. This paper investigates these aspects.

METHOD

Flow phantom

A detailed description of the flow phantom is given elsewhere (McDicken 1986; Hoskins et al. 1989). A short description will be given here. A gear pump was used to drive the blood or blood substitute around a circuit. The gear pump was driven by a stepping motor. The speed of the stepping motor was controlled by a BBC microcomputer enabling waveforms of different shapes to be generated. Thin walled

tubing made from transparent heat shrink tubing was used where insonation was required.

The artificial blood was a suspension of Sephadex particles in a mixture of 42% glycerol to 58% water. This has a viscosity of 0.004 kgm^{-1} s^{-1} at 20° C, identical to the viscosity of blood at 37° C. The flow phantom and artificial blood were kept at 20° C for the duration of the study. The artificial blood was prepared in such a manner as to remove air bubbles. Boiling water was added to the glycerol to remove the dissolved air.

The Sephadex was prepared by adding a weighed amount of dry Sephadex to the glycerol solution and heating for 2 to 3 hours at 85° C. This swells the particles to their final volume and removes dissolved air. As a precautionary measure the glycerol solution used and the Sephadex suspension were placed in an evacuated chamber of pressure less than 50 mmHg for one to two minutes to remove any final air bubbles. No air was observed to come off from the solution and suspensions. The flow phantom was flushed with water degassed by boiling and by exposing it to low pressure. Special care was taken to remove air trapped within the gear pump. This could be done by inverting the gear pump and running it at high speed. The presence of microbubbles was monitored using Doppler ultrasound. A microbubble produced a very high intensity Doppler signal. Flushing was repeated until no recirculating bubbles were observed. The flow phantom was further flushed with glycerol solution, then the Sephadex suspension introduced. Dilution of the original Sephadex suspension was performed using degassed glycerol solution carefully added to the Sephadex. Figure 1 shows the distribution of the swollen particle diameters. Diameter measurements were made using a microscope with a calibrated eyepiece. The mean and 2 standard deviations of the diameter are 46 ± 26 μm which gives a range of approximately 20 to 70 μm.

Human blood was taken from a willing volunteer. This was withdrawn slowly through a 19 gauge butterfly into 50 mL syringes to prevent bubble formation. This was emptied carefully into a beaker. 0.25 mL of heparin at a concentration of 1000 units per mL were used with each 50 mL of blood to prevent clotting.

Gear pumps are known to cause damage to particulate suspensions. During the course of the experiments the damage to the Sephadex particles was minimal as observed through a microscope. The red blood cells are more fragile and so were not recirculated. The blood was sucked through the system so that the blood did not encounter the gear pump until after it had passed the insonation site.

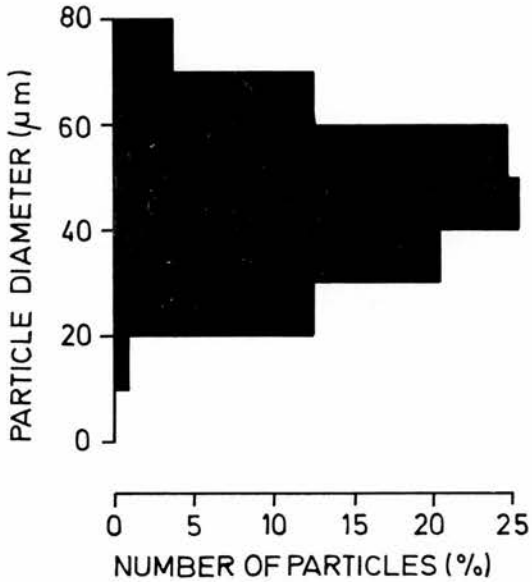

Fig. 1. Diameter distribution of swollen Sephadex particles. This was calculated from diameter measurements made on 500 particles.

Doppler spectra were acquired using a Doptek continuous wave unit. The transducer-vessel distance was 7.4 cm, the beam-vessel angle was 47° and the vessel inner diameter was 4 mm. This set up is similar to that which occurs in practice when Doppler waveforms are acquired from vessels in the body. A 1 cm layer of tissue equivalent attenuator (reticulated foam) was placed between the vessel and the transducer to avoid saturation of the Doppler signal when the higher concentrations of Sephadex were used. A 4 MHz transducer focused at 5 cm was used with the transducer face submerged under water. The wall thump filter was 70 Hz. The wall thickness of the vessel was 0.33 mm.

Measurement of statistical parameters

The initial Sephadex concentration was 50% by volume. The flow rate of the pump was set to a constant value which gave a 3 kHz maximum frequency shift. This corresponds to a maximum velocity of about 0.8 m s^{-1}. The suspension was allowed to circulate for 15–20 seconds to give a uniform concentration of particles. The Doptek frequency range was 4 kHz; that is the highest displayed frequency was 4 kHz. A new spectral line was produced every 10 ms. The Doppler gain was adjusted to keep pixel saturation to a minimum. A spectrum of 240 lines (2.4 seconds) was transferred to the BBC microcomputer. Dilution of the Sephadex was performed taking care not to create air bubbles. This procedure was repeated until the Sephadex concentration was between 1% and 8%.

Without touching the transducer, attenuator, or vessel, the Sephadex was flushed from the flow phantom using degassed water. Blood was introduced and spectra were acquired. All spectra were transferred to the BBC microcomputer and then to an Archimedes microcomputer for analysis.

For each spectrum the 240 consecutive spectral profiles were used to generate data on the standard deviation of pixel values as a function of the mean pixel value. A single data point was derived by calculating the mean and standard deviation of the 240 values corresponding to a particular frequency. This was repeated for all frequencies from 100 to 2850 Hz. The mean and standard deviation are parameters describing the first order statistics of the Doppler spectrum.

Second order statistics refer to the relationship between the value of a pixel and that of the surrounding pixels. This can be described by the normalised autocovariance function NAF(k).

$$\mathrm{NAF}(k) = \frac{1}{N-k} \frac{\sum_{i=1}^{N-k} [P(i) - \bar{P}][P(i+k) - \bar{P}]}{\sum_{i=1}^{N} [P(i) - \bar{P}]^2} \quad (1)$$

where $P(i)$ is an array of N elements, $\bar{P}$ is its mean value and $k = 0, 1, 2 \cdots$ is the lag variable.

If this function has a simple shape it can be characterised by its full width at half maximum height (FWHM). This value gives an indication of the size of the speckle seen on the image. The NAF was calculated in both the time and the frequency direction. Calculation along the time axis was performed over a period of 2.4 s (240 points) for each frequency from 1000 Hz to 2850 Hz. The average NAF along the time axis, NAF_t was then calculated. Calculation of the NAF along the frequency axis, NAF_f, was performed over the interval from 1900 to 2850 Hz (20 points). This was performed for each of the 10 ms spectral lines and the average value taken. For calculation of NAF_f ideally the region should be uniform; that is the mean pixel value should not be a function of frequency. Along the frequency direction the mean pixel value increases as the frequency increases. This is a consequence of the relative geometry of the beam and velocity profile of the vessel. The maximum variation of average pixel values over the region 1900 to 2850 Hz was ±13%. Along the time axis the mean pixel value does not change. Normalisation removes any dependency of the autocovariance function on the mean value for that line hence the requirement for uniformity in the frequency direction is not so strict.

Measurement of relative Doppler power

The measurement of relative power can be explained with the help of Fig. 2. The Doppler signal is a fluctuating signal $V_1(t)$. $V_1(t)$ is the Doppler signal after directional demodulation. The upper channel only was used. The power of the signal is related to the average value of $V_1^2(t)$. In Fig. 2 R_{out} is the output resistance of the Doptek unit. R_A is a digital attenuator reading from 0 to 1000. R_{in} is the input resistance of an RMS voltmeter. After the introduction of the Sephadex of 50% concentration the attenuation value was set to 100, corresponding to a high attenuation, and the RMS voltage noted. Subsequent dilution of the Sephadex suspension produced a different output power. The attenuation resistance was adjusted so that the RMS voltage level returned to its baseline value. From the equivalent circuit the ratio M of V_1 to V_2 is

$$M = \frac{V_1}{V_2} = \frac{(R_1 + R_{\mathrm{out}}) \times (R_{\mathrm{in}} + R_2)}{(R_{\mathrm{in}} \times R_2)} + 1. \quad (2)$$

Using this the power P of the Doppler measurement relative to the first measurement can be calculated

$$\frac{P_n}{P_1} = \frac{M_n^2}{M_1^2}. \quad (3)$$

The attenuation values R_1 and R_2 were measured directly using an ohmeter. The input and output impedances were measured using the standard electrical techniques. An alternative method of power measurement is to use the power readings direct from the RMS meter. Nonlinearities in the calibration of the meter could be present which would affect the measurements. Using the meter as a null device meant that the meter was being used at fixed point hence nonlinearities were not relevant.

The measurement of the relative power of blood using the flow phantom was found to be difficult. This was due to the limited time available as the blood could not be recirculated. An alternative ap-

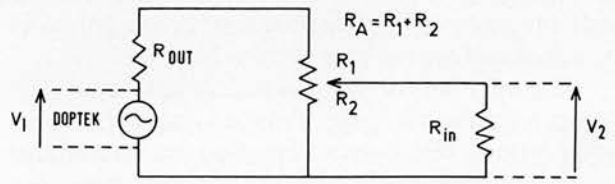

Fig. 2. Circuit for the calculation of relative Doppler power. R_{out} is the Doptek output impedance and R_{in} the input impedance of the RMS voltmeter. R_A is an attenuator. R_A is split into R_1 and R_2. The values of R_1 and R_2 depend on the attenuation needed to maintain V_2 constant.

proach was devised. A 60 mL syringe was connected to a 1 m length of silicon rubber tubing whose outlet was placed in a beaker. Blood or Sephadex suspension at a concentration of 20% by volume was introduced. Doppler measurements from the fluid in the silicon rubber tubing could be taken by emptying and refilling the syringe. The beam-vessel angle and transducer-vessel distance were identical to the values used in the previous measurements. It was possible to pass blood then Sephadex, after flushing, through the tubing without disturbing the beam-vessel geometry. Maximum frequencies of 2.8 to 3.2 kHz were produced by this method which gave a stable power reading for a sufficient length of time to enable the measurements to be performed. Air bubbles were found not to be a problem. Using this method the relative power of blood and Sephadex at 45% concentration by volume was measured.

RESULTS

The relative Doppler power is plotted as a function of Sephadex concentration by volume in Fig. 3. The relative power peaks at approximately 40% concentration and falls as the concentration increases. A similar effect has been shown to occur for blood, where the backscattering coefficient reaches a peak for a haematocrit between 12% and 25% (Shung et al. 1976; Mo and Cobbold 1986a). Newhouse et al. (1982) measured backscattered power as a function of the concentration of cellulose MN300 particles and demonstrated that the power plateaus, rather than peaks. It was suggested that this effect was caused by settling out of the powder at higher concentrations, so that the concentration of suspended powder approaches an almost constant value. The plateau concentration of suspended powder was suggested to be dependent on stirrer speed and geometry, so that for example at higher speeds the concentration of suspended powder would be higher, as would the plateau power. In our apparatus we attempted to keep all of the Sephadex in suspension by using a high stirrer speed. No deposition of Sephadex was observed in the tubing or beaker. The power of blood was less than the power of Sephadex of similar concentration by a factor of approximately 150–250.

Figure 4 shows the standard deviation of pixel values for a given frequency plotted against the mean pixel value. The points represent measurements taken from four blood spectra (224 points in all). For Sephadex measurements, 46 spectra were taken resulting in a total number of 2576 points. Because of the very large number of points only two solid curves showing the spread of the results (average $\pm$ 2 $\times$ standard deviation) are displayed in Fig. 4. There was no dependence of this data on Sephadex concentration. Nearly all the points for the blood spectra lie within the two solid curves, indicating that the first order statistics of blood and Sephadex are identical.

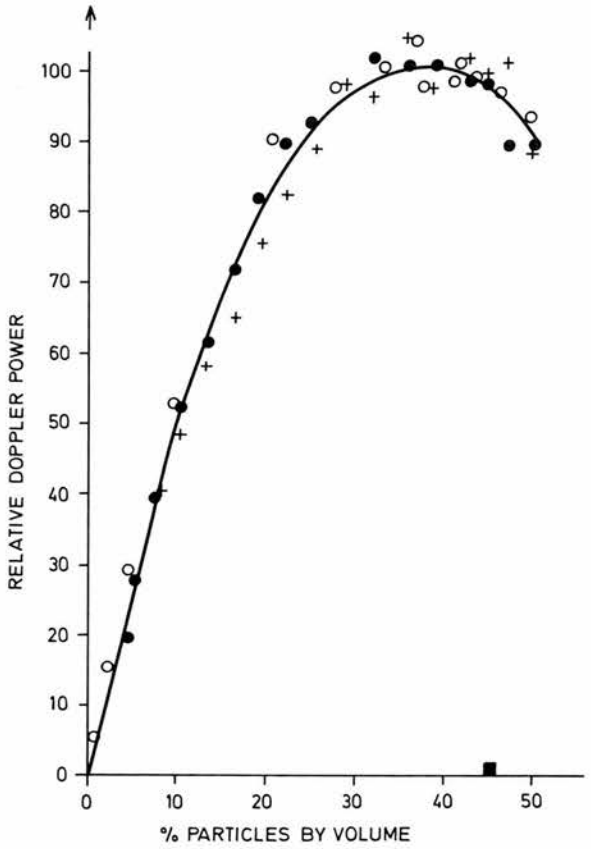

Fig. 3. Doppler power for Sephadex as a function of concentration, and for blood. Three series of measurements are shown for Sephadex indicated by ○, ●, and +. The measurement for blood is shown as ■. The solid line is a line of best fit.

The Doppler shift signal $x(t)$ from a random scattering medium is commonly modelled as a Gaussian process of the form

$$x(t) = \sum_{m=1}^{M} a_m \cos(2\pi f_m t + \phi_m)$$

where a_m are independent Rayleigh variables and ϕ_m are independent random variables uniformly distributed in the range $[0, 2\pi]$. In this case it is known that the amplitude level of any particular Doppler frequency (which is what the Doptek instrument actually displays) follows a Rayleigh distribution (Mo and Cobbold 1986b; Luckman et al. 1988). Consequently the points of Fig. 4 should lie in a straight line passing through the origin of the axes, since the mean of a

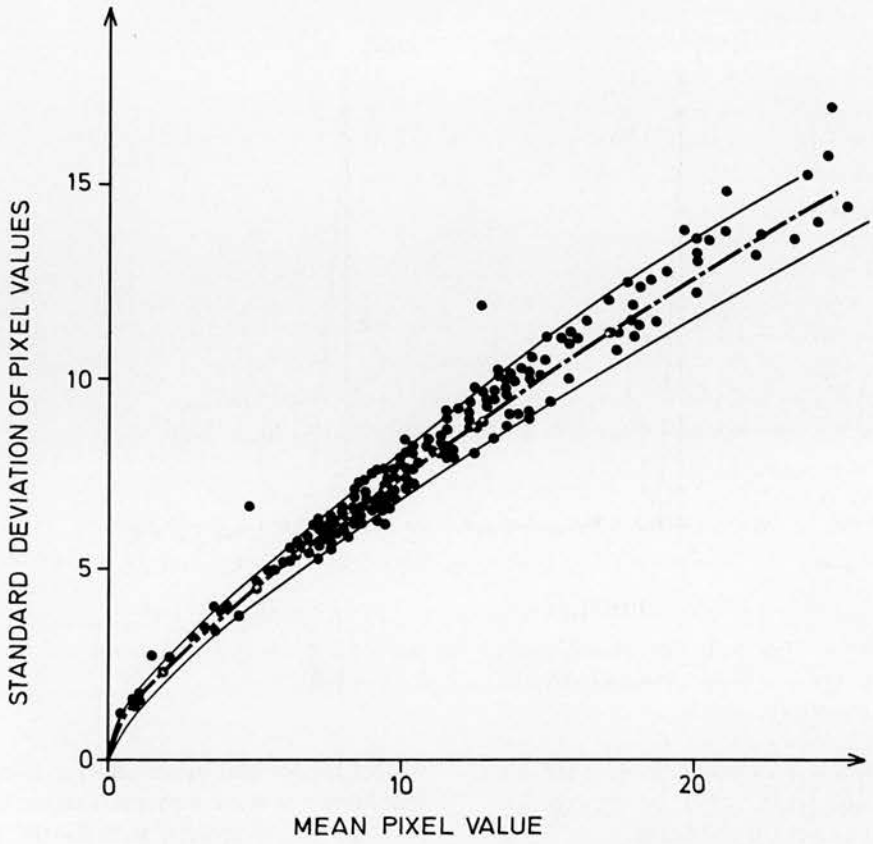

Fig. 4. Standard deviation of pixel values is plotted as a function of mean pixel value. The solid curves represent the average ± 2 × standard deviation for the Sephadex spectra. The broken curve is that from theoretical modelling when there is a baseline shift of 5%. The data for blood is shown as ●.

Rayleigh random variable is proportional to its standard deviation. In an attempt to explain the discrepancy between the theoretically expected and experimental results it was assumed that the deviation from Rayleigh statistics is due to a signal processing operator applied to the spectral data. One such operator, which can be used before displaying the spectral information in order to reduce the background noise, is known as baseline shift. This operator subtracts an amount C from each signal amplitude. If the resulting signal level is less than zero it is set to zero. The broken curve of Fig. 4 was obtained using the first-order statistics of a Rayleigh variable after baseline shift by a level C which represents 5% of the available dynamic range (see Appendix). This value provides good agreement with the experimental results, as can be seen from Fig. 4.

A typical example of NAF_t is shown in Fig. 5a. NAF_t drops to the noise level after 10 ms (1 pixel) indicating no correlation between the value of neighbouring points along the time axis. This was the case for all the Sephadex spectra and for blood. With the frequency range used the frequency resolution was 50 Hz and the length of the data sweep 20 ms. Overlapping of adjacent data by 50% is employed in order to generate a new profile every 10 ms. With this degree of overlap the measured lack of correlation along the time axis warrants further investigation. A possible explanation is that the autocovariance function is proportional to the square of the overlap between data in the time domain. In order to test this hypothesis the whole process was simulated by computer. This involved generation of Doppler signals in the time domain using the speckle model of Mo and Cobbold (1986a), calculation of the Fourier transform of the time domain data, calculation of the sample autocovariance function (128 of them), and averaging in order to obtain an estimate of the ensemble autocovariance function. For a rectangular window with 50% overlap the value of the NAF_t for lag one was 0.23, whereas for a Hanning window NAF_t for lag one was 0.04. The Doptek uses a Hanning window and the value of 0.04 is consistent with the experimental observation that NAF_t drops to the noise level after one pixel. On the other hand NAF_f drops to the noise level after 100 Hz (2 pixels). If it is assumed

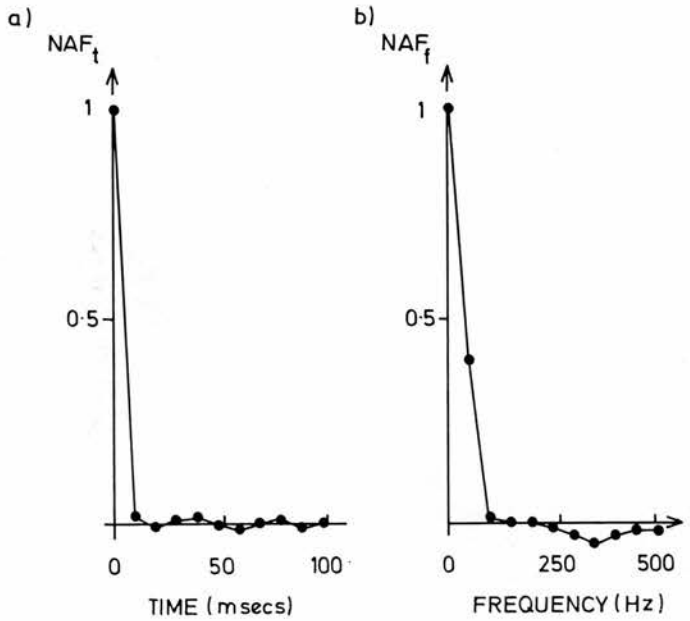

Fig. 5. Typical examples of the normalised autocorrelation function along the time axis (a) and frequency axis (b).

that the Doppler signal is a Gaussian process the autocovariance of the spectrum would be expected to behave like a delta function (Jenkins and Watts 1968). The spread observed in the experimentally measured NAF_f (see Fig. 5b) is consistent with the use of a Hanning window by the Doptek instrument before spectral analysis; an operation which increases the width of the autocovariance of the spectrum of a random process (Jenkins and Watts 1968). The FWHM was estimated by linear interpolation from the NAF_f values at 0 and 50 Hz. These are plotted as a function of concentration in Fig. 6. There is no dependence of the FWHM on concentration of Sephadex. The mean FWHM is 41.5 ± 0.8 Hz for Sephadex and 42.8 ± 0.7 Hz for blood. These values are significantly different ($p < 0.001$) however the difference is still small.

DISCUSSION

Under the conditions that have been used in this experiment it has been shown that the first and second order statistics of blood and a Sephadex suspension are very similar. Two factors are discussed below where care is needed before implementation of these conclusions. The first is the time resolution of the device used. A 10 ms time resolution has been used in this study as that is commonly used in our hospital. Measurements of NAF_t demonstrated a δ-correlation; that is no correlation for lags of 1 pixel or greater. If a lower time resolution was used it is possible that there would be correlation at shorter time intervals. The second factor is the frequency of the transducer. If the particle size is much less than the wavelength it is known that Rayleigh scattering occurs. In this experiment, with a 4 MHz transducer, the wavelength was 380 μm. The Sephadex particle diameters were 20–70 μm; that is 5%–18% of the wavelength which is a small proportion. The similarity of the first and second order statistics of blood and Sephadex, and the agreement between the measured first order statistics

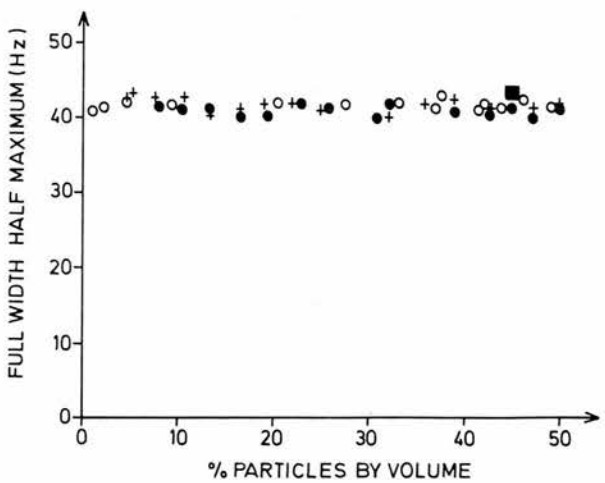

Fig. 6. FWHM of the NAF_f as a function of Sephadex concentration. Three series of measurements are shown indicated by ○, ●, and +. The measurement for blood is shown as ■.

and the mathematical model gives support to the validity of assuming Rayleigh scattering in this case. At higher frequencies the particle diameters will be a larger fraction of the wavelength and there may come a point where Rayleigh scattering can be no longer assumed to apply.

CONCLUSION

Under the conditions in which these measurements have been made it has been shown that the first and second order statistics of blood and a suspension of Sephadex particles in a glycerol solution are very similar. This suggests that Doppler speckle may be investigated in the laboratory using a flow phantom. The statistical parameters are also independent of Sephadex concentration, so no special measures need to be taken to ensure a suspension of the correct concentration. The relative Doppler power from blood is much lower than the power from the Sephadex suspension, hence care must be taken when aspects related to Doppler power are investigated using Sephadex.

Acknowledgements—Thanks to Mr. A. Millar, Mr. T. Anderson and Mr. I. Marshall for helpful advice and comments. Thanks to Mrs. D. Nicholson and Miss A. Faichnie for secretarial work.

REFERENCES

Abramowitz, M.; Stegun, I. A. Handbook of mathematical functions. Washington, DC: U.S. Government Printing Office; 1964: chap. 7.

Angelson, B. A. J. A theoretical study of the scattering of ultrasound from blood. IEEE Trans. Biomed. Eng. BME27:61–67; 1980.

Atkinson, P.; Berry, M. V. Random noise in ultrasonic echoes diffracted by blood. J. Phys. A 7:1293–1302; 1974.

Cobbold, R. S. C.; Veltink, P. H.; Johnston, K. W. Influence of beam profile and degree of insonation on the CW Doppler ultrasound spectrum and mean velocity. IEEE Trans. Sonic Ultrason. SU30:364–370; 1983.

Evans, D. H. Some aspects of the relationship between instantaneous volumetric blood flow and continuous wave Doppler ultrasound recordings. I: The effect of ultrasonic beam width on the output of maximum frequency, mean frequency and RMS frequency processors. Ultrasound Med. Biol. 8:605–609; 1982.

Hoskins, P. R.; Anderson, T.; McDicken, W. N. A computer controlled flow phantom for generation of physiological Doppler waveforms. Phys. Med. Biol. [1989].

Jenkins, G. M.; Watts, D. G. Spectral analysis and its applications. San Francisco: Holden-May; 1968; chap. 6.4.

Luckman, N. P.; Skidmore, R.; Evans, J. M.; Jenkins, D.; Wells, P. N. T. The effect of acoustic speckle on ultrasonic Doppler studies of blood flow. In: Physics in medical ultrasound II. IPSM Report No. 57; 1988:119–124.

McDicken, W. N. A versatile test object for the calibration of ultrasonic Doppler flow instruments. Ultrasound Med. Biol. 12:245–249; 1986.

Mo, L. Y. L.; Cobbold, R. S. C. A stochastic model of the backscattered Doppler ultrasound from blood. IEEE Trans. Biomed. Eng. BME33:20–27; 1986a.

Mo, L. Y. L.; Cobbold, R. S. C. "Speckle" in continuous wave Doppler ultrasound spectra: A simulation study. IEEE Trans. Ultrasonics, Ferroelectrics and Frequency Control UFFC33:747–753; 1986b.

Newhouse, V. L.; Nathan, R. S.; Hertyler, L. W. A proposed standard target for ultrasound Doppler gain calibration. Ultrasound Med. Biol. 8:313–316; 1982.

Papoulis, A. Probability, random variables and stochastic processes. New York: McGraw-Hill; 1981: chap. 5.

Shung, K. K.; Sigelman, R. A.; Reid, J. M. Scattering of ultrasound by blood. IEEE Trans. Biomed. Eng. BME23:460–467; 1976.

Shung, K. K. On the ultrasound scattering from blood as a function of haematocrit. IEEE Trans. Sonics Ultrason. SU29:327–331; 1982.

APPENDIX: FIRST-ORDER STATISTICS OF A RAYLEIGH VARIABLE AFTER BASELINE SHIFT

The probability density function $f_x(x)$ of a Rayleigh random variable x is given by

$$f_x(x) = \begin{cases} (x/\alpha)\exp(-x^2/2\alpha) & x \geq 0 \\ 0 & x < 0. \end{cases} \quad (1)$$

As it was explained before, baseline shift sets to zero signals whose level is lower than C. This operation can be expressed as a transformation of the form $y = g(x)$, where

$$y = g(x) = \{|x - C| + x - C\}/2 = \begin{cases} x - C & x \geq C \\ 0 & x < C. \end{cases} \quad (2)$$

Using a theorem which provides the probability density function $f_y(y)$ of the random variable y in terms of $f_x(x)$ (Papoulis 1981) it can be proven that

$$f_y(y) = \begin{cases} \{(y + C)/\alpha\}\exp\{-(y + C)^2/2\alpha\} & y > 0 \\ 1 - \exp(-C^2/\alpha) & y = 0 \\ 0 & y < 0 \end{cases} . \quad (3)$$

Based on $f_y(y)$ the first two moments of y can be calculated.

$$m_1 = \int_{-\infty}^{+\infty} y f_y(y) dy = (\pi\alpha/2)^{1/2}\{1 - \mathrm{erf}[C/(2\alpha)^{1/2}]\} \quad (4)$$

and

$$m_2 = \int_{-\infty}^{+\infty} y^2 f_y(y) dy$$

$$= 2\alpha \exp(-C^2/2\alpha) + 2C(\pi\alpha/2)^{1/2}\{\mathrm{erf}[C/(2\alpha)^{1/2}] - 1\} \quad (5)$$

where $\mathrm{erf}(z)$ is the error function (Abramowitz and Stegun 1964). The mean μ_y and variance σ_y^2 of y are then equal to $\mu_y = m_1$ and $\sigma_y^2 = m_2 - m_1^2$, respectively. Of course, for $C = 0$ the mean and variance of the Rayleigh distribution are obtained.

Ultrasound in Med. & Biol. Vol. 16, No. 4, pp. 375–389, 1990
Printed in the U.S.A.

0301-5629/90 $3.00 + .00

●*Original Contribution*

A COMPARISON OF THREE DIFFERENT FILTERS FOR SPECKLE REDUCTION OF DOPPLER SPECTRA

P. R. HOSKINS, T. LOUPAS and W. N. MCDICKEN
Department of Medical Physics and Medical Engineering, Royal Infirmary of Edinburgh, Scotland

(*Received* 26 *June* 1989; *in final form* 19 *October* 1989)

Abstract—This paper is concerned with speckle suppression in Discrete Fourier Transform based Doppler signals by means of digital image processing. The Doppler spectrum is treated as a greyscale image, and three different noise smoothing algorithms are applied to it. These are the Double Window Modified Trimmed Mean filter, which is nonlinear, and Lee's and the directional filter, which are adaptive in the sense that the smoothing performed by them at each point of the image is controlled by a local image measure. In order to evaluate the performance of the filters, they were applied to a variety of regular waveforms obtained from a physiological flow phantom. Ensemble averaging of a large number of unfiltered spectra was used as the "gold standard" in the evaluation, *i.e.*, as the output of an ideal filter which reveals the exact nature of the underlying Doppler spectrum after speckle has been eliminated. Comparison of the "gold standard" with the ensemble averaged filtered data allowed the noise reduction, bias and distortion of the maximum frequency envelope introduced by filtering to be examined. Overall, the best performance was offered by the directional filter whose action was controlled by the combination of the local edge content and the slope of the least-squares-fit line passing through the data points along each particular direction.

Key Words: **Doppler waveforms, Imaging processing, Speckle.**

INTRODUCTION

The Doppler signal received from an artery is due to scattering of ultrasound by red blood cells. The wavelets emanating from cells moving within the same velocity resolution cell interfere with each other in a way very similar to that observed in ultrasonic B-mode images (Mo and Cobbold 1986). This interference effect gives rise to the characteristic granular pattern, known as Doppler speckle, of spectra obtained from Fourier transform (FT) based analysers. This is discussed in more detail in the next section. The magnitude of speckle is comparable with the magnitude of the underlying Doppler signal as can be seen in Fig. 1. The large random fluctuations of the instantaneous spectra can obscure trends in a single spectral profile. Reduction of the speckle content of Doppler waveforms could be valuable in a number of areas. Two examples will be given. Firstly, it may be possible to calculate quantitative information based upon the Doppler spectrum, such as spectral broadening indices of carotid artery Doppler traces (Rittgers et al. 1983; Sheldon et al. 1983) with less variability. Secondly, automatic maximum frequency followers, which in general are very sensitive to noise in the spectrum, may perform better after speckle reduction.

Other spectral estimation techniques have been described (Kay and Marple 1981), some of which are less sensitive to Doppler speckle than the FT. For example, Vaitkus et al. (1988a,b) have shown using simulated Doppler signals that autoregressive (AR) and autoregressive-moving average (ARMA) algorithms produce consistently smooth spectra which are closer to the theoretical spectral density than the ones obtained from the FT. However, although a real-time autoregressive analyser has very recently been described (Schlindwein and Evans 1989), all of the current commercial Doppler analysers rely on FT based spectral analysis. Speckle reduction of FT spectra can be achieved using standard spectral smoothing techniques such as ensemble averaging and windowing (Oppenheim and Schafer 1975). Ensemble averaging of waveforms has been shown to be a viable technique of speckle reduction for very regular waveforms produced by a flow phantom (Luckman et al. 1988). However, the large number of regular waveforms required will put limitations on its use in routine clinical practice where, for example, physiological changes such as heart rate variation are oc-

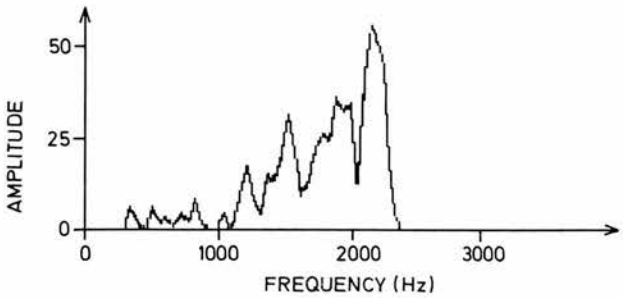

Fig. 1. Profile of a single spectral line from a discrete FT based spectrum analyser.

curring, or where the artery or patient is moving quickly such as in paediatric cases or in the fetus. On the other hand, windowing operates on a single segment of Doppler data and although it is mainly used in order to reduce spectral leakage, it can also smooth out random spectral fluctuations. The main drawback of this technique is that a window which is powerful enough to eliminate speckle will also cause severe loss of frequency resolution. An alternative approach to the problem of Doppler speckle suppression is to treat the Doppler spectrum as a greyscale image and take advantage of recent progress in digital image processing algorithms for noise smoothing. This paper compares three different filtering methods which can be applied to all current FT based spectra.

Two types of noise are present in the Doppler spectrum. Firstly, there is Doppler speckle which has an acoustic origin and is a characteristic of the Doppler waveform,* and secondly there is extraneous background noise which is electronic in origin and which manifests itself when the gain of the Doppler amplifier needs to be high in order to display low power Doppler signals. In the context of Doppler ultrasound, a noise smoothing filter should possess the following desirable properties:

1. Give maximum reduction of extraneous noise above the Doppler waveform;
2. Give maximum reduction of Doppler speckle for those areas of the Doppler waveform which are relatively uniform;
3. Introduce as little distortion as possible to the underlying true spectrum by preserving, for example, the edge content in the vicinity of the maximum frequency envelope.

The performance of the filters proposed here was evaluated in terms of their ability to satisfy the three requirements listed above. In order to achieve this, the filters were applied to a variety of spectra obtained from a physiological flow phantom. Because of the regular nature of the data produced by the phantom, ensemble averaging of a large number of unfiltered spectra enabled the underlying Doppler spectrum, after speckle had been eliminated, to be revealed. This served as a "gold standard," *i.e.*, as the output of an ideal filter which is capable of suppressing speckle completely without introducing any distortion to the true signal. Comparison of the filters' output with the "gold standard" allowed the noise reduction and bias of the spectrum, and distortion of the maximum frequency envelope introduced by filtering to be examined. These procedures are described in detail in the Methods Section below.

* Throughout this paper, the term "Doppler waveform" is used to describe those parts of the spectrum which lie below the maximum frequency envelope.

DOPPLER SPECKLE

As mentioned above, the mechanisms associated with the production of Doppler speckle are acoustic in origin. This phenomenon can be understood by considering a model developed by Mo and Cobbold (1986). According to this model, the backscattered Doppler signal $x(t)$ is a band-limited, wide-sense stationary, Gaussian random process which can be approximated by a sum of sinusoids having discrete frequencies f_m $(m = 1, \cdots M)$ which cover the whole available frequency range $[O, f_{\max}]$.

$$x(t) = \sum_{m=1}^{M} a_m \cos(2\pi f_m t + \phi_m) \qquad (1)$$

where ϕ_m are uniformly distributed random phases and M is the number of bins in which the frequency range has been subdivided.

The amplitude a_m of each sinusoid is determined by the interference between the wavelets from scatterers moving within the same velocity resolution cell, *i.e.*, whose velocities translate into Doppler shifts falling inside the frequency bin centered around f_m. Because the wavelets can interfere constructively as well as destructively, the resultant amplitude a_m is a random variable (it can be shown to follow the Rayleigh distribution) which fluctuates considerably. Since the FT decomposes a signal into its sinusoidal components and provides their amplitudes, these random fluctuations (speckle) become apparent in the displayed spectrum.

Doppler speckle depends on the characteristics of the ultrasonic transducer, the insonation geometry and the signal processing system. A question which is very relevant to this study is if speckle also depends on the type of scattering medium, or more specifically if a flow phantom with artificial instead of

human blood could be used in the investigation of speckle. This question was examined in a previous study (Hoskins et al. 1990) and the conclusion was that spectra from human blood and artificial blood have almost identical first- and second-order statistics. It is, therefore, justified to use a flow phantom with a blood substitute for investigating aspects related to Doppler speckle. The study also revealed that the spectrum analyser used introduced a slight deviation from the theoretically expected Rayleigh first-order statistics and that the second-order statistics of speckle along the frequency and time axes are influenced by the window function and the amount of overlap between consecutive time data segments, respectively.

FILTERING TECHNIQUES

Filtering of an image in the spatial domain is performed by replacing the greyscale level of a pixel by a combination of the levels in a predefined neighbourhood (usually referred to as the filter window) of that pixel. Early noise smoothing filters were linear. These filters assume that signal and noise occupy different nonoverlapping parts of the spatial frequency spectrum.[†] Smoothing is performed by suppressing those parts of the spatial frequency spectrum, usually high frequencies, which correspond to noise. In general such filters have proved to be of limited usefulness in image processing. This is mainly due to the fact that images contain sharp greyscale variations, such as edges, whose spatial spectral content extends to infinity and therefore overlaps with noise. Consequently, any attempt to suppress noise is accompanied by blurring of important information-bearing features and loss of fine image detail. In addition, even when signal and noise are completely separated in the spatial frequency domain, linear filters are optimum in the sense that they offer maximum noise reduction for a given window size, only if the signal is corrupted by additive, Gaussian noise (Bovik 1983). In recent years nonlinear filters have been described which attempt to overcome the limitations of linear filters. In general, the mathematical analysis of such filters is extremely complex, so that filter design is based upon empirical principles. The three nonlinear filters used in this study are described below.

Double Window Modified Trimmed Mean (DWMTM) filter

The DWMTM filter is a combination of a median and a running mean filter. This was first described by Lee and Kassam (1985). In median filtering the pixels in a window surrounding the central pixel are ordered and the median value is taken as the filter output. In contrast, the output of the running mean filter is the average value of the pixels in the window. The median filter tends to perform well in suppressing noise consisting of 'spikes', *i.e.,* large excursions from the surrounding values, and also at preserving edges. The running mean filter performs worse in these respects causing blurring of edges and smearing out of spikes. These features are demonstrated in Fig. 2. However, in a uniform area corrupted by noise the running mean gives very good noise reduction compared to the median. The DWMTM filter attempts to combine the properties of both the median and running mean filter by using two windows. The median of the terms inside a small window provides a first estimate of the 'true' image value. Then from the larger second window those elements which are within a specified limit of the median are included in a running mean, which is the filter output. In this way a compromise is reached between the edge preserving properties of the median and the noise reduction properties of the mean. The amount of each property is controlled by the choice of the specified limit. If this limit is large there will be substantial noise reduction in the image at the expense of edge preservation, but if the limit is small the opposite is true.

The DWMTM is an example of a nonadaptive, nonlinear filter. The next two filters are examples of adaptive filters whereby the proportion of edge preservation or smoothing at each point of the image is controlled by the value of some local image measure at that point. Adaptive filtering is computationally more complex than nonadaptive filtering as the calculation of the local image measure has to be repeated at each point. However, this drawback is compensated by their ability to provide noise reduction while preserving the important features of an image.

Lee's filter

This filter, which was suggested by Lee (1980), is described by

$$O(x, y) = m(x, y) + C(I(x, y) - m(x, y)) \quad (2)$$

where $I(x, y)$ is the value of the central pixel, $m(x, y)$ is the local mean of terms inside the filter window, $O(x, y)$ is the filter output and C is a controlling parameter which depends on a local image measure.

The value of C determines the amount of smoothing performed at each point. The local image

[†] The term spatial frequency spectrum refers to the two-dimensional FT of an image (in our case the image is the greyscale spectrogram) and should not be confused with the Doppler frequency spectrum.

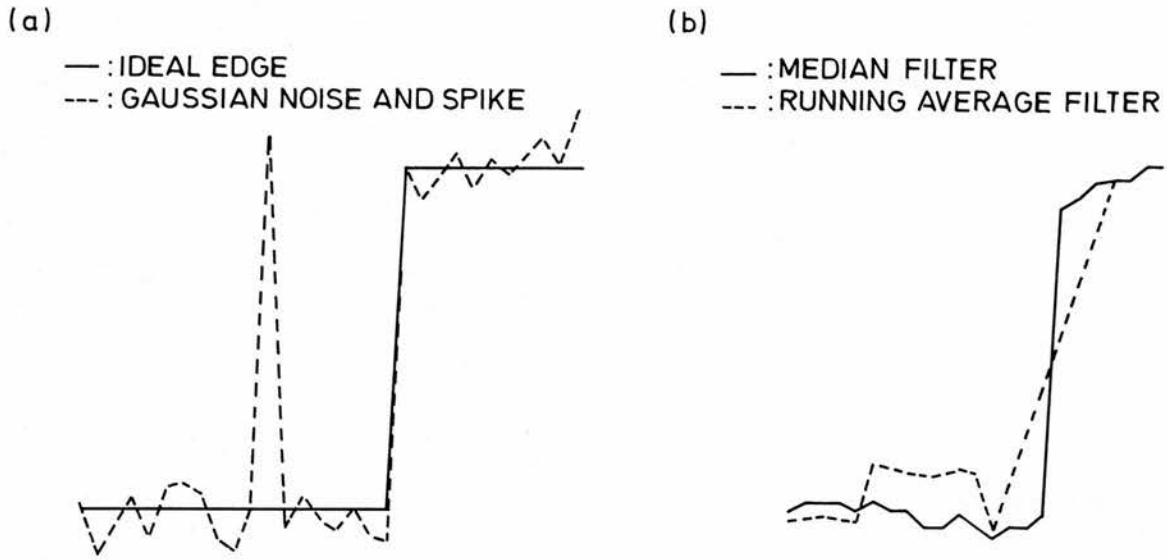

Fig. 2. Noise reduction by the median and running mean filters. An ideal edge is corrupted by Gaussian noise and a spike (a). The median filter gives good edge preservation and removes the spike, whereas the running mean filter blurs the edge and smears out the spike (b).

measure should be formulated to give values of C near zero in a uniform area, resulting in maximum smoothing ($O(x, y) = m(x, y)$ for $C = 0$), and values of C near 1 at an edge, so that the little smoothing is performed and edges are preserved ($O(x, y) = I(x, y)$ for $C = 1$). Filters based on eqn (2) have been used for general noise reduction (Lee 1980; Chan and Lim 1985), synthetic aperture radar speckle suppression (Lee 1981, 1986; Kuan et al. 1987) and ultrasonic B-scan speckle suppression (Bamber and Daft 1986; Bamber and Cook-Martin 1987).

Directional filtering

The action of most adaptive filters, such as Lee's filter, varies from maximum noise smoothing in uniform areas where only noise is present to no smoothing at all near edges. This procedure will prevent blurring of edges and loss of image detail but it will not do anything to restore noisy edges. An alternative approach which can overcome this drawback is to perform adaptive directional filtering. Methods for image enhancement which utilise directional information have been described by Chan and Lim (1985), Kim and Jung (1987) and Peli (1987). Loupas (1988) described a directional two-stage filter which gave combined smoothing and sharpening of ultrasonic B-scan images. In this paper only the smoothing stage is used, where the filter output $O(x, y)$ is given by eqn (3) below.

$$O(x, y) = \frac{\sum_{d=1}^{8} m(d) \times [C(d)]^k}{\sum_{d=1}^{8} [C(d)]^k} \quad (3)$$

where $m(d)$ is the mean value of elements in a window aligned along the direction d, $C(d)$ is the local image measure along the same direction and k is a parameter which determines the relative contributions of the directional means $m(d)$ to the final output.

The values of the local image measure $C(d)$ determine the amount of smoothing performed by the filter. $C(d)$ should be formulated so that in a uniform area the values $C(d)$ for $d = 1, \ldots, 8$ are all comparable, and by accepting equal contributions from all the directional means maximum smoothing is achieved; on the other hand, in the presence of an edge $C(d)$ should become maximum along the edge direction so that only smoothing parallel to the edge axis is performed, something which should improve its definition without introducing much blurring.

LOCAL IMAGE MEASURES

Lee's filter and the directional filter are adaptive in the sense that their action at each pixel is controlled by the local image content characterised by C for Lee's filter and $C(d)$ for the directional filter. Maximum smoothing is performed if a pixel belongs

to a uniform area corrupted by noise whereas the amount of smoothing is reduced when the pixel is part of a resolvable structure which must be retained. The image content at each pixel can be described by a combination of image measures calculated in a predefined neighbourhood of the pixel. Three possibly useful types of image measures are considered below.

Local statistics

Local statistics have been used by a number of authors as a useful image measure. The exact expression for an image measure based on local statistics is determined by the type of noise present in the image. For example Lee (1981) has demonstrated theoretically and experimentally that the ratio σ/m of the local standard deviation σ to the local mean m can characterise speckle in synthetic aperture radar images (multiplicative noise). Following a similar methodology, Loupas (1988) has shown that ultrasonic speckle can be characterised by the ratio σ^2/m. Measurements of spectra obtained from a commercial Doppler device (Doptek, Chichester) suggest that for this device Doppler speckle falls somewhere between the cases of multiplicative noise and square-root noise mentioned above (Hoskins et al. 1990). For this reason both the σ/m and σ^2/m image measures were applied to Doppler spectra in order to determine which one is the most suitable.

Slope

A second approach is to use the slope $SL(d)$ of the least-squares-fit line passing through the data points along a specific direction d. The use of this quantity as a local image measure is justified by the argument that for a uniform area the slope should have a low value but near an edge it should become higher.

The slope $SL(d)$ was calculated along eight directions spaced at equal intervals of 22.5°. A set of nine values was used in the calculation of the slopes, with each value corresponding to the average of the three adjacent pixels lying perpendicularly to the direction of interest.

Edge parameter

Consider Fig. 3 and eqn (4). The directional mean is shown aligned along a direction d with two background areas, one on either side of the directional mean window. A parameter $R(d)$ can be formed, eqn (4), which gives high values when the directional mean window lies along an edge

$$R(d) = m(d) - \frac{(2 \times B_1(d) \times B_2(d)) \times \lambda}{(B_1(d) + B_2(d))} \qquad (4)$$

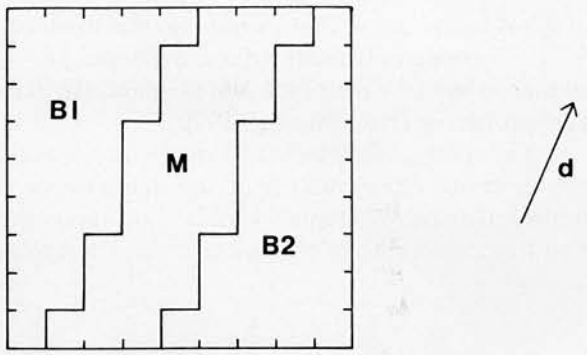

Fig. 3. Windows used for the calculation of the edge parameter $R(d)$. M is the 3×9 directional mean window, B_1 is a background window above M and B_2 is a background window below M.

where $m(d)$ is the mean value of elements in the directional mean window, $B_1(d)$ is the mean value of elements in the background region B_1, $B_2(d)$ is the mean value of elements in the background region B_2 and λ is a factor controlling the amount of background subtracted.

In effect, $R(d)$ represents a directional edge detection operator. In relatively uniform areas, for any given direction d the directional mean $m(d)$ will be similar to the background means $B_1(d)$ and $B_2(d)$. Consequently, all the edge parameters $R(d)$ will have small and very similar values. The presence of an edge will manifest itself by a value of $R(d)$ along the edge axis which is considerably larger than the rest. The maximum value of $R(d)$ at a particular point is called RMAX. In order to reduce the sensitivity of $R(d)$ to noise, a value of $\lambda = 1.5$ was chosen and negative values of $R(d)$ were set to zero.

METHODS

Data acquisition

Doppler waveforms were acquired from a physiological flow phantom. A detailed description of the flow phantom is given elsewhere (Hoskins et al. 1989; McDicken 1986). A short description will be given here. A gear pump driven by a stepping motor was used to circulate artificial blood around a loop. The gear pump was driven by a stepping motor. The speed of the stepping motor was controlled by a microcomputer (BBC Master 128, Acorn Computers, Cambridge) enabling waveforms of different shapes to be produced. Thin-walled tubing made from transparent heat shrink tubing was used where insonation was required.

The artificial blood was a suspension of Sephadex G25 superfine particles in a mixture of 42% glycerol to 58% water to give a suspension with a viscosity

of 0.004 kg m^{-1} s^{-1} at 20°C, similar to that of blood at 37°C. The spectra from blood and Sephadex are very similar in terms of their first- and second-order statistical properties (Hoskins et al. 1990).

The tubing diameter was 3 mm which was chosen as being representative of the diameter of the umbilical artery. A Doptek 4 MHz continuous-wave unit was used for waveform acquisition. Three examples of 'good' waveforms were acquired, each having different pulsatility. Three examples of 'poor' waveforms were also acquired, corresponding to a high beam-vessel angle, a large offset between the beam axis and vessel axis, and a large amount of overlying tissue. These are shown in Fig. 4. In each of the six cases, 42 screens of data corresponding to 168 waveforms were acquired, transferred from the Doptek to

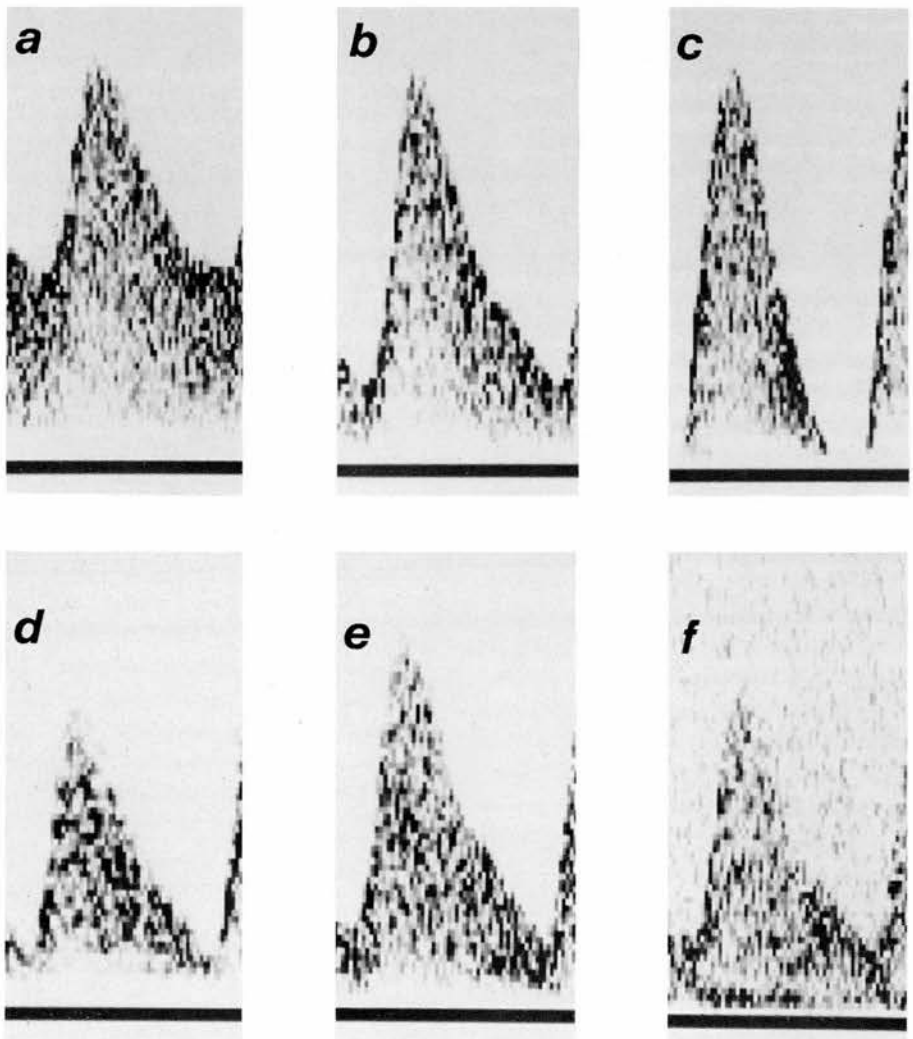

Fig. 4. Doppler waveforms used for filter development. Values of physical parameters associated with each waveform are given in the table below:

Waveform	Θ	*d*	*b*	*a*	*RI*
(a)	45	5	0	1	0.6
(b)	45	5	0	1	0.85
(c)	45	5	0	1	1.0
(d)	15	5	0	1	0.85
(e)	45	5	1.1	1	0.85
(f)	45	8	0	6	0.85

where Θ is the beam-vessel angle (degrees), *d* is the transducer-vessel depth (cm), *b* is the beam-axis vessel-axis distance (cm), *a* is the thickness of attenuating material (cm) and *RI* is the waveform resistance index.

the microcomputer (BBC Master, Acorn Computers, Cambridge) in a serial pixel-by-pixel fashion and stored on disk. The BBC microcomputer was used as a data logger only. Subsequent analysis of the Doppler spectra was performed by a second microcomputer (Archimedes 440, Acorn Computers, Cambridge) which was approximately 25 times faster than the BBC microcomputer during image processing. The waveforms corresponding to Figs. 4a–c and 4e–f were acquired using a time resolution of 10 ms and a frequency resolution of 50 Hz. For the waveform of Fig. 4d the time and frequency resolution were 10 ms and 25 Hz respectively. A Hanning window was employed by the Doptek analyser in all cases. The overlap between windowed data segments used to generate adjacent spectral profiles was 50% for a frequency resolution of 50 Hz and 75% for a frequency resolution of 25 Hz.

Filtering

All filtering programmes were written in interpreted Basic. Filtering 2.4 s of data, which was four waveforms or 240 × 80 pixels, took between 25 min and 160 min depending on the filter complexity. Batch processing programmes were written which enabled filtering of many screens of data to be performed without operator intervention.

For the DWMTM filter the large window size was 9 × 9 and the small window was a five-pixel cross. For Lee's filter and the directional filter a 9 × 9 window was used. The directional means were calculated using a 3 × 9 window within the 9 × 9 window. A value $k = 1$ was used for the directional filter.

Ensemble averaging of waveforms

This was performed on the unfiltered and the filtered waveforms in order to examine the noise reduction offered and the bias introduced by the filters. Each screen of data from the Doptek consisted of four waveforms each of duration 500 ms. For each waveform type, 168 waveforms were averaged. For the first screen the position of the start of the waveform was entered manually. This was the only point for which it was critical that the operator make no error. The registration of subsequent waveforms was calculated automatically as follows. For the first screen ensemble averaging of the waveforms was performed on the basis of the manually entered point and the 500 ms period between waveforms. For subsequent screens the approximate start position was entered manually. This position was then refined by calculating the correlation between the current averaged waveform and the current Doppler waveform for waveform start values up to five pixels on either side of the manual guess. The true start of the waveform was calculated as the point where the correlation is maximum. The averaged waveform was saved to disc. Calculation of the ensemble averaged standard deviation at each point in the Doppler waveform was performed using the same registration technique.

Assessment of filter performance

Comparison of the filters was performed in terms of the filters' ability to satisfy the three desirable requirements listed in the Introduction.

A number of parameters were calculated from the ensemble averaged waveforms to examine bias and noise reduction produced by filtering. These parameters are described below. In all cases subscript f indicates ensemble averaged filtered waveform and subscript r indicates ensemble averaged unfiltered waveform.

The coefficient of variation (CV) at a particular location of the waveform was calculated from the values of the ensemble averaged standard deviation (σ) and mean at that location (CV = 100 × σ/mean). Three regions from the waveform were chosen to allow comparison of the noise reduction properties of different filters. The first region was a relatively uniform 9 × 9 area in the centre of the waveform (CA = central area). The mean coefficient of variation CV_{CA} was calculated over the 81 locations for this central area. The second region was the leading edge of the waveform (LE = leading edge). This is a highly nonuniform region. The coefficient of variation of pixels in this region gives an indication of the noise reduction properties of the filter in the presence of an edge. The coefficient of variation was calculated for locations along the leading edge between 1000 and 1500 Hz and from them the mean value CV_{LE} was derived. The third region was a 9 × 9 area above the Doppler waveform, which was chosen to examine the smoothing of extraneous electronic noise produced by filtering (UR = upper region). The mean coefficient of variation CV_{UR} was calculated only for the Doppler spectrum of Fig. 4f as this is the only case with extraneous noise. Having calculated the mean coefficients of variation for both raw and filtered data, their ratio could then be derived (eqns 5–7 below). These quantities indicate the factor by which noise, as measured by the coefficient of variation, has been reduced by filtering.

$$RCV_{CA} = \frac{CV_{CA(r)}}{CV_{CA(f)}}, \qquad (5)$$

$$RCV_{LE} = \frac{CV_{LE(r)}}{CV_{LE(f)}}, \quad (6)$$

$$RCV_{UR} = \frac{CV_{UR(r)}}{CV_{UR(f)}}. \quad (7)$$

The bias produced by filtering in each of the three regions was also examined. In each case, the average height of pixel values in the region of the ensemble averaged filtered waveform and the ensemble averaged raw waveform was calculated and the change in height produced by filtering derived (eqns 8–10 below).

$$RH_{CA} = \sum_{CA(f)} \text{pixel values} / \sum_{CA(r)} \text{pixel values}, \quad (8)$$

$$RH_{LE} = \sum_{LE(f)} \text{pixel values} / \sum_{LE(r)} \text{pixel values}, \quad (9)$$

$$RH_{UR} = \sum_{UR(f)} \text{pixel values} / \sum_{UR(r)} \text{pixel values}, \quad (10)$$

The 'smearing' of the edges produced by filtering was examined further by considering the maximum frequency envelope of the ensemble averaged waveform. A threshold maximum frequency follower with a threshold value of 5 was used. For a particular Doppler profile the maximum frequency is defined as that point at which the pixel value first exceeds the threshold value of 5, starting from the high frequency end. A number of parameters were calculated which describe differences between the maximum frequency envelopes of the ensemble averaged filtered and unfiltered waveforms. These parameters are described by eqns (11) and (12) (see also Fig. 5).

$$\delta MAXF = MAXF(PS)_f - MAXF(PS)_r \quad (11)$$

where MAXF (PS) is the maximum frequency at peak systole for a threshold of 5.

$$\delta MINF = MINF(ED)_f - MINF(ED)_r \quad (12)$$

where MINF (ED) is the maximum frequency at end diastole for a threshold of 5. δMAXF and δMINF indicate the average amount of distortion of the maximum frequency envelope produced at peak systole and end diastole. These are two commonly used points from which indices such as resistance index (Pourcelot 1974) are calculated.

The average amount of distortion of the maximum frequency envelope produced by the filter at the downslope and upslope of the waveform is indicated by δMFE, and is given by eqn (13).

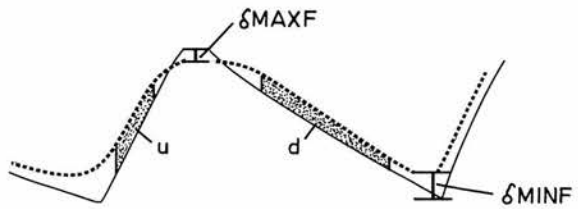

Fig. 5. The effect of filtering on the maximum frequency envelope. Envelopes are shown for the ensemble averaged unfiltered waveform (solid line) and for the ensemble averaged filtered waveform (dashed line). The differences have been exaggerated for clarity, δMAXF and δMINF relate to the blurring of the peak and trough respectively. δMFE relates to blurring in the region of the upslope (u) and downslope (d).

$$\delta MFE = \sum_{upslope} (MAXF(U)_f - MAXF(U)_r) + \sum_{downslope} (MAXF(D)_f - MAXF(D)_r) \quad (13)$$

where MAXF is the maximum frequency at a threshold of 5, U is the upslope of the waveform excluding the peak and trough and D is the downslope of the waveform excluding the peak and trough.

RESULTS

Parametric images

Local image measures were generated using a 9 × 9 window from one of the 'good' waveforms with a resistance index of 0.85. These are shown as parametric images in Fig. 6a–e. A parametric image is an image where the pixel value at a point is proportional to the value of the parameter under consideration at that point. It is the purpose of the local image measure to 'tell' the adaptive filter where a true structure is, so that the filter can apply minimum smoothing there. In this respect a parametric image which has high pixel values in the region of the edges of the waveform and low values elsewhere is desirable. Examination of these images will help to choose which local image measure may be useful in Lee's filter. The edge detection parameter RMAX gives a strong peak at the waveform outline with a small amount of noise above the outline (Fig. 6a). The maximum directional slope was relatively noisy; however, the sum Σ $SL(d)$ of the directional slopes was better (Fig. 6b). This parameter peaks just above, and for the leading edge, just below the waveform outline. The parameter standard deviation/mean (σ/m) peaked well above the waveform outline (Fig. 6c). This parameter also

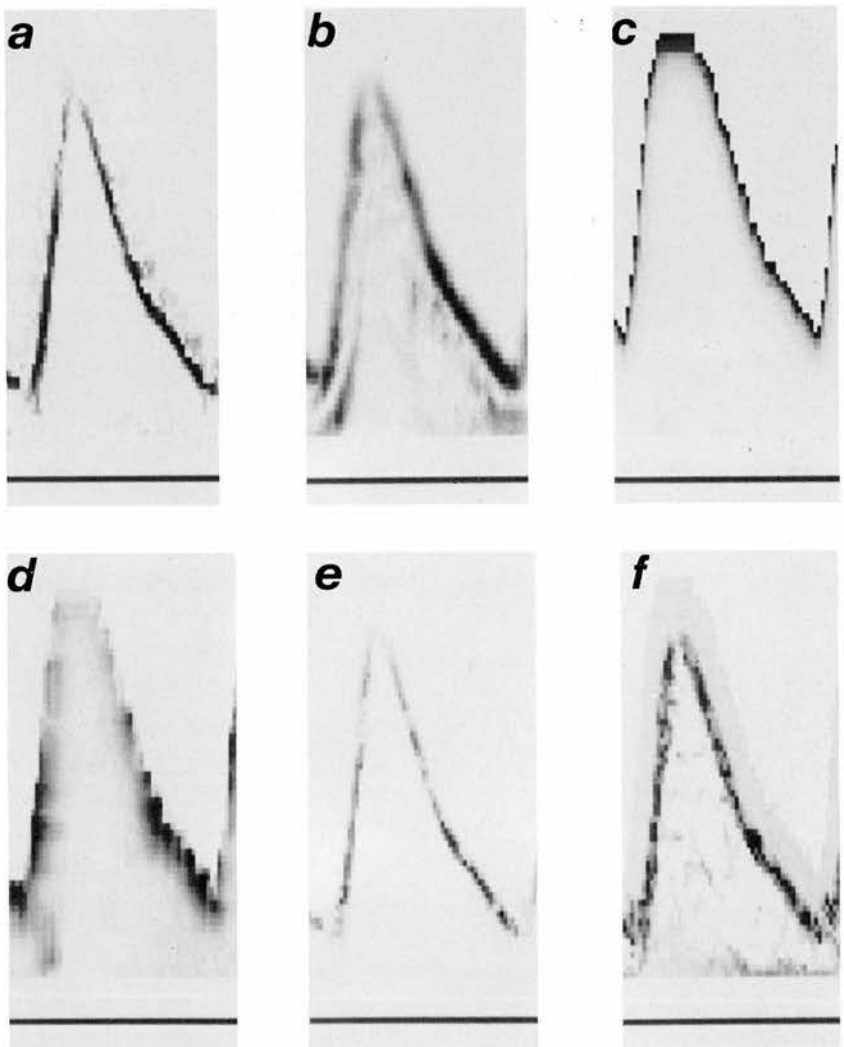

Fig. 6. Parametric images generated using waveform (b) of Fig. 4. (a) to (e) were produced using a 9×9 window. (a) Edge parameter *R*MAX; (b) $SL(d)$; (c) σ/m; (d) σ^2/m; (e) $(R(d)/SL(d))$ max; (f) was generated using eqn (10) where $C(d) = 1 + R(d)/SL(d)$.

gives extremely large values in the presence of a small amount of background noise above the waveform and is therefore not useful. The parameter variance/mean (σ^2/m) gives some peaking just above the waveform outline (Fig. 6d); however, this is inferior to that of the sum of slopes $\Sigma\, SL(d)$, so it will not be considered further. The parameter $R(d)/SL(d)$ can be calculated for each direction and the maximum value $[R(d)/SL(d)]_{max}$ found. This gives an image very similar to that of *R*MAX except that the noise above the outline has been removed (Fig. 6e).

For the directional filter it is not possible to display a single parametric image because the filter's action is controlled by eight normalised directional image measures (see eqn 3). However, by using the parameter P, defined below in eqn (14), it is possible to visualise those parts of the image where one of the directional image measures $C(d)$ is dominant.

$$P = \frac{\sum_{d=1}^{8} [C(d)]^2}{[\sum_{d=1}^{8} C(d)]^2}. \qquad (14)$$

Figure 6f shows the parametric image for P when $C(d) = 1 + R(d)/SL(d)$. This shows that there is a dominant directional value of $C(d)$ around the edge of the waveform with noise directly above this.

Comparison of filters

A comparison between the filters with associated local image measures chosen from above was per-

formed using the 'good' waveform with a resistance index of 0.85. Examples of this waveform after a variety of filters have been applied are shown in Fig. 7. Table 1 shows the indices of maximum frequency envelope distortion, bias and noise reduction calculated from the ensemble of waveforms.

From Table 1 it can be seen that all the filters perform very well in the uniform central area. They offer considerable noise reduction, by a factor varying between 4.06 and 5.75, and also introduce almost negligible bias as indicated by the values of RH_{CA} which are very close to 1. However, as far as the leading edge region is concerned, significant differences in performance can be found. Filters (a) and (b) reduce the edge height considerably, by 46% and 43% respectively, while offering only moderate noise reduction. Filters (c) and (d) preserve the edge height but at the expense of negligible noise reduction. On the other hand, the directional filters (e) and (f) offer a reasonable compromise between noise reduction and edge preservation. This is due to the fact that in the vicinity of an edge smoothing is performed only along the edge axis, something which improves its definition without introducing excessive blurring.

The same conclusions about the superiority of filters (e) and (f) can be drawn by visual examination of the images in Fig. 7. The filtered spectra (a) to (d) are composed of smooth areas together with very noisy edges and overall have a very unbalanced appearance. On the other hand, the spectra (e) and (f)

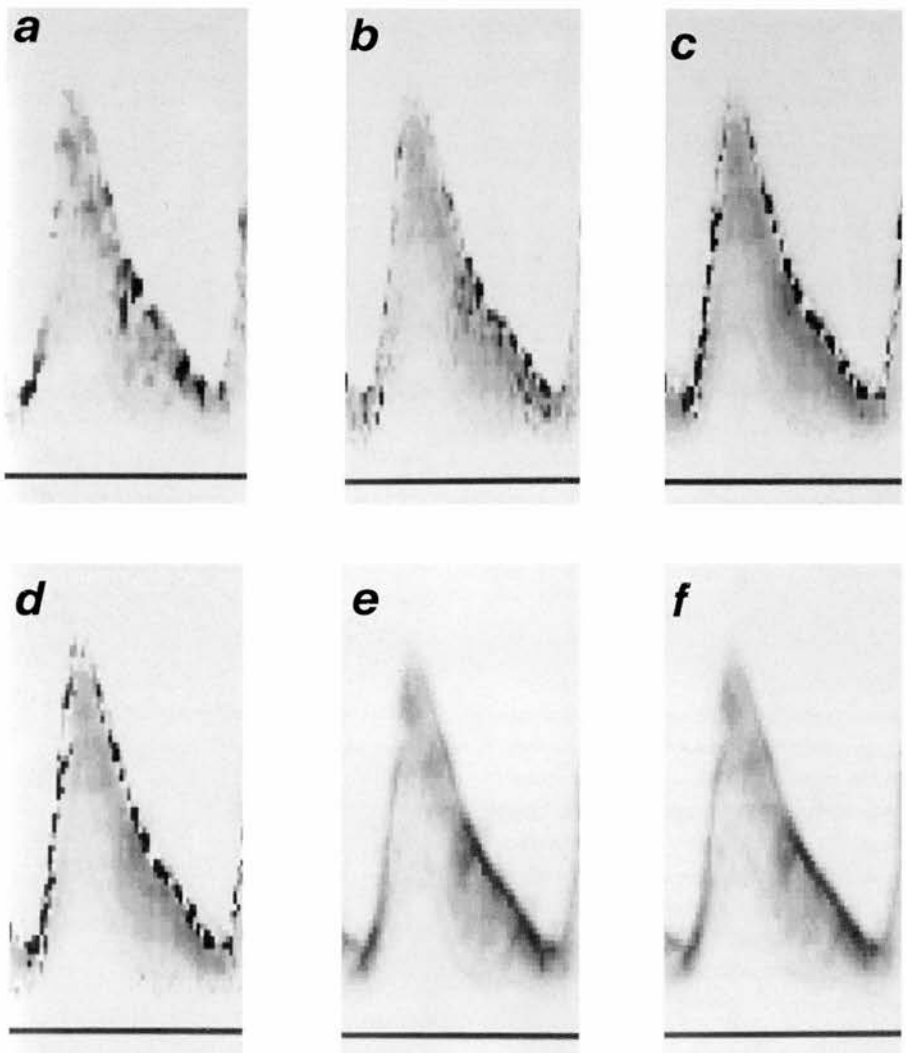

Fig. 7. Processing using different filters. Waveform (b) of Fig. 4 was used in each case. (a) DWMTM; (b) Lee filter with sum of slopes parameter $SL(d)$; (c) Lee filter with edge parameter RMAX; (d) Lee filter with $[R(d)SL(d)]$max; (e) Directional filter with edge parameter $R(d)$; (f) Directional filter with parameter $1 + R(d)/SL(d)$.

Table 1. Indices of bias and variance for unfiltered data and for filtered data. Waveform (b) of Fig. 4 was used in each case.

Filter or raw data	Parameter C or $C(d)$	MFE indices			Leading edge		Uniform central area	
		δMAXF (Hz)	δMINF (Hz)	δMFE (Hz)	RH_{LE}	RCV_{LE}	RH_{CA}	RCV_{CA}
(a) DWMTM	—	−100	0	−46	0.54	1.37	0.95	4.06
(b) Lee	$\Sigma\, SL(d)$	−50	0	40	0.57	1.70	1.04	5.31
(c) Lee	RMAX	−50	+200	81	1.00	1.02	1.05	5.75
(d) Lee	$\left(\frac{R(d)}{SL(d)}\right)_{\max}$	−50	0	70	0.94	1.00	1.05	5.31
(e) Direc.	$R(d)$	−50	+150	104	0.72	3.15	1.03	4.31
(f) Direc.	$1 + \frac{R(d)}{SL(d)}$	−100	+100	70	0.74	3.15	1.04	4.31

are much more balanced. There is very little to choose between (e) and (f). However, on the basis of the maximum frequency envelope indices and especially δMFE (see Table 1), the directional filter (f) which is controlled by the local image measure $C(d) = 1 + R(d)/SL(d)$ is preferable.

The effectiveness of speckle suppression is demonstrated by Fig. 8 where it can be seen that the spectral profile obtained from ensemble averaging of 168 raw waveforms is very similar to the profile of a single waveform smoothed by filter (f). Figure 9 shows the application of this filter to the six different waveforms

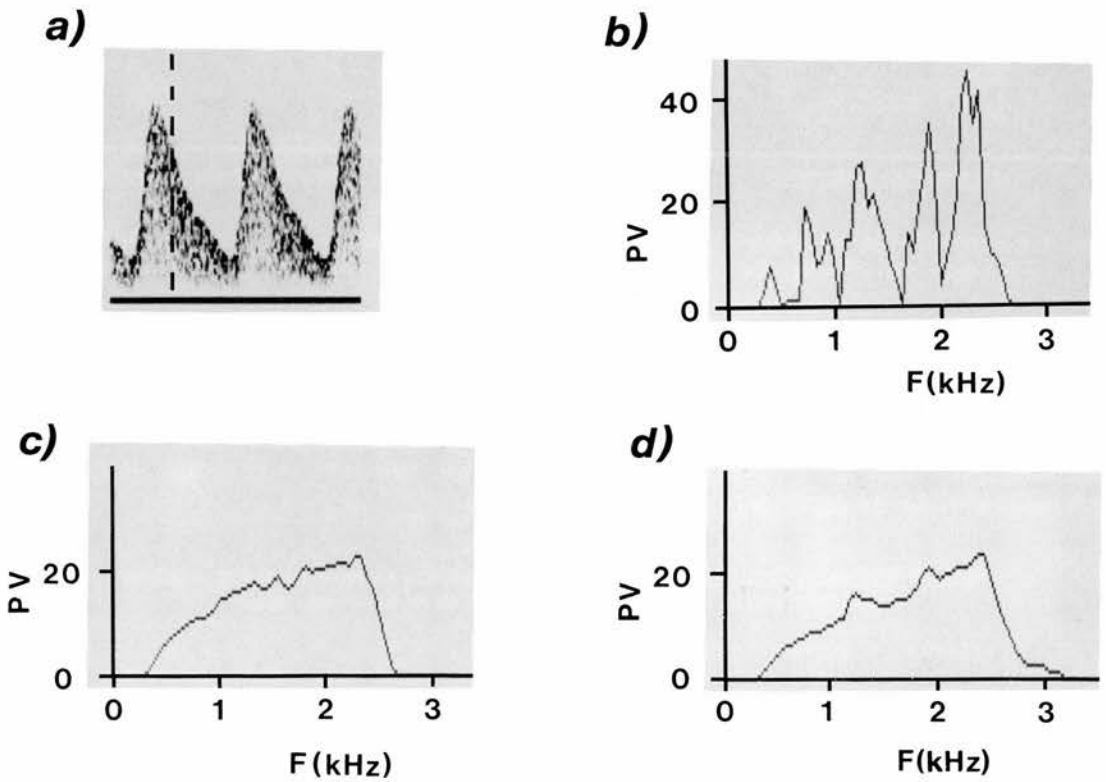

Fig. 8. Profiles from waveform (b) of Fig. 4 (a) Single unfiltered waveform—the profile position is indicated by the dashed line; (b) Profile from a single unfiltered waveform; (c) Profile from ensemble averaging of 168 unfiltered waveforms; (d) Profile from a single filtered waveform.

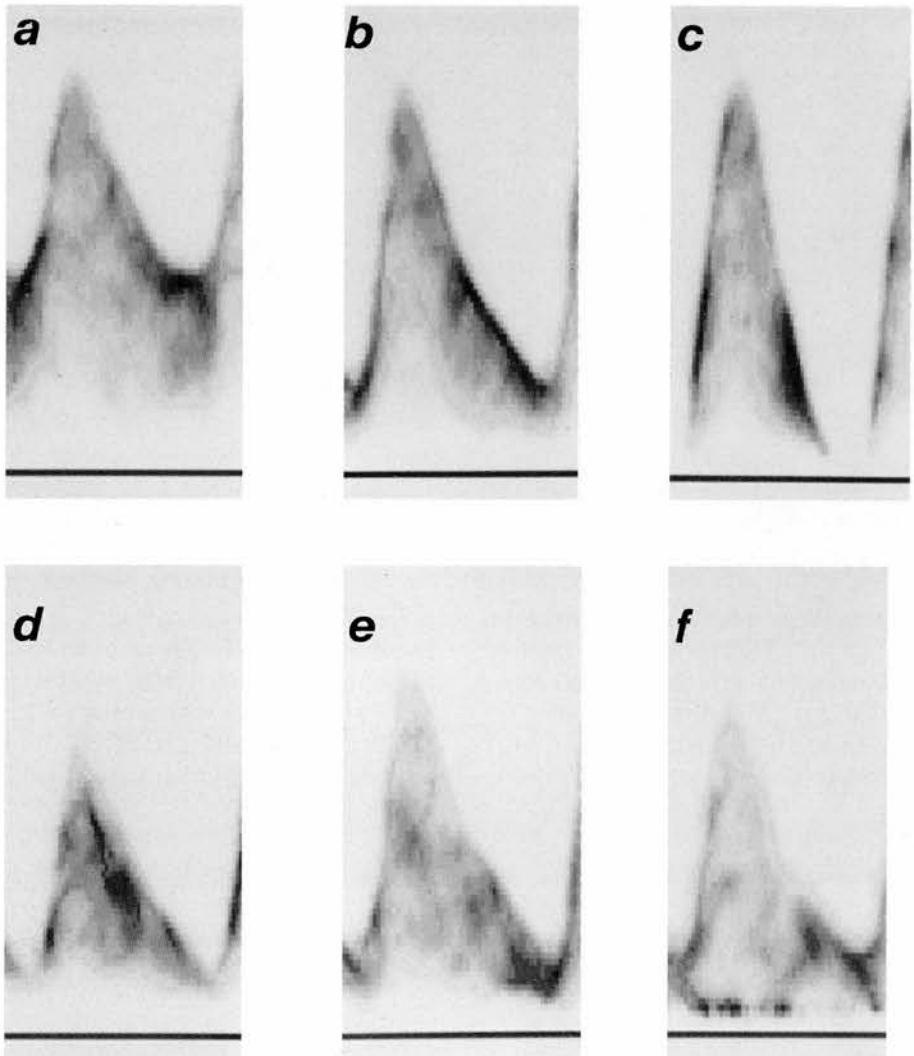

Fig. 9. Examples of individual filtered waveforms. These are the filtered versions of the waveforms shown in Fig. 4. The filter was the directional filter with parameter $1 + R(d)/SL(d)$ in each case.

of Fig. 4 whereas Table 2 lists the quantitative indices related to each waveform type. The upper region (UR) indices are presented only for waveform (f) because it is the only one with background noise above the waveform outline. There are differences in each of the other indices for the six waveforms, which are, however, small. Since the waveforms used were chosen to represent the range of shapes encountered in practice, this suggests that the directional filter controlled by the parameter $C(d) = 1 + R(d)/SL(d)$ will perform similarly over a wide range of waveform types.

Table 2. Indices of bias and variance for the six different waveforms of Fig. 4 when the directional filter with parameter $1 + R(d)/SL(d)$ was used.

Waveform	δMAXF (Hz)	δMINF (Hz)	δFME (Hz)	RH_{LE}	RCV_{LE}	RH_{CA}	RCV_{CA}	RH_{UR}	RCV_{UR}
(a)	0	50	53	0.78	3.81	0.98	5.03	—	—
(b)	−100	+100	70	0.74	3.15	1.04	4.31	—	—
(c)	−50	0	82	0.65	3.10	1.03	5.65	—	—
(d)	−50	+50	38	0.80	2.52	1.06	4.36	—	—
(e)	−50	+100	28	0.84	4.13	1.03	5.19	—	—
(f)	−50	+100	82	0.78	4.57	1.04	4.82	1.05	4.18

Table 3. Indices of bias and variance averaged over the six waveforms of Fig. 9.

Location	Index	Value
Maximum frequency envelope	$\delta MAXF$	−50 Hz
	$\delta MINF$	+67 Hz
	δMFE	+59 Hz
Leading edge	RH_{LE}	0.77
	RCV_{LE}	3.4
Central area	RH_{CA}	1.03
	RCV_{CA}	5.0
Upper region	RH_{UR}	1.05
	RCV_{UR}	4.2

Table 3 presents the mean values of the quantitative indices for the six waveforms. These can be considered as a measure of the filter's average performance. The indices describing the distortion introduced by the filter to the maximum frequency envelope have small values, indicating a small yet systematic bias in threshold maximum frequency calculations. The performance in edge preservation described by RH_{LE} shows a 23% average loss of height for the leading edge. The bias introduced by the filter in the uniform central area and the upper region with background noise is very small (RH_{CA} = 1.03, RH_{UR} = 1.05). Filtering has resulted in noise reduction varying between a factor of 3.4 at the leading edge and 5.0 at the central area.

DISCUSSION

This study has demonstrated that Doppler speckle reduction can be performed to reveal the underlying Doppler spectrum. The filtered spectrum will have a degree of bias in those regions of the spectrum containing edges. However, this is a natural consequence of performing noise reduction by averaging over a finite area. Though a detailed investigation of the applications of this technique is beyond the scope of this publication, two examples of possible uses will be discussed below.

A common problem in Doppler ultrasound is the detection of the maximum frequency envelope. A widely used maximum frequency follower for a single Doppler profile defines the maximum frequency as the location of the first pixel whose value is greater than a specified threshold. However, when extraneous background noise is present, a threshold higher than the largest noise value must be chosen to avoid detection of artefactually high maximum frequencies. Figure 10a shows the maximum frequency envelope from a set of waveforms with high background noise. Unfortunately, the necessary use of a high threshold value has caused underestimation of the maximum frequency at a number of points and the envelope is very noisy. Figure 10b shows the maximum frequency envelope from the same set of waveforms after filtering by the optimal directional filter. In this case there is much better detection of the maximum frequency envelope with fewer erroneous

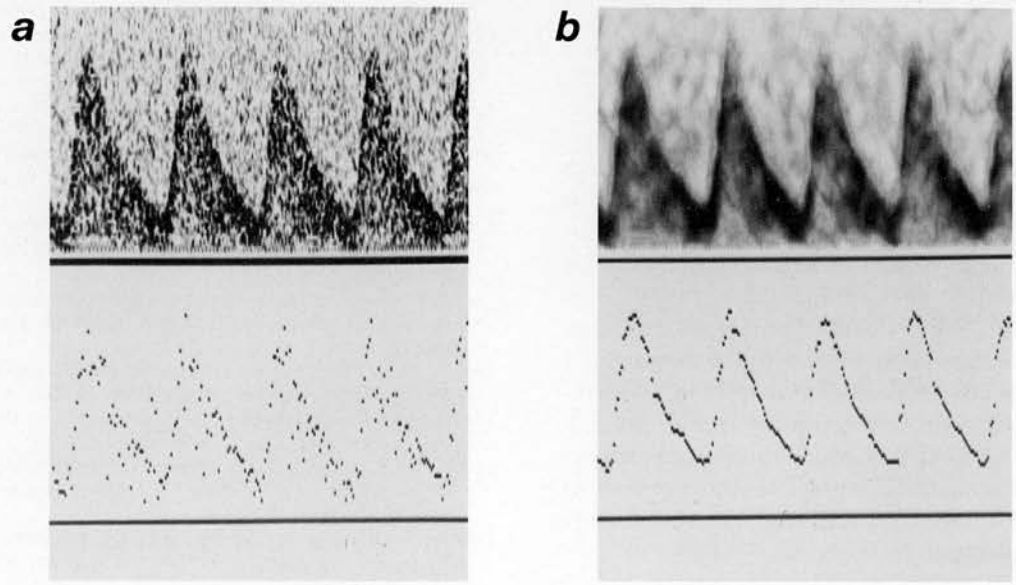

Fig. 10. Doppler spectra of waveforms with a large amount of background noise, (a) before filtering and (b) after filtering with the optimal directional filter. The maximum frequency envelope is detected with fewer erroneous points when calculated from the filtered spectra of (b).

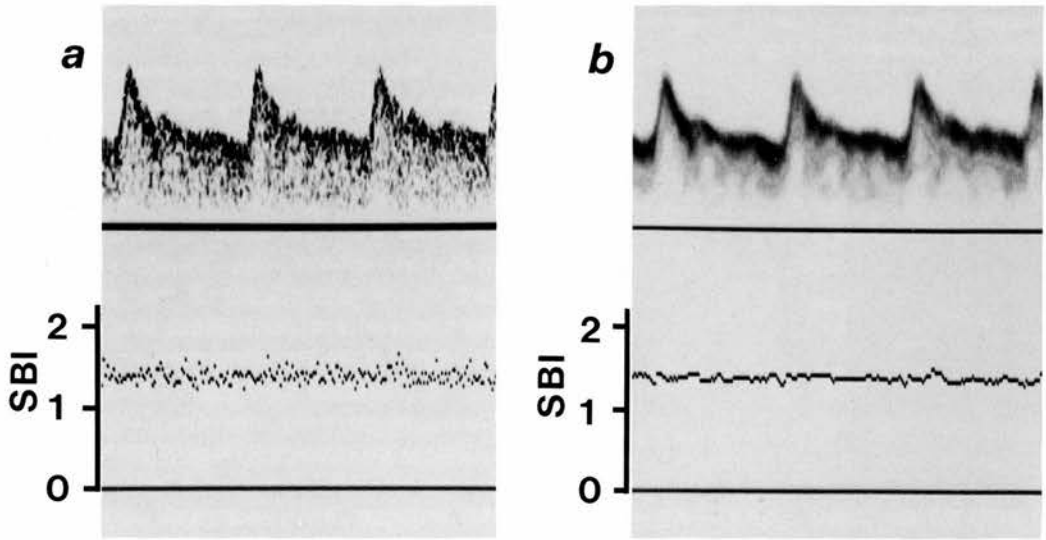

Fig. 11. Internal carotid artery Doppler spectra, (a) before filtering and (b) after filtering with optimal directional filter. The spectral broadening index SBI is F_{max}/F_{mean}. This index shows less variability with time when calculated from the filtered Doppler waveforms.

points. This is a consequence of the lower threshold value which can be used when the noise level has been reduced.

Figure 11 shows an unprocessed normal internal carotid artery waveform and also the same waveform after filtering using the optimal directional filter. Also shown is the change in the commonly used spectral broadening index F_{max}/F_{mean} (Sheldon et al. 1983) with time. It can be seen that there is less variation of F_{max}/F_{mean} for the filtered waveform resulting in a more robust and reliable estimate of the spectral broadening index.

CONCLUSION

This paper investigated the application of image processing techniques for speckle reduction in Doppler spectra. Three different filters with associated local image measures were compared. The filter giving the best performance, in terms of compromise between bias introduced and noise reduction offered, was the directional filter with the parameter $1 + R(d)/SL(d)$. This technique may be of use for improved performance of maximum frequency followers and in the calculation of quantitative information based upon the Doppler spectrum, such as spectral broadening indices for carotid artery Doppler waveforms.

Acknowledgements—Thanks to Mrs. A. McMillan and Mrs. D. Nicholson for secretarial work.

REFERENCES

Bamber, J. C.; Cook-Martin, G. Texture analysis and speckle reduction in medical echography. SPIE Proc. 768:120–127; 1987.

Bamber, J. C.; Daft, C. Adaptive filtering for reduction of speckle in ultrasonic pulse echo images. Ultrasonics 24:41–44; 1986.

Bovik, A. C.; Huang, T. S.; Munson, D. C., Jr. A generalisation of median filtering with linear combinations of order statistics. IEEE Trans. Acoust. Speech Sig. Proc. 31:1342–1350; 1983.

Chan, P.; Lim, J. S. One dimensional processing for adaptive image restoration. IEEE Trans. Acoust. Speech Sig. Proc. 33:117–126; 1985.

Hoskins, P. R.; Anderson, T.; McDicken, W. N. A computer controlled flow phantom for generation of physiological Doppler waveforms. Phys. Med. Biol. 34:1709–1717; 1989.

Hoskins, P. R.; Loupas, T.; McDicken, W. N. A comparison between human blood and artificial blood used in a flow phantom. Ultra. Med. Biol. 16:141–147; 1990.

Kay, S. M.; Marple, S. L., Jr. Spectrum analysis—a modern perspective. IEEE Proc. 69:1380–1419; 1981.

Kim, N. C.; Jung, S. H. Adaptive image restoration using local statistics and directional gradient information. Electronics Lett. 23:610–611; 1987.

Kuan, D. T.; Sawchuck, A. A.; Strand, T. C.; Chavel, P. Adaptive restoration of images with speckle. IEEE Trans. Acoust. Speech Sig. Proc. 35:373–383; 1987.

Lee, J. S. Digital image enhancement and noise filtering by use of local statistics. IEEE Trans. Pat. Anal. Mach. Int. 2:165–168; 1980.

Lee, J. S. Speckle analysis and smoothing of synthetic aperture radar images. Comp. Graph. Im. Proc. 24:255–269; 1981.

Lee, J. S. Speckle suppression and analysis for synthetic aperture radar images. Opt. Eng. 25:636–643; 1986.

Lee, Y. H.; Kassam, S. A. Generalised median filtering and related nonlinear filtering techniques. IEEE Trans. Acoust. Speech Sig. Proc. 33:672–683; 1985.

Loupas, T. Digital image processing for noise reduction in medical ultrasonics. Edinburgh, Scotland: University of Edinburgh; 1988. Ph.D. thesis.

Luckman, N. P.; Skidmore, R.; Evans, J. M.; Jenkins, D.; Wells, P. N. T. The effect of acoustic speckle on ultrasonic Doppler

studies of blood flow. In: Evans, D. H.; Martin, K., eds. Physics in medical ultrasound II. York, England: IPSM; 1988.

McDicken, W. N. A versatile test-object for the calibration of ultrasonic Doppler flow instruments. Ultra. Med. Biol. 12:245–249; 1986.

Mo, L. Y. L.; Cobbold, R. S. C. 'Speckle' in continuous wave Doppler ultrasound spectra; a simulation study. IEEE Trans. Ultra. Ferr. Freq. Contr. 33:747–753; 1986.

Oppenheim, A. B.; Schafer, R. W. Digital signal processing. Englewood Cliffs, NJ: Prentice Hall; 1975.

Peli, E. Adaptive enhancement based on a visual model. Opt. Engin. 26:655–660; 1987.

Pourcelot, L. Applications cliniques de l'examen Doppler transcutané. In: Vélocimétrie ultrasonore Doppler, Séminaire INSERM, Paris; 1974:213–240.

Rittgers, S. E.; Thornhill, B. M.; Barnes, R. W. Quantitative analysis of carotid artery Doppler spectral waveforms: Diagnostic value of parameters. Ultra. Med. Biol. 9:255–264; 1983.

Schlindwein, F. S.; Evans, D. H. A real-time autoregressive spectrum analyser for Doppler ultrasound signals. Ultra. Med. Biol. 15:263–272; 1989.

Sheldon, C. D.; Murie, J. A.; Quin, R. O. Ultrasonic Doppler spectral broadening in the diagnosis of internal carotid artery stenosis. Ultra. Med. Biol. 9:575–580; 1983.

Vaitkus, P. J.; Cobbold, R. S. C. A comparative study and assessment of Doppler ultrasound spectral estimation techniques. Part I: estimation methods. Ultra. Med. Biol. 14:661–672; 1988a.

Vaitkus, P. J.; Cobbold, R. S. C.; Johnston, K. W. A comparative study and assessment of Doppler ultrasound spectral estimation techniques. Part II: methods and results. Ultra. Med. Biol. 14:673–688; 1988b.